5-2006

Numerical Simulation of Flow over a Surface-mounted Cube with the Vorticity Confinement Method

Min Xiao
University of Tennessee - Knoxville

To the Graduate Council:

I am submitting herewith a dissertation written by Min Xiao entitled "Numerical Simulation of Flow over a Surface-mounted Cube with the Vorticity Confinement Method." I have examined the final electronic copy of this dissertation for form and content and recommend that it be accepted in partial fulfillment of the requirements for the degree of Doctor of Philosophy, with a major in Engineering Science.

John S. Steinhoff, Major Professor

We have read this dissertation and recommend its acceptance:

John E. Caruthers, Boris Kupershmidt, K. C. Reddy

Accepted for the Council:
Dixie L. Thompson

Vice Provost and Dean of the Graduate School

(Original signatures are on file with official student records.)

To the Graduate Council:

I am submitting herewith a dissertation written by Min Xiao entitled "Numerical Simulation of Flow over a Surface-mounted Cube with the Vorticity Confinement Method." I have examined the final electronic copy of this dissertation for form and content and recommend that it be accepted in partial fulfillment of the requirements for the degree of Doctor of Philosophy, with a major in Engineering Science.

John S. Steinhoff

Major Professor

We have read this dissertation
and recommend its acceptance:

John E. Caruthers

Boris Kupershmidt

K. C. Reddy

Accepted for the Council:

Anne Mayhew

Vice Chancellor and Dean of
Graduate Studies

(Original Signatures are on file with official student records.)

NUMERICAL SIMULATION OF FLOW OVER A SURFACE-MOUNTED CUBE WITH THE VORTICITY CONFINEMENT METHOD

A Dissertation
Presented for the
Doctor of Philosophy
Degree
The University of Tennessee, Knoxville

Min Xiao
May 2006

Dedication

This dissertation is dedicated to my parents, Runchang Xiao and Cui’e Chen, and my husband, Xiaohai Chen, for always supporting and encouraging me. Without their love, support and patience, this work would not have been possible.

Acknowledgement

I would like to express my deepest gratitude to my advisor, Professor John Steinhoff, for his continuous inspiration, encouragement and technical instruction throughout my graduate studies.

Sincere thanks are extended to other committee members: Dr. K.C. Reddy, Dr. John Caruthers, Dr. Boris Kupershmidt, for their knowledgeable comments and advice.

Special thanks to my colleagues in UTSI and Dr. Wenren Yonghu and Dr. Lesong Wang of Flow Analysis, Inc. for the valuable discussions and assistance.

Abstract

Over the last several years, Vorticity Confinement has been shown to be a very efficient method to simulate the vortex-dominated flows over complex configurations. To calculate these flows, no high-order numerical scheme and body conforming grids are required for this method and only a fixed, uniform Cartesian grid is employed.

First, an overall description of the original Vorticity Confinement method (VC1) is presented, followed by an introduction of the newly developed Vorticity Confinement method (VC2). The advantage of VC2 over VC1 is the ability to conserve the Momentum. Two different numerical schemes are shown for VC1 and VC2. The one for VC2 is much simpler than that of VC1. Results of VC1 and VC2 for convecting vortices and scalars in 1-D and 2-D will be presented.

Numerical results are presented for the three dimensional flow over a surface-mounted cube. Comparisons have been made with experimental and Large Eddy Simulation (LES) data. It is observed that with a coarse uniform Cartesian grid, Vorticity Confinement is able to get results in better agreement with the experimental results than the LES simulation results on a fine grid. This method is shown to be more effective than trying to model and discretize more complex system of equations in the traditional methods, when solving complex high Reynolds number flow problems.

Contents

List of Figures

Nomenclature

$\vec{q}$	Velocity defined at the grid point
$\vec{q}_\infty$	Free stream velocity
CFL	Courant-Friedriches-Lewy number
P	Pressure
t	Time
C_p	Pressure Coefficient
u, v, w	Velocity components along the x, y, z directions
ε	Vorticity Confinement coefficient
μ	Diffusion coefficient
$\hat{n}$	Unit vector
N	Total number of points in harmonic mean
ρ	Density
a	Weighting factor for Vorticity Confinement
F	A function that defines the sold body surface
Δt	Computational time step
$\vec{\omega}$	Vorticity vector
$\vec{s}$	Vorticity Confinement vector
x, y, z	Coordinates of the Cartesian grid
Φ	Harmonic mean of a scalar variable
ϕ	Scalar variable
C_l	Weighting factor of the harmonic mean
$< Q >$	Centroid of the velocity
δ	Small number to avoid numerical overflow
$\vec{W}$	Harmonic mean vector
$< \vec{X} >$	Centroid of the confined scalar variables

P_{∞}	Pressure at the infinity
η	Scalar field
$\Delta x, \Delta y, \Delta z$	Computational grid spacing along the x, y, z directions
H	Cube dimension
$u_{\infty,} v_{\infty}$	Uniform free stream flow velocity components

Chapter 1 Introduction

1.1 Background

The establishment of the theory of fluid dynamics and the practical application of that science has been under way since the age of Newton. Over the last 250 years, fluid dynamics has been studied from two main approaches: theoretical analysis and experimental observation. The modern theoretical development of fluid dynamics focuses (initiated by Euler [1]) mainly on the construction and resolution of the governing equations for different types of flow problems and the study of various approximations to these equations. On the other hand, experimental fluid dynamics has played an important role in providing reliable measurement data to validate and delineate the limits of the various approximations to the governing equations. It was realized a long time ago that there were a large number of complex flow problems which were not amenable to theoretical solutions; indeed the known exact solutions available for the governing equations are of little practical application. At the same time, experimental measurements, though very effective and accurate, may take a significant amount of time and resources, such as the equipment and personnel, etc. In addition, many important quantities are very difficult to measure.

The era of Computational Fluid Dynamics (CFD) began with the advent of high speed and large-memory computers. Since the early 1960s, as computers became fast and large enough to make it possible to perform direct numerical simulation of complex flow

problems, more and more scientific research effort was focused upon the development of advanced numerical algorithms for solving real-world problems. By the early 1970s, the computation of fluid problems were undertaken, which has led to CFD becoming the third division of simple fluid dynamic research combined with the expeditious development of large computers. As a new branch of fluid mechanics, CFD complements experimental and theoretical fluid dynamics by providing an alternative cost-effective tool to simulate real flows, focusing on the development and employment of computer-based tools to solve the partial differential equations (pde's), which describe the fluid flow. Over the past four decades, CFD has been developed to become a broadly-used practical means employed by engineers in virtually every industry. It is now becoming a significant method in the industry application, such as design and analysis of the performance of aircraft, flow machinery and, to a lesser extent, in the automobile industries.

In retrospect the beginning of CFD as an independent science was in 1928 with the precursory work of Courant, Friedrich and Lewy [2] who introduced the concept of the stability requirement (CFL condition) for hyperbolic partial differential equations. In 1950, Von Neumann [3] further developed the stability criteria for parabolic time-marching problems. With the exponential growth of high-speed computers and considerable fundamental research, tremendous progress was witnessed in the 1950s and 1960s towards the numerical simulations of inviscid compressible flow problems. Starting with the shock-capturing technique of Lax [4], a great many methods have been developed and the most important and fundamental two are finite difference methods (FDM) and finite elements methods (FEM). These basic schemes used in the numerical simulations of pde's are based upon different concepts. Earlier publications of FDM include Courant, Friedrichs and Lewy [2], Godunov [5], Lax and Wendroff [6], McCormack [7], and many others. Earlier research work on FEM include Zienkiewicz and Cheung [8], Baker [9], and Pepper and Heinrich [10]. In the late 1970s and 1980s

extensive interest has been evinced on the techniques for simulating flows over arbitrary shaped geometries. Methods for transforming complex geometries into simple ones have been proposed and excellent discussion on these methods are provided in the book by Thompson, Warsi and Mastin [11].

Considering two essential characteristics of CFD, the economy and ability of handling complex geometry, it is very important to develop methods that are cost effective and easy to adapt for various problems across different areas [12]. However, most of the conventional CFD methods typically require large computer resources and difficult grid generation when dealing with complex flow situations. Meanwhile, most of the real-world flows are at high Reynolds numbers and turbulent. This implies that they are characterized by concentrated vorticity, which can convect over long distance, either as thin vortex filaments or as blunt body wakes. Due to lack of sufficient computer resources and adequate mathematical model support, complex flow problems can only be simulated through some approximate models. As a result, conventional CFD methods involve first formulating the pde's and modeling turbulence in turbulent flow regions. These modeled pde's are then discretized in the turbulent regions and solved. The problem is that resolving even the modeled pde's requires very fine computational grids, which must conform to the body geometry to capture the boundary layer. Further, these methods typically dissipate thin filaments and vortical structures as they are convected in the wake. The problem is intrinsic to the discretization of the convective terms and made worse by use of the dissipative terms to model turbulence and to present numerical stability.

Turbulence, one of the most exciting research topics in modern science, has most of its solution procedures using turbulence models which are approximations of the real physical phenomena and the success of such models depends on the choice of some

empirical coefficients. Accuracy of the results will definitely depend on the correctness of the models. In recent time there is an approach, which is known as Direct Numerical Simulation (DNS) of the Navier-Stokes equation for turbulence (Rai and Moin [13]) and provides us direct insight into turbulence if a fine enough grid can be used. LES is another modeling technique intermediate between DNS and turbulence models. In the LES method, the contribution of small scales is modeled while that of large scales is computed accurately [13]. Computers in the foreseeable future do not have the capacity for DNS due to small scales inherent to turbulence. Thus, although conventional methods may be efficient for some flows with relatively low Reynolds numbers or simple body geometries, they are inefficient and sometimes not even feasible for flows with multiple thin vortices convecting over long distances. The same is true for high Reynolds number flows over complicated bodies [11][14][15].

The main objective of this thesis is to describe the theory of an entirely new and more advanced CFD methodology, which is called the Vorticity Confinement method and was first developed by Steinhoff and his associates [16]. During the past sixteen years, Vorticity Confinement has already been demonstrated to be a very efficient and economical method to compute vortex dominated flows [14][15][17][18][19]. The basic idea behind the Vorticity Confinement method is similar to that of the shock-capturing method (Lax [4]). In the shock-capturing method, shocks are treated as thin features of only a few grid cells convecting in the computational domain and obeying discretized nonlinear equations. The theory of shock capturing can, in retrospect, be traced to as early as 1940s when Von Neumann brought forward a central difference scheme to treat the shock problems. Though efficient at keeping the shock features, there were numerical oscillations. To prevent these oscillations, Von Neumann and Richtmyer [3] in 1950 introduced a totally new methodology by adding a numerical viscous term to the

discretized equations of the shock problems. This added term was of the same order as the truncation error of the discretized equations and the oscillations were eliminated by adding this artificial viscosity. Like the shock-capturing method, Vorticity Confinement treats the thin vortical regions as a small flow feature spread over only a few grid cells on a coarse Cartesian grid. Hence, the main point of Vorticity Confinement is to model the internal structures of the vortical regions directly on the grids using nonlinear pde's. This contrasts with the conventional CFD methods, which model the governing pde's first and then discretize the modeled pde's and attempt to approximately resolve the modeled equations using finite difference methods. It should be mentioned that the shock-capturing method is much simpler than the Vorticity Confinement method due to the natural compressive action of shocks. After nearly two decades of investigation and endeavor, Vorticity Confinement has been proven to be more effective than trying to model and discretize the governing pde's when solving complex high Reynolds number flow problems.

As in the shock capturing method, the most prominent feature of Vorticity Confinement is the introduction of a nonlinear diffusion term to the governing pde's, which is negative, or "compressive". With this added term, the complex flow problems can be solved on coarse, uniform Cartesian grids and the thin vortical regions can convect without spreading over large distances. These modeled pde's can capture small vortical features with only two to three grid cells. But when treating the large scale features of the flow, this method works like conventional CFD methods and the confinement term disappears outside of the thin vortical regions. Therefore, the Vorticity Confinement method has not only the generality of standard CFD methods, but also treats vortical regions without numerical diffusion as they convect through flows even in regions where the computational grid is relatively coarse. The most advanced feature of this method is

that it is employed only on a fixed, uniform Cartesian grid without the need for a body-fitted grid or any other special arrangement to treat the thin vortical regions. Compared with the conventional CFD methods, the required computer resource and computational time are much less when Vorticity Confinement is applied. There is no need to make assumptions in order to model the governing pde's as in typical CFD methods, and the numerical algorithms employed in Vorticity Confinement are much simpler. Nowadays, Vorticity Confinement has grown to become a common numerical method, and it is not limited to complex fluid problems. A significant number of scientific problems, where the numerical spreading of small flow features is one of the major concerns, can be treated by this method. Acoustics wave problems are another area of application. One of the most exciting applications of the Vorticity Confinement method is in the movie industry to simulate smoke or tornados. Examples include <Harry Potter II>, <The Core>, <Terminator III>,<The Day after Tomorrow> and many others.

1.2 Objectives and Structure

1.2.1 Motivation

Early research on turbulent boundary layer flow first considered such flow as containing random fluctuations superimposed upon an otherwise mean flow. From the late 50's to the early 60's, experiments [20] revealed that the near-wall regions are dominated by organized coherent structures and since then much effort has been spent to identify these structures. Both experimental observations and numerical simulations have been used to illustrate these flow features. Theodorsen [21] was one of the first to identify the presence of these coherent structures. The hydrogen bubble studies Kline [20] showed that there were low-speed stream-wise streaks in the sub-layer and these low-speed streaks lift up and interacted with the outer-layer, in a "bursting process" and this was

originally believed to be a single process. The Flow visualization studies of Head and Bandyopadhyay [22] revealed that in the near wall region there existed a forest of hairpin-like or horseshoe-like structures inclining along the stream-wise direction and interacting with the outer region of the boundary layer. Nishioka [23] investigated the evolution of these hairpin-like structures and found that these vortices played an essential role in the turbulence and momentum transfer in the near wall regions. As the hairpin vortices were lifted they gave rise to the development of new hairpin vortices. This continuous process conforms to the self-sustaining characteristic of the turbulent boundary layer.

The review by Robinson [24] has summarized these coherent structures into eight categories: low-speed steaks in the near wall regions, ejections, sweeps, vortical structures, near-wall shear layers, near-wall pockets, large-scale motions in the outer regions and shear layer “backs” of large scale motions. The structure of Robinson’s hairpin vortex is shown in Fig.1-1. These eight elements provide basic insight into the coherent structure of a turbulent boundary layer and have been widely accepted nowadays. However, the number of constituting elements was deceptively large and many experiments were done to extract a much simpler structure to combine these eight elements. Recent experiments performed by Meinhart [25] and Meinhart and Adrian [26] have revealed the existence of inclined hairpin vortices in the wall turbulent layer. Many numerical simulations were performed to reveal the formation and development of hairpin vortices. Recent numerical results obtained by Zhou [27] offered strong insights of the mechanism of the formation of the new hairpin vortex and the development of a hairpin vortices packet. The initial flow field was a viscous, hairpin-like structure, which was referred as the parent vortex. In his results, new hairpin vortices were generated both downstream and upstream of the parent vortex, and after a certain time, a packet of hairpin vortices was formed.

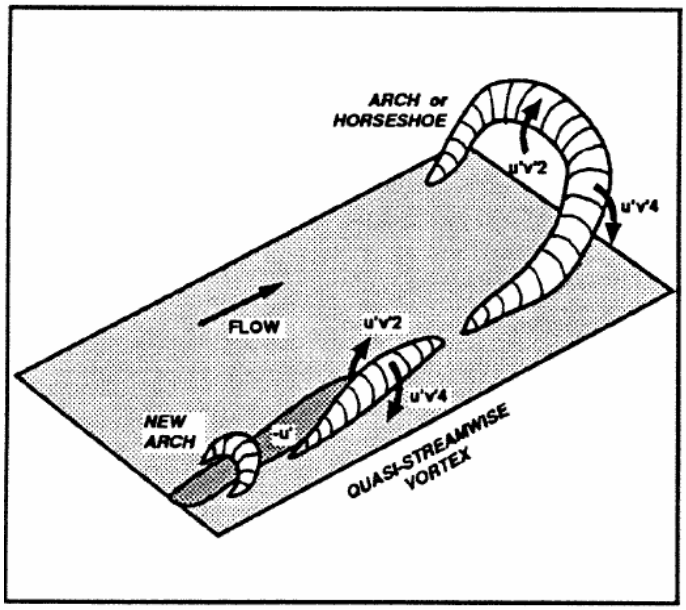

Figure 1-1: Vortical structures in a low Re flat plate boundary layer

Acarlar and Smith [28] gave a schematic of the formation of the hairpin vortex, which is shown in Fig.1-2. Above a height, fluid approaching the hemisphere from upstream will whirl around the core of two-counter-rotating vortex legs of the hairpin vortices and be convected downstream, as shown in Fig.1-2. Fluid particles under this height will pass into the formed standing vortex, the horseshoe vortex around the hemisphere, and are then convected downstream.

1.2.2 Objective

A numerical investigation of the flow over a surface-mounted cube has been undertaken using the Vorticity Confinement method. The result will be compared with that of the experimental study.

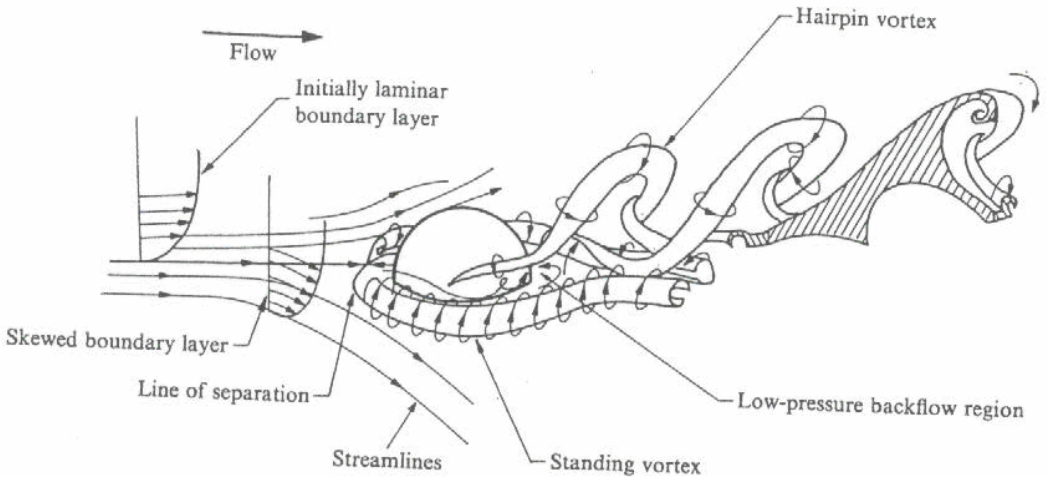

Fig. 1-2 Schematic of near-wake structure in the hemisphere wake

1.2.3 Organization

The dissertation is organized into five main chapters. The first Chapter is the review of the background of the current study. Some of the conventional CFD methods are briefly described.

The second Chapter is the summary of the current numerical method of Vorticity Confinement. The detailed numerical scheme is there presented. The third Chapter is dedicated to a thorough analysis of 2-D flow simulation results by Vorticity Confinement. Flow over a surface-mounted cube is investigated in a 3-D domain in Chapter 4. The results are presented and discussed in detail. Comparisons with experimental results are made whenever possible.

Some final remarks and recommendations for future studies conclude the dissertation in Chapter 5.

Chapter 2 Vorticity Confinement

Over the last few years, Vorticity Confinement has been proven to be a very efficient and effective method to simulate high Reynolds number flows and significant work has been done as reported in [30][31][32][33][34]. It is well-known that the governing pde's for fluid flow problems are the Navier-Stokes equations. In traditional CFD simulations, it is usual to use modeled dissipative terms to approximate high Reynolds number flows problems. When the Navier-Stokes equations are discretized, there is usually significant numerical diffusion beyond the natural viscous diffusion no matter what kind of numerical schemes is employed. To get accurate computational results, it is very important to reduce this diffusion so that viscous flow regions retain their correct length scales. Normally very fine grids must be used to achieve this, often with extensive refinement near the body surface, or adaptive grids with extensive refinement within shed vortex sheets and filaments. To do so, no doubt, will significantly increase both the computing time and the necessary computing storage.

In this chapter, a much simpler but more robust numerical method, Vorticity Confinement, will be introduced to compute high Reynolds number flows, including attached boundary layers or separating vortex sheets and filaments. Since first developed by Steinhoff [16], Vorticity Confinement has been studied and developed extensively during the past two decades and there are a large number of successful applications of

this method. Nevertheless, with the latest development of the new formulation for Vorticity Confinement, it is very important to have an organized description of this method. The present chapter is dedicated to such a full description of both the earlier aspect and the latest development of Vorticity Confinement.

In sections 2.2.1~2.2.2, the original Vorticity Confinement method, which is also called VC1, will be introduced; afterwards, the new Vorticity Confinement method, which is also known as the conservative confinement or VC2, will be presented. VC2 involves a better-founded mathematical and physical basis, using simpler but more accurate schemes and is proven to be conservative. A detailed study of some important features of Vorticity Confinement will be given later in this chapter.

2.1 The Governing Partial Differential Equations

The fundamental governing equations of fluid dynamics are based on the conservation laws of mass, momentum and energy. The most famous governing partial differential equations for general unsteady incompressible flows are the Navier-Stokes equations, which include the continuity and momentum equations. For unsteady incompressible flow these equations are:

Continuity Equation:

$$\nabla \cdot \vec{q} = 0 \tag{2.1}$$

Momentum equation:

$$\partial_t \vec{q} = -(\vec{q} \cdot \nabla)\vec{q} - \nabla(P/\rho) + \mu \nabla^2 \vec{q} \tag{2.2}$$

in which $\vec{q}$ defines the velocity vector; t is time; p, ρ and μ represent the pressure,

the constant density and the viscous diffusion coefficient respectively.

In a Cartesian coordinate system for 3-D flows, if u, v and w represent the x, y, z components of the velocity vector $\vec{q}$ respectively, then $\vec{q}$ is given by

$$\vec{q} = u\vec{i} + v\vec{j} + w\vec{k} \qquad (2.3)$$

2.2 The Vorticity Confinement Method

The primary objective of the Vorticity Confinement method is to model thin vortical regions, such as the thin boundary layers or separating vortex filaments, by using only a few grid points in the cross-section. Traditional CFD methods simulate complex flow problems, for instance turbulence, by first hypothesizing a turbulence model. Such models are based on the governing pde's and the properties of turbulence, and then numerically discretize and solve these equations. On the contrary, Vorticity Confinement models the internal structures of the vortical regions directly on the grids using the nonlinear terms. This contrasts with the conventional CFD methods, which use finite difference discretizations of the pde's to resolve modeled equations [34].

The basic theory behind Vorticity Confinement is to modify the conventional Navier-Stokes equations by adding a simple term to the momentum equation. When discretized and solved, these modified equations convect concentrated vortices which maintain a fixed size and do not spread over the flow field even with huge numerical diffusion in the discretized equations. By using Vorticity Confinement, a low order numerical scheme can be used to compute complex flow problems even on a coarse Cartesian grid and the thin vortex regions can be convected over long distance without

spreading. This approach is similar to the shock capturing method [3], in which the detailed internal structures of the shock waves are not computed; rather their positions and strength are determined. One of the advanced features of Vorticity Confinement is that it basically works as a velocity correction at each time step, so that it can be embedded into any conventional CFD method which will work as the basic solver.

For 3-D unsteady incompressible flows, the modified momentum equation for Vorticity Confinement is:

$$\partial_t \vec{q} = -(\vec{q} \cdot \nabla)\vec{q} - \nabla(P/\rho) + \mu\nabla^2\vec{q} - \varepsilon\vec{s} \qquad (2.4)$$

For the last term $\varepsilon\vec{s}$, ε is a numerical coefficient that is called the confinement coefficient. In Equation (2.4), the last two terms, $\mu\nabla^2\vec{q}$ and $\varepsilon\vec{s}$, control the size and time scales of the convecting vortical regions. Normally, the last term is referred to as the "confinement term".

This section includes two parts. First, an extensive development of the original Vorticity Confinement method (or VC1), will be presented, and afterwards, the newly developed Vorticity Confinement method, which is also known as conservative confinement or VC2, will be considered.

2.2.1 VC1 formulation

VC1 has been developed for about sixteen years and has already been proven to be a very robust numerical method for computing vortical flows. The only difference

between VC1 and VC2 is in the definition of the confinement term. This difference will be made clear below.

In VC1, the confinement term is defined as,

$$\vec{s} = \hat{n} \times \vec{\omega} \tag{2.5}$$

in which $\vec{\omega}$ is the local vorticity vector given by

$$\vec{\omega} = \nabla \times \vec{q} \tag{2.6}$$

and $\hat{n}$ is a unit vector, the definition of which depends on whether the confinement is applied in the field or at a surface. For the field confinement, the definition of $\hat{n}$ is presented as

$$\hat{n} = \frac{\nabla|\vec{\omega}|}{|\nabla|\vec{\omega}||} \tag{2.7}$$

where $|\vec{\omega}|$ is the magnitude of the vector $\vec{\omega}$.

Since $\vec{\omega}$ is defined as the local vorticity vector, the definition of $\hat{n}$ represents the normalized gradient of the local vorticity magnitude and normalized vector $\hat{n}$ points toward the centroid of the local vortical region. The main function of the field confinement is to convect vorticity $\vec{\omega}$ back towards the centroid as it is diffused away by the $\mu\nabla^2\vec{q}$ term and by any other numerical diffusion that may be present.

When the surface confinement is applied on the body geometry, $\hat{n}$ is defined as the unit vector to the solid surfaces of the bluff bodies as below,

$$\hat{n} = \frac{\nabla\eta}{|\nabla\eta|} \tag{2.8}$$

where $\eta = |F|$, with $F = 0$ defining the surface. $F > 0$ outside the bluff body, and $F < 0$ inside the body. The detailed definition for F will be given in section 2.4.2.

To understand the property of the surface confinement, we consider it as a simple turbulent boundary layer model. The reason is that the surface confinement acts by controlling the separation characteristics of the flow near the bluff body by adjusting the confinement coefficient [34]. It is important to realize that just setting $\vec{q}$ to zero inside will result in large, diffusing boundary layers that are not related to physical high Re ones. Vorticity Confinement keeps these thin and realistic.

2.2.2 Important features of VC1

Most flow fields can be divided into inner and outer flows. The inner flows are referred to small vortical regions, such as turbulent boundary layers or vortex sheets and filaments, which are only about several grid cells thick. The outer flows are flow fields outside of the small vortical regions. Outside of the vortical region, since the vorticity vector $\vec{\omega} = 0$ the added extra confinement term, $\varepsilon\vec{s} = 0$. Also the diffusion term, $\mu\nabla^2\vec{q} = -\mu(\nabla \times \vec{\omega}) = 0$, vanishes outside of the inner flow. Thus, the outer flows are not sensitive to the values of the parameters ε and μ over a wide range since both the added extra confinement term and the diffusion term vanish outside the inner flow regions. The correction of the velocity vector field takes effect only in the small vortical regions. The parameters of Vorticity Confinement, ε and μ, work like some numerical coefficients in many convectional CFD methods. The confined vortex core size, which may be only ~2 or 3 grid cells in diameter, depends on the values of ε and μ selected, within a range and the value approximately equal to μ/ε. The detailed analysis will be given below.

To illustrate some prominent features of VC1, an analytical solution of an isolated axi-symmetric vortex (Fig. 2-1) in a two-dimensional domain is considered. The momentum equations for the two dimensional incompressible flows are

$$\begin{aligned}\frac{\partial u}{\partial t}+u\frac{\partial u}{\partial x}+v\frac{\partial u}{\partial y}&=-\frac{1}{\rho}\frac{\partial p}{\partial x}+\mu\left(\frac{\partial^2 u}{\partial x^2}+\frac{\partial^2 u}{\partial y^2}\right)\\ \frac{\partial v}{\partial t}+u\frac{\partial v}{\partial x}+v\frac{\partial v}{\partial y}&=-\frac{1}{\rho}\frac{\partial p}{\partial y}+\mu\left(\frac{\partial^2 v}{\partial x^2}+\frac{\partial^2 v}{\partial y^2}\right)\end{aligned} \qquad (2.9)$$

where u and v are velocity components of velocity vector $\vec{q}$ along the x and y coordinates respectively.

In polar coordinates, with $\bar{r}$, which is the position vector defined with respect to the center of the vortex, and the polar angle θ, the above equations can be written as

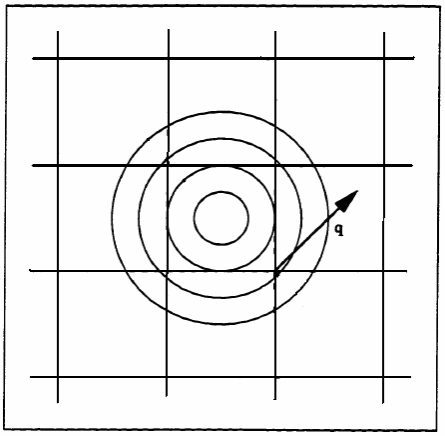

Fig. 2-1 The isolated axi-symmetric vortex

$$\frac{\partial q_r}{\partial t}+q_r\frac{\partial q_r}{\partial r}+\frac{q_\theta}{r}\frac{\partial q_r}{\partial \theta}-\frac{q_\theta^2}{r}=-\frac{1}{\rho}\frac{\partial p}{\partial r}+\mu\left(\frac{\partial^2 q_r}{\partial r^2}+\frac{1}{r}\frac{\partial q_r}{\partial r}+\frac{1}{r^2}\frac{\partial^2 q_r}{\partial \theta^2}-\frac{q_r}{r^2}-\frac{2}{r^2}\frac{\partial q_\theta}{\partial \theta}\right)$$

$$\frac{\partial q_\theta}{\partial t}+q_r\frac{\partial q_\theta}{\partial r}+\frac{q_\theta}{r}\frac{\partial q_\theta}{\partial \theta}-\frac{q_\theta q_r}{r}=-\frac{1}{\rho r}\frac{\partial p}{\partial \theta}+\mu\left(\frac{\partial^2 q_\theta}{\partial r^2}+\frac{1}{r}\frac{\partial q_\theta}{\partial r}+\frac{1}{r^2}\frac{\partial^2 q_\theta}{\partial \theta^2}+\frac{q_\theta}{r^2}+\frac{2}{r^2}\frac{\partial q_r}{\partial \theta}\right) \quad (2.10)$$

For an isolated vortex in a uniform flow, we have

$$\begin{aligned} q_r &= 0 \\ \frac{\partial q_\theta}{\partial \theta} &= 0 \\ \frac{\partial p}{\partial \theta} &= 0 \end{aligned} \quad (2.11)$$

The above equations can be simplified to the following forms

$$\begin{aligned} -\frac{q_\theta^2}{r} &= -\frac{1}{\rho}\frac{\partial p}{\partial r} \\ \frac{\partial q_\theta}{\partial t} &= \mu\left(\frac{\partial^2 q_\theta}{\partial r^2}+\frac{1}{r}\frac{\partial q_\theta}{\partial r}+\frac{q_\theta}{r^2}\right) \end{aligned} \quad (2.12)$$

For Equation (2-12), the solution is

$$\vec{q}=\vec{q}_\infty+T(r,t)\hat{e}_\theta \quad (2.13)$$

where $T(r,t)$ is defined as

$$T(r,t)=\frac{T_0}{r}\left(1-e^{-\frac{r^2}{2\mu t}}\right) \quad (2.14)$$

and q_∞ is the velocity of the uniform flow at the far field and $\hat{e}_\theta$ is the unit vector in the azimuthal direction. This solution identifies a continually spreading vortical region with radius ~ $\sqrt{2\mu t}$ and no nontrivial steady state solution.

With Vorticity Confinement added to the momentum equation, we have, in the frame convecting with the vortex,

$$\partial_t \vec{q} = \mu \nabla^2 \vec{q} - \varepsilon \vec{n} \times \vec{\omega} \qquad (2.15)$$

When $\varepsilon > 0$, the steady solution for Equation(2.9) with $\partial_t \vec{q} = 0$ is

$$T = [T_0 / r]\left(1 - (1 + r/a)e^{-r/a}\right) \qquad (2.16)$$

where $a = \mu / \varepsilon$ is the length scale for the motion. The existence of the steady solution shows that the added confinement term effectively balances the diffusion by convecting vorticity back toward the vortex center.

It is important to consider the conservative feature of the Vorticity Confinement method. That is, whether mass, vorticity and momentum are conserved or not after the velocity correction due to the extra confinement term. As discussed in the beginning of this section, the velocity correction $\varepsilon \vec{s}$ vanishes outside the vortical region. Mass is conserved due to pressure correction and vorticity is conserved because of the vanishing of the velocity correction outside the vortical region [34].

In general 3-D flows

$$\begin{aligned} \delta I_m &= \varepsilon \int \nabla \cdot \vec{s} dv = 0 \\ \delta I_\omega &= \varepsilon \int \nabla \times \vec{s} dv = 0 \end{aligned} \tag{2.17}$$

where $\delta I_m, \delta I_\omega$ are the total change of mass and vorticity integrated over the vortical region respectively. The correction of the velocity effectively convects vorticity back towards the local maximum of the vortical region and therefore the total vorticity is conserved.

To discuss the total change of momentum induced by Vorticity Confinement, a simple 2-D thin vortical tube of slowly-varying cross section is considered. The total change of the momentum induced by the added confinement term is

$$\delta I_M = \varepsilon \int \vec{s} dA = \varepsilon \int \hat{n} \times \vec{\omega} dA \tag{2.18}$$

in which A is a 2-D cross section of the vortical tube. δI_M will not be zero in general. But in some cases, where the distribution of $\vec{\omega}$ is symmetric in this 2-D cross section, δI_M will reduce to zero due to the symmetry. In many computational flow fields where the confinement term has been used, the viscous term is intended to symmetrize the distribution of $\vec{\omega}$ due to the basic numerical convection process or added explicitly. Hence, though the momentum is not conserved the total change of the momentum is expected to be small. The new Vorticity Confinement formulation, VC2, which is developed most recently, explicitly conserves the momentum in a simpler way and will be discussed below in section 2.2.3.

2.2.3 VC2 formulation

As mentioned in section 2.2.2, though proven to be a very successful method to compute some complex flow problems, such as flow over complex configurations, turbulent boundary layers, and the basic free vortices, VC1 conserves mass and vorticity, and approximately conserves momentum. But VC2 conserves mass, vorticity and momentum exactly and the formulation of VC2 is much simpler than that of VC1.

This section will present a detailed description of the formulation of VC2. The basic idea of VC2 is based on the mathematical concept of a harmonic mean. A harmonic mean Φ of N discrete ϕ_l (where $l = 1,2,...,N$) is defined as

$$\Phi = \left[\frac{\sum_l C_l (\phi_l)^{-1}}{\sum_l C_l} \right]^{-1} \tag{2.19}$$

where the coefficients C_l can be varied and allow a weighted average.

To illustrate the mathematical and numerical properties of the formulation for VC2, a simple iteration for a single-signed 2-D passive scalar will be discussed first without the convection. The iteration for a scalar ϕ with "harmonic mean" Vorticity Confinement is

$$\phi_{i,j}^{n+1} = \phi_{i,j}^{n} + \Delta t \cdot \mu \nabla^2 \phi_{i,j}^{n} - \Delta t \cdot \varepsilon \nabla^2 \Phi \tag{2.20}$$

where Φ is a "harmonic mean" confinement term and can be defined as

$$\Phi_{ij}^{n} = \left[\frac{\sum_{1}^{N} \left(\tilde{\phi}_{i,j}^{n} \right)^{-1}}{N} \right]^{-1} \tag{2.21}$$

where

$$\tilde{\phi}_{i,j}^{n} = | \phi_{i,j}^{n} | + \delta \tag{2.22}$$

and N is the total number of the surrounding nodes which are taken to compute the harmonic mean Φ; δ is a small positive constant ($\sim 10^{-8}$) to prevent numerical singularities and n is the iteration time step. The sum is taken over a set of grid points in the neighborhood of the grid node (i, j), including the node (i, j) itself. It is important to know that all the terms in the iteration, Equation (2-20), are homogenous of degree 1 so that Vorticity Confinement works without any scaling concerns.

To extend the concept to the governing flow equations, let the scalar ϕ be replaced by the vorticity magnitude so that the harmonic mean of the vorticity magnitude is defined as

$$\left| \vec{W}^{n} \right| = \left[\frac{\sum_{l} C_l (\tilde{\omega}_l^{\,n})^{-1}}{\sum_{l} C_l} \right]^{-1} \tag{2.23}$$

where $\tilde{\omega} = |\vec{\omega}| + \delta$, $\vec{\omega}$ is the vorticity vector of the corresponding flow field and δ is a small positive constant ($\sim 10^{-8}$).

To match with the vorticity vector field, the harmonic mean vector $\vec{W}$ can be defined as

$$\vec{W}^{n} = \frac{\vec{\omega}}{|\vec{\omega}|}\left[\frac{\sum_{l} C_l (|\vec{\omega}|_l^{\,n})^{-1}}{\sum_{l} C_l}\right]^{-1} \tag{2.24}$$

The new Vorticity Confinement term is presented as

$$\varepsilon\vec{s} = \varepsilon\nabla\times\vec{W} \tag{2.25}$$

Substituting Equation $(2-25)$ into the momentum equation, the governing partial differential equation for VC2 is

$$\partial_t\vec{q} = -(\vec{q}\cdot\nabla)\vec{q} - \nabla(P/\rho) + \mu\nabla^2\vec{q} - \varepsilon\nabla\times\vec{W} \tag{2.26}$$

For the diffusion term $\mu\nabla^2\vec{q}$, since $\nabla\cdot\vec{q} = 0$, then

$$\mu\nabla^2\vec{q} = \mu\nabla\times(\nabla\times\vec{q}), \tag{2.27}$$

since

$$\vec{\omega} = \nabla\times\vec{q}$$

The diffusion term can be written as

$$\mu\nabla^2\vec{q} = \mu\nabla\times\vec{\omega} \tag{2.28}$$

Substituting Equation (2.28) into Equation (2.26), yields:

$$\partial_t\vec{q} = -(\vec{q}\cdot\nabla)\vec{q} - \nabla(P/\rho) + \nabla\times(\mu\vec{\omega} - \varepsilon\vec{W}) \tag{2.29}$$

or, in iteration form,

$$\vec{q}^{\,n+1} = \vec{q}^{\,n} - \Delta t \cdot (\vec{q} \cdot \nabla)\vec{q} - \Delta t \cdot \nabla(P/\rho) + \Delta t \cdot \nabla \times (\mu\vec{\omega} - \varepsilon\vec{W}) \qquad (2.30)$$

Together, with the continuity Equation (2.1), Equation (2.30) constitutes the governing pde's for VC2.

From Equation (2.26), it can be concluded that the added new Vorticity Confinement term conserves momentum. The new confinement term convects vorticity to a thin vortical region. The use of the harmonic mean function as the form for the new Vorticity Confinement term makes the system a stable anti-diffusion mechanism, and convects vorticity stably over long distances without diffusion and retains the shape of the vortical regions [33]. Compared with VC1, which only conserves mass and vorticity, VC2 conserves mass and vorticity, and momentum [16][33].

2.3 Analysis of VC2

2.3.1 Analysis of zero convection form

Equation (2.20) is considered with a zero convection formulation with only diffusion and confinement and, but no pressure term. The diffusion term and confinement term can be combined into the following discretized form:

$$\phi_{i,j}^{n+1} = \phi_{i,j}^{n} + \Delta t \cdot \nabla^2(\mu\phi_{i,j}^{n} - \varepsilon\Phi) \qquad (2.31)$$

It is important to analyze the above formulation. Assuming as $n \to \infty$, the equation achieves convergence, so that the following equilibrium is obtained:

$$\nabla^2(\mu\phi - \varepsilon\Phi) = 0 \tag{2.32}$$

For the Laplace equation $\nabla^2\phi = 0$, it is known that if the function is zero on the boundary, it is zero everywhere. Then, according to this principle, since ϕ (and hence Φ) vanishes outside the flow feature of interest, we have

$$\mu\phi - \varepsilon\Phi = 0 \tag{2.33}$$

Thus

$$\varepsilon\Phi = \mu\phi \tag{2.34}$$

Considering a 2-D problem, let $C_l = 1$ and $i, j = 0$, then the harmonic mean term Φ is,

$$\Phi = \left(\frac{\sum_l \phi_l^{-1}}{N} \right)^{-1} \tag{2.35}$$

Substituting Equation (2.35) into Equation (2.34), we have

$$\phi_0^{-1} - \frac{\mu}{\varepsilon N} \sum_l \phi_l^{-1} = 0 \tag{2.36}$$

A solution for Equation (2.36) can be presented as

$$\phi_{ij} = \frac{1}{4} A \sec h[\alpha(x_i - x_0)] \sec h[\alpha(y_j - y_0] \tag{2.37}$$

in which A, x_0 and y_0 are arbitrary constants and $x_i = ih$, $y_j = jh$, h is the grid cell size [35].

Since

$$\sec h(z) = \frac{1}{\cosh(z)} = \frac{2}{e^{z} + e^{-z}} \tag{2.38}$$

Then, we have

$$\phi_{ij}^{-1} = A^{-1} X_i Y_j \tag{2.39}$$

where

$$\begin{aligned} X_i &= e^{\alpha hi - \alpha x_0} + e^{-\alpha hi + \alpha x_0} \\ Y_j &= e^{\alpha hj - \alpha y_0} + e^{-\alpha hj + \alpha y_0} \end{aligned} \tag{2.40}$$

Substituting Equation (2.37) into Equation (2.36), rearrange and combine some terms, the following equation is obtained:

$$(X_{i+1} + X_i + X_{i-1})(Y_{j+1} + Y_j + Y_{j-1}) - \frac{\varepsilon N}{\mu} X_i Y_j = 0 \tag{2.41}$$

or

$$(e^{\alpha h} + 1 + e^{-\alpha h})(e^{\alpha h} + 1 + e^{-\alpha h}) - \frac{\varepsilon N}{\mu} = 0 \tag{2.42}$$

Hence,

$$ch(\alpha h) = \frac{1}{2}[(\frac{\varepsilon N}{\mu})^{\frac{1}{2}} - 1] \tag{2.43}$$

which determines α. This implies that there is only one solution for $\varepsilon > \mu$, since $N = 9$ here. Again, similar to the solution for a concentrated vortex, the width of the resulting pulse is determined by the ratio of $a = \varepsilon / \mu$ [40].

2.3.2 Convection of the centroid

VC2 not only conserves mass, vorticity and momentum exactly, but also the centroid of the confined properties. This is easy to demonstrate since the confinement term is given in terms of second derivatives (or differences).

For the convecting passive scalar ϕ,

$$\partial\phi_t = -\nabla\cdot(\vec{q}\phi) + h^2\nabla^2(\mu\phi^n_{i,j} - \varepsilon\Phi)/\Delta t \qquad (2.44)$$

From the continuity equation, it is known that $\vec{\nabla}\cdot\vec{q} = 0$. Then Equation (2.44) can be written in the discretized form

$$\phi^{n+1} = \phi^n - \Delta t\nabla\cdot(\vec{q}\phi) + h^2\nabla^2(\mu\phi - \varepsilon\Phi) \qquad (2.45)$$

Define the total amplitude of the scalar ϕ as

$$<\Psi> \equiv \sum_{i,j}\phi^n_{i,j} \qquad (2.46)$$

where $\sum_{i,j}$ represents the sum over all grid nodes in the computational domain. Since VC2 conserves exactly mass, vorticity and momentum, the sum $<\Psi>$ should be independent of the iteration step n.

The centroid of the confined scalar ϕ is defined as,

$$< \vec{X} >^n \equiv \sum_{i,j} \vec{x}_{i,j}^{\,n} \phi_{i,j}^n / < \Psi > \qquad (2.47)$$

where $\vec{x}_{i,j}^{\,n}$ is referred to the position vector of a given node (i, j) at time step n. Define the weighted mean velocity as

$$< \vec{Q} >^n \equiv \sum_{i,j} \vec{q}_{i,j}^{\,n} \phi_{i,j}^n / < \Psi > \qquad (2.48)$$

where $\vec{q}_{i,j}^{\,n}$ is the velocity at that node (i, j), then the centroid evolves according to:

$$< \vec{X} >^{n+1} = < \vec{X} >^n + \Delta t < \vec{Q} >^n \qquad (2.49)$$

For vortices, the self-induced velocity which is included in the above sum exactly cancels and, as in the passive scalar case, the $\vec{q}_{ij}$ can be taken to be an externally applied (irrotational) velocity. The above result then still holds.

Since we are, at this point, only interested in the "expectation values" of scalars or vorticity for thin features and that the features remain compact, spread over only a few cells, this relation is exactly what is needed. Only the variables of importance are, effectively, solved for. This shows that the features, when isolated, evolve as particles with essentially no internal dynamics. However, we keep the very important Eulerian feature that the number of features is not fixed. We could, for example, create additional solitary waves by inserting a source: No additional computational markers need be created, as in Lagrangian schemes. For this study, it is shown that features can automatically merge and reduce in number. This will be seen in the results of Chapter 3. As for the earlier Vorticity Confinement method, this property is crucial for the general treatment of interacting vortical regions, especially in 3-D [15][16][30][32].

2.4 Numerical Approach

2.4.1 F function

Vorticity Confinement has already been proven to be a very robust numerical scheme for computing complex flows, especially flows over bluff bodies. When treating flows with solid surfaces, no specific logic to determine the solid surfaces is required. In this method, the solid surfaces involved are specified by a scalar function F, which is defined on the fixed Cartesian grid to specify the surfaces as different "level sets". This function, $F(\vec{x})$, is computed on the each grid node of a regular Cartesian computational domain and the value of it can be first generated from the given body configurations, such as negative inside the body surface, positive outside the body surface and zero on the body surface. Several numerical methods can be used to decide the distribution of this function to define the body configurations. One if them is to take the distance from the grid node to the body surface as the value of the function, $F(\vec{x})$. Thus, $F(\vec{x}) = 0$ implicitly defines the solid surface over which the fluid is flowing.

According to the definition above, at each grid point, the level set $F(\vec{x})$ can be defined as

$$\begin{cases} F > 0, \text{for nodes outside the body} \\ F = 0, \text{for nodes on the surface} \\ \mathrm{F} < 0, \text{for nodes inside the body} \end{cases} \qquad (2.50)$$

Simultaneously, based on the definition of $F(\vec{x})$ above, a filter function defined for the velocity damping, $\lambda(F)$, can be written as

$$\lambda(F)=\begin{cases}1, \mathrm{F}>0\\ 0, \mathrm{F}\le 0\end{cases} \qquad (2.51)$$

which is sufficient to satisfy the continuity and no-slip boundary condition as shown before.

2.4.2 The fractional-step method

Time integration of the Navier-Stokes equations is often carried out by means of the fractional-step procedure, which was first adopted by Harlow and Welch [36] and Chorin [37] and approximately solved the momentum equation. With the Chorin's method at each time step an incompressible form of the momentum equation is integrated to yield an approximate velocity vector field, which in general will not be divergence free, then a correction will be applied to that velocity vector field to yield a divergence free flow field. The correction of the flow field is an orthogonal projection in the sense that it projects the initial flow field onto the divergence free flow field without changing vorticity. The step is called the projection step, and schemes that use this approach are often called projection methods. The original Chorin method was modified for use with the finite volume method defined on a staggered grid by Kim and Moin [38], and has since been used by many researchers for the simulation of unsteady flows.

The fractional-step method has been used with VC1 to solve incompressible flow problems on uniform Cartesian grids for several years. The steps involve convection, confinement and diffusion followed by the pressure correction. The three main steps are described as follows.

Starting with the governing equations for the incompressible flow with Vorticity

Confinement,

$$\partial_t \vec{q} = -(\vec{q} \cdot \nabla)\vec{q} - \nabla(P/\rho) + \left[\mu \nabla^2 \vec{q} - \varepsilon \vec{s}\right] \qquad (2.52)$$

The first order forward difference operator representing the time derivative is used for the time discretization. For convection, the computation based on the following space discretized formulation is performed to simulate the convection step. For each time-step (identified by the index (n)), the following computations are executed:

1. Velocity damping in body

First, the "level set" F function is defined, then the velocity, $\vec{q}$, is multiplied by a function of F; $\lambda(F)$, such that it is reduced for F < 0. This factor increases to 1 near the surface and no reduction is made in the new velocity at further distances:

$$\vec{q}' = \lambda(F)\vec{q}^{\,n} \qquad (2.53)$$

2. Convection

In the fractional-step method, the velocity convection is computed separately on the Cartesian grid in this form:

$$\vec{q}'' = \vec{q}' - \Delta t \cdot (\vec{q}' \cdot \nabla)\vec{q}' \qquad (2.54)$$

where $\vec{q}^{\,''}$ is the velocity vector field after the convection and $\vec{q}'$ is the velocity vector field at the previous step. There are many existing accurate numerical convection schemes that can be applied to compute the above equation. A simple, first order scheme in space is used here.

3. Velocity diffusion and Vorticity Confinement

To capture vorticity and overcome the effects of numerical diffusion in the convection

step, Vorticity Confinement is employed next and calculated from the equation:

$$\vec{q}''' = \vec{q}'' + \Delta t(\mu \nabla^2 \vec{q}'' - \varepsilon \vec{s}) \qquad (2.55)$$

where $\vec{q}'''$ is the velocity after the confinement correction.

A standard central difference scheme will be used for the diffusion term $\nabla^2 \vec{q}''$ on the right hand side but the numerical scheme for VC1 and VC2 will be different and the details of both schemes will be given in section 2.5 when discussing the numerical procedure.

4. Mass balance

The above computation steps will not initially satisfy continuity and a correction must be applied to the velocity vector field to produce a divergence free flow field.

$$\vec{q}^{n+1} = \vec{q}''' + \nabla \phi \qquad (2.56)$$

where

$$\phi = -\Delta t \frac{P}{\rho} \qquad (2.57)$$

The conservation law of mass requires

$$\nabla \cdot \vec{q}^{n+1} = 0 \qquad (2.58)$$

Substituting Equation (2.56) into Equation (2.58), we get a Poisson equation

$$\nabla^2 \phi = -\nabla \cdot \vec{q}''' \qquad (2.59)$$

To solve the above Poisson equation for ϕ, any existing Poisson solver can be used. A

Cartesian grid Poisson solver, which includes two FORTRAN subprograms, HW3CRT and HWSCRT of FISHPAK [39], was used in the present study for the 2-D and 3-D Poisson equations respectively.

2.4.3 Boundary conditions

1. No-slip boundary condition for the velocity on the solid surface.

On the solid body surface, a no-slip boundary condition is used, that is,

$$\vec{q}\big|_s = 0 \qquad (2.60)$$

where S indicates the solid body surface. When employed into the computational code, the no-slip boundary condition can be applied by the filter function $\lambda(F)$ as described in section 2.4.1, which defines $\lambda(F) = 0$ inside the solid surface. Thus, after multiplied by the filter function $\lambda(F)$, the velocity goes to zero on the solid surface.

2. Far field boundary conditions

At the far field, the flow velocity and the pressure are set to be equal to the free stream flow, that is,

$$\vec{q}\big|_f = \vec{q}_\infty \qquad (2.61)$$

$$P\big|_f = P_\infty \qquad (2.62)$$

Where f indicates the far field boundary and $\vec{q}_\infty$ is the free stream velocity and P_∞ indicates the pressure at the far field.

3. T**he inlet boundary conditions**

On the inlet, the velocity is specified as,

$$\vec{q}_{in} = \begin{cases} 0, & \text{on the solid surface} \\ \vec{q}_{\infty}, & \text{the free stream velocity} \end{cases} \tag{2.63}$$

On the inlet boundaries, the pressure is specified to be the pressure at infinity to ensure a correct free stream pressure input:

$$P_{in} = P_{\infty} \tag{2.64}$$

4. The outlet boundary condition

On the outlet boundaries, the velocity is extrapolated from the inner velocity vector field by specifying

$$\left.\frac{\partial \vec{q}}{\partial n}\right|_{out} = 0 \tag{2.65}$$

On the outlet boundary condition, the following condition is imposed to insure that there is no pressure constraints enforced by the free boundaries:

$$\left.\frac{\partial P}{\partial n}\right|_{out} = 0 \tag{2.66}$$

2.5 Numerical Scheme of VC1 and VC2

2.5.1 Velocity convection and diffusion

The continuity and momentum equations can be described in their conservative forms as

$$
\begin{aligned}
&\frac{\partial u}{\partial x}+\frac{\partial v}{\partial y}+\frac{\partial w}{\partial z}=0 \\
&\frac{\partial u}{\partial t}+\frac{\partial u^2}{\partial x}+\frac{\partial uv}{\partial y}+\frac{\partial uw}{\partial z}=-\frac{1}{\rho}\frac{\partial p}{\partial x}+\mu\left(\frac{\partial^2 u}{\partial x^2}+\frac{\partial^2 u}{\partial y^2}+\frac{\partial^2 w}{\partial z^2}\right) \\
&\frac{\partial v}{\partial t}+\frac{\partial vu}{\partial x}+\frac{\partial v^2}{\partial y}+\frac{\partial vw}{\partial z}=-\frac{1}{\rho}\frac{\partial p}{\partial y}+\mu\left(\frac{\partial^2 v}{\partial x^2}+\frac{\partial^2 v}{\partial y^2}+\frac{\partial^2 v}{\partial z^2}\right) \\
&\frac{\partial w}{\partial t}+\frac{\partial wu}{\partial x}+\frac{\partial vw}{\partial y}+\frac{\partial w^2}{\partial z}=-\frac{1}{\rho}\frac{\partial p}{\partial z}+\mu\left(\frac{\partial^2 w}{\partial x^2}+\frac{\partial^2 w}{\partial y^2}+\frac{\partial^2 w}{\partial z^2}\right)
\end{aligned}
\qquad (2.67)
$$

Here the velocity vector $\vec{q}'$ after the velocity damping is

$$\vec{q}' = u'\vec{i} + v'\vec{j} + w'\vec{k} \qquad (2.68)$$

The velocity after the convection is $\vec{q}''$ and is derived from

$$\vec{q}'' = \vec{q}' - \Delta t \cdot (\vec{q}' \cdot \nabla)\vec{q}' \qquad (2.69)$$

The above equation can be written in the u, v, w components forms as

$$
\begin{aligned}
u'' &= u' - \Delta t \cdot (\frac{\partial u'^2}{\partial x} + \frac{\partial u'v'}{\partial y} + \frac{\partial u'w'}{\partial z}) \\
v'' &= v' - \Delta t \cdot (\frac{\partial v'u'}{\partial x} + \frac{\partial v'^2}{\partial y} + \frac{\partial v'w'}{\partial z}) \\
w'' &= w' - \Delta t \cdot (\frac{\partial w'u'}{\partial x} + \frac{\partial v'w'}{\partial y} + \frac{\partial w'^2}{\partial z})
\end{aligned}
\qquad (2.70)
$$

To discretize Equation (2.70), a second order central difference scheme is used to preserve the stability of the numerical scheme. The discretizated equations used here for the convection step are

$$
\begin{aligned}
u''_{i,j,k} &= u''_{i,j,k} - \Delta t \cdot \left(\frac{u'_{i+1,j,k} \cdot u'_{i+1,j,k} - u'_{i-1,j,k} \cdot u'_{i-1,j,k}}{2 \cdot \Delta x} + \frac{v'_{i,j+1,k} \cdot u'_{i,j+1,k} - v'_{i,j-1,k} \cdot u'_{i,j-1,k}}{2 \cdot \Delta y}\right. \\
&\quad \left. + \frac{u'_{i,j,k+1} \cdot w'_{i,j,k+1} - u'_{i,j,k-1} \cdot w'_{i,j,k-1}}{2 \cdot \Delta z}\right) \\
v''_{i,j,k} &= v''_{i,j,k} - \Delta t \cdot \left(\frac{u'_{i+1,j,k} \cdot v'_{i+1,j,k} - u'_{i-1,j,k} \cdot v'_{i-1,j,k}}{2 \cdot \Delta x} + \frac{v'_{i,j+1,k} \cdot v'_{i,j+1,k} - v'_{i,j-1,k} \cdot v'_{i,j-1,k}}{2 \cdot \Delta y}\right. \\
&\quad \left. + \frac{v'_{i,j,k+1} \cdot w'_{i,j,k+1} - v'_{i,j,k-1} \cdot w'_{i,j,k-1}}{2 \cdot \Delta z}\right) \\
w''_{i,j,k} &= w''_{i,j,k} - \Delta t \cdot \left(\frac{u'_{i+1,j,k} \cdot w'_{i+1,j,k} - u'_{i-1,j,k} \cdot w'_{i-1,j,k}}{2 \cdot \Delta x} + \frac{v'_{i,j+1,k} \cdot w'_{i,j+1,k} - v'_{i,j-1,k} \cdot w'_{i,j-1,k}}{2 \cdot \Delta y}\right. \\
&\quad \left. + \frac{w'_{i,j,k+1} \cdot w'_{i,j,k+1} - w'_{i,j,k-1} \cdot w'_{i,j,k-1}}{2 \cdot \Delta z}\right)
\end{aligned}
\qquad (2.71)
$$

where $u''_{i,j,k}, v''_{i,j,k}, w''_{i,j,k}$ are the velocity components of the convected velocity $\vec{q}''$ along the x, y, z directions.

In 2-D flow problems, a much simpler first order, but very robust numerical scheme has been used to compute the convection step, which is called image point method [41]. The velocity vector field $\vec{q}$ after time step Δt and at node (i, j) can be interpolated from the current flow field. Assume Δt is small enough, then the flow particle, which is convected to the node (i, j), is at point (o) originally as shown in Fig. 2-2. The areas $A(i), i = 1 \sim 4$ is used to determine the weighting parameters, which are derived as

$$
\begin{aligned}
A(1) &= (1 - S_x)(1 - S_y) \\
A(2) &= (1 - S_x) S_y \\
A(3) &= S_x (1 - S_y) \\
A(4) &= S_x S_y
\end{aligned}
\qquad (2.72)
$$

where

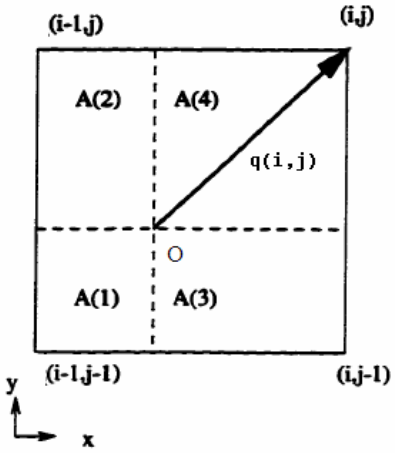

Fig. 2-2 The diagram for the image point location and weighting

$$S_x = u\Delta t / \Delta x$$

$$S_y = v\Delta t / \Delta y$$

The convected velocity $\vec{q}''$ is derived from

$$\vec{q}''_{i,j} = A(1)\vec{q}'_{i,j} + A(2)\vec{q}'_{i,j-1} + A(3)\vec{q}'_{i-1,j} + A(4)\vec{q}'_{i-1,j-1} \qquad (2.73)$$

This is a type of explicit first-order upwind scheme that is unconditionally stable [41]. This image point method is seldom used nowadays because of its low order characteristic. It's been used in some 2-D flow problems in this thesis. After the convection step, a diffusion step is applied to the velocity vector field to compute the physical diffusion of the flow, that is,

$$\vec{q}'' = \vec{q}'' + \Delta t \cdot \mu \nabla^2 \vec{q}'' \qquad (2.74)$$

A standard second order central differential scheme is used to discretize the

second derivative $\nabla^2 \vec{q}''$. The discretization equations to compute the diffusion for each grid node are

$$\vec{q}''_{i,j,k} = \vec{q}''_{i,j,k} + \Delta t \cdot \mu \left(\frac{\vec{q}''_{i+1,j,k} - 2\vec{q}''_{i,j,k} + \vec{q}''_{i-1,j,k}}{\Delta x^2} + \frac{\vec{q}''_{i,j+1,k} - 2\vec{q}''_{i,j,k} + \vec{q}''_{i,j-1,k}}{\Delta y^2} + \frac{\vec{q}''_{i,j,k+1} - 2\vec{q}''_{i,j,k} + \vec{q}''_{i,j,k-1}}{\Delta z^2} \right) \quad (2.75)$$

2.5.2 Velocity correction by VC1 and VC2

After the convection and diffusion steps, a velocity correction by Vorticity Confinement is applied to convect vorticity back toward the vortical region. The numerical scheme of the VC1 and VC2 will be discussed separately below.

1. Numerical scheme of VC1

The vorticity vector field $\vec{\omega}$ is given from the definition,

$$\vec{\omega} = \nabla \times \vec{q}''$$

where $\vec{q}''$ is the velocity vector field after the convection and diffusion steps and is defined in terms of its components as:

$$\vec{q}'' = u''\vec{i} + v''\vec{j} + w''\vec{k} \quad (2.76)$$

Thus, the components of the vorticity vector $\vec{\omega}$ in three directions are

$$\omega_x = \frac{\partial w''}{\partial y} - \frac{\partial v''}{\partial z}$$

$$\omega_y = \frac{\partial u''}{\partial z} - \frac{\partial w''}{\partial x} \qquad (2.77)$$
$$\omega_z = \frac{\partial v''}{\partial x} - \frac{\partial u''}{\partial y}$$

where u'', v'', w'' are obtained from Equation (2.71).

Discretizing Equation (2.78) in a 3-D Cartesian grid on each cell center, we have

$$\begin{aligned}
\omega_{xi,j,k} &= \frac{1}{4}(w''_{i,j+1,k} - w''_{i,j,k} + w''_{i+1,j+1,k} - w''_{i+1,j,k} + w''_{i,j+1,k+1} - w''_{i,j,k+1} + w''_{i+1,j+1,k+1} - w''_{i+1,j,k+1}) \\
&-\frac{1}{4}(v''_{i,j,k+1} - v''_{i,j,k} + v''_{i+1,j,k+1} - v''_{i+1,j,k} + v''_{i+1,j,k+1} - v''_{i+1,j,k} + v''_{i+1,j+1,k+1} - v''_{i+1,j+1,k}) \\
\omega_{yi,j,k} &= \frac{1}{4}(u''_{i,j,k+1} - u''_{i,j,k} + u''_{i+1,j,k+1} - u''_{i+1,j,k} + u''_{i+1,j,k+1} - u''_{i+1,j,k} + u''_{i+1,j+1,k+1} - u''_{i+1,j+1,k}) \\
&-\frac{1}{4}(w''_{i+1,j,k+1} - w''_{i,j,k+1} + w''_{i+1,j+1,k+1} - w''_{i,j+1,k+1} + w''_{i+1,j,k+1} - w''_{i,j,k+1} + w''_{i+1,j+1,k+1} - w''_{i,j+1,k+1}) \\
\omega_{zi,j,k} &= \frac{1}{4}(v''_{i,+1j,k} - v''_{i,j,k} + v''_{i+1,j+1,k} - v''_{i,j+1,k} + v''_{i+1,j,k+1} - v''_{i,j,k+1} + v''_{i+1,j+1,k+1} - v''_{i,j+1,k+1}) \\
&-\frac{1}{4}(u''_{i,j+1,k} - u''_{i,j,k} + u''_{i+1,j+1,k} - u''_{i+1,j,k} + u''_{i,j+1,k+1} - u''_{i,j,k+1} + u''_{i+1,j+1,k+1} - u''_{i+1,j,k+1})
\end{aligned} \qquad (2.78)$$

The original vorticity confinement term is defined in section 2.2.1 as

$$\vec{s} = \hat{n} \times \vec{\omega}$$

where the norm of $\hat{n}$ is represented by

$$\hat{n} = \frac{\nabla|\vec{\omega}|}{\left|\nabla|\vec{\omega}|\right|}$$

The magnitude of the vorticity vector $\vec{\omega}$ is

$$|\vec{\omega}| = \left(\omega_x^2 + \omega_y^2 + \omega_z^2\right)^{1/2} \qquad (2.79)$$

Or, in discretization form,

$$\left|\vec{\omega}\right|_{i,j,k} = \left({\omega^2}_{x\,i,j,k} + {\omega^2}_{y\,i,j,k} + {\omega^2}_{z\,i,j,k}\right)^{1/2} \tag{2.80}$$

The vector $\hat{n}$ represents the unit vector of the gradient of the scalar field $\left|\vec{\omega}\right|$ and points toward to centroid of the local vortical region.

A scalar field η is defined as

$$\eta = \left|\vec{\omega}\right|$$

Thus, the unit vector $\vec{n}$ can be written as

$$\vec{n} = \nabla\eta / \left|\nabla\eta\right|$$

The gradient $\nabla\eta$ is presented as

$$\nabla\eta = \frac{\partial\eta}{\partial x}\vec{i} + \frac{\partial\eta}{\partial y}\vec{j} + \frac{\partial\eta}{\partial z}\vec{k} \tag{2.81}$$

and the magnitude of the $\nabla\eta$ is

$$\left|\nabla\eta\right| = \left((\frac{\partial\eta}{\partial x})^2 + (\frac{\partial\eta}{\partial y})^2 + (\frac{\partial\eta}{\partial z})^2 \right)^{1/2} \tag{2.82}$$

The components of $\nabla\eta$, that is, $\frac{\partial\eta}{\partial x}, \frac{\partial\eta}{\partial y}, \frac{\partial\eta}{\partial z}$ can be discretized as

$$\begin{aligned}
\frac{\partial\eta}{\partial x}_{i,j,k} &= \frac{1}{4}(\eta_{i+1,j,k} - \eta_{i,j,k} + \eta_{i+1,j+1,k} - \eta_{i,j+1,k} + \eta_{i+1,j,k+1} - \eta_{i,j,k+1} + \eta_{i+1,j+1,k+1} - \eta_{i,j+1,k+1}) \\
\frac{\partial\eta}{\partial y}_{i,j,k} &= \frac{1}{4}(\eta_{i,j+1,k} - \eta_{i,j,k} + \eta_{i+1,j+1,k} - \eta_{i+1,j,k} + \eta_{i,j+1,k+1} - \eta_{i,j,k+1} + \eta_{i+1,j+1,k+1} - \eta_{i+1,j,k+1}) \\
\frac{\partial\eta}{\partial z}_{i,j,k} &= \frac{1}{4}(\eta_{i,j,k+1} - \eta_{i,j,k} + \eta_{i+1,j,k+1} - \eta_{i+1,j,k+1} + \eta_{i,j+1,k+1} - \eta_{i+1,j,k} + \eta_{i+1,j+1,k+1} - \eta_{i+1,j+1,k})
\end{aligned} \tag{2.83}$$

The magnitude of $\nabla\eta$, $|\nabla\eta|$, is

$$(|\nabla\eta|)_{i,j,k} = \left((\frac{\partial\eta}{\partial x})^2{}_{i,j,k} + (\frac{\partial\eta}{\partial y})^2{}_{i,j,k} + (\frac{\partial\eta}{\partial z})^2{}_{i,j,k} \right)^{1/2} \qquad (2.84)$$

Since the definition of $\vec{n}$ is $\vec{n} = \nabla\eta / |\nabla\eta|$, $\vec{n}$ is computed as

$$\vec{n}_{i,j,k} = \left(\frac{\partial\eta}{\partial x}_{i,j,k} \vec{i} + \frac{\partial\eta}{\partial y}_{i,j,k} \vec{j} + \frac{\partial\eta}{\partial z}_{i,j,k} \vec{k} \right) / \left(|\nabla\eta| \right)_{i,j,k} \qquad (2.85)$$

For the surface confinement, the definition of the unit vector $\hat{n}$ is

$$\hat{n} = \frac{\nabla\eta}{|\nabla\eta|}$$

where $\eta = |F|$.

F is defined as the distance from the grid node to the body surface. The value of F is defined at the cell center as,

$$F_{C\,i,j,k} = \frac{1}{8}(F_{i,j,k} + F_{i,j+1,k} + F_{i,j,k+1} + F_{i,j+1,k+1} + F_{i+1,j,k} + F_{i+1,j+1,k} + F_{i+1,j,k+1} + F_{i+1,j+1,k+1}) \qquad (2.86)$$

Since,

$$\eta_{i,j,k} = |F_{C\,i,j,k}| \qquad (2.87)$$

Then, the unit vector of the surface confinement is

$$\hat{n}_{i,j,k} = \frac{\partial \eta_{i,j,k}}{\partial x}\vec{i} + \frac{\partial \eta_{i,j,k}}{\partial y}\vec{j} + \frac{\partial \eta_{i,j,k}}{\partial z}\vec{k} \tag{2.88}$$

The confinement term is defined as $\vec{s} = \hat{n} \times \vec{\omega}$ and the components of $\vec{s}$ are

$$\vec{s}_{i,j,k} = \left(s_{x\,i,j,k}\vec{i} + s_{y_{i,j,k}}\vec{j} + s_{z\,i,j,k}\vec{k}\right) \tag{2.89}$$

where $s_{x\,i,j,k}, s_{y_{i,j,k}}, s_{z\,i,j,k}$ are computed by

$$\begin{aligned} s_{x\,i,j,k} &= n_{x\,i,j,k}\omega_{y_{i,j,k}} - n_{y_{i,j,k}}\omega_{x\,i,j,k} \\ s_{y_{i,j,k}} &= n_{x\,i,j,k}\omega_{z\,i,j,k} - n_{z\,i,j,k}\omega_{x\,i,j,k} \\ s_{z\,i,j,k} &= n_{x\,i,j,k}\omega_{y_{i,j,k}} - n_{x\,i,j,k}\omega_{y_{i,j,k}} \end{aligned} \tag{2.90}$$

The velocity correction added to the velocity vector field by VC1 is

$$\delta\vec{q}'' = -\Delta t \cdot \varepsilon a_l \vec{s} \tag{2.91}$$

and then,

$$\vec{q}''' = \vec{q}'' + \delta\vec{q}'' \tag{2.92}$$

where $\vec{q}'''$ is the velocity after the confinement correction, ε is a confinement coefficient, and a_l is the weight number defined as

$$a_l = \frac{a_l'}{\sum_l a_l'} \tag{2.93}$$

where

$$a_l' = \min\left(0, \eta_l - \overline{\eta}\right)$$

Where $\overline{\eta}$ is the averaged value of η_l over the neighboring grid nodes.

The average value $\overline{\eta}$ of η is derived from

$$\overline{\eta}_{i,j,k} = \frac{1}{8}(\eta_{i,j,k} + \eta_{i,j+1,k} + \eta_{i,j,k+1} + \eta_{i,j+1,k+1} + \eta_{i+1,j,k} + \eta_{i+1,j+1,k} + \eta_{i+1,j,k+1} + \eta_{i+1,j+1,k+1}) \quad (2.94)$$

and weighting factors are:

$$\begin{aligned} a_1' &= \min(0, \eta_{i+1,j+1,k+1} - \overline{\eta}_{i,j,k}) \\ a_2' &= \min(0, \eta_{i+1,j+1,k} - \overline{\eta}_{i,j,k}) \\ a_3' &= \min(0, \eta_{i+1,j,k} - \overline{\eta}_{i,j,k}) \\ a_4' &= \min(0, \eta_{i+1,j,k+1} - \overline{\eta}_{i,j,k}) \\ a_5' &= \min(0, \eta_{i,j+1,k+1} - \overline{\eta}_{i,j,k}) \\ a_6' &= \min(0, \eta_{i,j+1,k} - \overline{\eta}_{i,j,k}) \\ a_7' &= \min(0, \eta_{i,j,k} - \overline{\eta}_{i,j,k}) \\ a_8' &= \min(0, \eta_{i,j,k+1} - \overline{\eta}_{i,j,k}) \end{aligned} \quad (2.95)$$

`

The weighting factors a_l are calculated by

$$a_l = \frac{a_l'}{\sum_{l=1}^{8} a_l' + \delta} \quad \text{for} \quad l = 1,8$$

where, again, δ is a small constant added to avoid computation overflow.

Then the velocity corrections at this numerical step, for the grid nodes around each cell center, is

$$\vec{q}''' = \vec{q}'' - \Delta t \cdot \varepsilon \, a_l \vec{s} \qquad (2.96)$$

where Δt is the computation time step.

2. Numerical scheme of VC2

The equation of VC2 is presented as

$$\varepsilon\vec{s} = \varepsilon \nabla \times \vec{W}$$

where

$$\vec{W}^n = \frac{\vec{\omega}}{|\vec{\omega}|}\left[\frac{\sum_l C_l (|\vec{\omega}|_l^{\,n})^{-1}}{\sum_l C_l}\right]^{-1}$$

and normally good results are obtained by simply setting C_l to 1. Discretizing the above harmonic mean equation in the x, y, z directions, respectively,

$$W_{x_{i,j,k}} = \frac{\omega_{x_{i,j,k}}}{|\vec{\omega}_{i,j,k}| + \delta}\left[\frac{\left(|\vec{\omega}_{i+1,j,k}|\right)^{-1} + \left(|\vec{\omega}_{i-1,j,k}|\right)^{-1} + \left(|\vec{\omega}_{i,j+1,k}|\right)^{-1} + \left(|\vec{\omega}_{i,j-1,k}|\right)^{-1} + \left(|\vec{\omega}_{i,j,k+1}|\right)^{-1} + \left(|\vec{\omega}_{i,j,k-1}|\right)^{-1}}{6}\right]^{-1}$$

$$W_{y_{i,j,k}} = \frac{\omega_{y_{i,j,k}}}{|\vec{\omega}_{i,j,k}| + \delta}\left[\frac{\left(|\vec{\omega}_{i+1,j,k}|\right)^{-1} + \left(|\vec{\omega}_{i-1,j,k}|\right)^{-1} + \left(|\vec{\omega}_{i,j+1,k}|\right)^{-1} + \left(|\vec{\omega}_{i,j-1,k}|\right)^{-1} + \left(|\vec{\omega}_{i,j,k+1}|\right)^{-1} + \left(|\vec{\omega}_{i,j,k-1}|\right)^{-1}}{6}\right]^{-1} \qquad (2.97)$$

$$W_{z_{i,j,k}} = \frac{\omega_{z_{i,j,k}}}{|\vec{\omega}_{i,j,k}| + \delta}\left[\frac{\left(|\vec{\omega}_{i+1,j,k}|\right)^{-1} + \left(|\vec{\omega}_{i-1,j,k}|\right)^{-1} + \left(|\vec{\omega}_{i,j+1,k}|\right)^{-1} + \left(|\vec{\omega}_{i,j-1,k}|\right)^{-1} + \left(|\vec{\omega}_{i,j,k+1}|\right)^{-1} + \left(|\vec{\omega}_{i,j,k-1}|\right)^{-1}}{6}\right]^{-1}$$

Taking the curl of $\vec{W}$

$$\nabla \times \vec{W} = \left(\frac{\partial W_z}{\partial y} - \frac{\partial W_y}{\partial z} \right) \vec{i} + \left(\frac{\partial W_x}{\partial z} - \frac{\partial W_z}{\partial x} \right) \vec{j} + \left(\frac{\partial W_y}{\partial x} - \frac{\partial W_x}{\partial y} \right) \vec{k} \qquad (2.98)$$

Discretizing $\nabla \times \vec{w}$ on the grid center using the second order center difference scheme, the confinement correction to the flow field is calculated by

$$\delta \vec{q}'' = \varepsilon \nabla \times \vec{W}^{\,n} \qquad (2.99)$$

Then the corrected velocity can be written as:

$$\vec{q}''' = \vec{q}'' + \Delta t \delta \vec{q}'' \qquad (2.100)$$

2.5.3 Mass balance

A potential ϕ is solved on the Cartesian grid so that the sum of the gradient of the potential and with corrections the convected velocity enforces mass conservation.

$$\vec{q}^{\,n+1} = \vec{q}''' + \nabla \phi \qquad (2.101)$$

For the equation of continuity, $\vec{q}^{\,n+1}$ must satisfy

$$\nabla \cdot \vec{q}^{\,n+1} = 0 \qquad (2.102)$$

Thus, the potential, $\nabla \phi$, satisfied the Poisson equation

$$\nabla^2 \phi = -\nabla \cdot \vec{q}''' \qquad (2.103)$$

where

$$\nabla \cdot \vec{q}''' = \frac{\partial u'''}{\partial x} + \frac{\partial v'''}{\partial y} + \frac{\partial w'''}{\partial z}$$

The right-hand-side of the Poisson equation is evaluated at the cell centers.

Again, the Cartesian grid Poisson solver from the FISHPAK [39], was used as indicated above for both 2-D and 3-D Poisson equations. The Neumann boundary condition, $\frac{\partial \phi}{\partial n} = 0$, was imposed on each boundary of the computational domain.

Chapter 3 Verification of Vorticity Confinement

Numerical experiments on the two-dimensional flow problems will be presented in this chapter to demonstrate the ability of the Vorticity Confinement method to convect thin vortex regions over long distances without spreading. Three fundamental numerical experiments will be presented to test the salient features of the Vorticity Confinement method to indefinitely conserve thin vortical features without spreading the vortical region due to diffusion. These three cases include: a single stationary point vortex, a free single vortex moving with a uniform free stream, and a pair of vortices of either opposite signs or the same signs convecting in their own induced velocity vector field. The incompressible fluid dynamic equations with Vorticity Confinement, Equation (2.4), were discretized and solved using the fractional-step method described in Section (2.4.1). Results presented here are two dimensional.

3.1 A Single Stationary Point Vortex

To illustrate the most important ability of the Vorticity Confinement method to indefinitely preserve small vortical features, a single stationary vortex is simulated. Fig.3-1[I] shows the initial velocity vector field for the stationary vortex. Fig.3-2 shows the initial vorticity contours distribution for the stationary vortex. The computational domain

[I] All the figures in Chapter 3 are located in the Appendix

is 129×129 grid resolution and the single vortex is located at the center of the domain, where $x_{i,j}=0$ and $y_{i,j}=0$. The cell size is 1×1 and the initial velocity induced by the single stationary vortex is specified as

$$\begin{cases} u=-y/r^2 \\ v=x/r^2 \end{cases} \quad for \quad r>1 \qquad (3.1)$$

$$\begin{cases} u=-y \\ v=x \end{cases}, \quad for \quad r\le 1$$

where u,v are velocity components along the x,y directions respectively and r represents the distance from the center of the domain (also the vortex center $x=0, y=0$) to the given node.

In the figures, the vorticity contour levels extend from about one fourth of the maximum initial value to the maximum so that the size of the confined region can be determined. Results are presented after 100 and 1000 time iterations, for vorticity and velocity in two dimensions. The value of the diffusion and confinement coefficients used were $\mu=0.2$, $\varepsilon=0$ and $\varepsilon=1.5\mu$ for both VC1 and VC2.

Fig.3-3 and Fig.3-4 show velocity vector field and vorticity contours after 100 time iterations without Vorticity Confinement. As expected, the velocity vector field diffuses rapidly and the vortex core spreads to over 14 grid cells. The maximum vorticity value of the core has been reduced to about 1% of the initial maximum vorticity value. Instead, Fig.3-5 and Fig.3-6 show the velocity vector field and vorticity contours after 100 iterations by using VC2. It can be seen that after 100 iterations the velocity vector field still keeps the shape and the vortex core has only spread about 4 grid cells. The maximum vorticity value of the vortex core keeps above 50% of the initial maximum value. The results of the velocity vector field and vorticity contours shown in Fig.3-7 and

Fig.3-8 are the results after 1000 iterations obtained by VC2. It clearly shows that even after 1000 iterations, the vortex core is still preserved with the added Vorticity Confinement term despite the huge numerical diffusion.

The results presented in Fig.3-9 – Fig.3-12 are the velocity vector field and vorticity contours obtained by using VC1 after 100 and 1000 time iterations. Though different confinement terms are used the results still strongly illustrate the ability of the Vorticity Confinement method to preserve small vortical features and cancel self-induced motions. Fig.3-13 shows the initial velocity magnitude distribution with respect to the radius r, which is defined as the distance from the given node to the vortex center. The magnitude of the velocity is normalized as,

$$\begin{cases} |\vec{q}| \cdot r & if \quad r > 1 \\ |\vec{q}| / r & if \quad r \le 1 \end{cases} \tag{3.2}$$

Fig.3-14 and Fig.3-15 show the velocity magnitude distribution after 100 and 1000 time iterations without Vorticity Confinement. The radius of the vortex is defined up to the points whose magnitude of the velocity is 0.9 of the maximum velocity magnitude. It can be seen that the radius of the vortex core is spreading to nearly 10 grid cells after 100 time iterations and 30 grid cells after 1000 time iterations. Fig.3-16 and Fig.3-17 show the velocity magnitude distribution after 100 and 1000 time iterations by adding VC2. The radius of the stationary single vortex is confined to only about 4 grid cells even after 1000 time iterations. The results in Fig.3-18 and Fig.3-19 are obtained by using VC1, which are same as those obtained by VC2.

So it can be concluded that small scales are confined and Vorticity Confinement is very robust and stable for an isolated vortex.

3.2 A Single Vortex Moving with a Free Stream

In this section, a single vortex moving with a weak uniform flow will be considered. The computational domain is the square with 128×128 grid size. This single initial vortex is the same as the single stationary vortex presented in the section 3.2.1. But it is imposed on a uniform weak free stream, and the center of the vortex is located at $(-50,-50)$, the left low corner of the computational domain. The center of the domain is $(0,0)$.

The velocity of the free weak stream flow is defined as,

$$u/U_\infty = 0.06$$
$$v/U_\infty = 0.05$$

in which u and v are the velocities along the x and y directions respectively, and U_∞ is the uniform flow and set to 1. To set the free stream flow much smaller than the dominant velocity induced by the convecting single vortex is a good numerical experiment to determine the accuracy of the Vorticity Confinement method. A small iteration step is taken with Δt =0.4.

Without Vorticity Confinement the convecting single vortex will diffuse very quickly. The velocity vector field after 500 time iterations, compared to the initial velocity vector field in Fig.3-20, is shown on Fig.3-22. The velocity vector has diffused expeditiously and became trivial.

To analyze the velocity magnitude distribution with regard to the radius r, which is defined as the distance from the given node to the moving vortex center, whose centroid of the vortical region is defined as

$$x_{\omega}^{n} = \frac{\sum |\vec{\omega}| x}{\sum |\vec{\omega}|}$$
$$y_{\omega}^{n} = \frac{\sum |\vec{\omega}| y}{\sum |\vec{\omega}|} \qquad (3.3)$$

with $x_{\omega,} y_{\omega}$ being the x, y coordinates of the centroid of the vortical region after n time steps. Thus, the radius r is computed by

$$r_{i,j} = \left(\left(x_{i,j} - x_{\omega} \right)^2 + \left(y_{i,j} - y_{\omega} \right)^2 \right)^{1/2} \qquad (3.4)$$

In Fig.3-23, the simulation result of the velocity magnitude distribution is plotted vs. radius r. The analytical distribution of the velocity magnitude, which is derived from Equation (2.13), is shown in the same figure. According to Equation (3.9), after 500 time iterations, the vortex core will spread about 13~14 grid cells, which is clearly shown in the Fig.3-23. It can also be observed that the numerical result is in accordance with the analytical result approximately and after 500 time iterations the vortex core spreads about to a width of 13 cells. Fig.3-22 shows the velocity vector field after 500 time iterations and it can be seen that the whole field diffuses extensively compared with the initial velocity vector field shown in Fig.3-20. Therefore, it can be concluded that the convecting vortical region diffuses rapidly without Vorticity Confinement.

Then to demonstrate the effect of the Vorticity Confinement method, first, VC1 is applied to compute the convecting single vortex. Fig.3-24~Fig.3-27 show the velocity vector field and vorticity contours of the single convecting vortex after 500 and 3000 time iterations. It can be seen that the vortex keeps its shape and vorticity magnitude and

moves along with the weak stream. In Fig.3-28, the trajectory of the moving vortex is given by recording the vortex position every 500 time steps. After 3000 time steps, the centroid of the vortex moves to $x = 27, y = 12$ which is about a 7 grid cell error compared with the analytical trajectory in the x direction and 8 grid cells in the y direction. Such a deviation is expected since VC1 can't conserve the total momentum and thus the centroid of the vortex can not be preserved. As mentioned in section 2.2.2, the non-conservative nature of VC1 has been a most disappointing feature and restricted it from being further applied. This is the main reason why the VC2 methodology was introduced.

When VC2 is used to replace VC1 the results are presented in Fig.3-29 ~Fig.3-34. Fig.3-33 gives the trajectory of the convecting vortex every 500 time steps compared with the analytical trajectory. The movement of the vortex is consistent with the analytical trajectory exactly, which demonstrates the conservative characteristic of VC2. Fig.3-34~Fig.3-37 shows the normalized velocity distributions after 500 and 3000 time iterations with VC1 and VC2 respectively. Trajectories obtained from VC2 are much smoother than the ones obtained from VC1.

3.3 Paired Vortices of the Opposite Signs

In this section, a pair of vortices with opposite signs are investigated to illustrate the mutual effect between these two vortices under the condition of no free stream flow. Two vortices will convect under their own induced velocities. The results are presented for a sequence of time steps to demonstrate the movements of two vortices. Different cases will be considered as the distance between two vortices varies. Both VC1 and VC2 methods will be investigated.

First, two opposite sign vortices are set 8 cells apart and VC2 is employed. Fig.3-38 shows the movement of two vortices and the analytical trajectory. For the analytical trajectory, the centroids of the two vortices will convect under the mutually induced velocities $U_\infty = 0.088, V_\infty = 0.088$ along the x, y directions. After 3000 time steps, the two vortices should move from $x_1 = -27, y_1 = -33$ and $x_2 = -33, y_2 = -27$ to $x_1 = 25, y_1 = 20$ and $x_2 = 20, y_2 = 25$, in which $\Delta t = 0.2$. But the motion of the centroids of the two vortices obtained by computation shown in Fig.3-38 does not exactly agree with the analytical trajectory. The main reason for this disparity is that though VC2 can conserve the total momentum the distance between the two vortices is too small and there will be some mutual interaction between them. In Fig.3-47, the result of two 8-cell-apart vortices obtained by VC1 is shown. Since this method is not able to conserve the momentum two vortices interact with each other and vorticity is exchanged only after 1000 time steps and eventually the two vortices lose their individualities and begin to merge.

Fig.3-39 and Fig.3-40 present the results of two vortices of 16-cell-apart and 32-cell-apart with VC2. Since the total momentum is conserved and the distance between the two vortices is large enough, the movement of the centroid of the two vortices agree exactly with the analytical trajectory. The self-induced velocity of each vortex, although several times the convecting velocity of the centroid, automatically cancels and has no effect because the method conserves momentum.

Even as the distance between the two vortices is increased, the movement of the vortices will not agree with the analytical trajectory if VC1 is employed. This is due to the non-conservative characteristic of the total momentum intrinsic in this method. Results presented in Fig.3-45 and Fig.3-46 demonstrate exactly this. With two vortices

set 16 cells apart and 32 cells apart, the movement of the two vortices greatly deviates from the expected trajectory.

3.4 Paired Vortices of the Same Signs

It is interesting to trace the movement of a pair of vortices with the same sign. What is expected is that the two vortices will rotate around each other under their induced velocities if the distance between the two vortices is sufficient. Otherwise the two vortices will merge.

First, the vortices are set 8 cells apart and the initial vorticity contours are shown in Fig.3-48. Fig.3-49 presents the vorticity contours after 1000 time steps with VC2 and it can be seen that two vortices have already begun to merge. After 3000 time steps, the vortices totally mix together and become one vortex.

Then, the vortices are initially separated by 16 cells, which are shown in Fig.3-51. After 3000 time steps, the two vortices keep their shapes and rotate around each other. The results shown in Fig.3-52. Fig.3-53 and Fig.3-54 present the results of two vortices rotating around each other in the 1^{st} loop and 2^{nd} loop. The positions of the paired vortices in these loops are recorded every 900 time iterations and they will form a circle as shown in Fig.3-53 and Fig.3-54. The vortices can be seen to be essentially the same at the end (after 7,200 time steps) as initially.

Chapter 4 Flow over a Surface-Mounted Cube

From the discussion in Chapter 1 and Chapter 2, we already know that large coherent vortical structures exist in near wall regions of turbulent boundary layers and that these vortical structures play a crucial role in generating, sustaining and developing the energy and momentum of the turbulence. In the wall turbulence study, great importance is attributed to the horseshoe vortices for the maintenance of the turbulence.

4.1 Background

Over the past forty years, enormous experimental results provide strong evidence that there are thickly populated inclined hairpin or horseshoe vortices in the wall of the turbulent boundary layer. These have been observed by using either oil visualization or particle image velocimetry (PIV). However, due to the lack of either advanced experimental or proper numerical techniques, it is hard to identify and track a single 3-D horseshoe vortex in the turbulent boundary layer. Research work had to turn to the generation of horseshoe vortices by small perturbation, such as hemisphere or small fluid injection to investigate the development of such vortices. Experimental results shown in Fig.4-1 were obtained in the Fluid Dynamics Laboratory of Eindhoven University of Technology**,** Netherlands [29] by H_2-bubble visualization, and in these pictures a street of hairpin vortices was clearly shown, which were generated by the protuberance of a hemisphere and are shedding and convecting downstream in the flow. These horseshoe

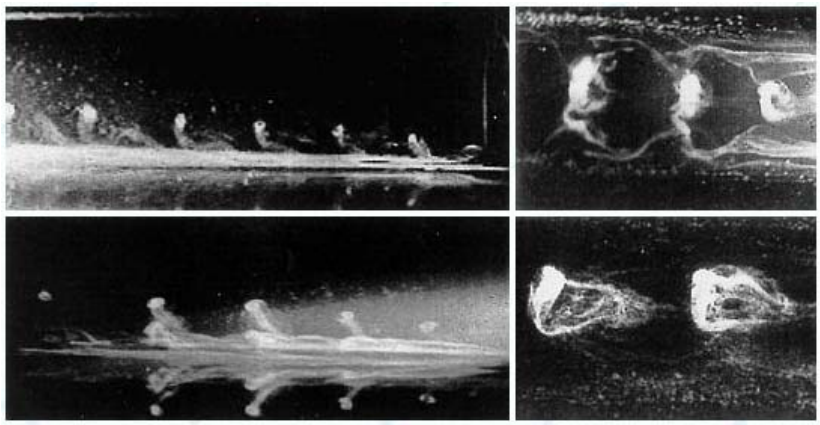

Fig. 4-1 Experimental observation of horseshoe vortices by H_2-bubble visualization

vortices are not perfectly symmetric, but they show the characteristic of the arches and heads, which make them more like horseshoe vortices rather than the inclined quasi-stream-wise vortices.

At the same time, many numerical simulations were performed to reveal the artificial generation and subsequent development of hairpin vortices. Recent numerical results obtained by Zhou [27] using DNS offer strong insights of the mechanism of the formation of the new hairpin vortex and the development of a hairpin-vortex packet. The initial flow field of his computation is a viscous, hairpin-like structure, which is referred to as the parent vortex. In his computation, a stretched grid was employed in the vertical direction, with about 0.096 grid spacing close to the wall and 5.96 in the center of the computational domain. New hairpin vortices were generated both downstream and upstream of the parent vortex, and after a certain time, a packet of hairpins was formed. To identify the hairpin vortex in the boundary layer, Zhou employed the imaginary part of the eigenvalue of the velocity gradient tensor. The numerical result obtained for the iso-surface of the hairpin vortices street is shown in Fig.4-2, which looks similar to the packet of the hairpin vortices shown in Fig. 4-1.

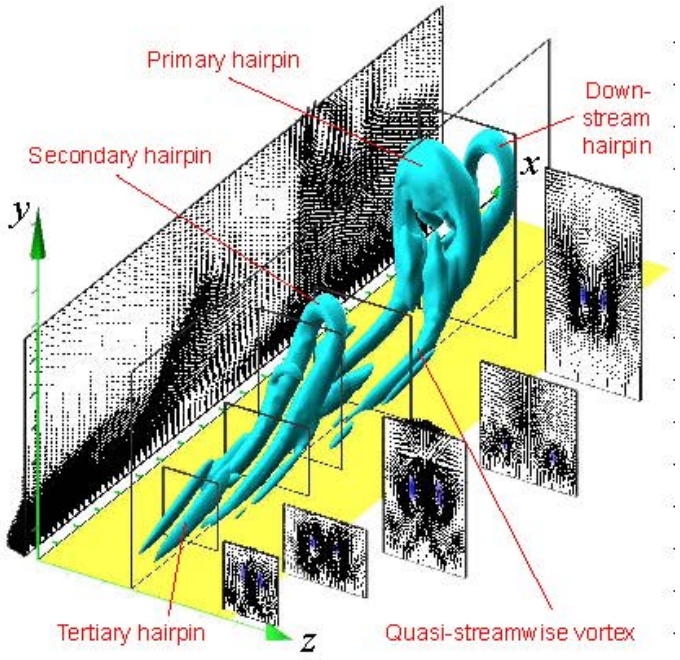

Fig. 4-2 Computational result of Zhou, the iso-surface of the hairpin vortices street

Other researchers have stimulated the study of hairpin vortices by means of small perturbations in the channel or flat-plate flows. Tufo [42] used DNS to compute the interaction between a flat-plate boundary flow and a hemispherical roughness element. The mechanism associated with the artificially generated hairpin vortices in the near wake region could then be studied. These studies were interested in the formation of hairpin-like vortices which are generated in the wake of a hemisphere and lift away from the wall. Schematic of the numerical results obtained by Visualization Toolkit (VTK) in Fig.4-3 show clearly the formation and development of a street of hairpin vortices, which is in agreement with experimental observation in Fig.4-2. Though these results were obtained for a surface-mounted hemisphere, one can get strong insights from them about the evolution of the hairpin vortices.

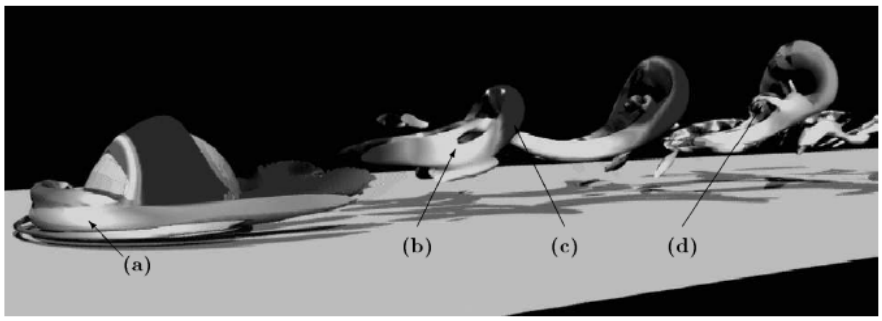

Fig. 4-3 Key vortices structure from Tufo: standing hairpin vortex(a), interlaced tails(b), hairpin head(c), and bridge(d). Vorticity iso-surface

To better understand the dynamics of coherent vortical structures in the turbulent boundary layer, flow over a surface-mounted cube is simulated in this thesis to study the structure of the shedding hairpin vortex and its development in the wake region. Although the geometry looks simple, the flow over a surface-mounted cube has been a long-lasting topic not only for academic research but also for industry applications. This three-dimensional sharp-edged cube produces complicated flow separation, and especially in the wake region, an intense turbulent wake is created. Flow is characterized by periodic shedding of vortices and experiences different separations at different locations. These include the corner in front of the cube, the top surface of the cube and back face of the cube.

Due to the complexity of the flow properties, most of the research work performed on vortical structures of flow over a surface-mounted cube has concentrated on the region very near the back face of the cube and little work has been done on the generation of hairpin vortices and the development of the hairpin vortex street. In this thesis, the interest is in the large-scale and small-scale vortical structures near the back face of the cube and in the wake of the cube. In particular the details of the formation of

hairpin vortices and thereafter the development of the hairpin vortices packet will be revealed. There are very few simulation results that have revealed the formation of the hairpin vortices packet even using DNS or LES [42] with higher order resolution. A strong packet of hairpin vortices behind the back face of the cube will be observed in the thesis. This is achieved, for the first time by using only a very coarse uniform Cartesian grid, which demonstrates the efficiency and power of the Vorticity Confinement method.

4.2 Flow Structures

The vortical structure in the wake region is very complicated. The flow experiences multiple separations, reattachments and recirculations. As the flow reaches the cube, the main separation vortex and secondary ones are formed in front of the cube. Due to the adverse pressure gradient caused by the blockage effect of the three dimensional cube and the lower wall, the main flow experiences separation near the junction of the lower wall and the base of cube. Therefore, the boundary layer separates and forms a vortex, which wraps around the cube and convects to the downstream of the flow. The overall shape of the formed vortex is bent like a horseshoe or hairpin vortex, which is originally observed by Theodorsen [21] and called horseshoe or hairpin vortex due to its shape.

Based on the distance to the back face of the cube, the weak region, downstream of the cube, can be divided into two regions: first, the near-wake region, where the boundary layer separates from the surface of the obstacle and the horseshoe vortices are generated; second, a far-wake region, which is the zone after the near-wake region where generated horseshoe vortices are convected further down stream of the obstacles and a packet of horseshoe vortices is formed. As the velocity of the main flow increases, the structure of

the horseshoe vortex system becomes unsteady and complicated. The hairpin-like vortices keep shedding from the cube, and are convected downstream and form a street of hairpin vortices, as shown in Fig.4-2. The region downstream of the cube contains various flow phenomena, such as a free-shear layer, re-circulating flow and redeveloping turbulent boundary layer, etc. The hairpin vortices behind the cube are characterized with the regeneration and mutual merging of hairpin vortices. According to Acarlar and Smith [28], the main mechanism of the formation of the horseshoe vortex is based on the interaction between the separated boundary layer and the base pressure (the low pressure region behind the back face of the cube). When the main flow separates from the top of the cube, there is a low pressure region right downstream of the cube and the separated boundary layer will pull the flow downstream. The streamlines will be forced to curve inward as the region between the lower wall and the separated boundary layer is reduced by the outer region flow. As the streamlines are curved, a centrifugal force field will be developed to resist the pressure across the curved streamlines and the vortex lines spiral inwards and concentrate to form the horseshoe vortices. The formation of horseshoe vortices is a process of build-up and release of concentrated vorticity. Once horseshoe vortices are formed and separated from the cube, they will be convected downstream and a street of horseshoe vortices will be formed.

As mentioned before, little research work has been done on the formation and development of the horseshoe vortices and their mutual interaction downstream of the cube either by experimental observations or numerical simulations. In this thesis, the generation and subsequent development of the horseshoe vortices, which are produced by the rolling-up of the shedding vortex yielded from the three-dimensional flow separation at the back face of the cube, are discussed in detail. The numerical work is carried out on a very coarse and uniform Cartesian grid and Vorticity Confinement is applied.

4.3 Numerical Geometry and Boundary Conditions

The geometrical model for the flow over a cube is shown in Fig 4-4. H in the schematic figures is the dimensional size of the cube. To simulate the formation and development of the horseshoe vortices, two grid resolutions are employed to test the ability of the Vorticity Confinement method to conserve the vortical structure. First, a uniform Cartesian grid resolution of $161\times61\times61$ along the x, y and z directions respectively is used, which is referred as the case of the large cube. The 161 grid points are distributed within 8 times of the cube dimension H in the stream-wise direction; the 61 grid points were dispersed about 3 times cube dimension H along the span-wise and vertical direction. So, there are 20 grid cells along each side of the large cube. Then, we attempt to simulate the flow field within a grid resolution of $91\times31\times31$, where the 91 grid points are arranged within 15 times of the cube dimension H in the stream-wise direction; 31 grid points were dispersed about 5 times cube dimension H along the span-wise and vertical direction. The second case is referred as the case of the small cube or 6x6x6 cube since the number of grid cells along each side of the small cube is 6. Both grids are uniform, coarse Cartesian grids, that is, $\Delta x=\Delta y=\Delta z=1$. The sufficiency of such a coarse grid resolution has been verified by comparing the results with those obtained by LES simulations. Comparison with experimental data will also be made. For both cases, the cube is located near the front of the computational domain.

The flow field is investigated mainly for two different grid sizes for the surface-mounted sharp- edged cubes to illustrate the whole process of generation and evolution of horseshoe vortices. The large cube is set between x=20~40, y=20~40 and z=0~20 along the x,y,z directions and the small cube is located between $x=13\sim19$, $y=13\sim19$ and $z=0\sim6$ along the x,y,z directions.

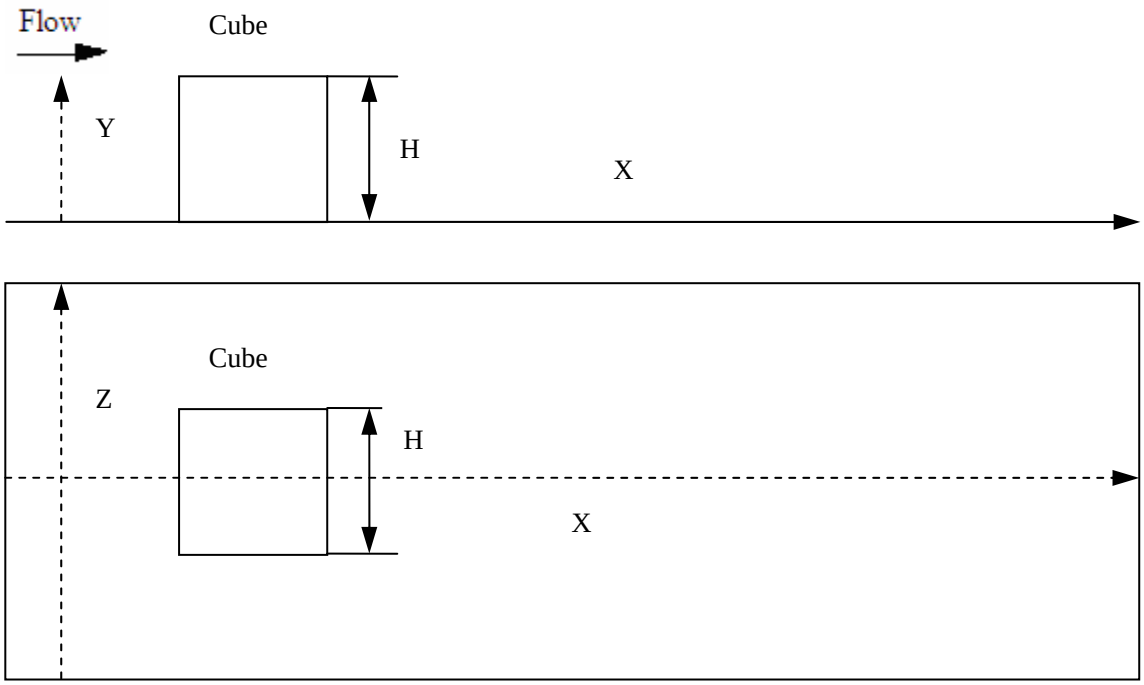

Fig 4-4 Geometry of the computation domain

The initial velocity vector field was set to $U_0 = U_\infty, V_0 = 0, W_0 = 0$ along the x,y,z directions respectively everywhere, except on the flat-plate and cube surfaces where the velocity is set to zero according to the no-slip boundary condition. U_∞ is the free stream flow velocity and set to 1. Different values of the numerical diffusion and confinement coefficients, μ and ε, are used to study the ability of Vorticity Confinement to control the size and time scales of the convecting vortical regions or vortical boundary layer. Results without Vorticity Confinement are compared with those simulated with Vorticity Confinement. The most often used diffusion coefficient and confinement coefficients are set as $\mu = 0.4$ and 0.2 and $\varepsilon_f = 0.4$. The time step is $\Delta t = 0.2$ and the CFL number is 0.2. Periodic boundary conditions are applied in the span-wise direction. The pressure at the exit boundary is extrapolated from the closest interior points and the no-slip boundary conditions are employed on the wall of the cube and the floor of the plate. Most of the results are obtained by VC1. Further research work on VC2 is still under the way, and will be mentioned in Chapter 5.

4.4 Results

4.4.1 Directly upstream and downstream of the cube

Directly downstream of the cube, a three-dimensional wake is formed. Due to the blockage influence of the cube, the main flow is separated. One part of fluid travels against the adverse pressure gradient and rolls up to form vortices against the front wall of the cube. Another part of the fluid goes downstream of the cube to form the horseshoe vortices around the cube or the street of horseshoe vortices in the wake.

Fig.4-5 shows the experimental results [43][44] of the streamlines distributions on the symmetry plane and on the flat plate. In Fig.4-5(a), clearly seen is that there is a separation point upstream of the cube, which is often called a saddle point. The streamline passes through the saddle point and wraps around the cube, forming a horseshoe vortex. The streamline distributions on the floor plane in Fig.4-5(b) show this horseshoe vortex around the cube and trailing downstream.

Fig.4-72[II] presents the simulation results of streamline distributions on the symmetry $x-z$ plane (at $y=6$) obtained by VC1 after 50 time steps for the small cube. What can be observed is that upstream of the cube the main flow experiences separation and a saddle point exists in front of the cube, which is in correspondence with the experimental result shown in Fig.4-5(a). A part of the fluid experiences an adverse pressure gradient and rolls up to form a vortex against the cube wall. There is an attachment point in front of the cube.

[II] Fig.4-6 – Fig.4-124 in Chapter 4 are located in the Appendix

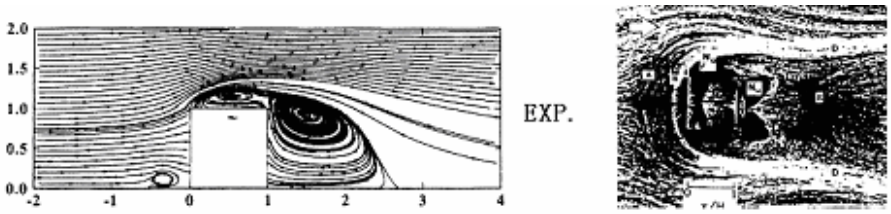

(a) (b)

Fig. 4-5 Experimental distributions of streamlines on the symmetry plane and on the floor of the channel

Upstream of the cube, the flow separates and the follow-up vortex roll-up are essential for the formation of the horseshoe vortex which wraps around the cube. Directly downstream of the cube, the approaching flow reaches the sharp edge of the cube, moves upwards, accelerates towards the sharp edge and then separates from the edge. The separated shear layer descends towards the flat plate while moving downstream and another separation zone is formed behind the cube. It can be seen in Fig.4-72 that the present computed length of the separation zones in front of the cube and behind the cube are close to the experimental ones compared with the cube sizes in the simulation results and in the experimental observation. The separation on the roof of the cube is not shown in Fig.4-72 and the possible reason is due to the limitation of the coarse grid resolution: the very small features can not be captured.

Directly downstream of the cube, two corner vortices are formed by the two sides of the cube and join on the symmetric plane to form an arch behind the back face of the cube. A three-dimensional iso-surface of the vorticity magnitude is shown in Fig.4-60 and Fig.4-64 in different views and an arch, which is clearly shown behind the back face of the cube can be observed from three views (top, end and side views) in Fig.4-68 (a),

Fig.4-69(a) and Fig.4-50(a). Two corner vortices are formed at the junction of the channel floor and the base of the cube due to the interaction of the mounted cube and the surface. These vortices will join at the symmetry plane and be connected by a narrow bridge to form a closed arch behind the cube. Fig.4-6 and Fig.4-17 present three-dimensional iso-surfaces of the vorticity magnitude for the large cube after 50 time steps from different viewing angles and this arch structure is perfectly shown behind the cube.

Fig.4-71 presents instantaneous velocity vector field and contours of the magnitude on the central plane at 50 time steps for the small cube. It can be seen that there are vortices shedding from the leading lateral edges of the cube. Upstream of the small cube, the blockage effect of the cube produces an adverse pressure gradient which forces the main flow to separate and wrap around the cube, creating a horseshoe vortex around the cube. In Fig.4-73(b), contours of the magnitude of vorticity on the lower level (at $z = 2$) after 50 time steps are presented and it's easy to identify the horseshoe-shaped region of strong vorticity around the cube.

4.4.2 Formation of the hairpin vortices

The low pressure region at the back face of the cube will cause the vortex lines to move inwards and the vortex lines will converge to form a vortex tube, which will shed from the downstream face of the cube as a single hairpin vortex. Once one hairpin vortex is generated and convected downstream, a second hairpin vortex will be formed in a similar sequence of events. Both instantaneous contours of the vorticity magnitude and velocity vector field on the symmetry plane are presented for a sequence of times for the

large cube and the small cube to illustrate the dynamics of vortex generation from the cube.

In Fig.4-39 the velocity vector field is presented for the large cube after 120 time steps. It can be seen that beyond the rear edge of the large cube, the shear layer becomes disturbed and a new vortex head is born and will be shed from the rear edge of the large cube. After 300 time steps, this new-born vortex is convected downstream, as shown in Fig.4-40 both for vorticity contours and velocity vector field. Then, after 400 time steps, this vortex is convected further downstream and after 600 time steps, another new vortex head is born right near the rear edge of the large cube just as the first vortex is moving away, as shown in Fig.4-41(a) and Fig.4-42(a).

After a sequence of times, it turns out that this process is repeated periodically. As the old vortices are convected away downstream, the new vortices will be born right near the rear edge of the cube and thus form a sequence of the vortex heads, as shown in Fig.4-48(a) and (b). This sequence of vortex heads demonstrates the existence of the coherent structure in the wake region due to the effect of the cube and the plate. The flow field near the front edge of the cube is nearly steady. For the small cube, the same procedure can be observed from the vorticity magnitude contours and velocity vector field for a sequence of times in Fig.4-71, Fig.4-74, Fig.4-75 and Fig.4-76.

Wang [45] used hotwire and PIV techniques to investigate the flow over a finite-length square prism. Though the geometry is different from the present study, strong insights can still be drawn from these experimental results. Fig 4-83 shows the instantaneous contours of the x component of the vorticity vector at the different x locations in the span-wise plane ($x/d = 1$ and $x/d = 3$, where d is the dimension of

the prism along the x direction). The experimental results display a pair of counter-rotating vortices near the prism base at $x/d=1$ in Fig.4-83(a). At $x/d=3$, a pair of counter-rotating vortices appear near the top edge of the prism, which show the characteristic of the horseshoe vortices.

We return to the present study where it is formed that the vorticity distribution near the free end of the cube is quite symmetrical and the upper vortex pair, with a peak vorticity of - 0.1 and 0.13, in Fig.4-82(a) is attributed to the free shear layer separating at the leading edge and rolling up to form the horseshoe vortices. The two counter-rotating vortices in Fig.4-82(b) are consistent with the horseshoe vortical structure, as illustrated in Fig.4-51(b). Fig.4-50 presents the instantaneous velocity vector field for the span-wise plane at $x/d=1$ after 120 time steps for the large cube, and a pair of counter-rotating vortices can be observed near the cube base, which is consistent with the experimental observation in Fig.4-82(a). After 400 time steps, two symmetric vortices appear near the top edge of the cube, which reveal the generation of a horseshoe vortex. The sequence of times sequences for the span-wise plane at $x/d=1$ reveal some structure information about the generation of the horseshoe vortices can be found in Fig.4-49~Fig.4-59. For the small cube case, similar numerical results were obtained.

4.4.3 Evolution and development of the hairpin vortices

While the instantaneous contours of the vorticity magnitude and the velocity vector field in both ream-wise and span-wise planes can provide a fair amount of information about the hairpin vortex evolution, they fail to reveal any three-dimensional details. A series of iso-surfaces for the vorticity magnitude are shown, as a sequence in

time, to illustrate the formation of the horseshoe vortices and the street of the horseshoe vortices. From the discussion above, we observed several vortical structures, some of which had not been identified prior to viewing the corresponding three-dimensional iso-surface of the vorticity magnitude. Fig.4-14, Fig.4-25 and Fig.4-32 present the iso-surface of the vorticity magnitude after 1600 time steps for the large cube. These are shown from different viewing angles. Fig.4-14 clearly shows a packet of classic horseshoe vortices downstream of the cube. From Fig.4-35(i), the top view of the iso-surface at 1600 time steps, it can be seen that there is an interlacing of the hairpin vortex tails. This was also observed by Acalar and Smith [28]; the hairpin heads, and vortex bridges, look similar to the numerical simulation results presented in Fig.4-2 and Fig.4-3. As the main flow separates from the rear edge of the cube, it drags fluid downstream with it. The streamlines will be curved since the outer region flow field tries to narrow the region between the plate wall and the separated boundary layer, and there is a low pressure region at the back face of the cube. The low-pressure region will cause the vortex lines to whirl inwards. As a result of the separated boundary layer and subsequent vortex lines spiraling inward, the concentrated vortex tubes will be discharged into the downstream direction as discrete single hairpin vortices. A subsequent horseshoe vortex system then develops in the wake region of the cube. The details of the horseshoe vortex formation and development will be discussed in the following. First, the formation of the primary horseshoe vortex is investigated.

a. Formation of primary hairpin vortex

In Fig.4-6, due to the adverse pressure gradient and the intersection of the flat plate with the base of the cube, the free shear layer separates from the rear edge of the cube and forms a horseshoe-like vortex at the back face of the cube. This initial separated flow evolves into a hairpin-like vortical structure as shown in Fig.4-10, Fig.4-21 and Fig.4-28. These plots are from different viewing angles and are after 600 time steps. This structure

will be referred to as the primary hairpin vortex. The top view, side view and end view for the vorticity iso-surface in Fig.4-35(e), Fig.4-36(e) and Fig.4-37(e) clearly show the structure of the horseshoe vortex: the head, the inclined stream-wise leg and the bridge. The geometry of the generated horseshoe vortex resembles the instantaneous hairpin vortex structure obtained in both experiments and computations results [28] [42].

We first consider the formation of the primary hairpin vortex for the large cube. At the beginning, the free-shear layer separates from both the rear edge of the cube and the two lateral faces of the cube, and forms an arch-like vortex as in Fig.4-6 (after 50 time steps). The initial quasi-stream-wise vortices lift away from the wall and the resulting vortical structure is curved upwards. As the quasi-stream-wise vortices lift up, the span-wise distance between them decreases. The magnitude of the vorticity of this vortex pair is stronger near the downstream end and thus the mutual interaction is stronger there. Therefore the downstream end of the vortex pair lifts up more rapidly than the upstream end. As the flow structure is convected further downstream, the upstream end of the lift-up process is strongly stretched because of the mean shear layer. At the same time, there is a low-speed fluid shear layer, which is pumped up and back from the wall as the vortex is meeting the high-speed mean flow. The two counter-rotating quasi-stream-wise vortices are curled further and the two legs of the horseshoe vortices have been extended further along the downstream; and the shear layer has further intensified, particularly near the top of the circled region. At this stage, the primary hairpin vortex structure is formed as shown in Fig.4-10, Fig.4-21 and Fig.4-28. From Fig.4-35(e), the top view of the iso-surface of the vorticity magnitude clearly shows a generated classic hairpin vortex, with identified vortex head, the inclined stream-wise leg and narrow bridge.

b. Formation of the secondary hairpin vortex

The formation of the secondary hairpin vortex is very like the formation of the primary hairpin vortex described above. As shown in Fig.4-12 and Fig.4-35(g), the second hairpin vortex is formed right after the primary hairpin vortex as the primary vortex is convected downstream. The previous discussion regarding the mutual interaction and vortex curvature can be extended to investigate the generation of the secondary hairpin vortex.

As the primary hairpin vortex is developed from the quasi-stream-wise vortices form to an Ω shaped vortex, a second hairpin vortex is produced upstream of the primary vortex. As shown in Fig.4-13, the downstream section of the primary vortex legs are about 40 grid cells long and have an approximate inclination of 20 degrees. The primary horseshoe vortex and the secondary horseshoe vortex are not perfectly symmetric as shown in Fig.4-13. The line joining the head of the primary and secondary vortices, which roughly characterize the envelop of the vortical packet formed by the primary and secondary vortices, has a characteristic slope of 20 degree.

For the small cube, the process of the formation and development of the primary and secondary horseshoe vortices not as clear as for the large cube. But still, from a series of iso-surface figures for a sequence of times several horseshoe-like vortices can be seen in Fig.4-60~ Fig.4-63.

c. Formation of a packet of vortices

With the formation of the primary and secondary hairpin vortices, a series of hairpin vortices will be generated downstream of the cube consistently and form a packet of hairpin vortices. The structure of the later born hairpin vortices is similar to the previously formed primary and secondary hairpin vortices. To see this packet of hairpin

vortices, significant resolution in space and time is required. It is quite important to carefully select the simulation results at the right time steps in order to present the completed street of hairpin vortices. After reviewing the iso-surface of the vorticity magnitude in a sequence of times, results at time step 1600, 1800 and 3000 are selected to present the formation of the packet of vortices from the different viewing angles.

In Fig.4-14, Fig.4-25 and Fig.4-32, the iso-surface of the vorticity magnitude is presented from different viewing angles at time step 1600 for the large cube. A clearly formed packet of horseshoe vortices can be seen in Fig.4-35(i) from the top view for the vorticity iso-surface. In the downstream region, three horseshoe vortices are convected downstream, which are connecting as a horseshoe loop. In the region near the cube, a new horseshoe vortex is being generated. As the horseshoe loop is convected downstream, the preceding vortices are stretching and disappearing as the result of the stretching-induced dissipation. In Fig.4-36(i), the side view of the iso-surface of the vorticity magnitude is consistent with the numerical simulation results obtained by DNS presented in Fig.4-2.

As the horseshoe loop is convected further downstream, after 1800 time steps, the primary vortex is diffusing and the legs and the heads of the hairpin vortices within the loop are stretched and diffused. The vortex becomes longer and thinner, as shown in Fig.4-15, Fig.4-26 and Fig.4-33 from different viewing angles. In Fig.4-16, Fig.4-27 and Fig.4-34, it can be seen that after 3000 time steps, the primary vortex has disappeared and only left are two stretched legs in the downstream end. The two legs of the hairpin vortices have the opposite signs. They are close to each other and not well resolved so that they will merge. At the same time, the heads of the hairpin vortices are all of the same signs and they remain. At the same time, a new born horseshoe vortex is appearing near the rear edge of the cube. Thus, it is demonstrated that the whole horseshoe vortex

generation system is characterized by a repeated pattern of generation, translation, and merging of the vortices. Four movie clips (1.avi~4.avi) are attached with this dissertation, which are made for the vorticity iso-surface for both the small cube and the large cube in a sequence of time steps. 1.avi and 2.avi are for the large cube and 3.avi and 4.avi are for the small cube. These movie clips clearly show the formation and development of hair-pin vortices from different viewing angles.

4.4.4 Comparison with experimental and LES results

To compare with the experimental and LES results, mean velocity profiles for the stream-wise velocity component and, a component of the mean turbulent stress, $\overline{u'^2}$, profiles are computed for several sequences of the hair-pin vortex shedding process. Fig.4-83~ Fig.4-85 show the comparison among VC1, LES [46] and the experiment results [43][44] for the profile of the mean velocity component U at several locations on the symmetry plane for the large size cube. The experimental and LES results were obtained in a channel so that there will be expected difference between the computational results in this thesis and the experimental and LES results near the upper wall. The Reynolds number for the experiment is about 10^5. In Fig.4-83, the result with VC1 shows there is a back flow region on the roof region of the cube which is similar to the LES and experimental results. The results with VC1 shown in Fig.4-83 and Fig.4-84 are in good agreement with the experimental and LES results, but further downstream, at the location $x/h = 2.5$, the result with VC1 deviates from the LES result. Most of the LES results for flow over a surface-mounted cube can't get the street of the hair-pin vortices as shown in Fig.4-16 even through very fine grids and complicated numerical schemes were taken. The comparison for mean turbulent stress ($\overline{u'^2}$) on the symmetry plane between VC1, experiments and LES are shown in Fig.4-86~Fig.4-89 at different

locations downstream of the cube. Fair agreement between the results with VC1 and experimental results can be observed.

Comparison of the mean velocity component U with the experimental and LES results for the small cube are shown in Fig.4-90~Fig.4-92. In Fig.4-90, there is no back flow on the roof region, as shown in Fig.4-83 for the large cube, since a very coarse grid is employed near the cube. Nevertheless, further downstream of the cube, at the location $x/h=1.3$, the mean velocity profile for the component U shows better agreement with the experimental results than does the LES result. The profiles of mean turbulent stress $\overline{u'^2}$ for the small cube are shown in Fig.4-93~Fig.4-96. Though a very coarse grid is employed, the agreement with the experimental results is still good.

The results without Vorticity Confinement for the large cube case are also shown In Fig.4-83~Fig.4-85 and poor agreement with both experimental results and LES results can be seen. Through the comparison with the experimental and LES results, the ability of the Vorticity Confinement method to capture thin vortical features without numerical spreading has been demonstrated.

4.4.5 Different diffusion and confinement coefficients

The diffusion and confinement coefficients are the two of the most important parameters used in the Vorticity Confinement method to control the size of vortical structures. The most used values in the computation of this thesis are $\mu=0.2$ and $\varepsilon=0.4$. Different values of μ and ε are used to test the efficiency of the Vorticity Confinement method. For the large cube case, the proper value of the field confinement coefficient is from 0.1~1. For the surface confinement coefficient, the proper value is <0.1. When the field confinement coefficient is bigger then 1 or the surface confinement

is larger than 0.1, the vorticity that has been added to the field is too strong and the flow field reduces to chaos. At the same time, if the field confinement coefficient is smaller then 1 or the surface confinement is smaller than 0.1, the whole flow field will diffuse and there will be no flow separation in the back face of the cube. The conditions for the small cube are the same as those of the large cube.

To better understand the effect of the confinement coefficient, the comparison has been made among different values of ε for mean velocity component U and mean turbulent stress ($\overline{u'^2}$) at the several locations in Fig.4-97 ~ Fig.4-109 for both the large and small cubes. The selected values of the confinement coefficients are $\varepsilon_f = 0.2, 0.4$ and 0.8. From the mean velocity component profiles shown in Fig.4-97 ~ Fig.4-99, the results of $\varepsilon_f = 0.4$ are obviously better than $\varepsilon_f = 0.2, 0.8$. The same conclusion can be made for the small cube. It is important to define the most appropriate range of values of the confinement coefficient ε. This is, of course, also true in the development of any LES or RANS model.

4.4.6 Grid dependence

To consider the grid effect for the computation of flow over a surface-mounted cube, three difference scales of cubes in relative smaller computational domains are selected in the code. The computational domain are set as, 6 times of the cube dimension H in the stream-wise direction and 3 times cube dimension H along the span-wise and vertical direction respectively and the grid cells along each side of the cube are set to 6, 20 and 40.

Fig.4-110, Fig.4-111 and Fig.4-112 present the comparison of the mean velocity profiles for the different scales of cubes on the symmetry plane at different locations. The

results for 40x40x40 cube are in better agreement with the experimental results than 6x6x6 cube and 20x20x20 cube due to the finer grid employed. The proper range of values for the coefficient of the field confinement ε_f is $0.1 \sim 1.0$ for all three cubes, and the proper values for the coefficient of surface ε_s decreases as the size of the cube increases. For 6x6x6 cube, the value of ε_s is around 0.1 and as the cube size increase to 20x20x20 cube, the value of ε_s is about 0.01. As the size of the cube increase, it is easier for the flow to roll-up and separate from the cube so that the coefficient of the surface confinement decreases.

4.5 Boundary Layer with a Small, Single Cell Cross-section Obstacle

A small aspect ratio obstacle is set in the front of the computation domain with 1x1 in the symmetrical plane ($x-z$ plane) and full size along the span-wise direction (y direction). The computational domain is set as $161\times61\times61$ and again a uniform Cartesian grid is employed. The numerical parameters and coefficients are the same as in the above cases. The inlet velocity is $U_0 = 1, V_0 = 0, W_0 = 0$ along the x,y,z directions respectively everywhere, except on the flat-plate. Vorticity iso-surfaces and vorticity contours for the symmetry plane are presented in a sequence of time steps. Fig.4-117 presents the vorticity iso-surface after 350 time steps. It can be seen that a huge amount of vorticity has been stimulated by Vorticity Confinement and resembles turbulence. If no Vorticity Confinement is employed, the flow will remain laminar for the coarse grids employed. Several vorticity iso-surfaces and vorticity contours for the symmetry plane are presented in different time steps on Fig.4-119 to Fig.4-124 and it is clearly seen that the strong vortices are stimulated and convected downstream of the rib and these vortices are very like the vortices in the turbulent boundary layer. Further work on Vorticity Confinement for the simulation of turbulent boundary layer flows has to be done in the near future.

4.6 Discussion

The main point of VC is to efficiently simulate complex incompressible flows with complicated vortical structures that can convect over long distances without diffusion. In this chapter, numerical simulations were performed to investigate the formation of the characteristics of the vortical structures for flow over a surface-mounted cube. Little work has been done to study the formation and development of the primary horseshoe vortex and the packet of the horseshoe vortices due to its complexity and there are very few simulation results that have revealed the hairpin vortices packet. In this chapter, the flow field is investigated both upstream and downstream in a sequence of times. The formed horseshoe vortex upstream of the cube and the hairpin vortices downstream of the cube and its formation to a packet of horseshoe vortices were studied in detail.

As the flow approaches the obstacle, it experiences separation and rolls up to form a vortex against the upstream of the cube. A subsequent horseshoe vortex is developed and wrapped around the cube. Downstream of the cube, the results are presented in a sequence of times to show the generation of the primary horseshoe vortex, the secondary horseshoe vortex and thereafter the street of horseshoe vortices. After a certain time of development (time steps 3000), a street of horseshoe vortices is clearly seen, which is in agreement with the experimental observation. The unsteady horseshoe vortex systems, characterized by a repeated pattern of generation, translation, and merging of the vortices, will be obtained in the wake region of the cube. The horseshoe vortices formed are not strictly symmetric and are clearly seen to have the long quasi-stream-wise legs and the span-wise heads. All these results are obtained on uniform Cartesian grids, which proves the power and robustness of the Vorticity Confinement method.

Chapter 5 Conclusion

Compared with the traditional CFD method, an entirely new but more efficient and economical methodology has been investigated and tested. This new method, which is called Vorticity Confinement and originally developed by Steinhoff [16]. After more than sixteen years' research, Vorticity Confinement has proven to be a very robust scheme to compute vortex dominated flows. Due to the non-conservative constriction of the original Vorticity Confinement method (VC1), which has been used for many years, a new conservative scheme is developed and studied in this thesis mainly in 2D flow problems. The most important features and the schemes of both VC1 and VC2 have been discussed in detail. Some numerical simulation of the one dimensional wave equation and two dimensional vortices have been done to test the efficiency of both VC1 and VC2. The comparison is made among the results obtained by the two different schemes. VC2, which is simpler and more efficient than VC1, is proven to be a robust scheme for vortex dominant flows.

The flow over a three-dimensional surface-mounted cube has been simulated and comparison was made with both experimental results and simulation results by DNS using VC1. These results show that Vorticity Confinement can efficiently simulate very complex flows using only uniform, coarse Cartesian grids, while other traditional methods have to use non-uniform stretched grids and complex numerical schemes. Vorticity Confinement is able to convect the vortex downstream and confine the

concentrated vorticity within a few grid cells in spite of numerical diffusion. Due to the limitation of the very coarse grid used, the very small features can't be captured. But the main characteristics of the flow phenomena are simulated reliably and the complex flow problems can be solved economically and reliably.

For future work, further study on VC1 and VC2 should be performed and more work on turbulent boundary layer will be expected.

LIST OF BIBLIOGRAPHY

LIST OF BIBLIOGRAPHY

[1] Euler, L., “Principia motus fluidorum”, 1761

[2] Courant, R., Friedrichs, K. and Lewy, H., “On Partial Differential Equations of Mathematical Physics”, Technical Report NYO- 7689, AEC Computing Facility, Institute of Mathematical Sciences, New York University, September, 1956 (English translation of the original paper, published in Math. Annalen 100 (1928) 32-74)

[3] Von Neumann, J., and Richtmyer, R.D., “A Method for the Numerical Calculation of Hydrodynamic Shocks”, J. Appl. Phys., Vol. 21, No. 3, 1950. pp. 232-237.

[4] Lax, P.D., “Weak solutions of nonlinear hyperbolic equations and their numerical computation”, Comm. Pure Appl. Math. 7 (1954) 159-193

[5] Godunov, S., “A difference scheme for numerical computation of discontinuous solution of hydrodynamic equations”. Math. Sbornik 43: (1959) 271-306.

[6] Lax, P.D. and Wendroff, B., “Systems of conservation laws”, Comm. Pure Appl. Math. 13 (1960), 217-237.

[7] MacCormack, R. W., “The Effect of Viscosity in Hypervelocity Impact Cratering”, AIAA, Paper 69-354, AIAA Hypervelocity Impact Conference, Cincinnati, Ohio. (1969)

[8] Zienkiewicz, O. C. and Cheung, Y. K., “Finite elements in the solution of field problems”, the Engineer, (1965) 507–510

[9] Baker, A.J., “Finite Element Computational Fluid Mechanics”, McGraw-Hill, Publisher, Hemisphere, New York, (1983) pp. 554 ISBN0-89116-472-3

[10] Pepper, D. and Heinrich, J., “The Finite Element Method: Basic Concepts and Applications”, Hemisphere Publishing Bristol, London, (1992) pp.256 ISBN 1-56032-104-0

[11] Thompson, J.F., Warsi, Z.U.A. and Mastin, C.W., “Numerical Grid Generation”. North-Holland, New York, (1985)

[12] Fan, M., Wenren, Y., Dietz, W., Xiao, M., Steinhoff, J., “Computing Blunt Body

Flows on Coarse Grids Using Vorticity Confinement", Journal of Fluids Engineering, Vol. 124, No. 4, pp.876-885, Dec. 2002.

[13]Rai, M. M. and Moin, P., "Direct simulations of turbulent flow using finite-difference schemes". J.Comput. Phys., 96, 15-53 (1991).

[14] Piomelli, U. and Liu, Junhui, "Large-eddy simulation of rotating channel flows using a localized dynamic model". Phys. Fluids, 7(4), 839-848 (1995).

[15] Steinhoff, J., Wenren, Y., Wang, L., Fan, M. and Braun, C., "The Computation of Flow over Helicopter Rotors and Complex Bodies Using Vorticity Confinement", Computational Fluid Dynamics Journal, vol. 9, No. 1 (2000).

[16] Steinhoff, J., Wenren, Y., Braun, C., Wang, L. and Fan, M., "Application of Vorticity Confinement to the prediction of the Flow over Complex Bodies", Frontiers of Computational Fluid Dynamics(D. Caughey and M. Hafez, eds). (2002)

[17] Steinhoff, J., Mersch, T., Underhill, D., Wenren, Y., and Wang, C., "Computational Vorticity Confinement: A Non-Diffusive Eulerian Method for Vortex Dominated Flows," UTSI preprint, (1992)

[18] Dietz, W., Fan, M., Steinhoff, J., Wenren, Y., "Application of Vorticity Confinement to the Prediction of the Flow Over Complex Bodies", AIAA-2001-2642. AIAA Anaheim meeting, June 2001.

[19] Fan, M., and Steinhoff, J., "Computation of Blunt Body Wake Flow by Vorticity Confinement", AIAA-2004-0592. AIAA Reno meeting, January 2004.

[20] Kline, S.J., Reynolds, W.C., Schraub, F.A. & Runstadler, P.W., "The structures of Turbulent Boundary layers", Journal of Fluid Mechanics, 95,741-773(1967)

[21] Theodorsen, T., "Mechanism of Turbulence", Proc. 2nd Midwestern conference on Fluid Mechanics, (1952)

[22] Head,M. R. & Bandyopadhyay, P., "New aspects of Turbulent Boundary layer structure". J. Fluid Mechanics, 175,135-162(1981).

[23] Nishioka, M. & Morkovin, M. V., "Boundary-layer receptivity to unsteady pressure gradients: experiments and overview." J. Fluid Mech. 171, 219–261(1986).

[24] Robinson, S.K., “Coherent Motions in the turbulent boundary layer.” Ann. Rev. Fluid Mech., 23,601-639(1991).

[25] Meinhart, C.D., “Investigation of turbulent boundary layer structure using particle-image velocimetry.” Mech. Sci. and technol., 4,619-626(1994).

[26] Meinhart, C.D. & Adrian, R.j., On the existence of uniform momentum zones in a turbulent boundary layer. Phys. Fluids,7,694-696, 1995.

[27] Zhou, J., Adrian, R.J. & Balachandar, S.., “Autogeneration of near wall vortical structure in channel flow", Phys. Fluids, 8, 288-291., 1996

[28] Acalar, M. S. & Smith, C. R., “A study of hairpin vortices in a laminar boundary layer. Part 1. Hairpin vortices generated by a hemisphere protuberance”. J. Fluid Mech. **175**, pp. 1-41(1987).

[29] H.A. Zondag , “The dynamics of hairpin vortices in a laminar boundary layer”. PhD thesis, Eindhoven University of Technology, The Netherlands. (1997).

[30] Steinhoff, J. and Underhill, D., “Modification of the Euler Equations for Vorticity Confinement Application to the Computation of Interacting Vortex Rings”, Physics of Fluids, 6, pp.2738-2743(1994).

[31] Steinhoff, J., Wenren, Y., Mersch, T., and Senge, H., “Computational Vorticity Capturing: Application to Helicopter Rotor Flow”, AIAA-92-0056 (Reno) (1992).

[32] Steinhoff, J., Fan, M., Wang, L., and Dietz, W., “Convection of Concentrated Vortices and Passive Scalars as Solitary Waves”, SIAM Journal of Scientific Computing, Vol.19, December 2003.

[33] Steinhoff, J. and Fan, M., “Vorticity Confinement for Computing Small Scales in Complex Flows, Including LES”, AIAA-2003-4099(1993).

[34] Steinhoff, J., Dietz, W., Haas, S., Xiao, M., Lynn, N., Fan, M., “Simulating Small Scale Features In Fluid Dynamics And Acoustics As Nonlinear Solitary Waves”, AIAA-2003-0078. AIAA Reno meeting, January 2003.

[35] Wenren, Y., Fan, M., Wang, L., Xiao, M., and Steinhoff, J., “Application of Vorticity Confinement to the Prediction of the Flow over Complex Bodies”, AIAA Journal, Vol. 41, No.5, May 2003, pp.809-816.

[36] Harlow, F., Welch E. “Numerical calculcation of time-dependent viscous incompressible flow of fluid with free surface”. Physics of Fluids, 8: 2182–2189(1965).

[37] Chorin A. J. “Numerical solution of the Navier-Stokes equations”. Math. Comput., 22: 745–762(1986).

[38] Kim J, Moin P. “Application of a fractional step method to incompressible Navier-Stokes equations”. J. Comp. Physics, 59: 308–323(1985).

[39] P. Swarztraouber, R. Sweet and J. Adams, “FISHPACK: Efficient FORTRAN Subprograms for the Solution of Elliptic Partial Differential Equations”, UCAR Publication, July 1999

[40] Steinhoff, J., Lynn, N. and L. Wang, “Computation of High Reynolds Number Flows Using Vorticity Confinement: I. Formulation”, UTSI Preprint, March 2005.

[41] Yu, L., “Vorticity Confinement Application to Flow around Circular Cylinders”, Master thesis, UTSI, July 1998.

[42] Tufo, H., P.F. Fischer, M.E. Papka, and K. Blom, “Numerical Simulation and Immersive Visualization of Hairpin Vortex Generation”, Proceedings of SC99, 10 pages (1999)

[43] A. Larousse, R. Martinuzzi and C. Tropea, “Flow Around Surface-Mounted, Three-Dimensional Obstacles,” in *Turbulent Shear Flows*, **8**, Selected Papers From Eighth International Symposium on Turbulent shear Flows edited by F. Durst, R. Friedrich, B.E. Launder, F.W. Schmidt, U. Schumann, J.H. Whitelaw, 1991, pp.137-139.

[44] Martinuzzi, R. and Tropea, C., “The Flow around Surface-Mounted, Prismatic Obstacles Placed in a Fully Developed Channel Flows”, Journal of Fluid Engineering, Vol.115, pp. 85-92(1993).

[45] Wang, H.F., Zhou, Y., Chan, C.K., Wong, W.O. and Lam, K.S., “Flow Structure Around A Finite-Length Square Prism”, 15th Australasian Fluid Mechanics Conference The University of Sydney, Sydney, Australia 13-17 December 2004

[46] Werner, H. and Wengle, “Large-Eddy Simulation of Turbulent Flow over and Around a Cube in a Plate Channel,” in *Turbulent Shear Flows*, **8**, Selected Papers From Eighth International Symposium on Turbulent Shear Flows, 1991, pp.156-168.

Appendix: Figures

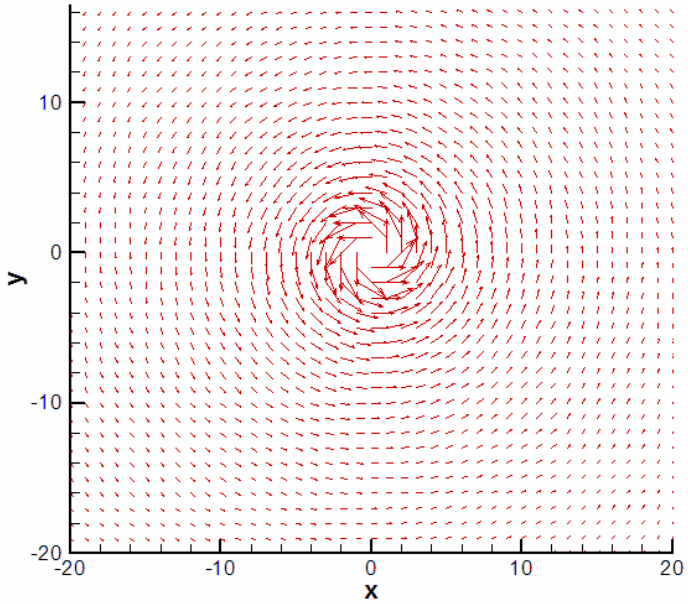

Fig. 3-1 Initial velocity vector field for a single stationary point vortex

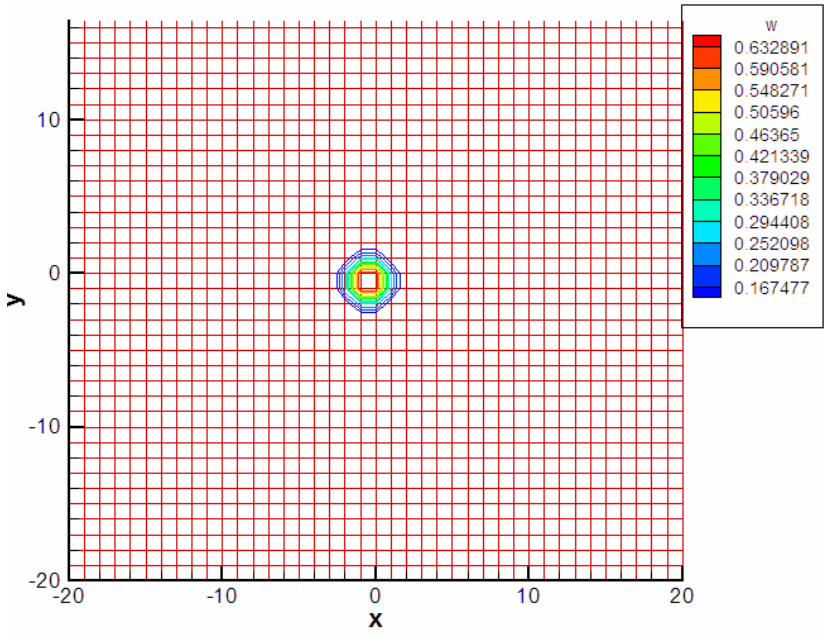

Fig. 3-2 Initial vorticity contours for a single stationary point vortex

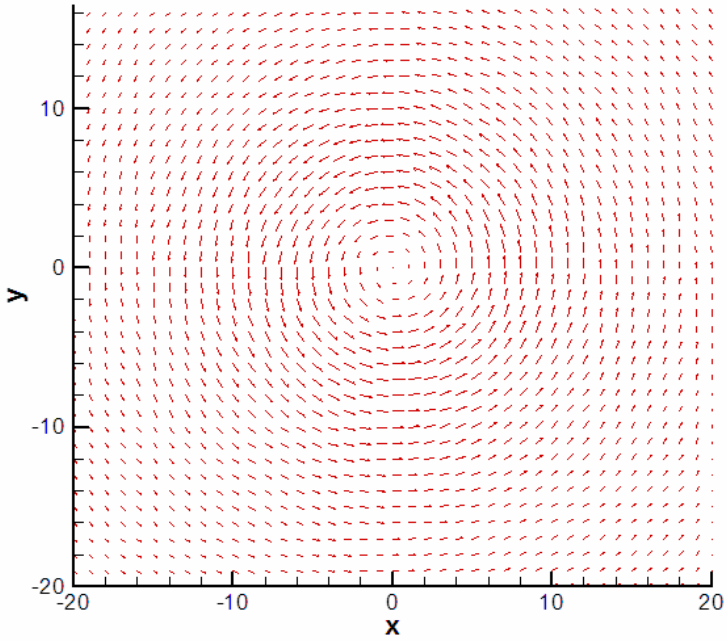

Fig. 3-3 Velocity vector field after 100 time iterations without Vorticity Confinement

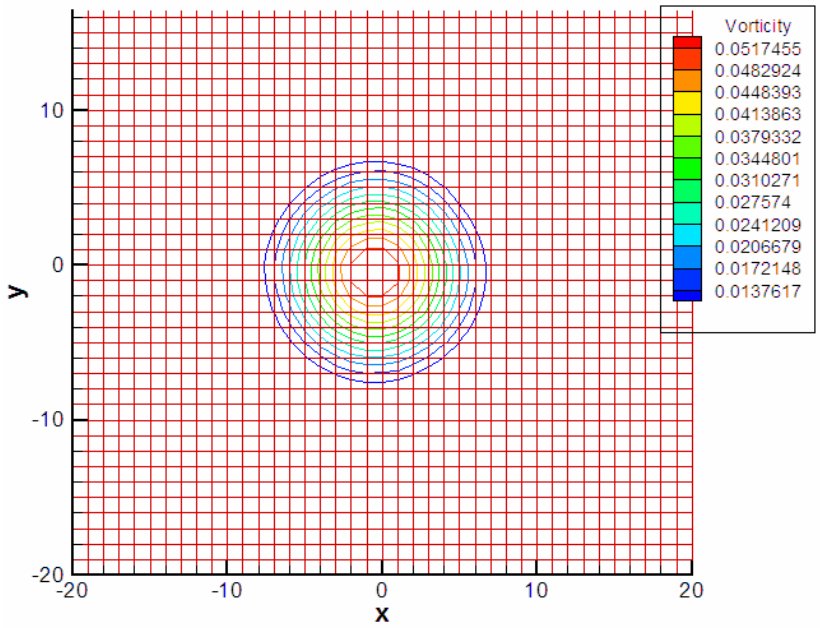

Fig. 3-4 Vorticity contours after 100 time iterations without Vorticity Confinement

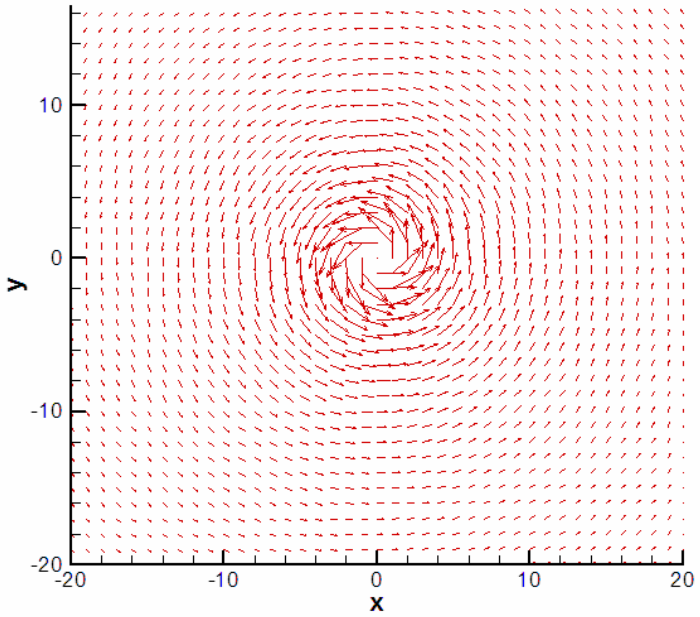

Fig. 3-5 Velocity vector field after 100 time iterations with VC2

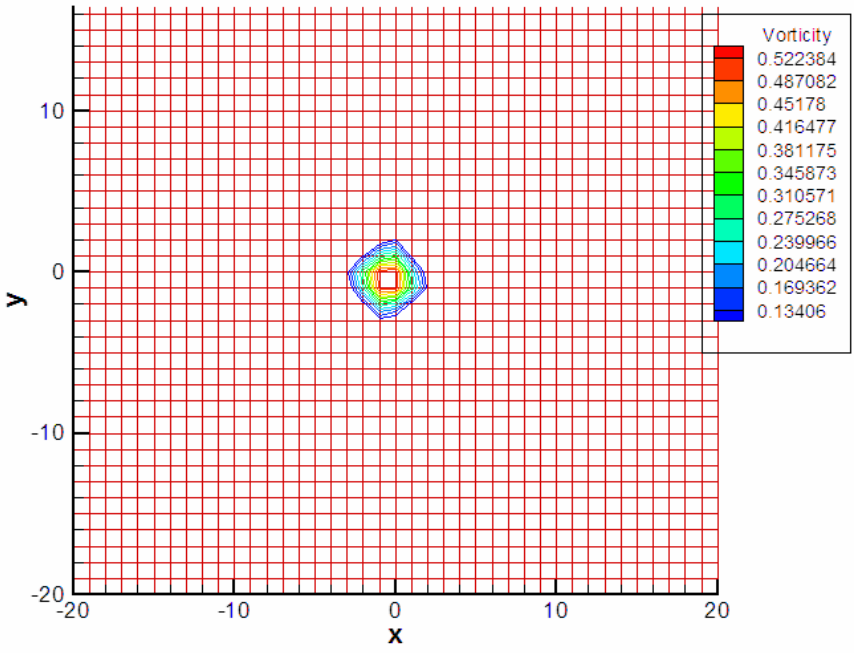

Fig. 3-6 Vorticity contours after 100 time iterations with VC2

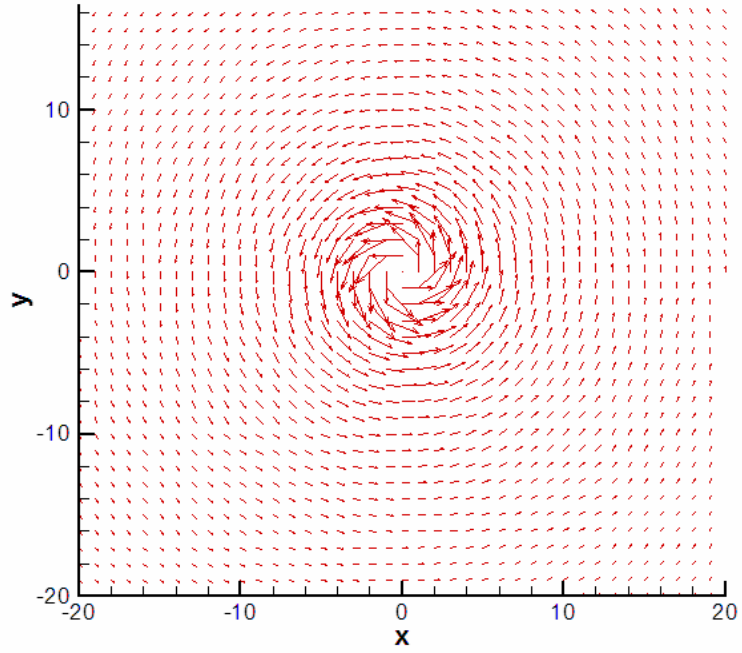

Fig. 3-7 Velocity vector field after 1000 time iterations with VC2

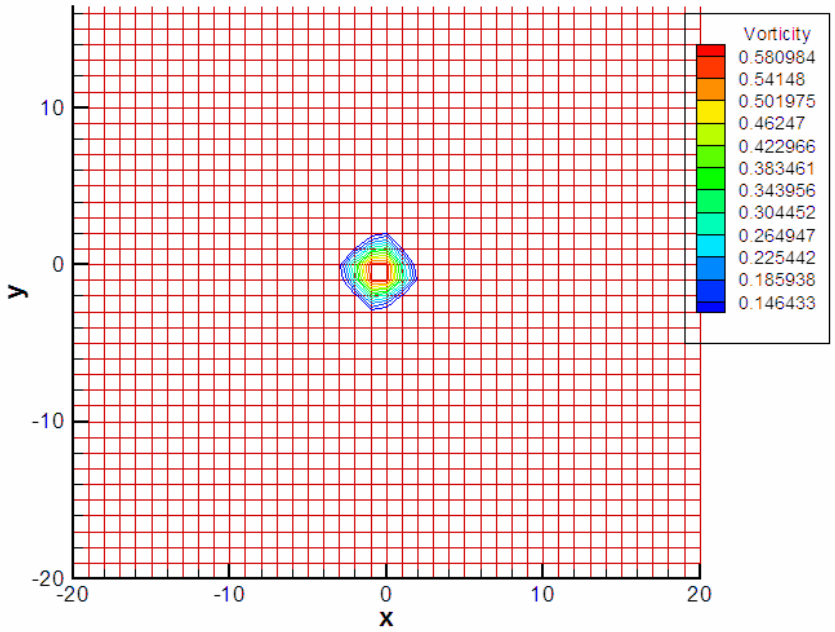

Fig. 3-8 Vorticity contours after 1000 time iterations with VC2

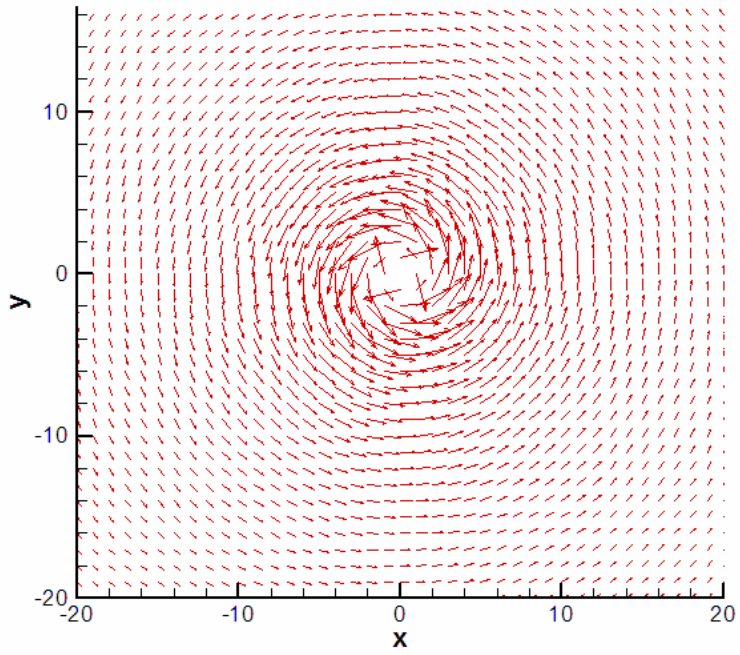

Fig. 3-9 Velocity vector field after 100 time iterations with VC1

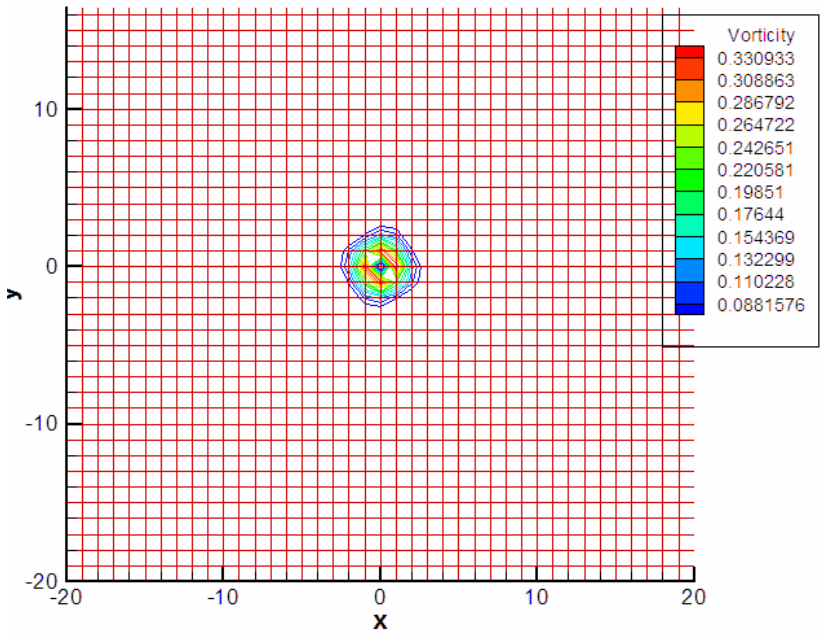

Fig. 3-10 Vorticity contours after 100 time iterations with VC1

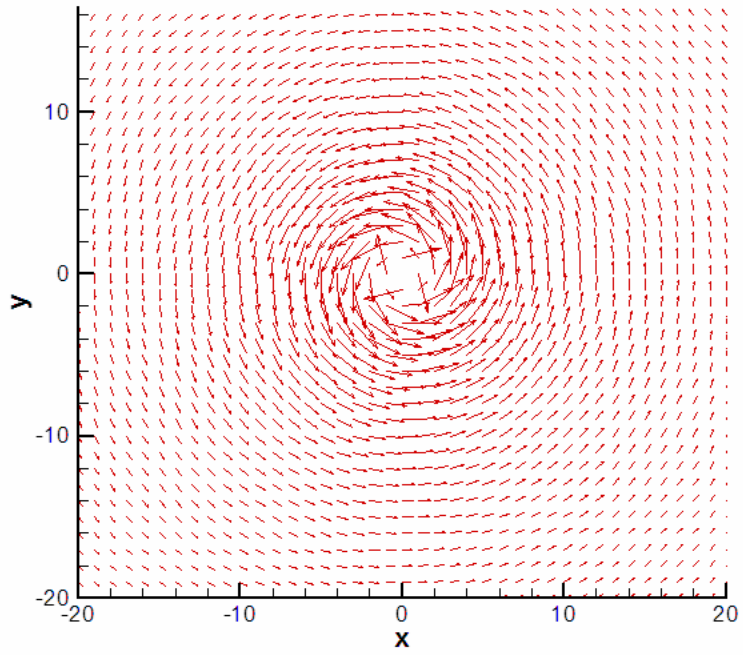

Fig. 3-11 Velocity vector field after 1000 time iterations with VC1

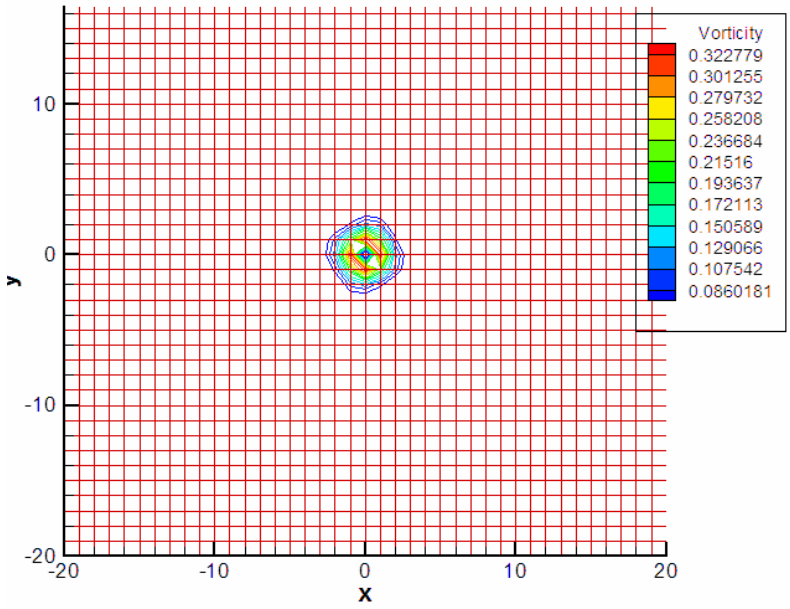

Fig. 3-12 Vorticity contours after 1000 time iterations with VC1

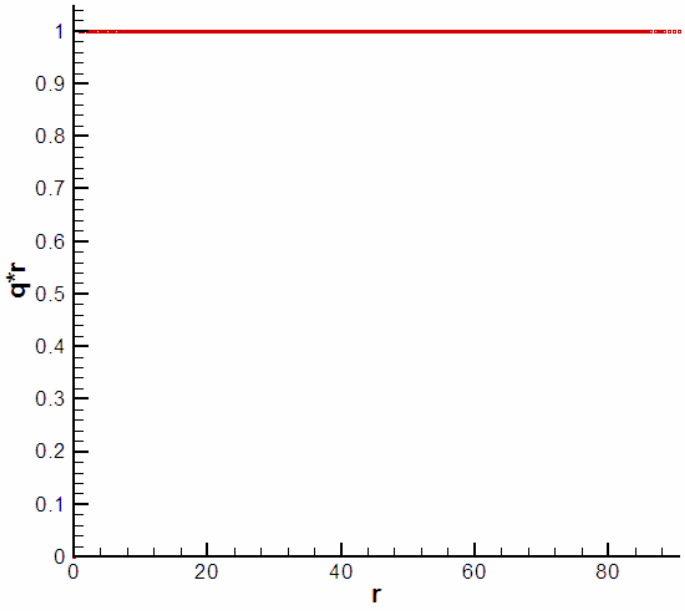

Fig. 3-13 Initial velocity magnitude distribution for the stationary vortex, q*r denotes the normalized velocity

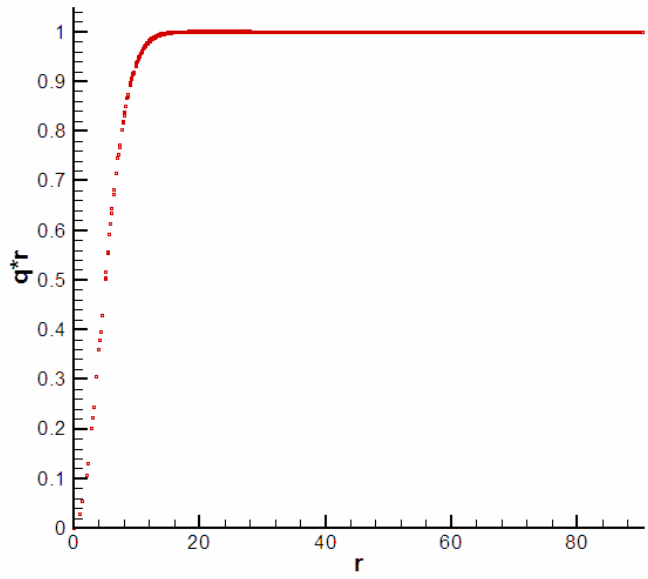

Fig. 3-14 Velocity magnitude distribution for the stationary vortex after 100 time iterations without Vorticity Confinement

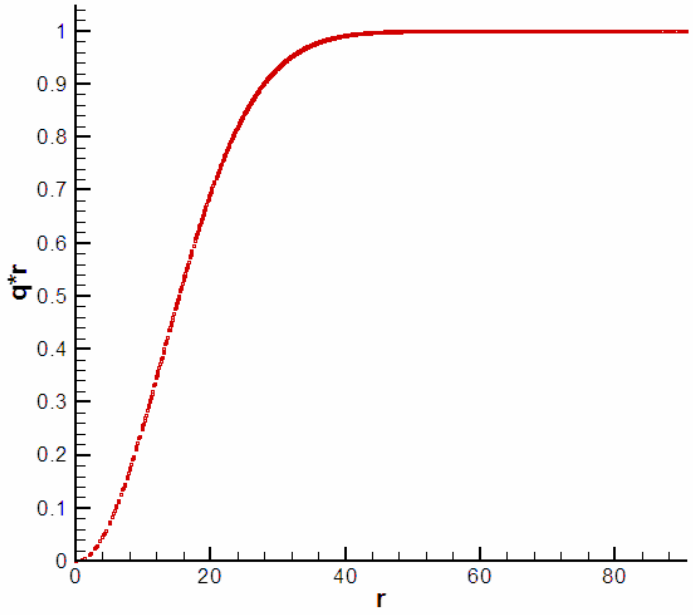

Fig. 3-15 Velocity magnitude distribution for the stationary vortex after 1000 time iterations without Vorticity Confinement

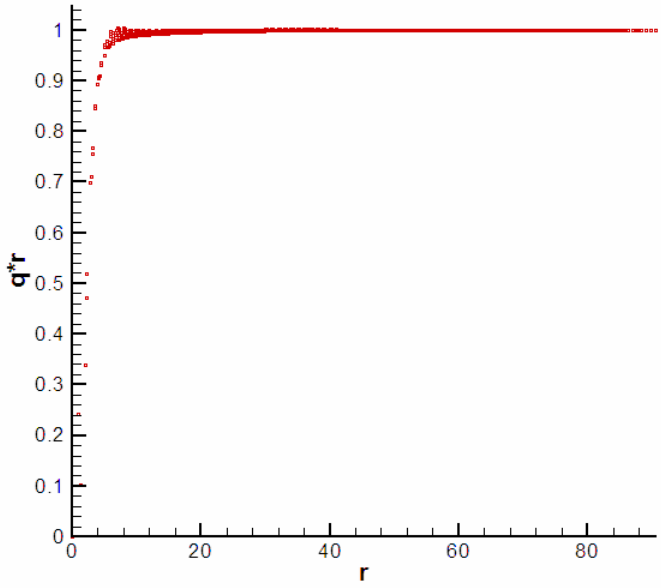

Fig. 3-16 Velocity magnitude distribution for the stationary vortex after 100 time iterations with VC2

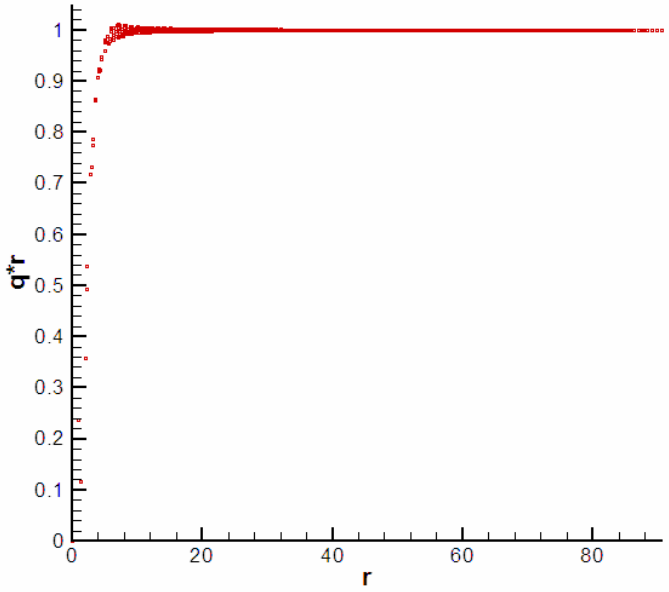

Fig. 3-17 Velocity magnitude distribution for the stationary vortex after 1000 time iterations with VC2

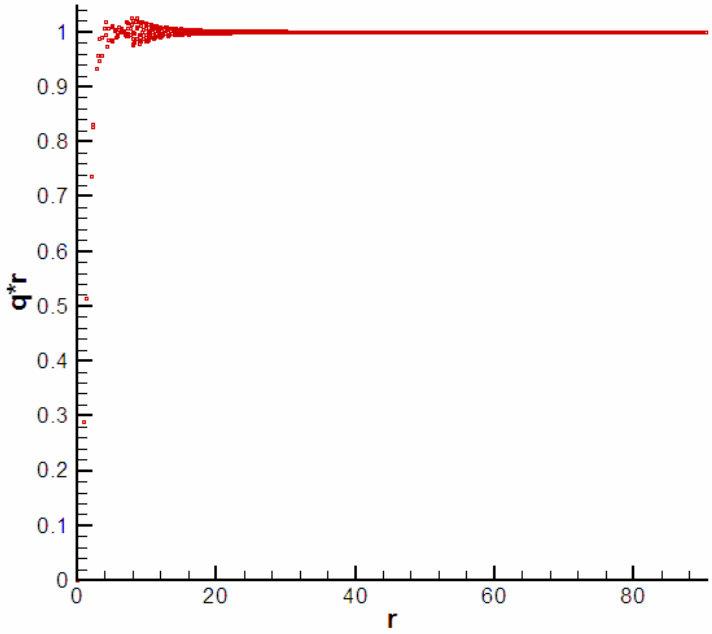

Fig. 3-18 Velocity magnitude distribution for the stationary vortex after 100 time iterations with VC1

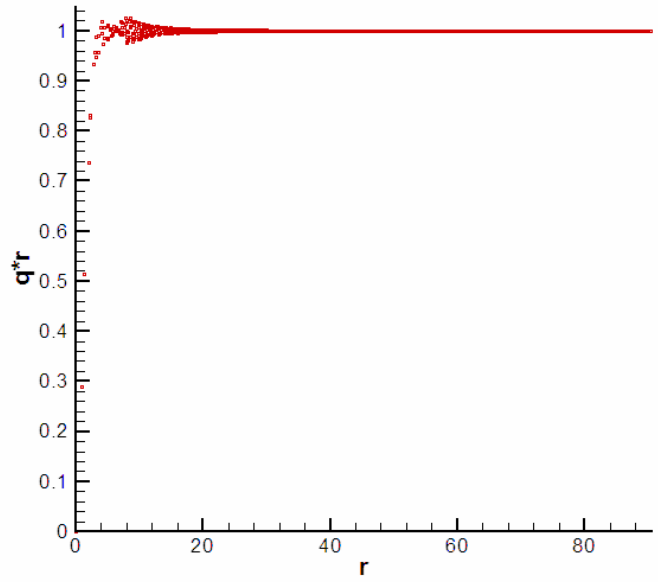

Fig. 3-19 Velocity magnitude distribution for the stationary vortex after 1000 time iterations with VC1

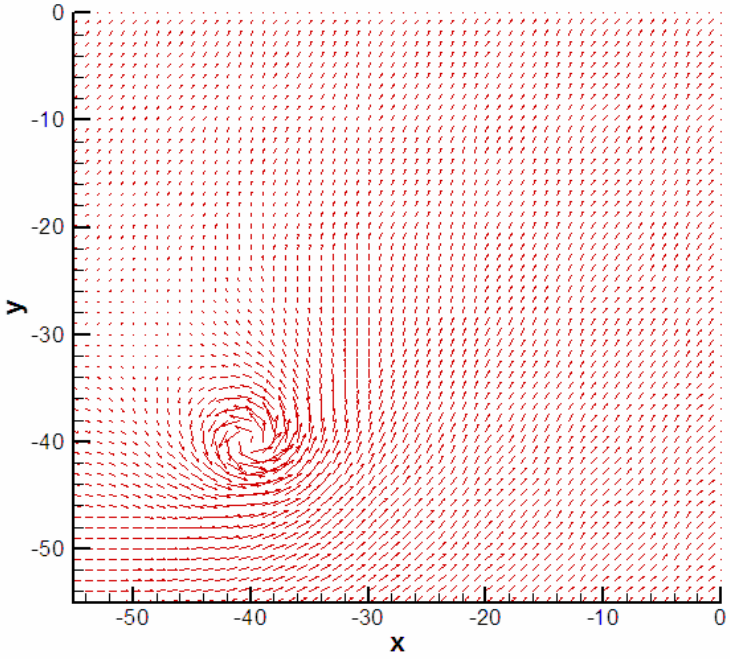

Fig. 3-20 Initial velocity vector field for the free convecting single vortex

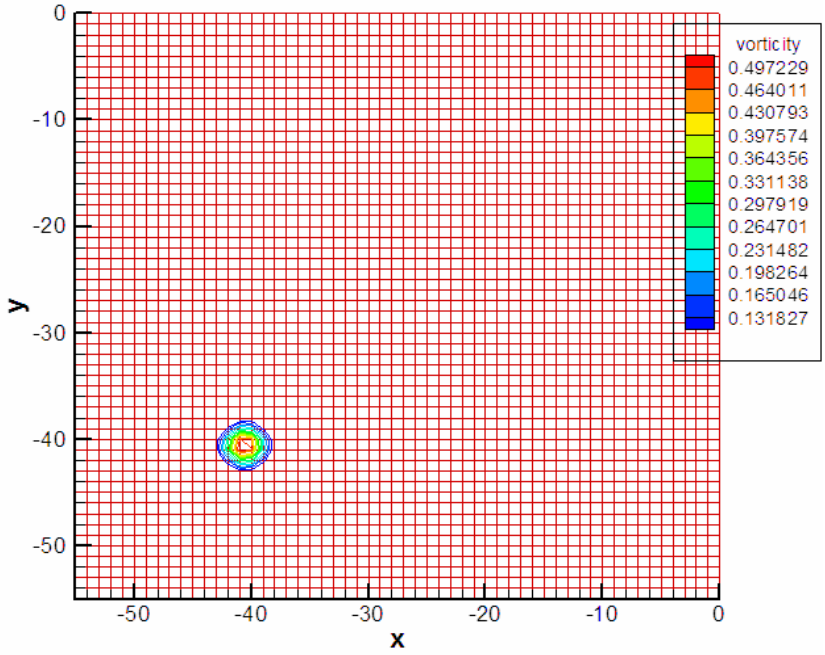

Fig 3-21 Initial vorticity contours for the free convecting single vortex

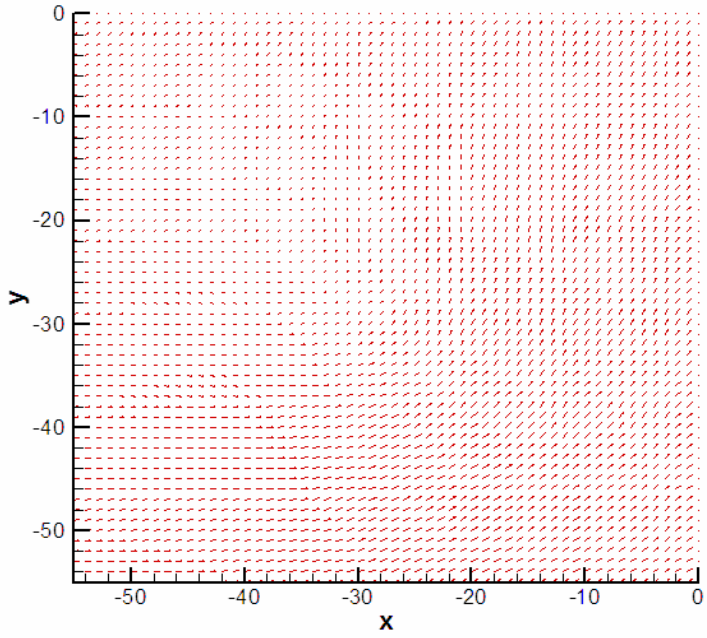

Fig. 3-22 Velocity vector field after 500 time iterations without Vorticity Confinement

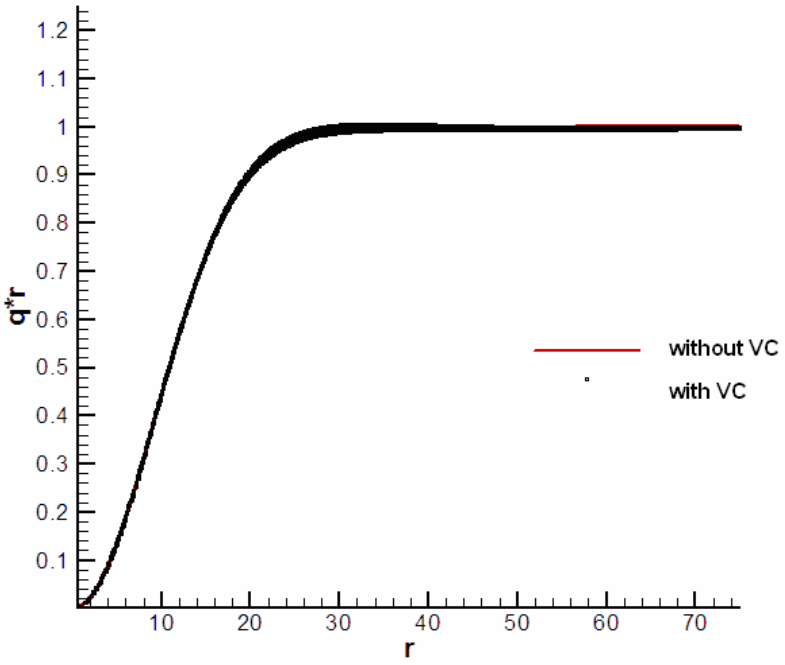

Fig. 3-23 Velocity magnitude distribution after 500 time iterations without Vorticity Confinement

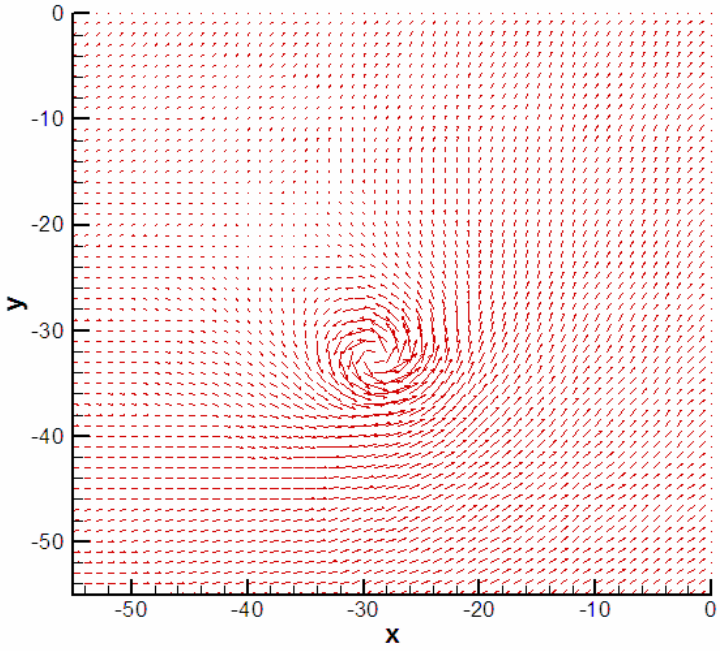

Fig.3-24 Velocity vector field after 500 time iterations with VC1

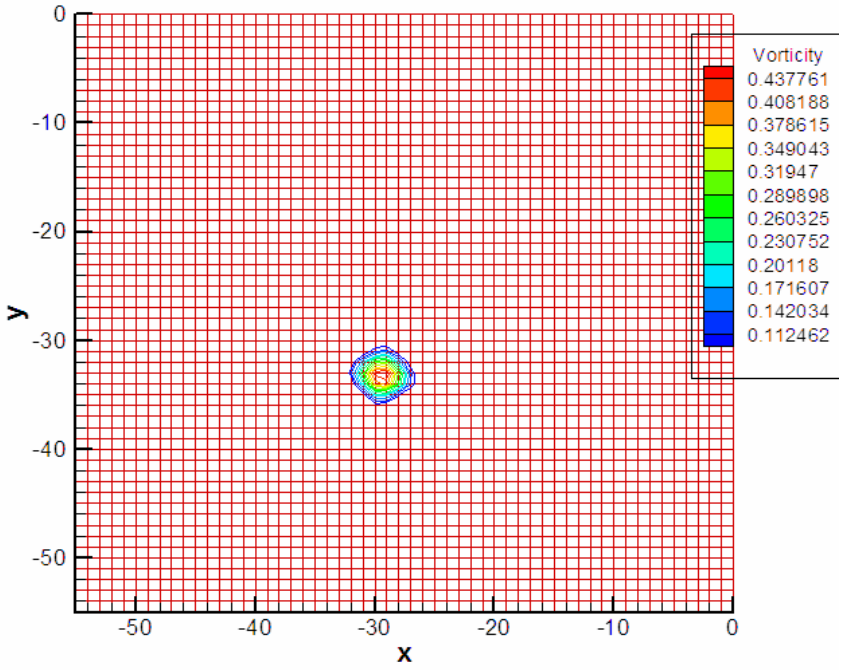

Fig. 3-25 Vorticity contours after 500 time iterations with VC1

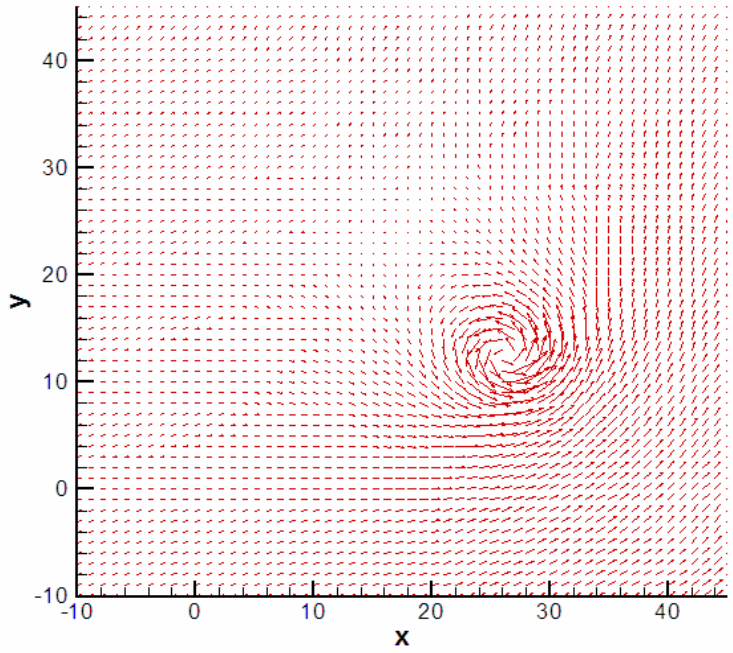

Fig.3-26 Velocity vector field after 3000 time iterations with VC1

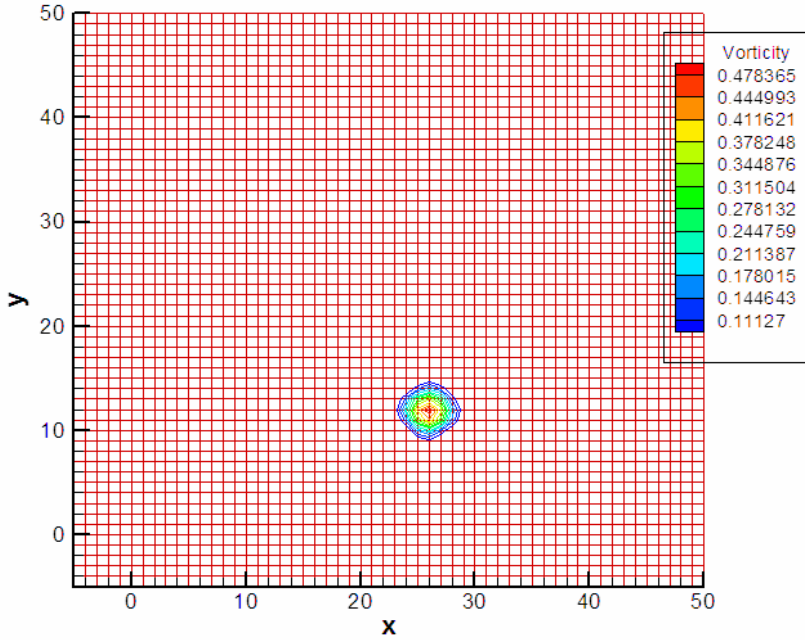

Fig. 3-27 Vorticity contours after 3000 time iterations with VC1

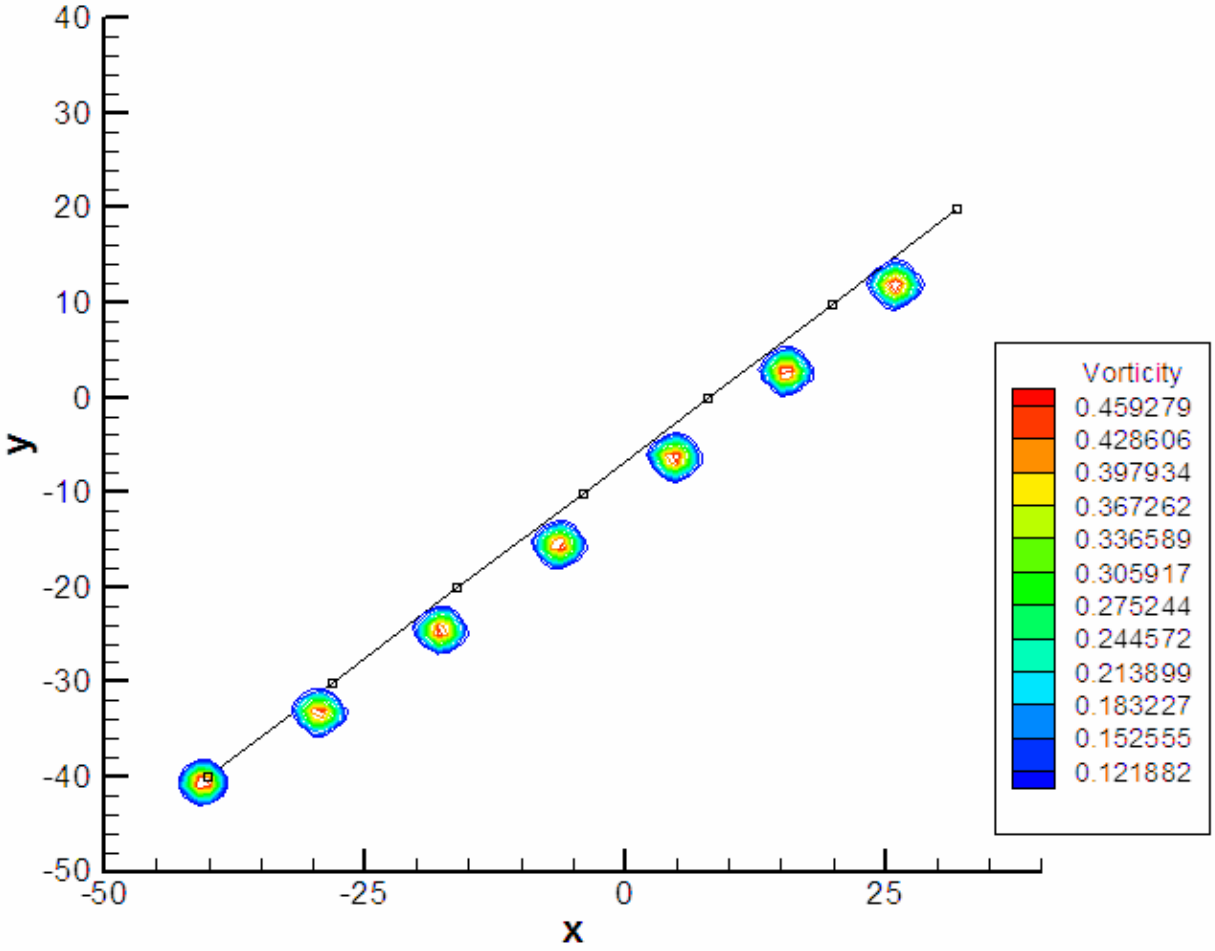

Fig. 3-28 Trajectory for a single free convecting vortex with VC1

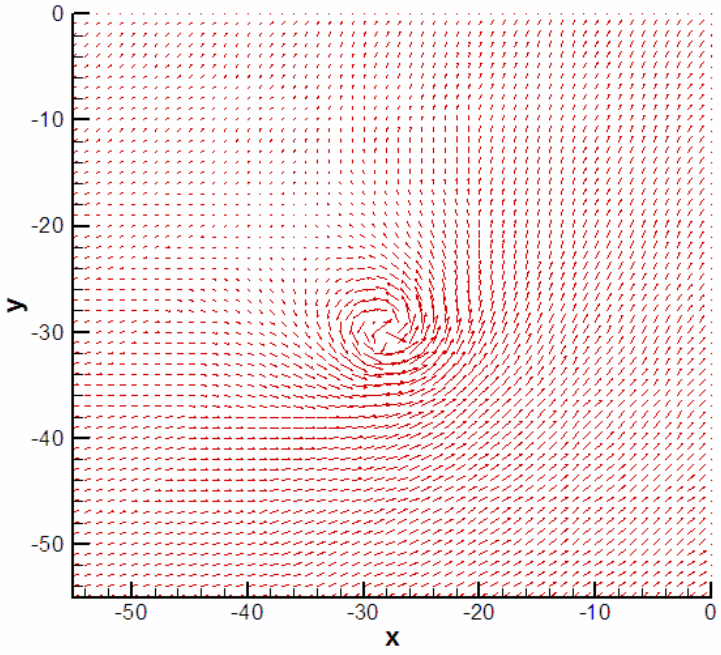

Fig. 3-29 Velocity vector field after 500 time iterations with VC2

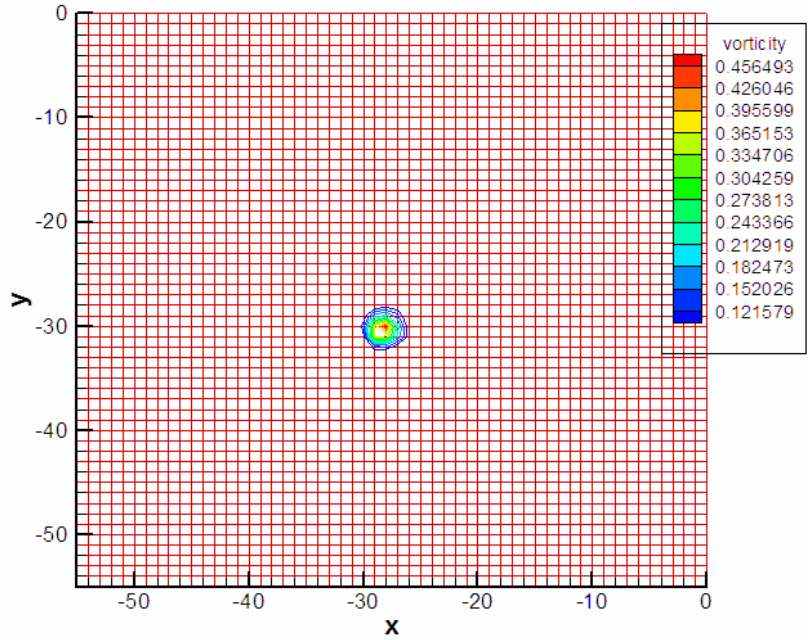

Fig. 3-30 Vorticity contours after 500 time iterations with VC2

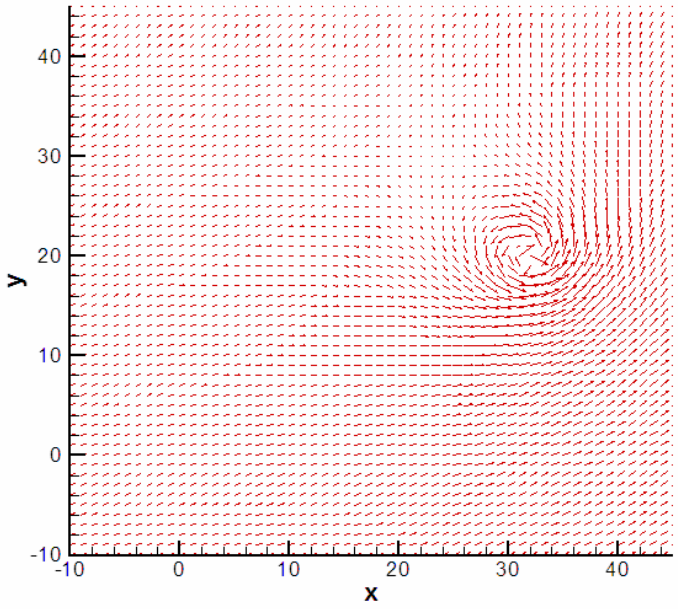

Fig. 3-31 Velocity vector field after 3000 time iterations with VC2

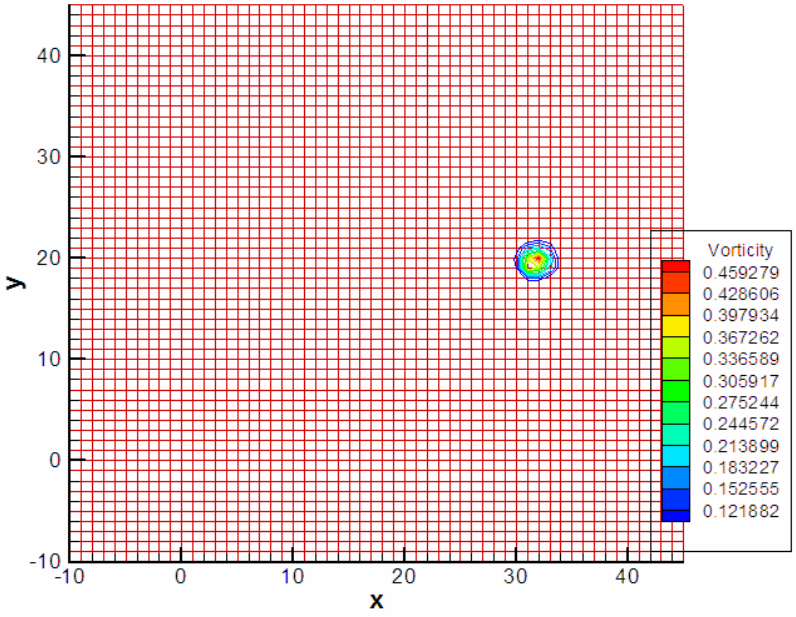

Fig.3-32 Vorticity contours after 3000 time iterations with VC2

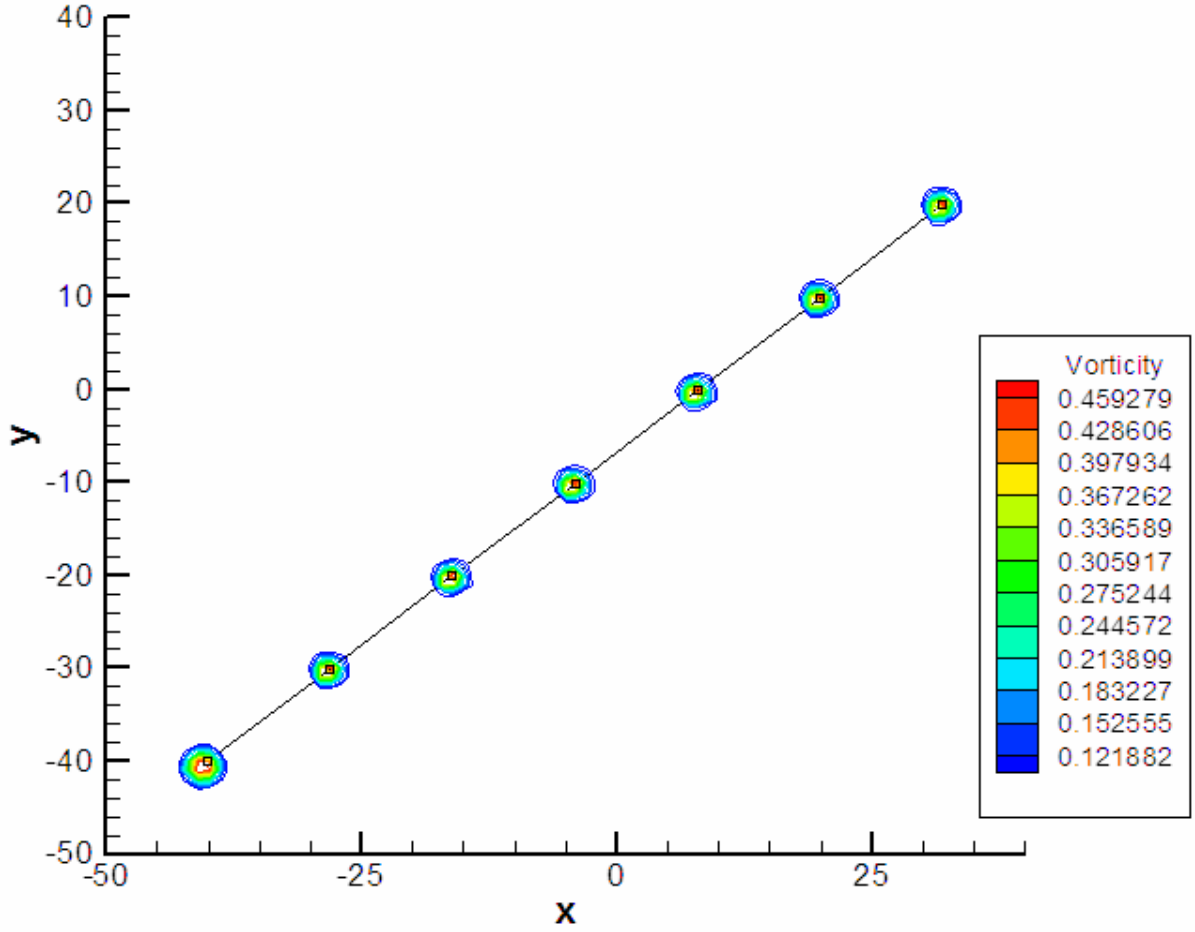

Fig. 3-33 Trajectory of a single free convecting vortex with VC2

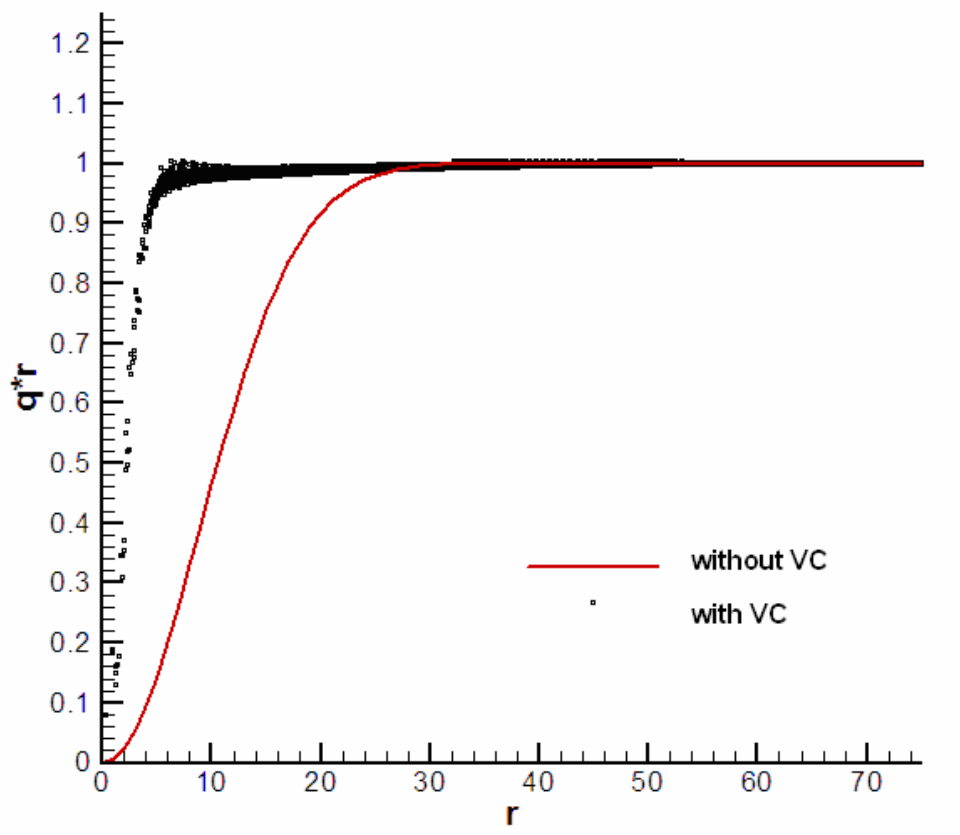

Fig. 3-34 Velocity magnitude distribution for a single convecting vortex after 500 time iterations with VC2

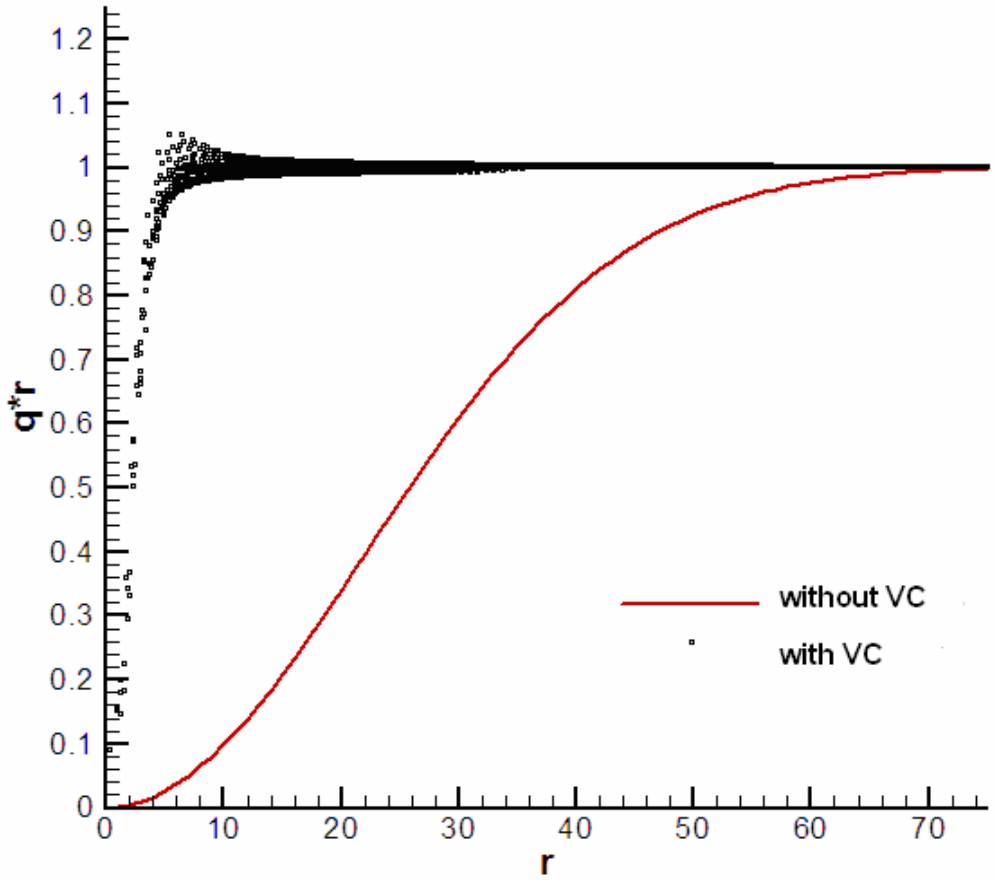

Fig. 3-35 Velocity magnitude distribution for a single convecting vortex after 3000 time iterations with VC2

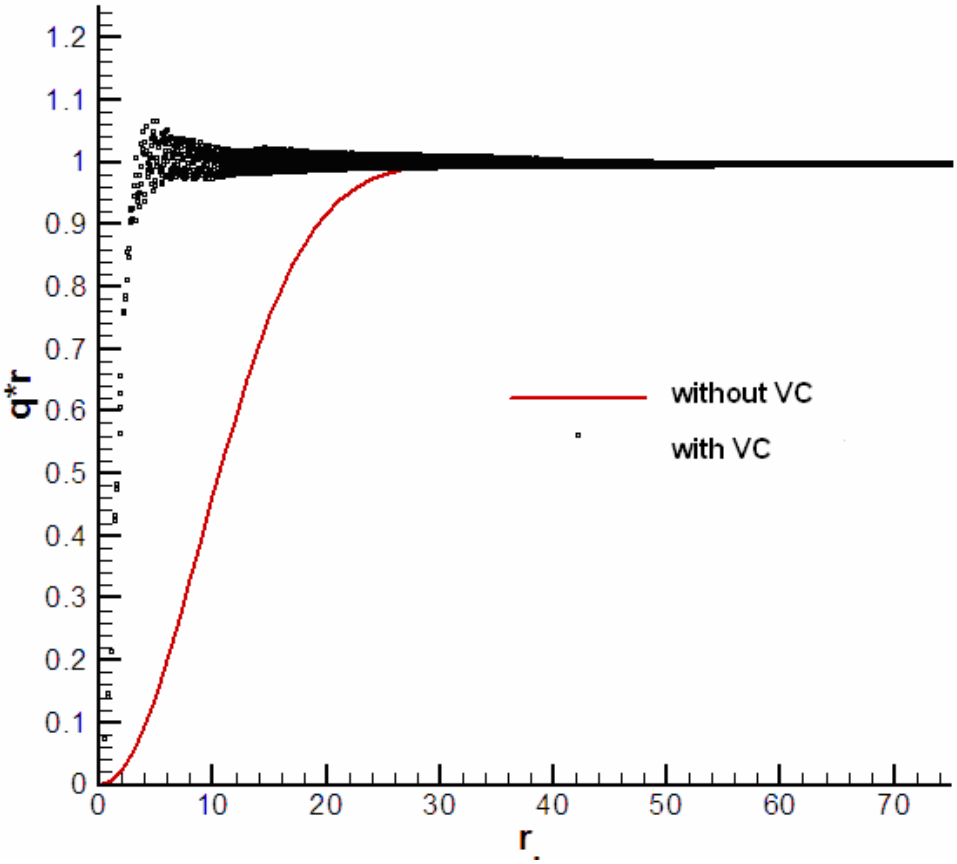

Fig.3- 36 Velocity magnitude distribution for a single convecting vortex after 500 time iterations with VC1

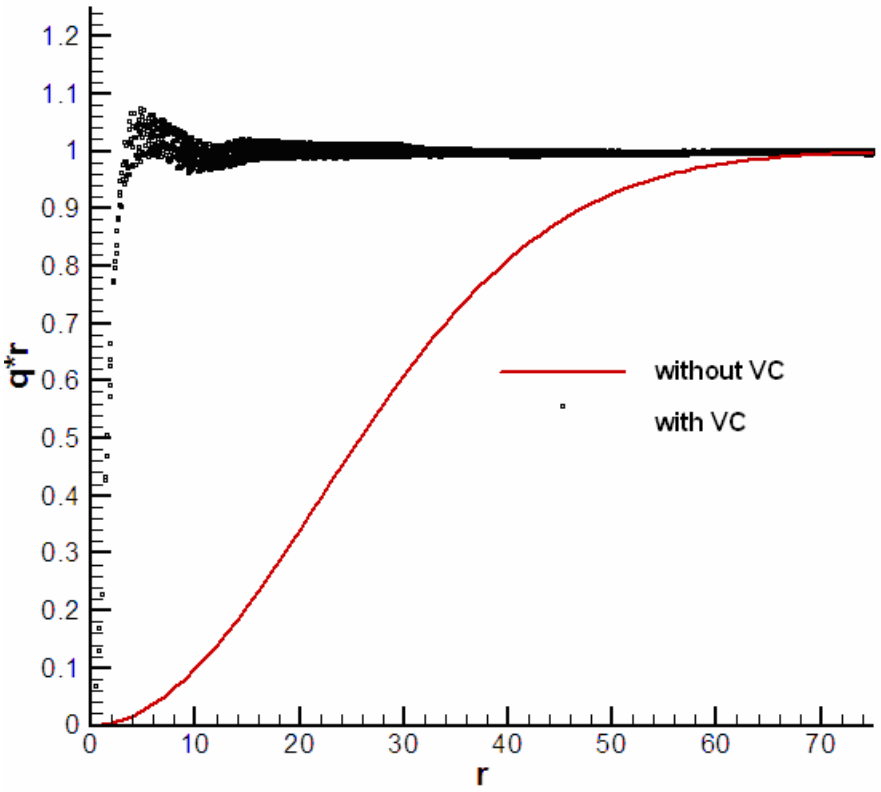

Fig.3-37 Velocity magnitude distribution for a single convecting vortex after 3000 time iterations with VC1

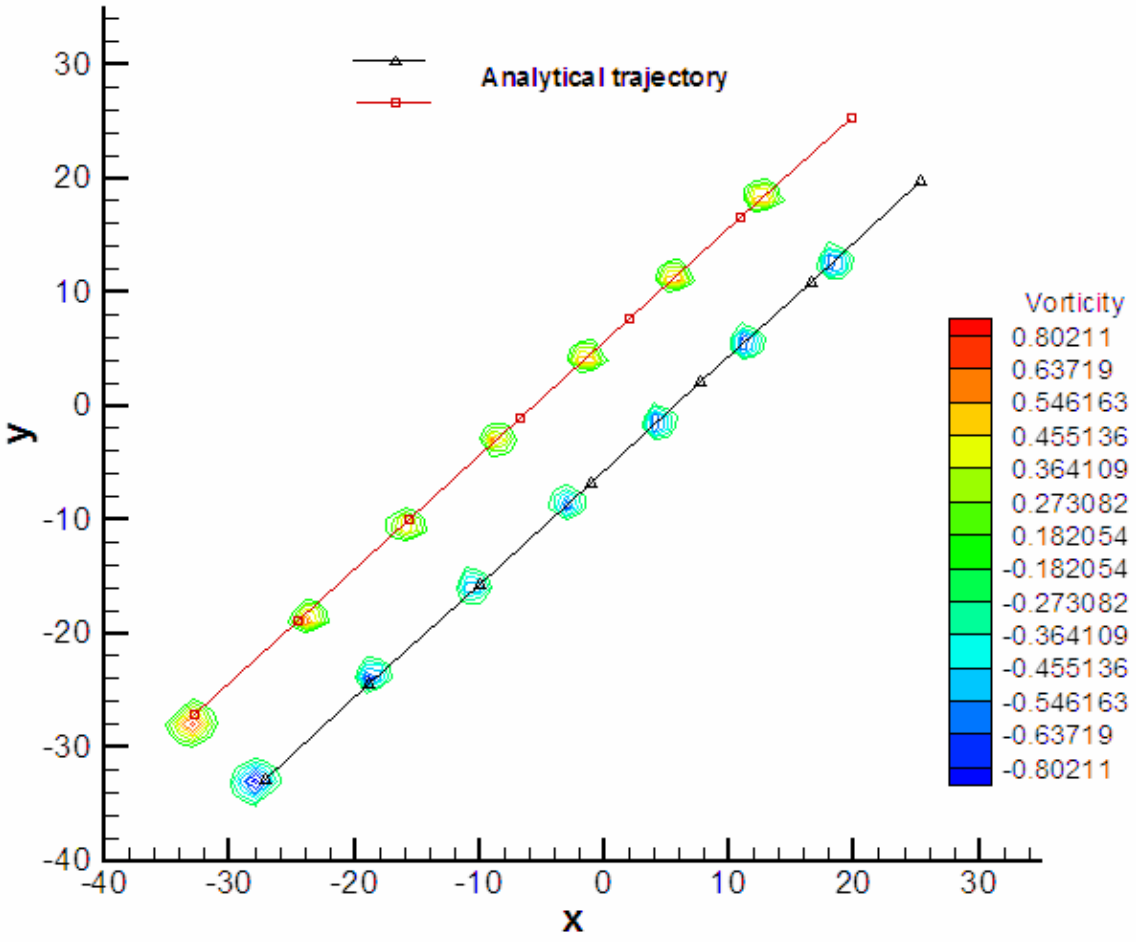

Fig. 3-38 Trajectory of paired vortices of the opposite signs with VC2, 8 cells apart

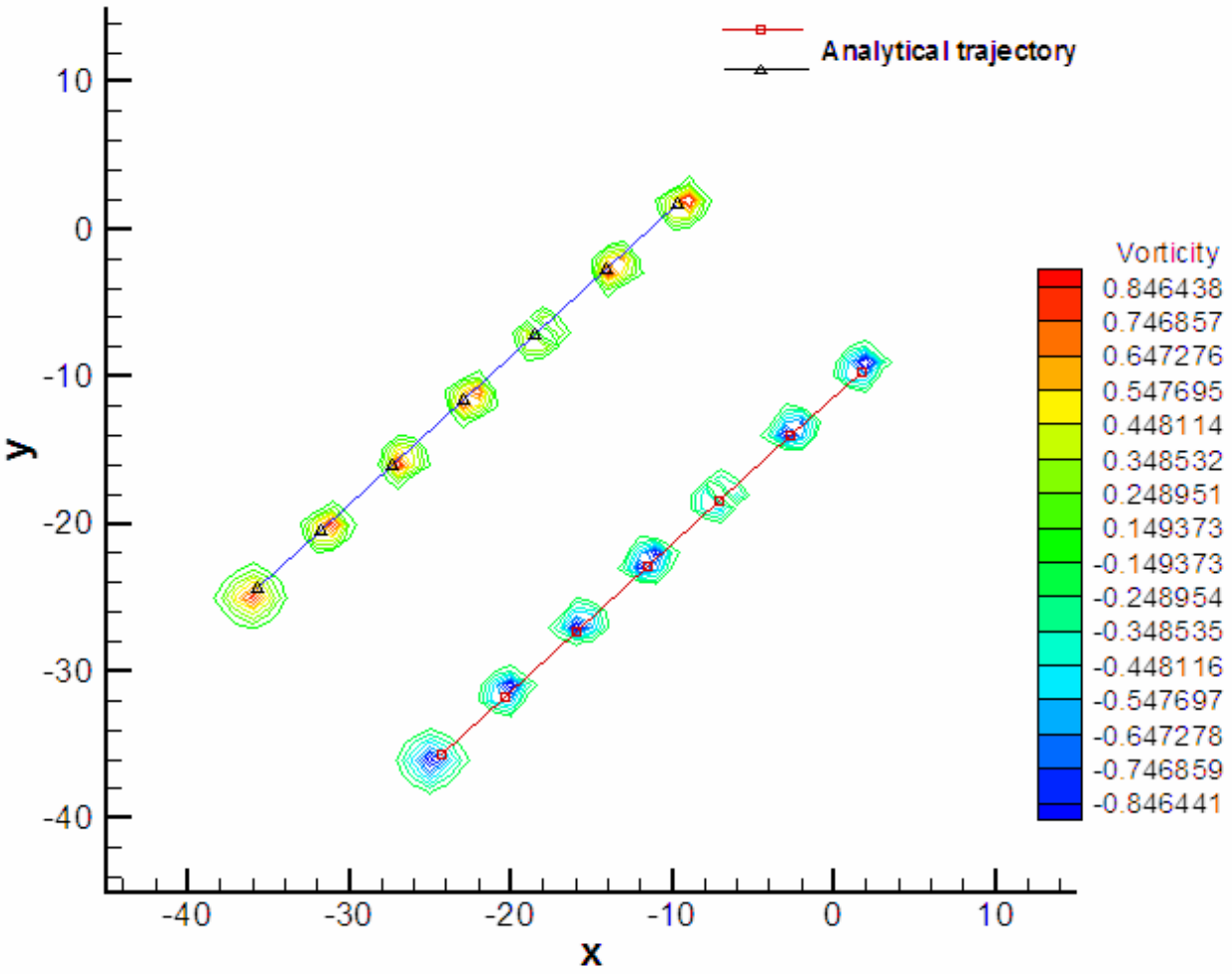

Fig. 3-39 Trajectory of paired vortices of the opposite signs with VC2, 16 cells apart

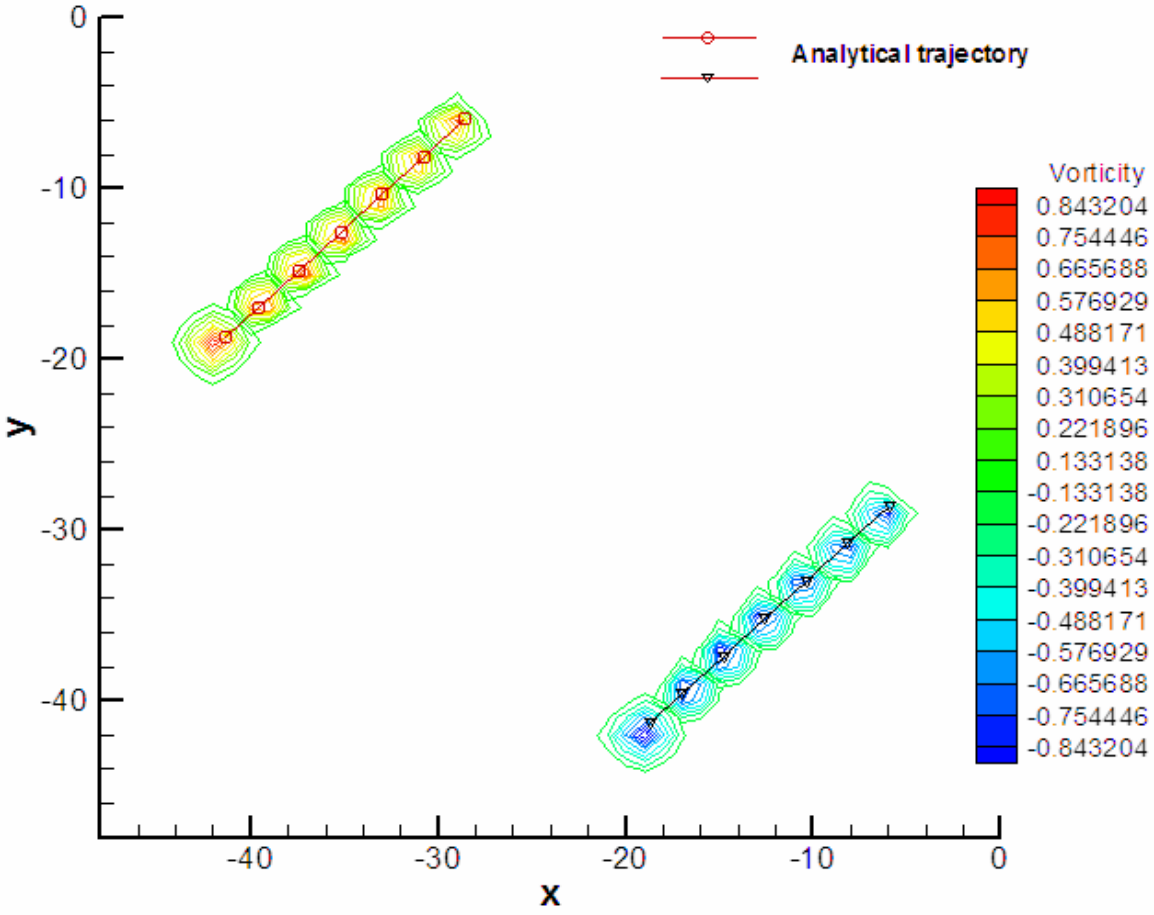

Fig. 3-40 Trajectory of paired vortices of the opposite signs withVC2, 32 cells apart

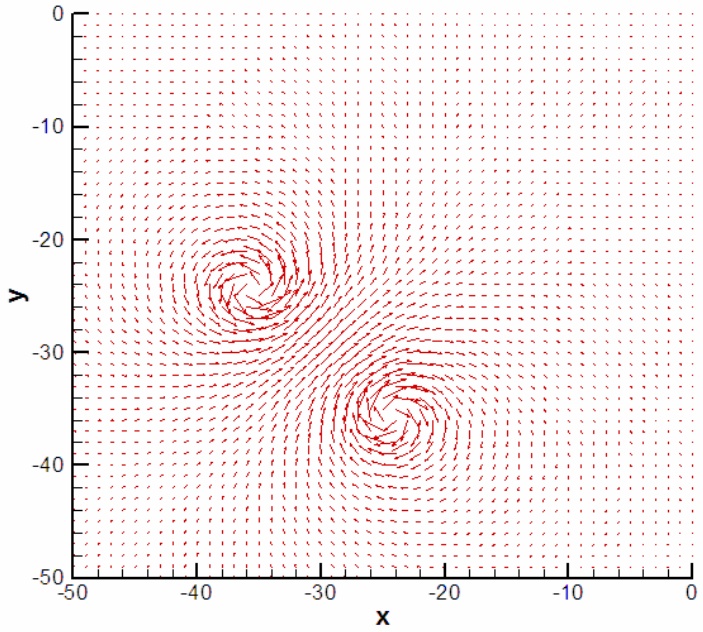

Fig. 3-41 Initial velocity vector field of paired vortices of the opposite signs

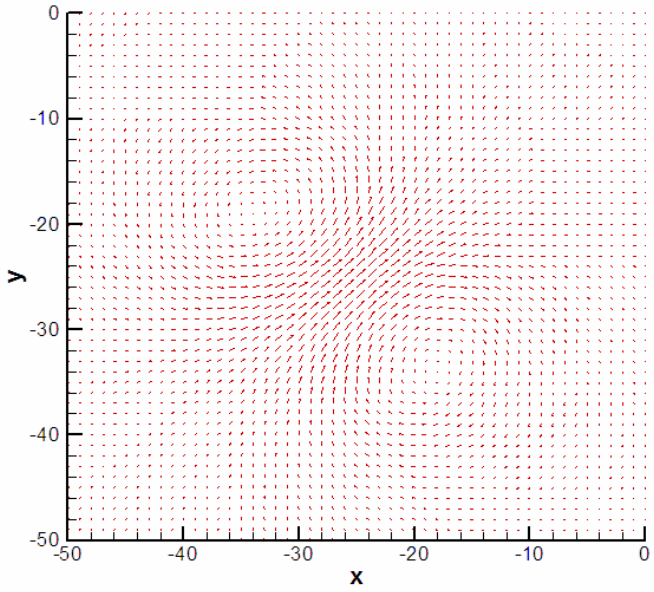

Fig. 3-42 Velocity vector field of paired vortices of the opposite signs after 500 time iterations without Vorticity Confinement

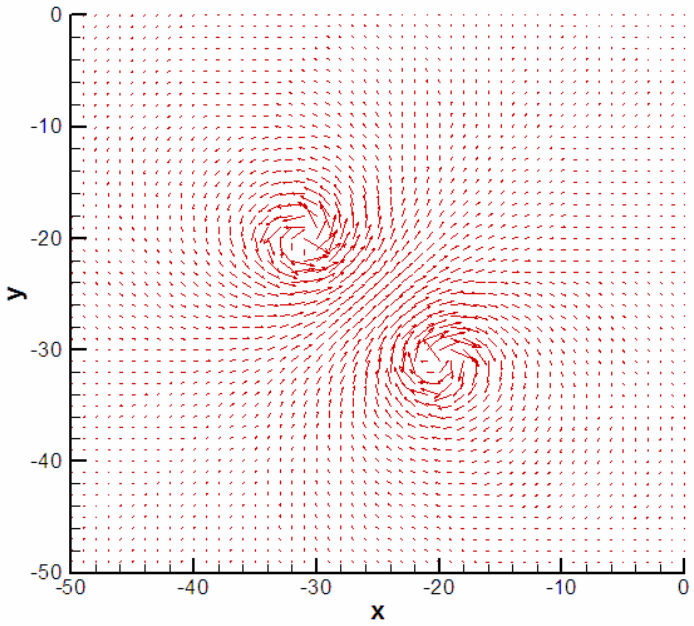

Fig. 3-43 Velocity vector field of paired vortices of the opposite signs after 500 time iterations with VC2

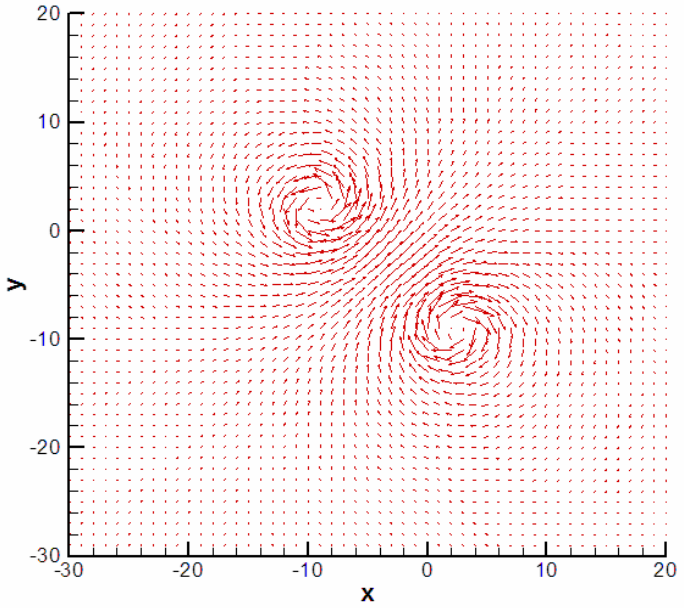

Fig. 3-44 Velocity vector field of paired vortices of the opposite signs after 3000 time iterations with VC2

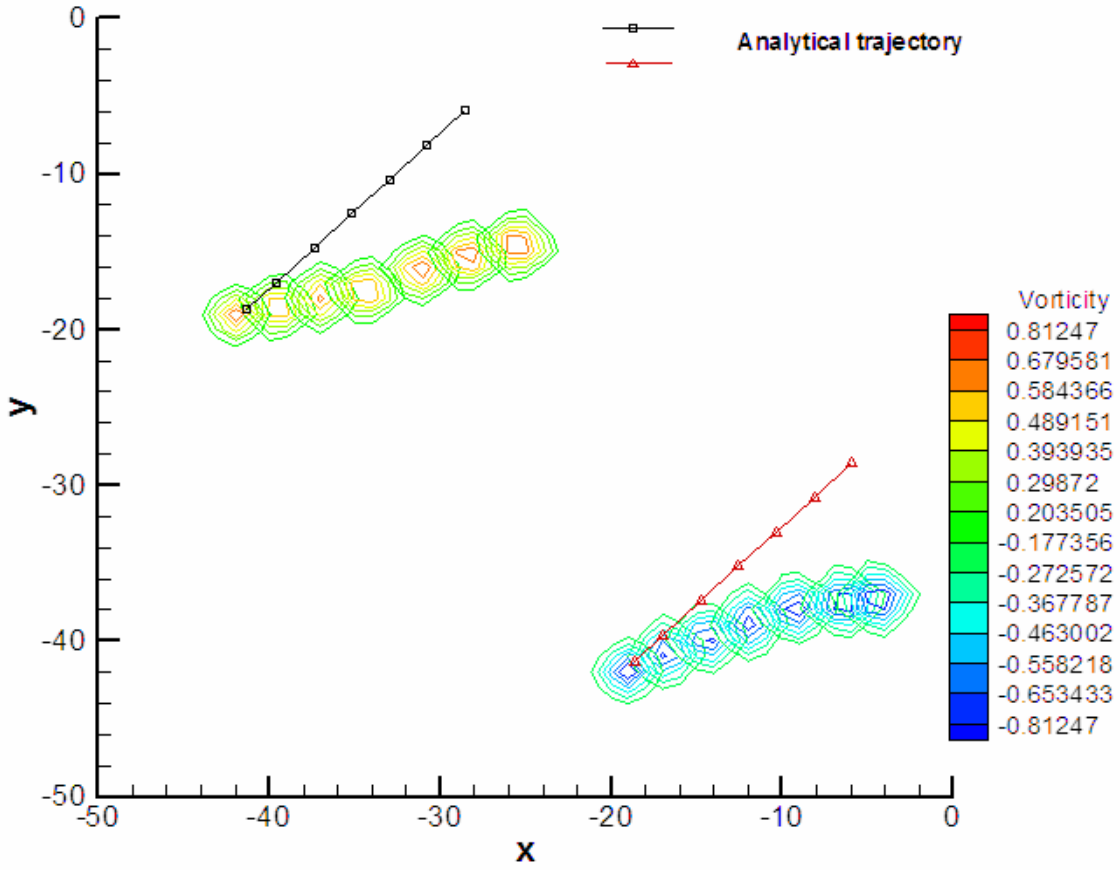

Fig. 3-45 Trajectory of paired vortices of the opposite signs withVC1, 32 cells apart

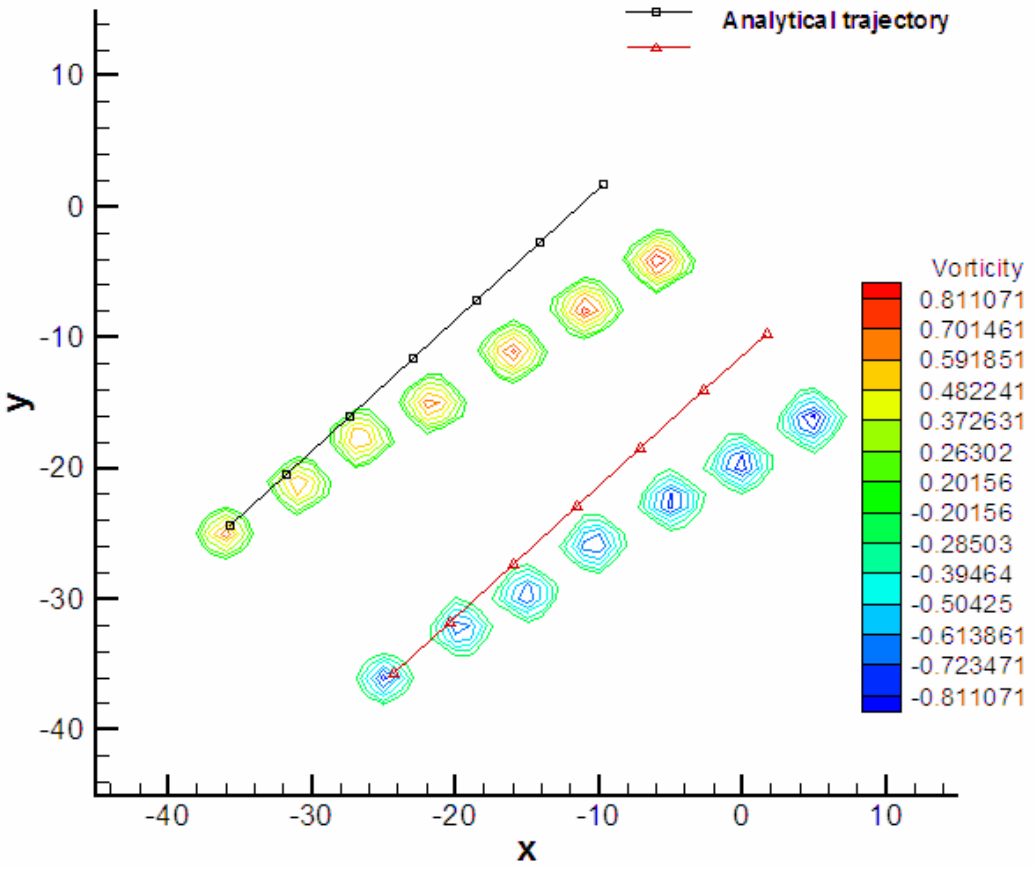

Fig.3-46 Trajectory of paired vortices of the opposite signs withVC1, 16 cells apart

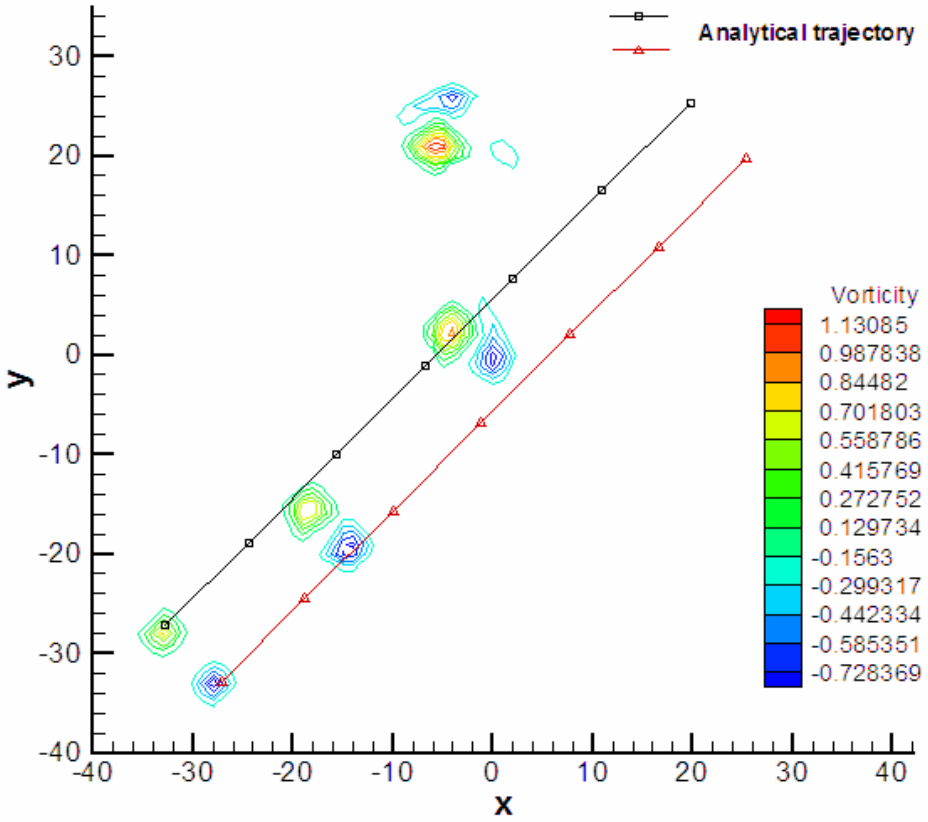

Fig. 3-47 Trajectory of paired vortices of the opposite signs withVC1, 8 cells apart

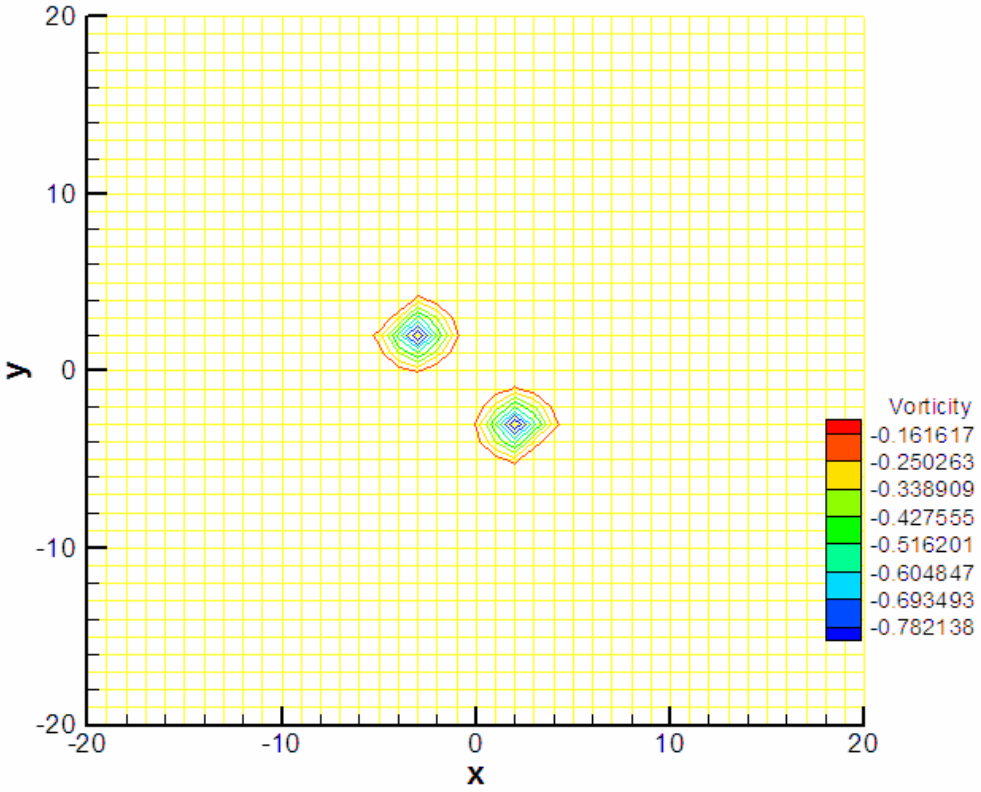

Fig. 3-48 Initial positions of paired vortices of the same signs, 8 cells apart

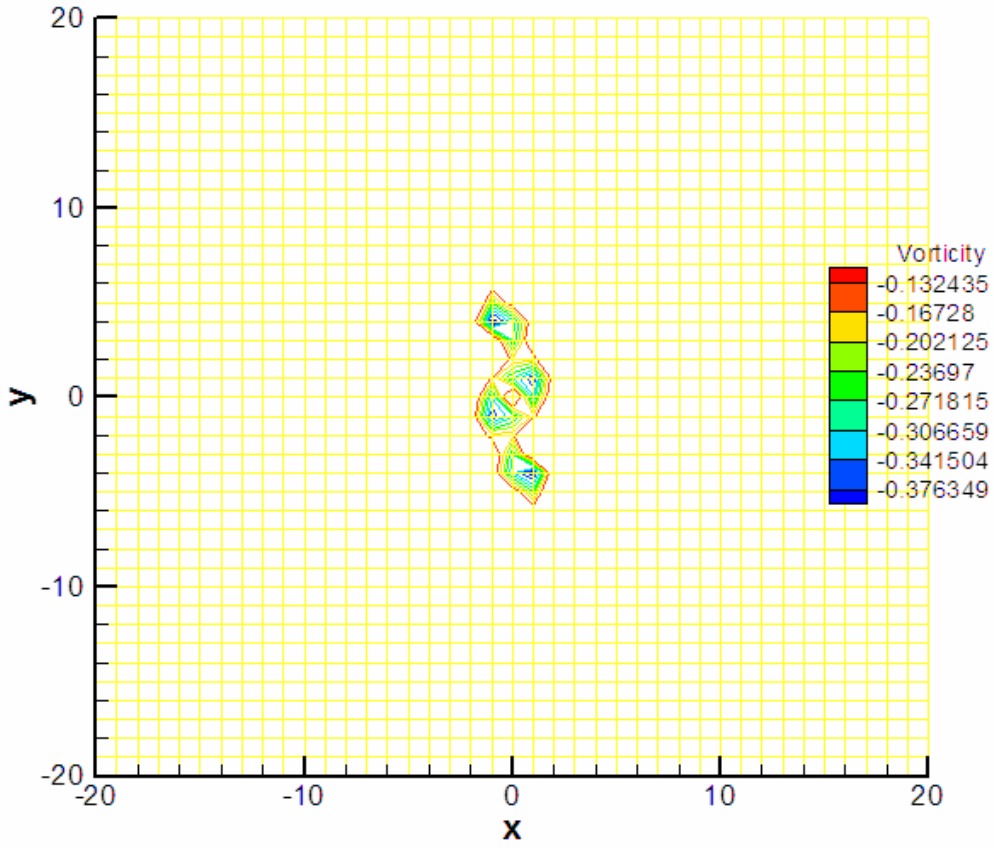

Fig. 3-49 Paired vortices of the same signs becoming merging after 1000 time iterations, 8 cells apart

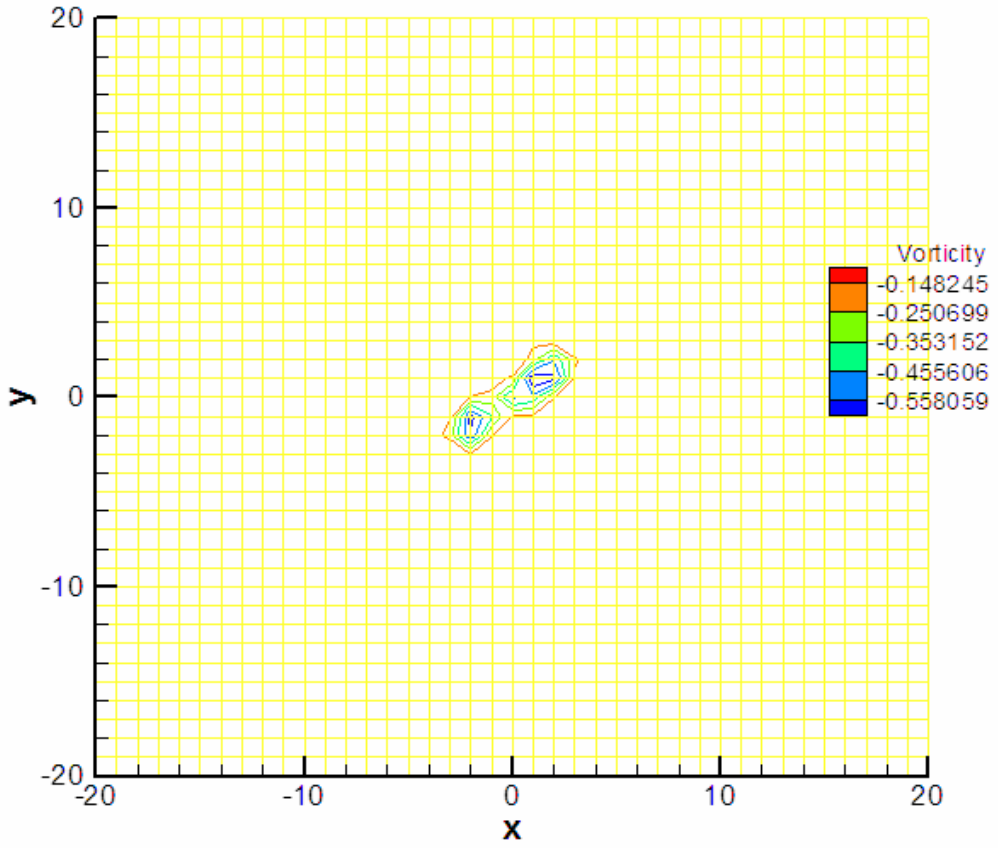

Fig. 3-50 Paired vortices of the same signs totally merge after 3000 time iterations, 8 cells apart

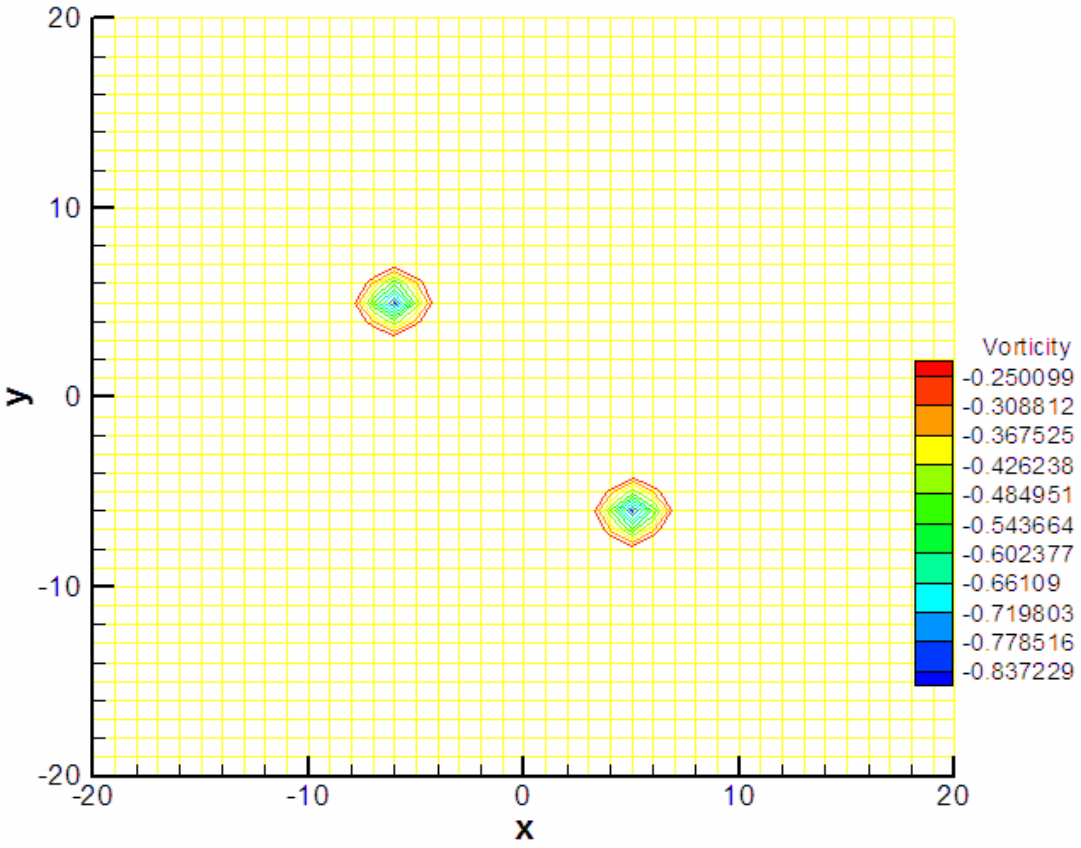

Fig. 3-51 Initial position of paired vortices of the same signs, 16 cells apart

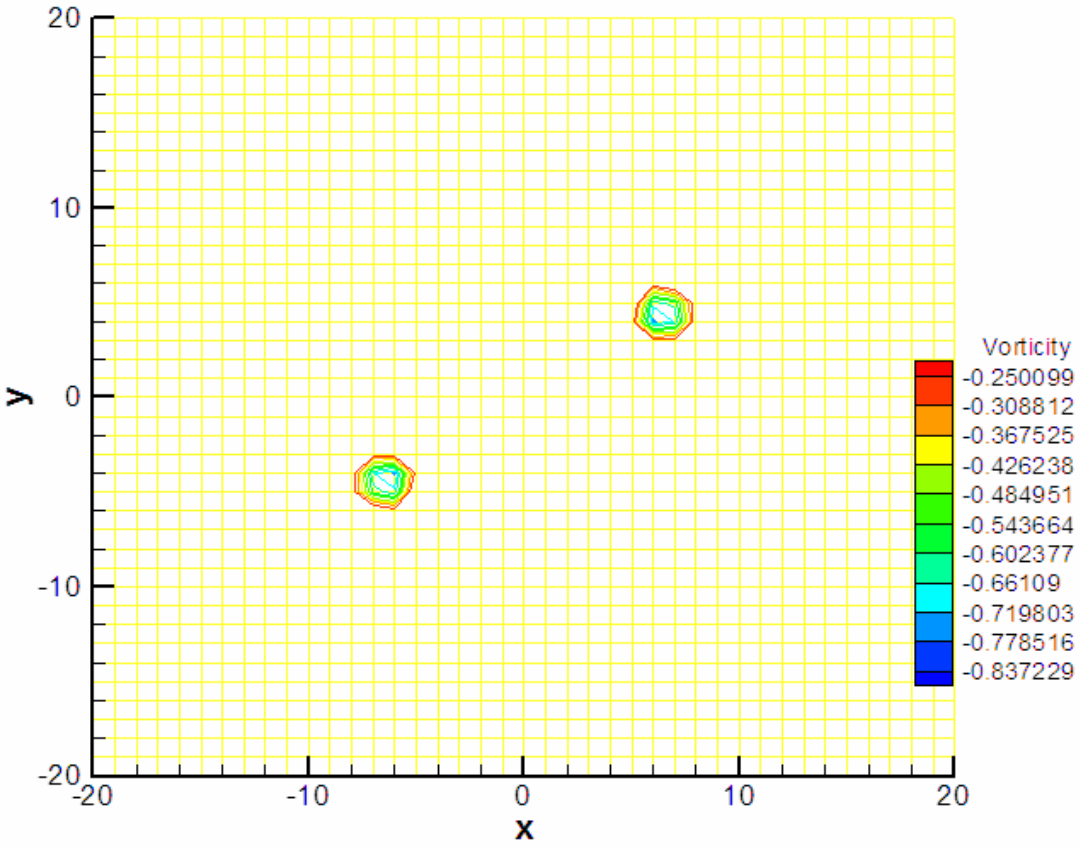

Fig. 3-52 Vorticity contours after 3000 time iterations, 16 cells apart

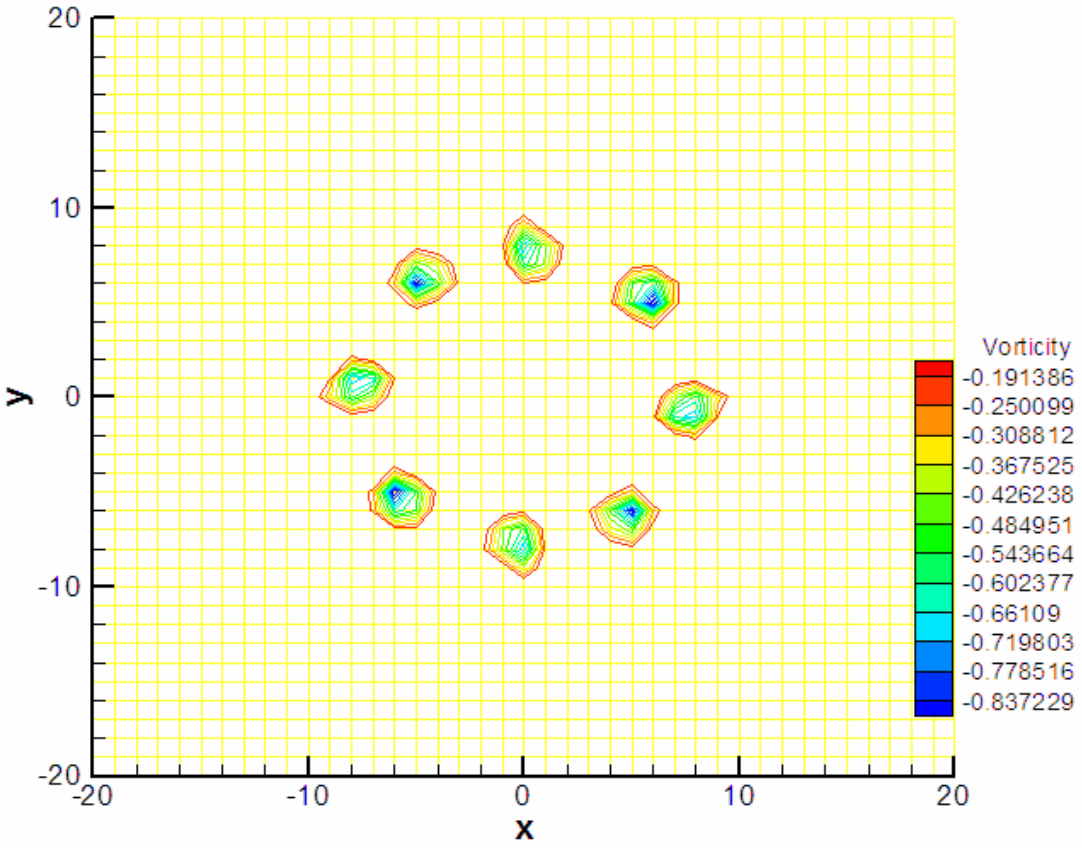

Fig. 3-53 Vorticity contours after 1st loop

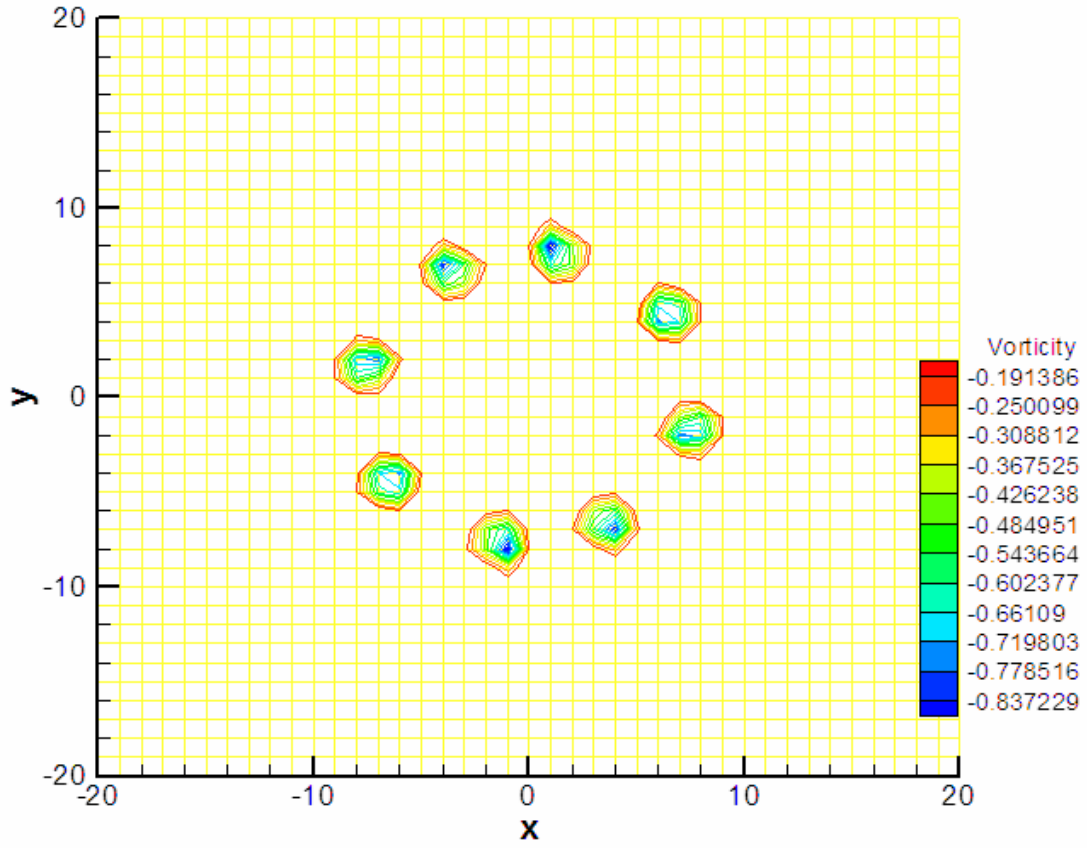

Fig. 3-54 Vorticity contours after 2nd loops

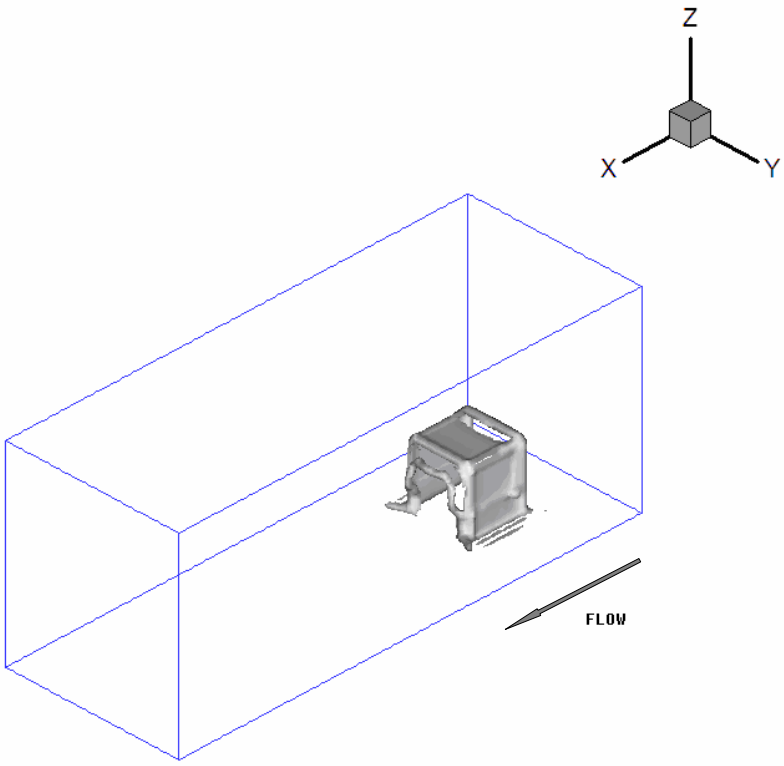

Fig. 4-6 Vorticity iso-surface, after 50 time steps

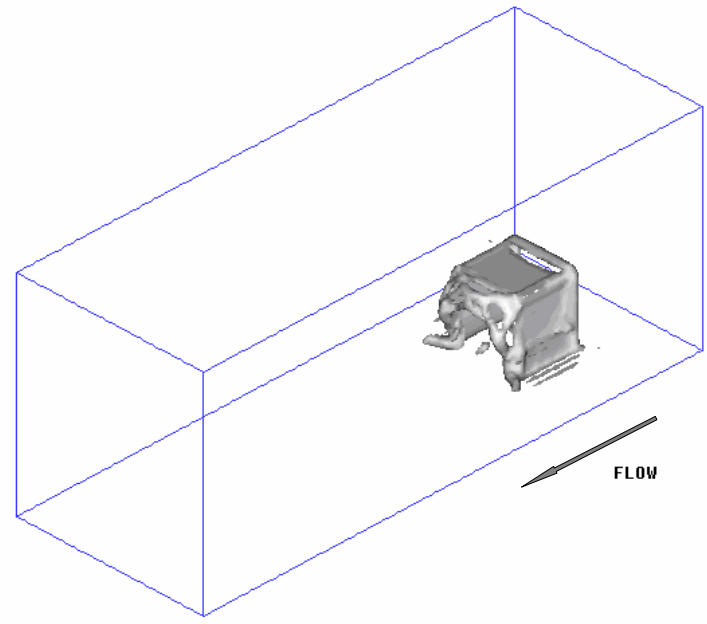

Fig 4-7 Vorticity iso-surface, after 120 time steps

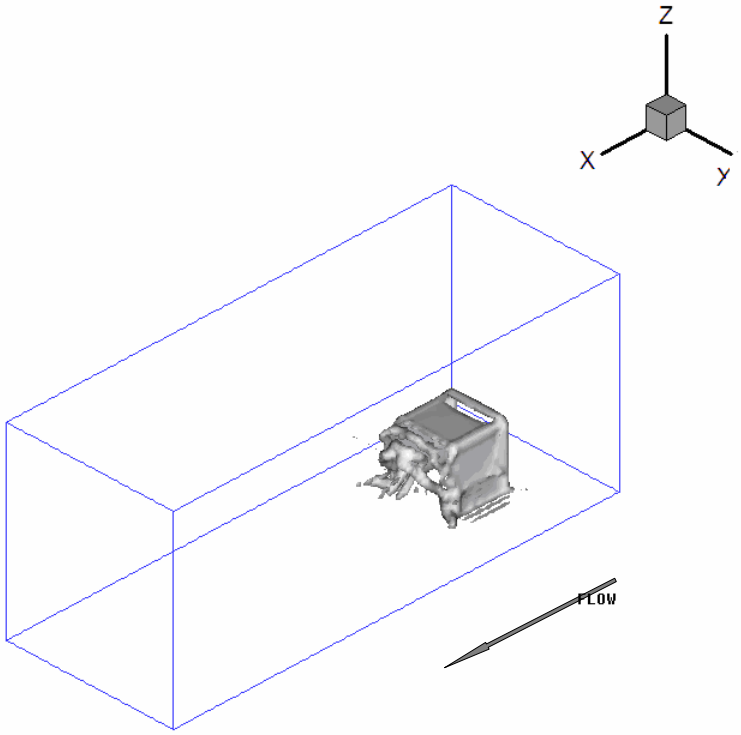

Fig 4-8 Vorticity iso-surface, after 300 time steps

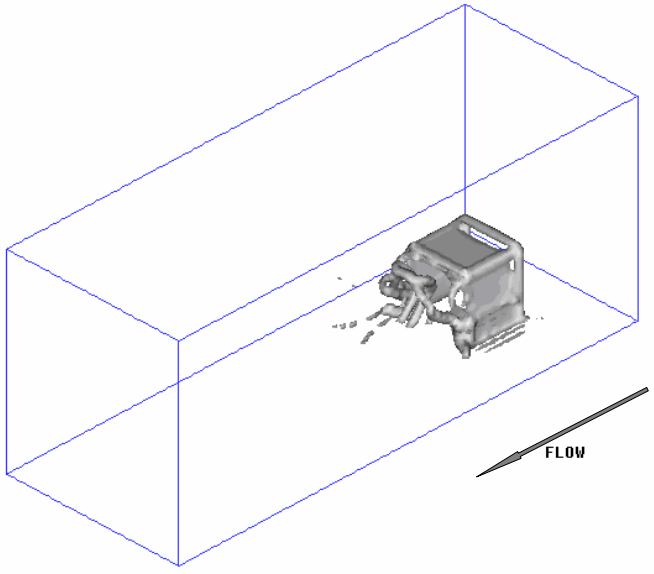

Fig 4-9 Vorticity iso-surface, after 400 time steps

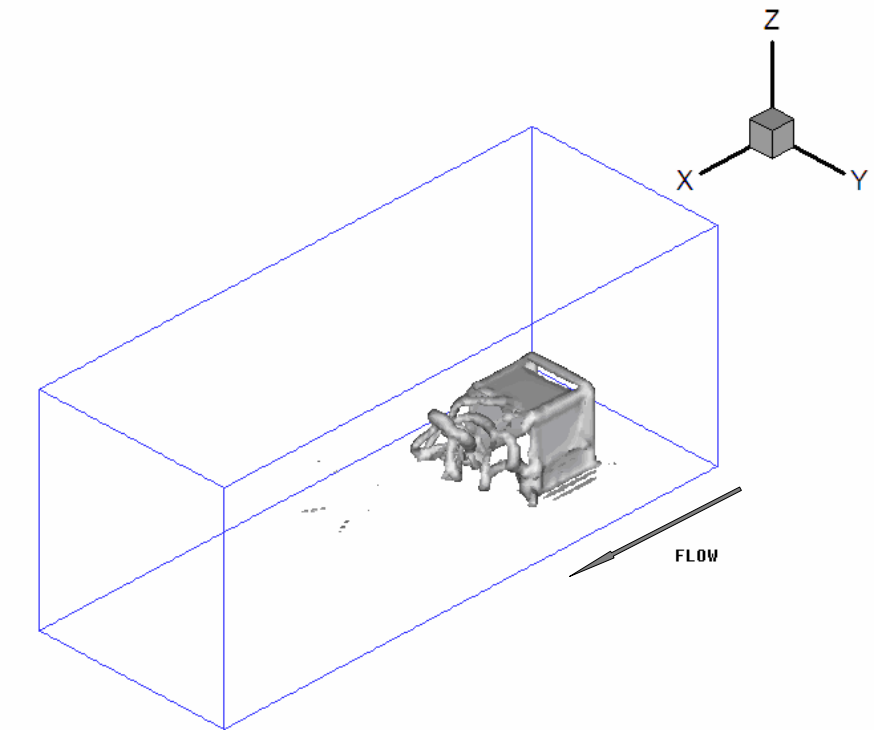

Fig 4-10 Vorticity iso-surface, after 600 time steps

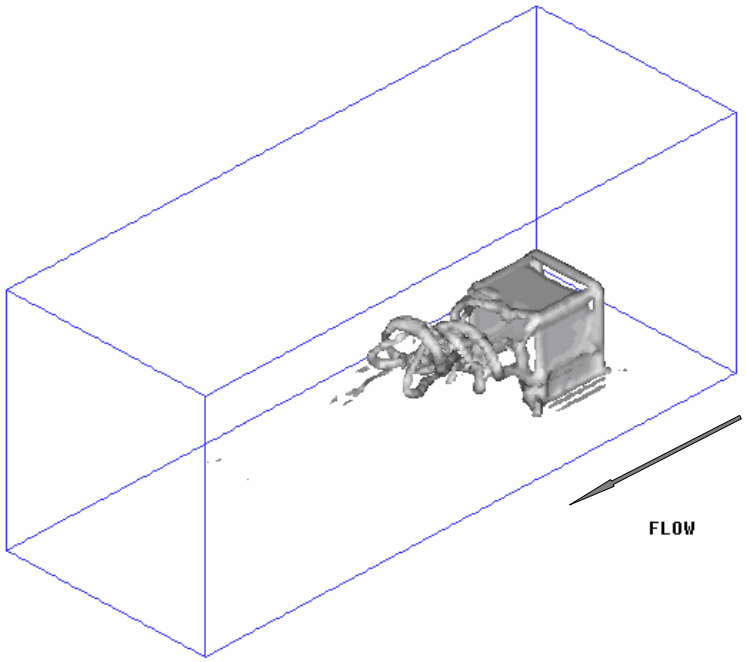

Fig 4-11 Vorticity iso-surface, after 700 time steps

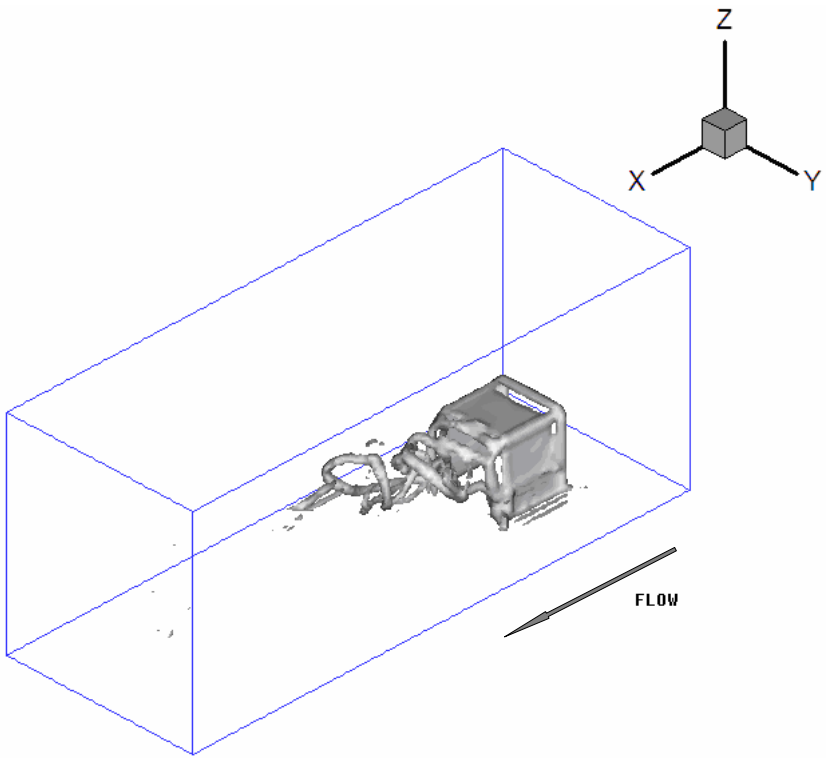

Fig 4-12 Vorticity iso-surface, after 900 time steps

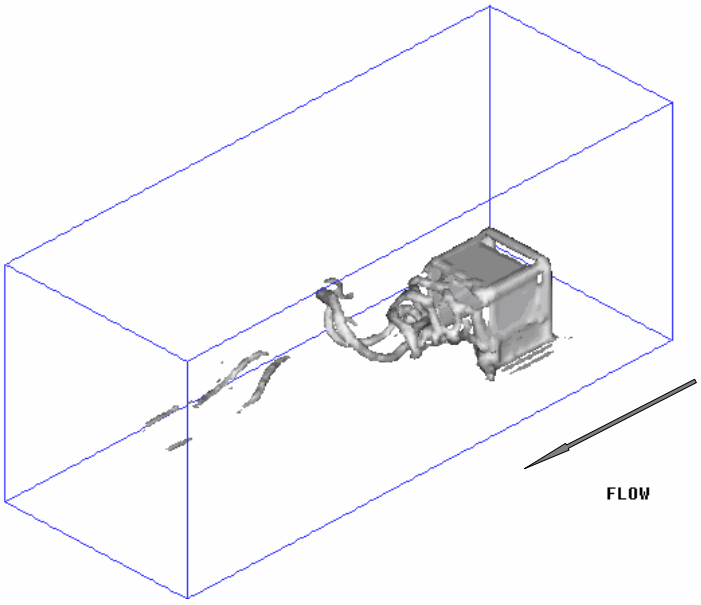

Fig 4-13 Vorticity iso-surface, after 1200 time steps

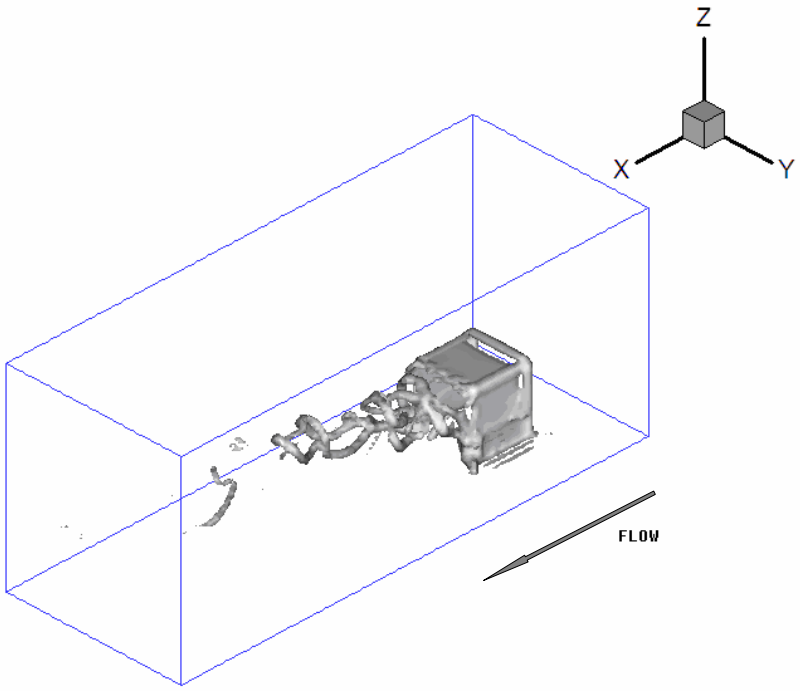

Fig.4-14 Vorticity iso-surface, after 1600 time steps

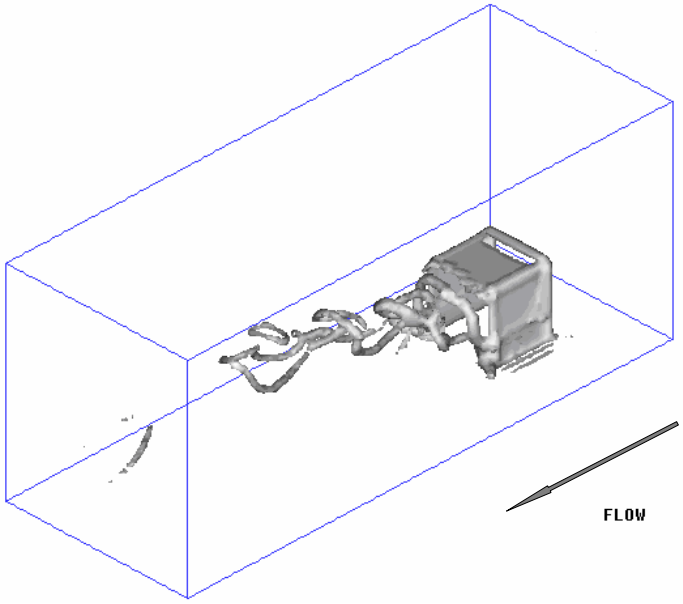

Fig 4-15 Vorticity iso-surface, after 1800 time steps

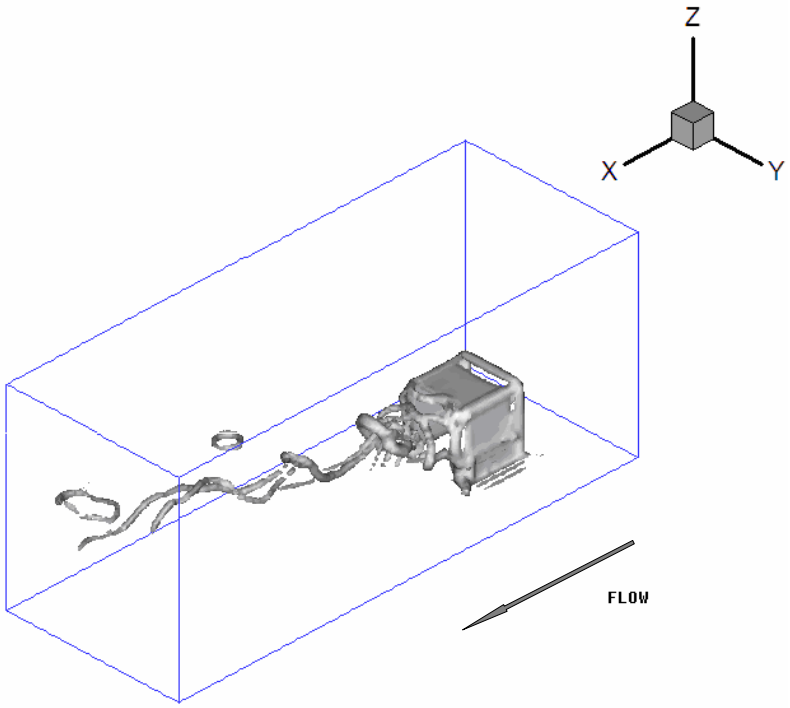

Fig 4-16 Vorticity iso-surface, after 3000 time steps

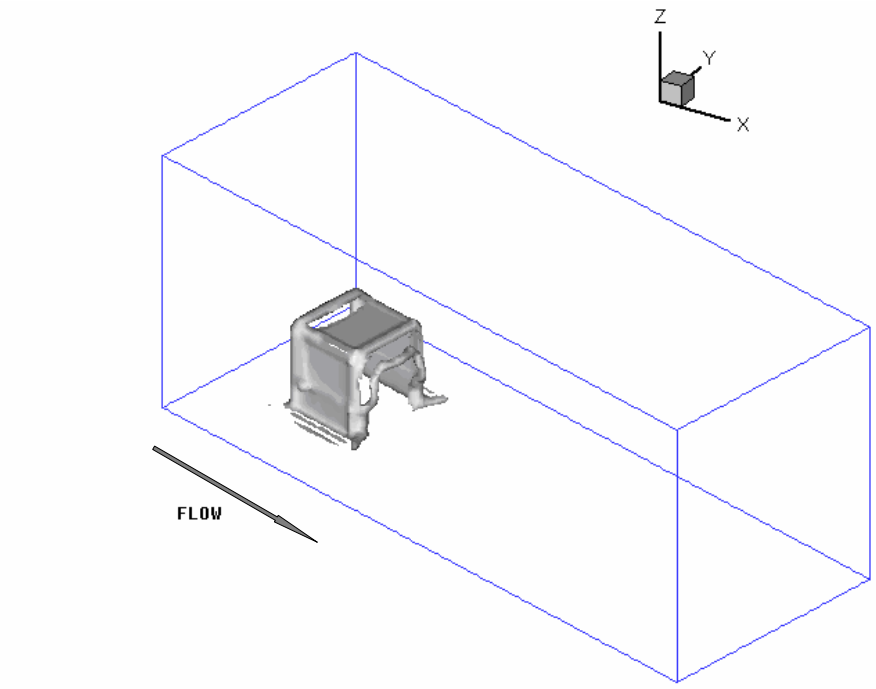

Fig 4-17 Vorticity iso-surface from the different viewing angle, after 50 time steps

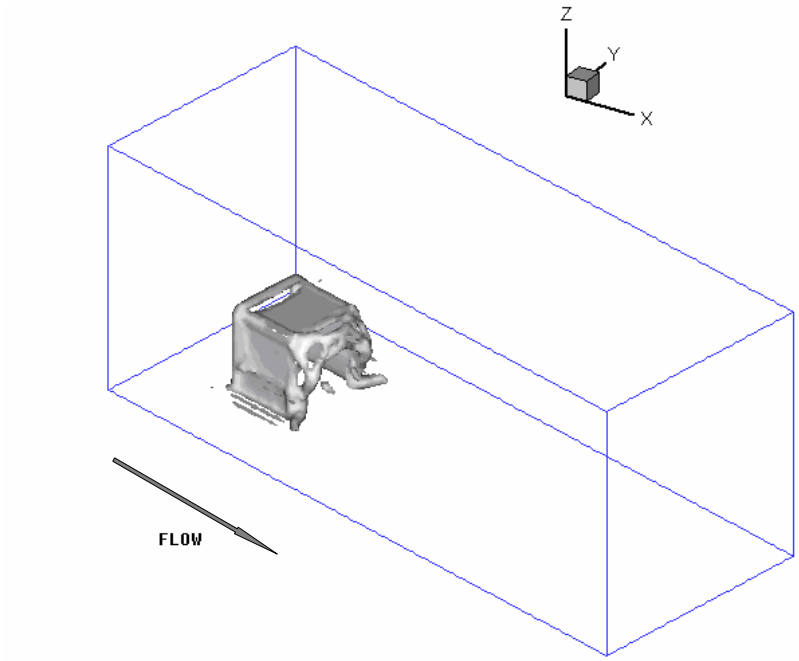

Fig 4-18 Vorticity iso-surface from the different viewing angle, after 120 time steps

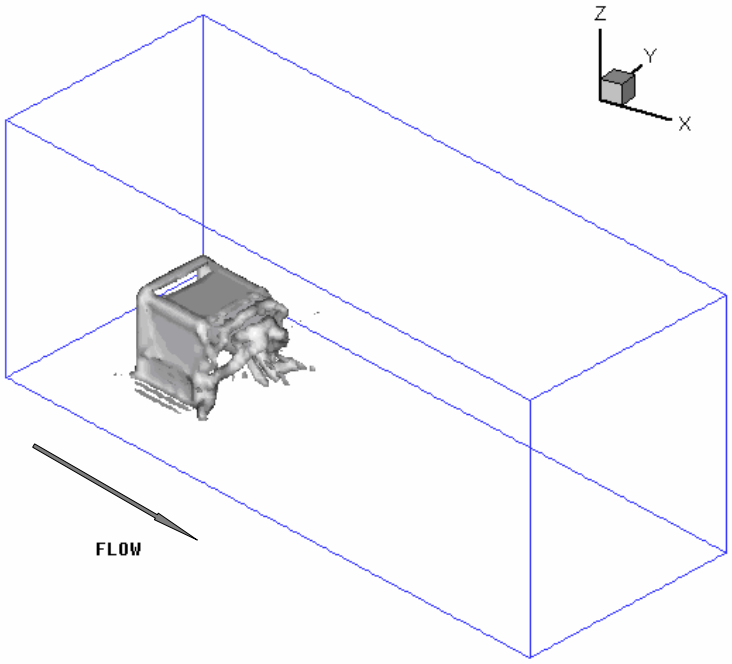

Fig 4-19 Vorticity iso-surface from the different viewing angle, after 300 time steps

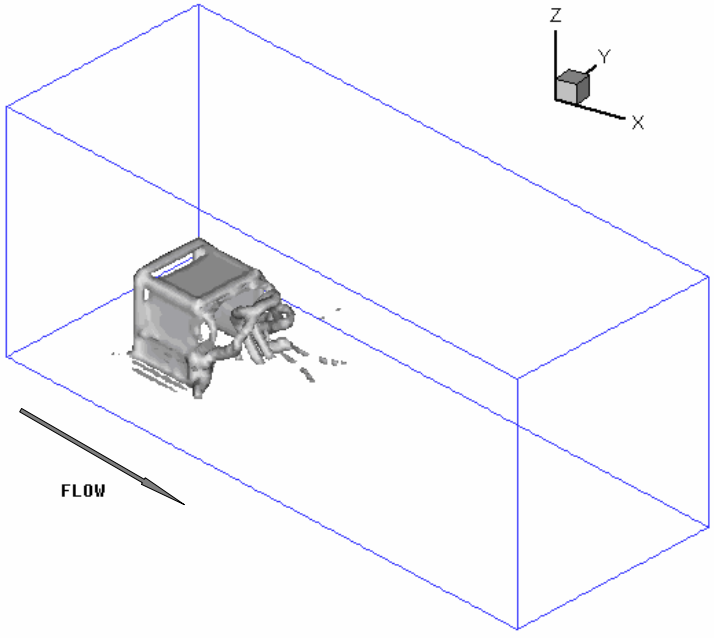

Fig 4-20 Vorticity iso-surface from the different viewing angle, after 400 time steps

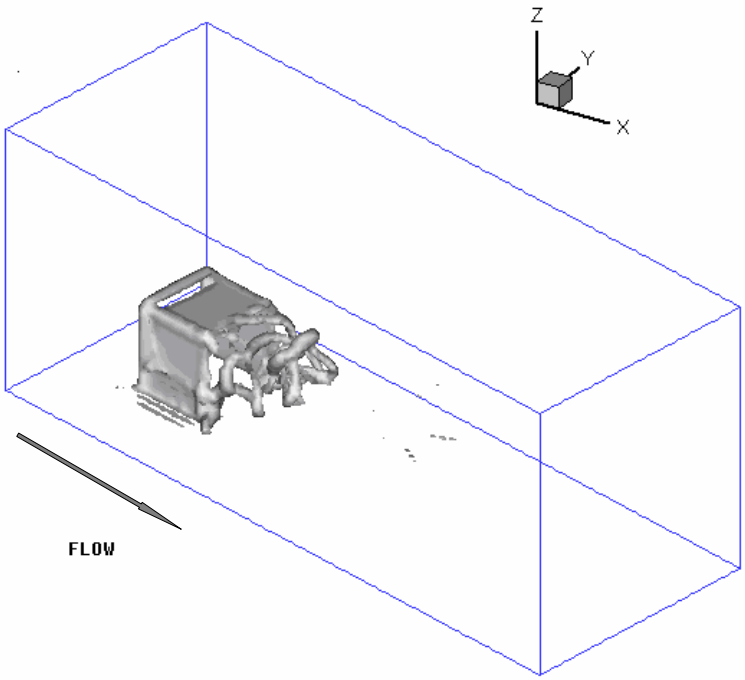

Fig 4-21 Vorticity iso-surface from the different viewing angle, after 600 time steps

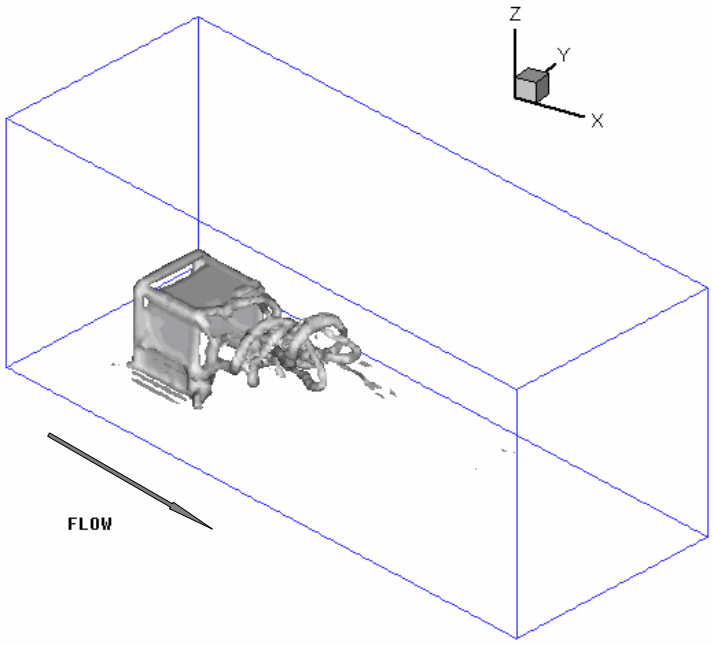

Fig 4-22 Vorticity iso-surface from the different viewing angle, after 700 time steps

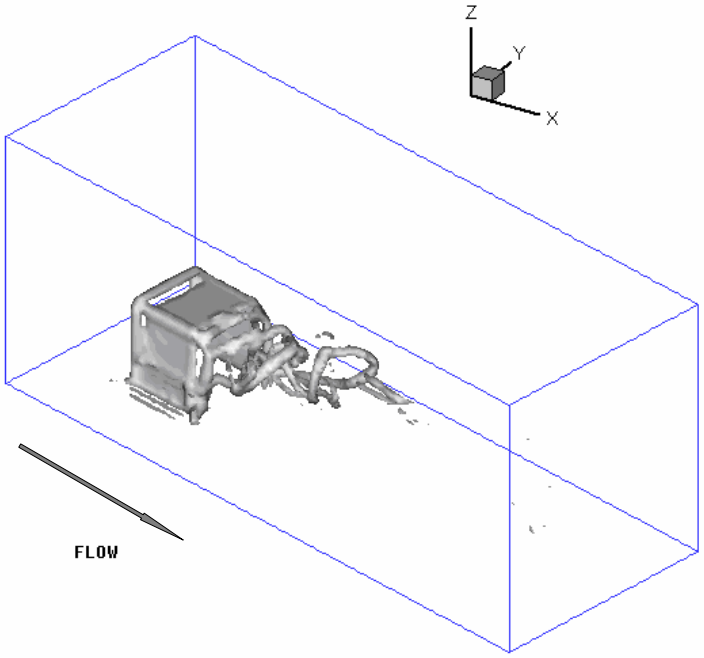

Fig 4-23 Vorticity iso-surface from the different viewing angle, after 900 time steps

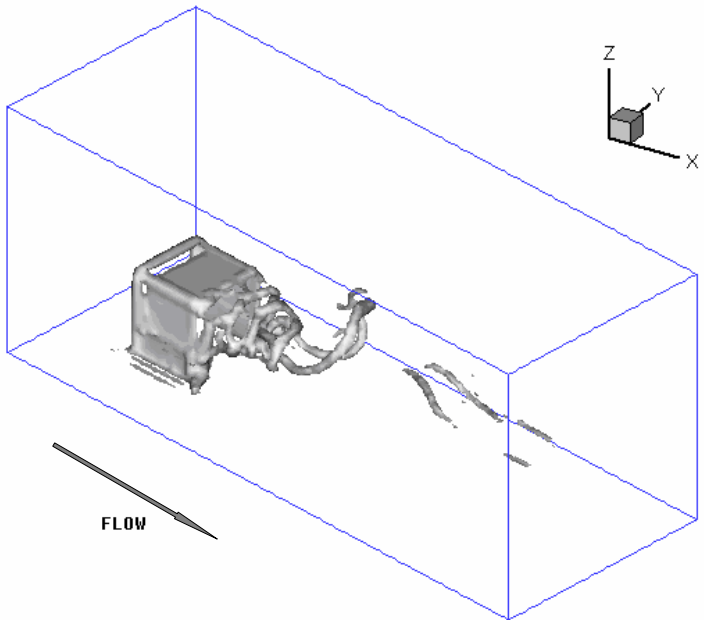

Fig 4-24 Vorticity iso-surface from the different viewing angle, after 1200 time steps

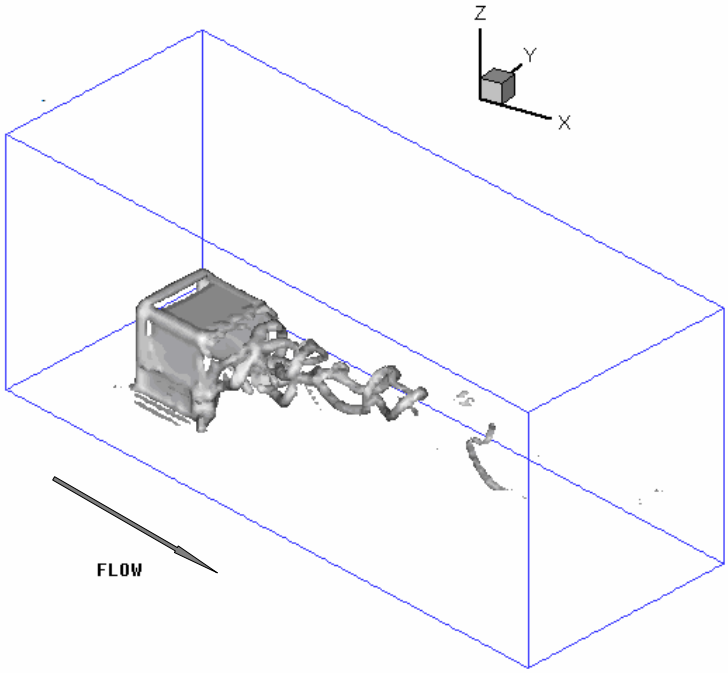

Fig 4-25 Vorticity iso-surface from the different viewing angle, after 1600 time steps

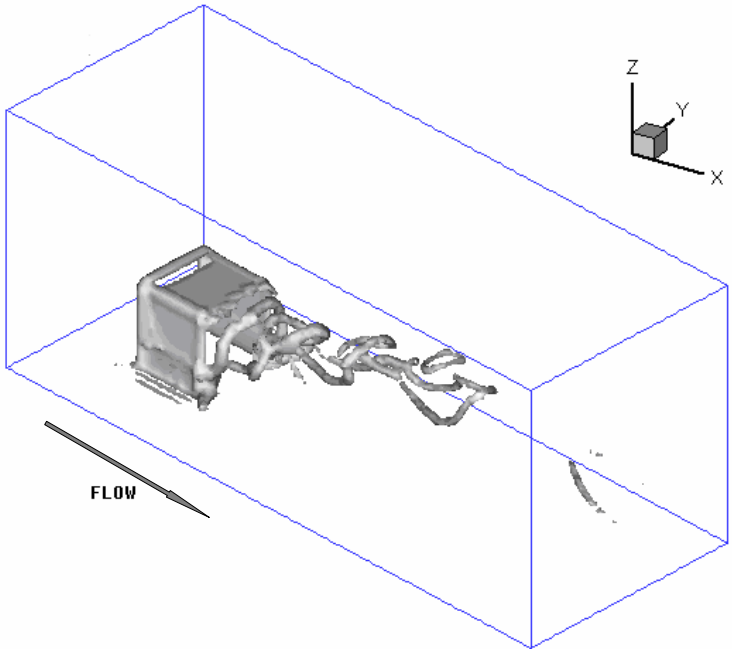

Fig 4-26 Vorticity iso-surface from the different viewing angle, after 1800 time steps

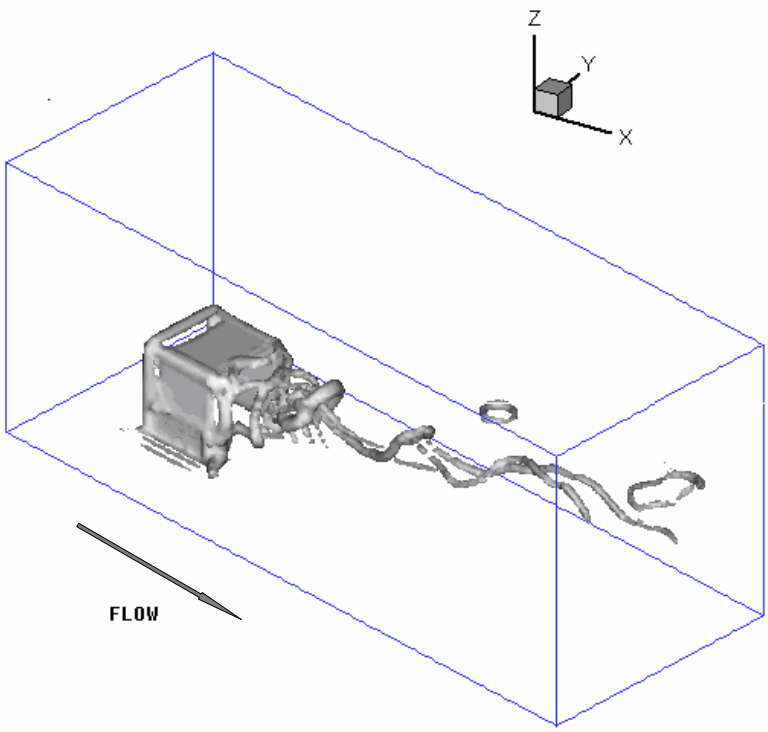

Fig 4-27 Vorticity iso-surface from the different viewing angle, after 3000 time steps

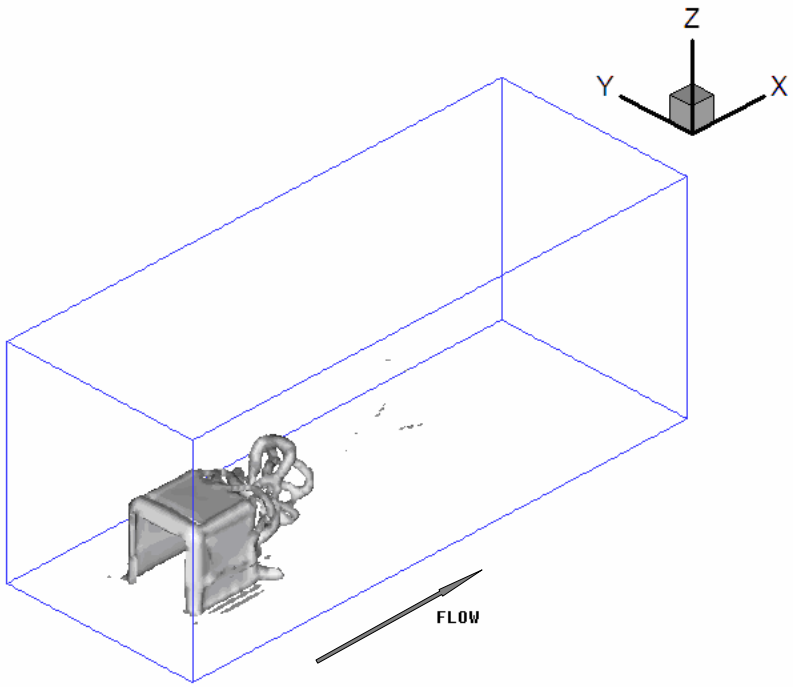

Fig 4-28 Vorticity iso-surface from the different viewing angle, after 600 time steps

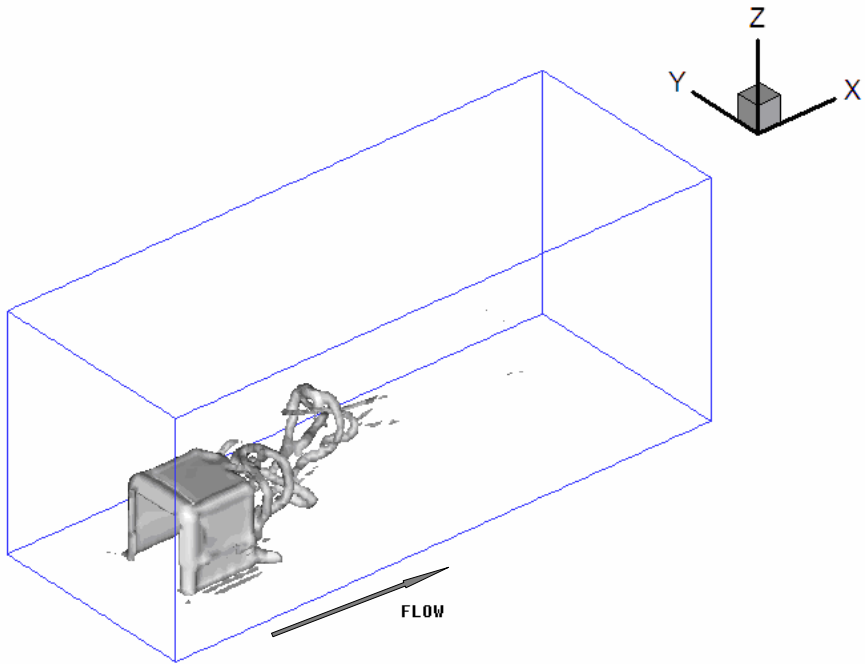

Fig 4-29 Vorticity iso-surface from the different viewing angle, after 700 time steps

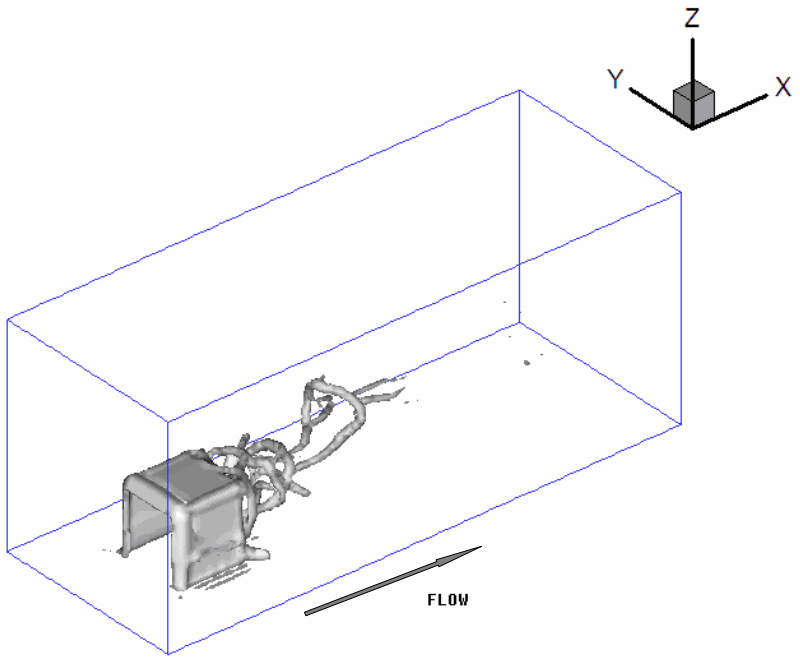

Fig 4-30 Vorticity iso-surface from the different viewing angle, after 900 time steps

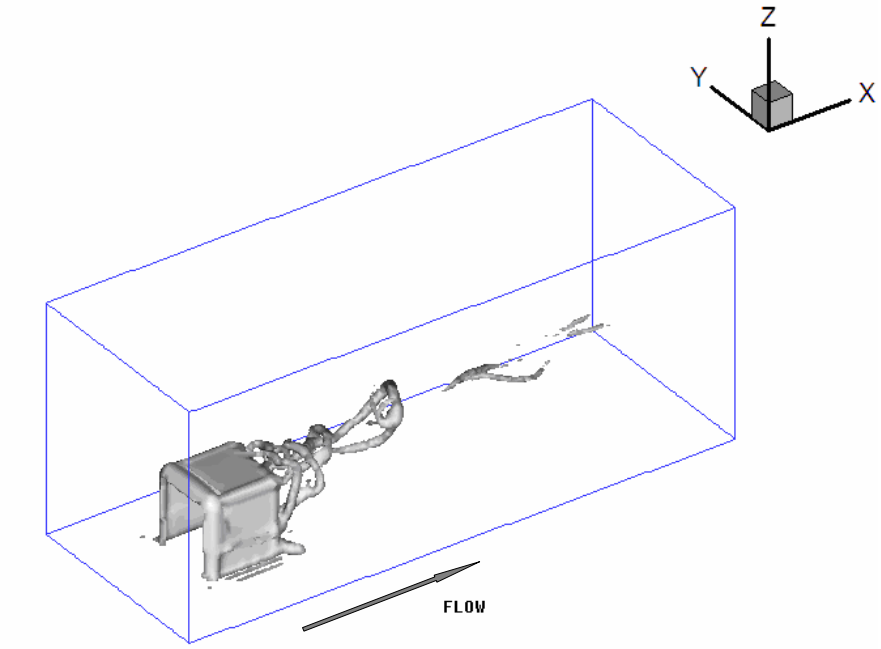

Fig 4-31 Vorticity iso-surface from the different viewing angle, after 1200 time steps

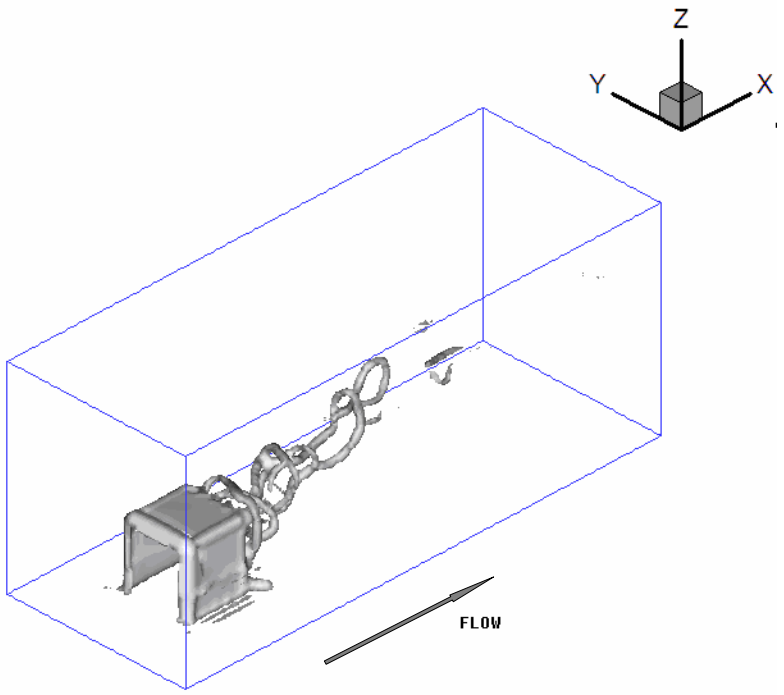

Fig 4-32 Vorticity iso-surface from the different viewing angle, after 1600 time steps

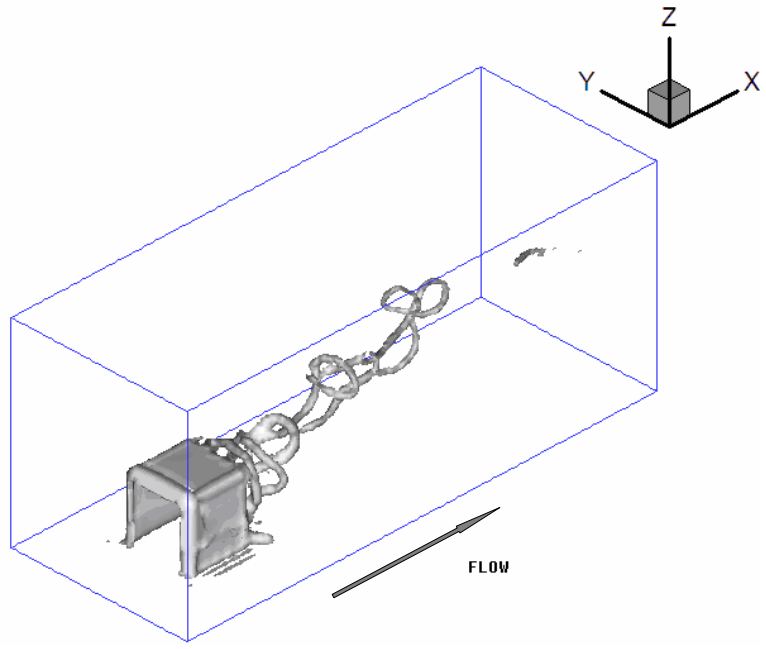

Fig 4-33 Vorticity iso-surface from the different viewing angle, , after 1800 time steps

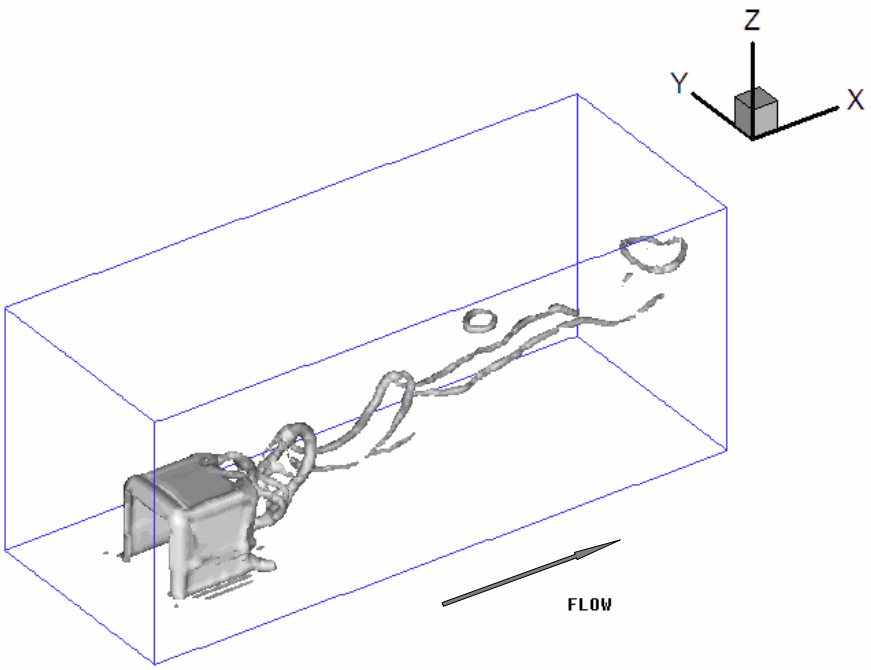

Fig 4-34 Vorticity iso-surface from the different viewing angle, after 3000 time steps

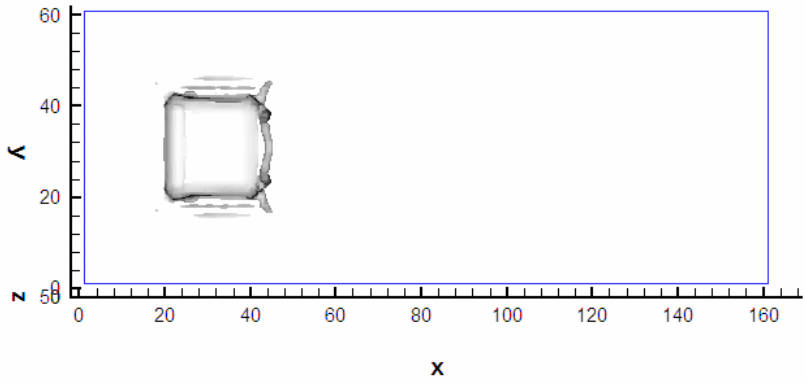

(a) 50 time steps

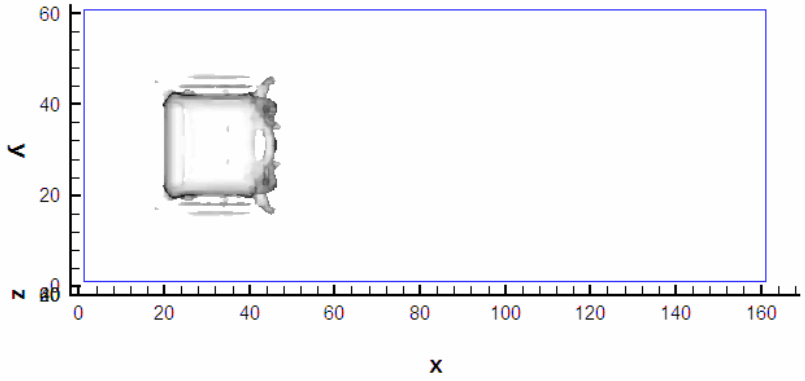

(b) 120 time steps

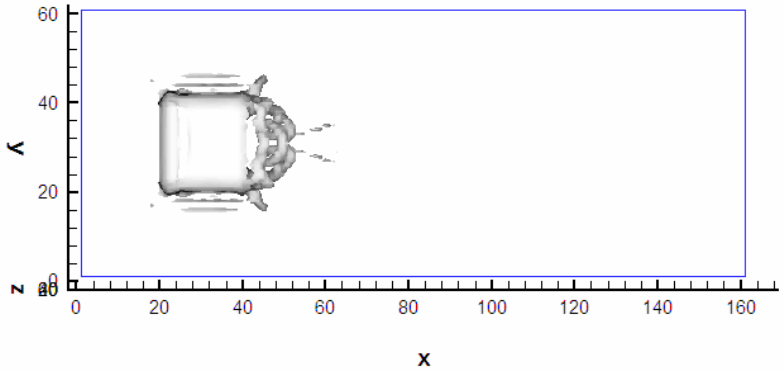

(c) 300 time steps

Fig. 4-35 Vorticity iso-surface from the different viewing angle, top views in a sequence of time steps

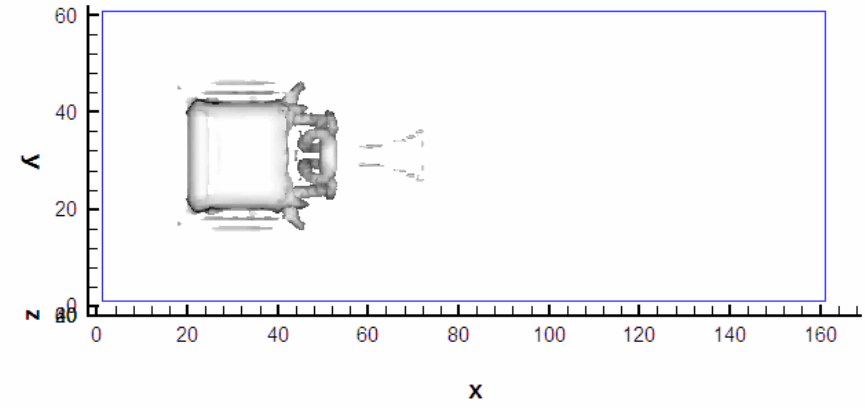

(d) 400 time steps

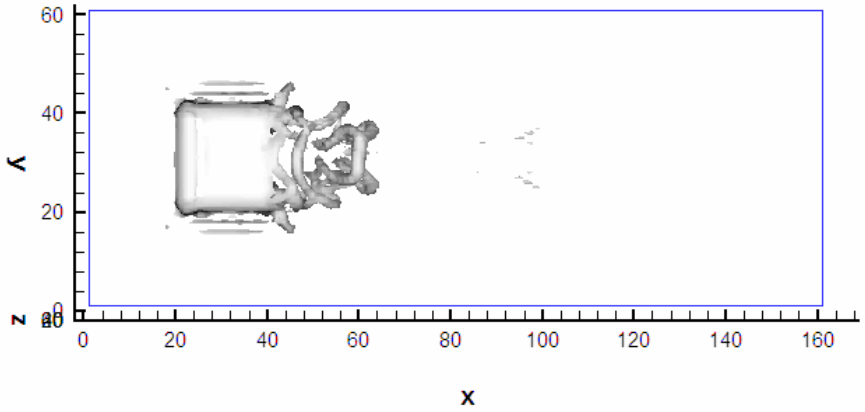

(e)600 time steps

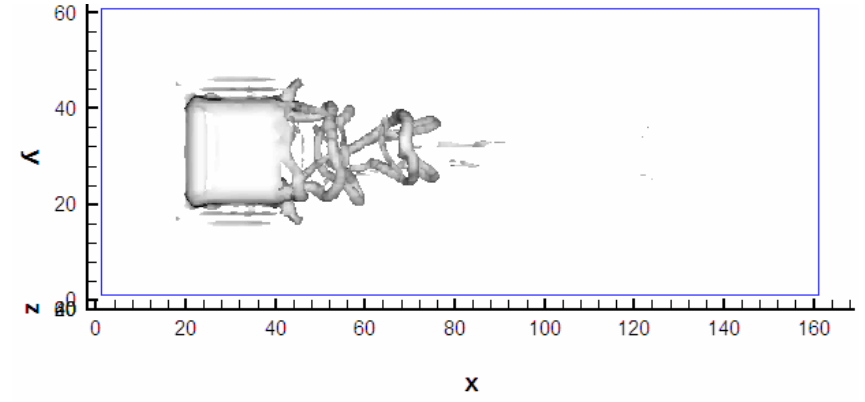

(f) 700 time steps

Fig. 4-35 Continued

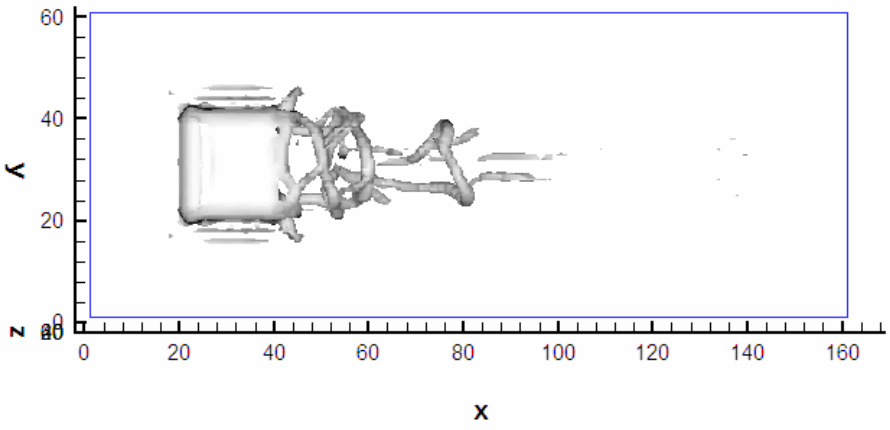

(g) 900 time steps

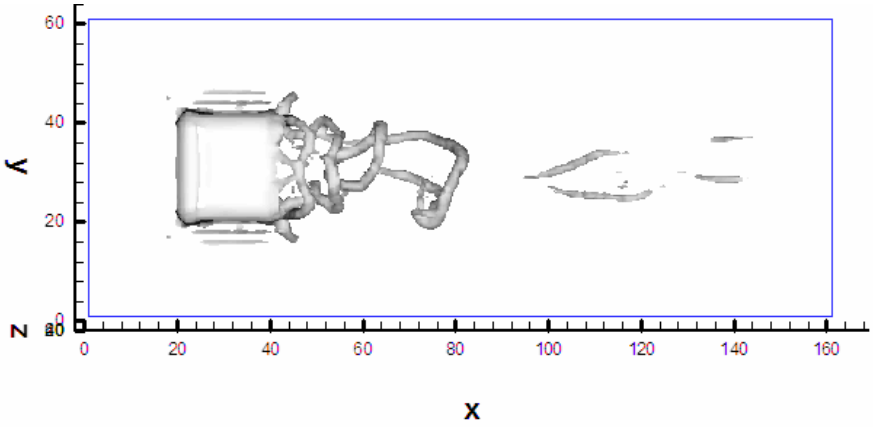

(h) 1200 time steps

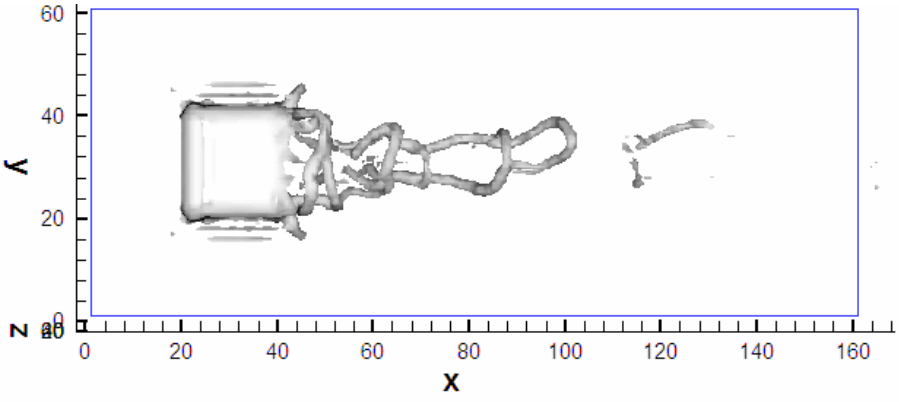

(i) 1600 time steps

Fig. 4-35 Continued

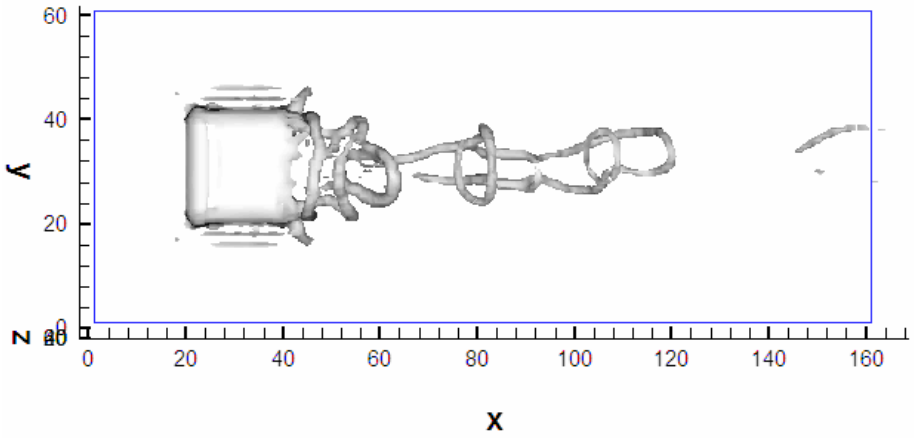

(j) 1800 time steps

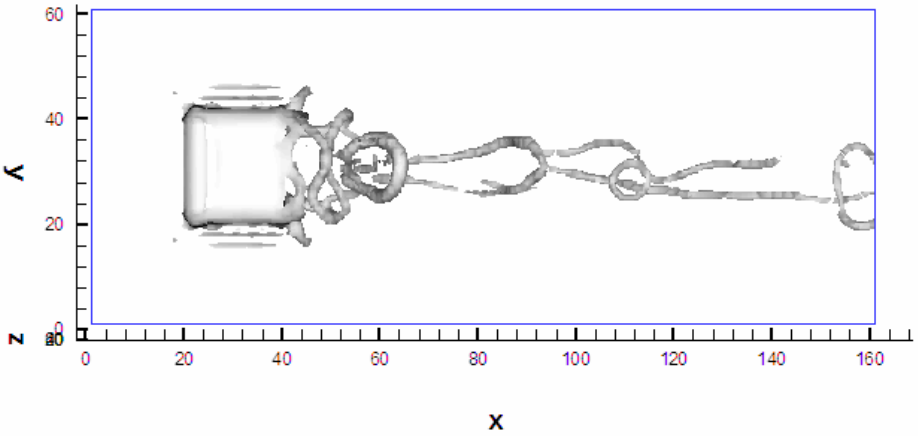

(k) 3000 time steps

Fig. 4-35 Continued

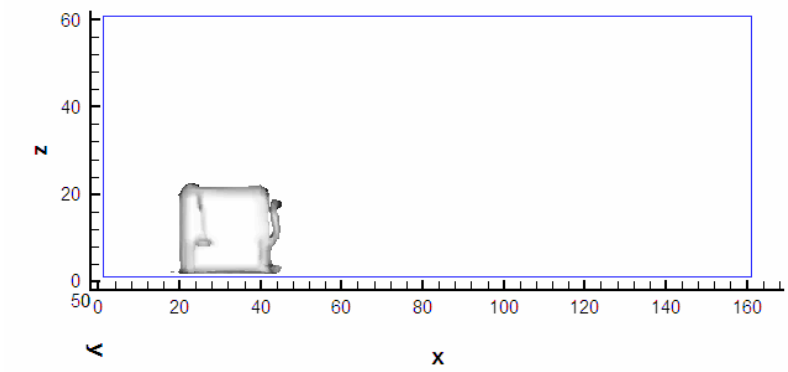

(a) 50 time steps

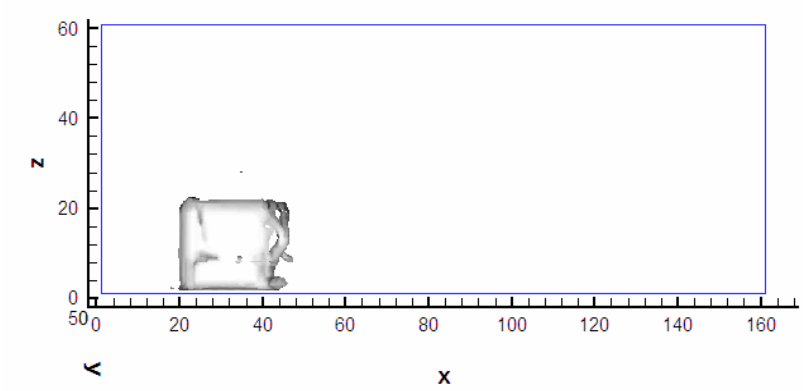

(b) 120 time steps

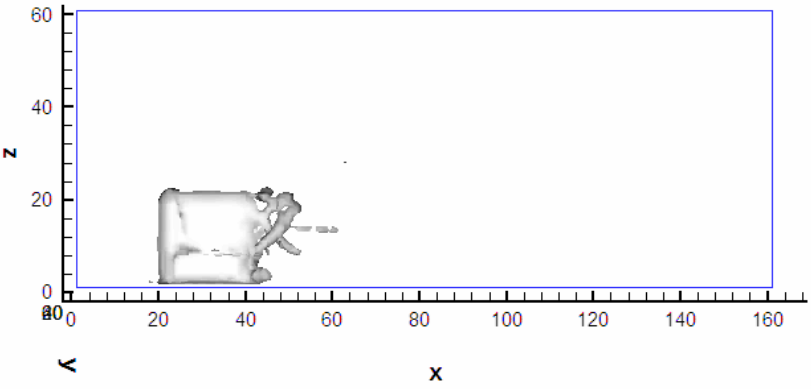

(c) 300 time steps

Fig. 4-36 Vorticity iso-surface from the different viewing angle, side views in a sequence of time steps

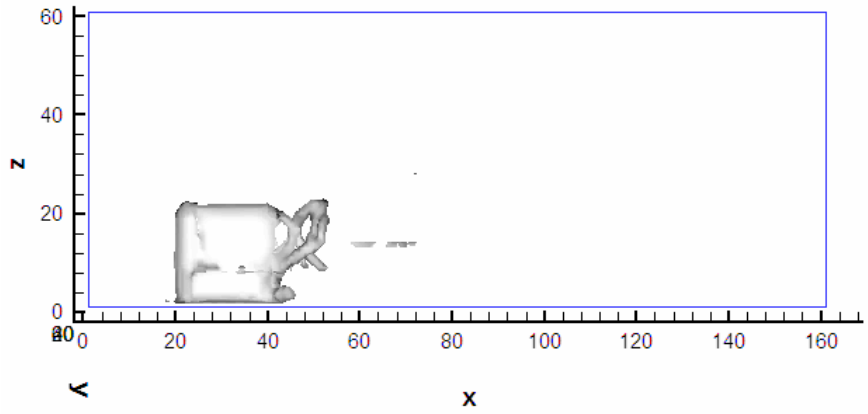

(d) 400 time steps

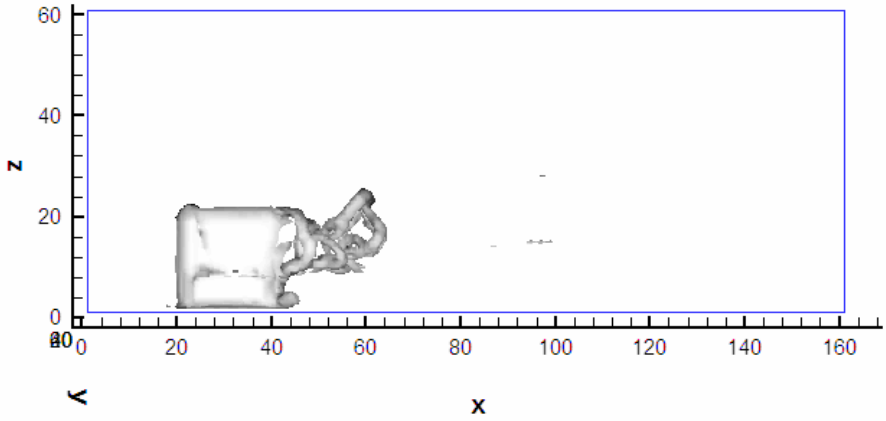

(e) 600 time steps

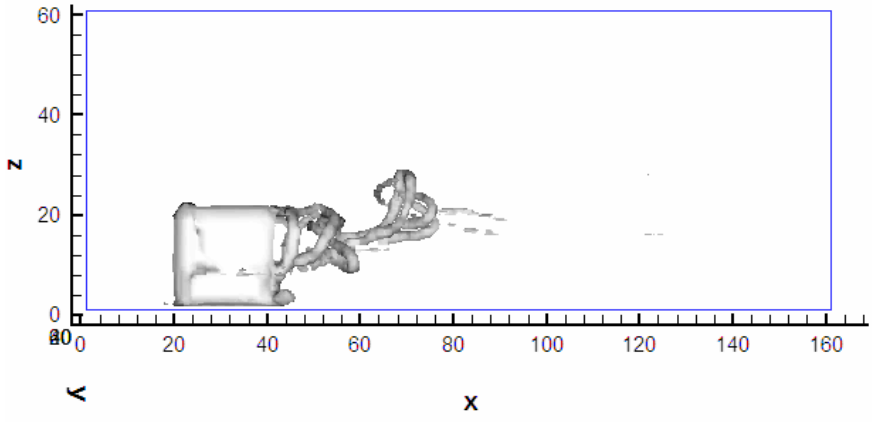

(f)700 time steps

Fig. 4-36 Continued

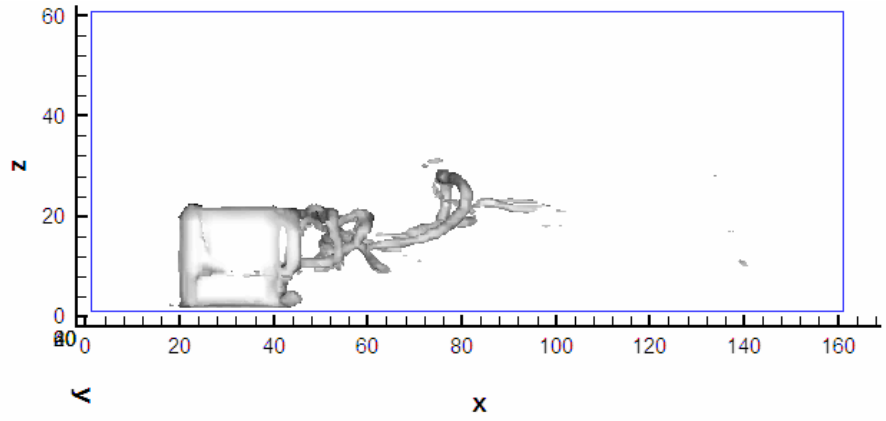

(g) 900 time steps

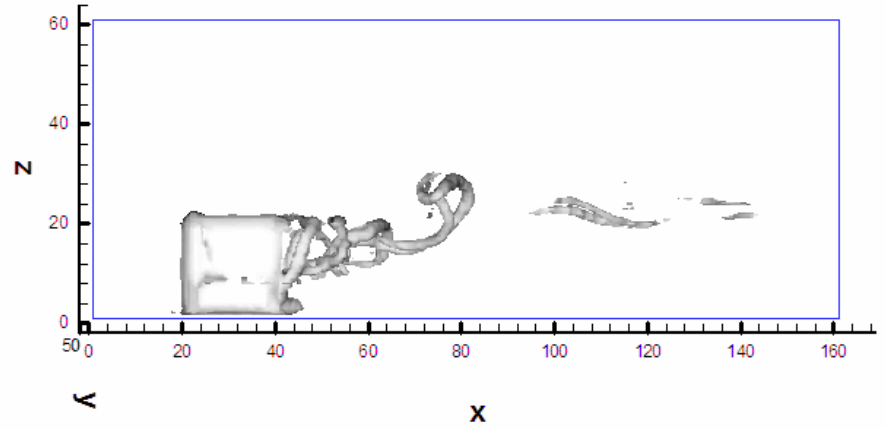

(h) 1200 time steps

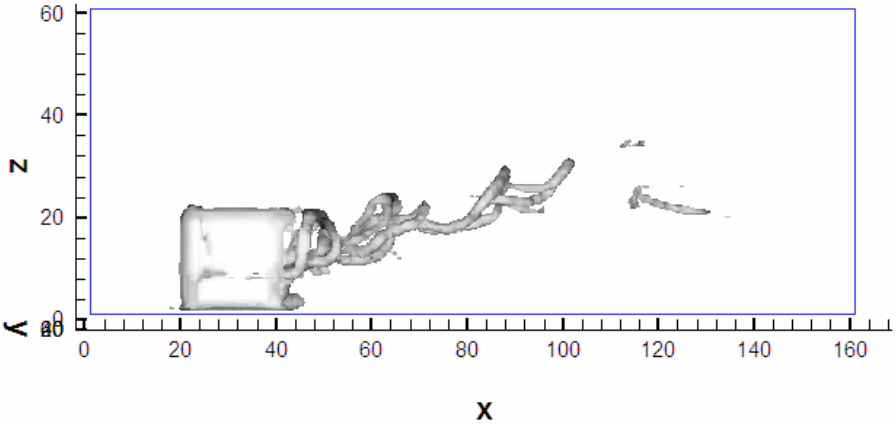

(i) 1600 time steps

Fig. 4-36 Continued

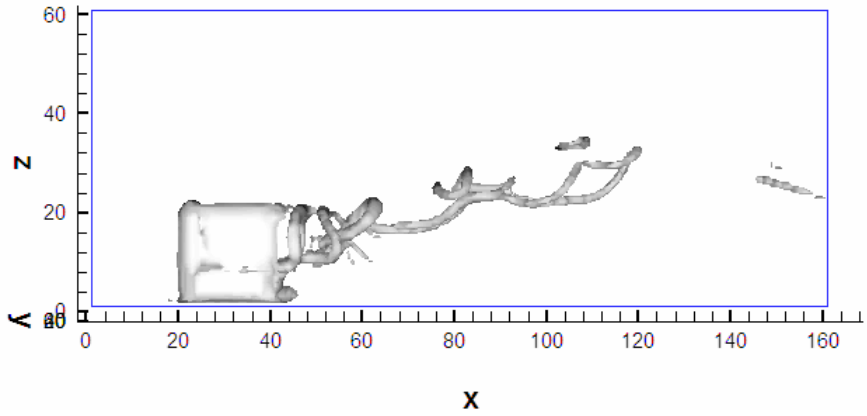

(j) 1800 time steps

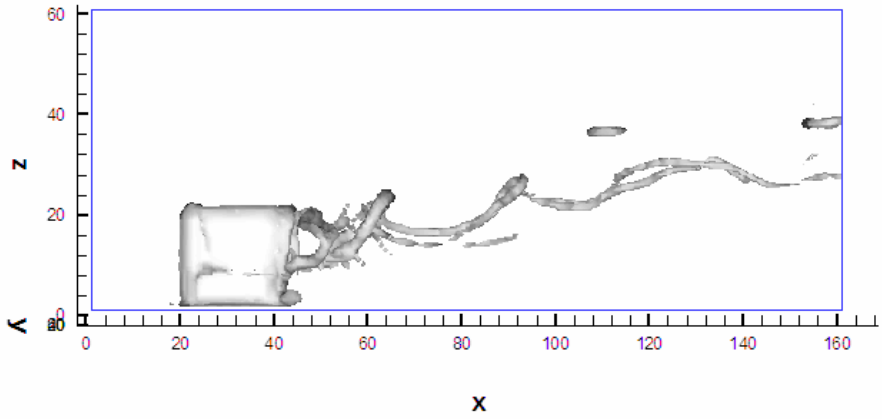

(k) 3000 time steps

Fig. 4-36 Continued

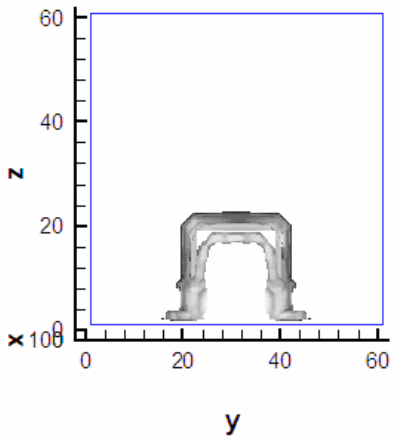

(a) 50 time steps

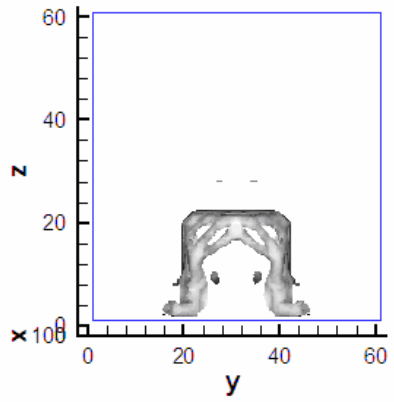

(b) 120 time steps

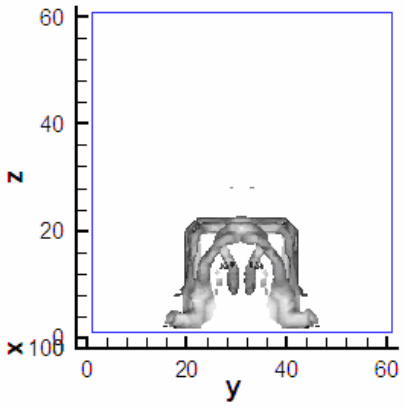

(c) 300 time steps

Fig. 4-37 Vorticity iso-surface from the different viewing angle, end views in a sequence of time steps

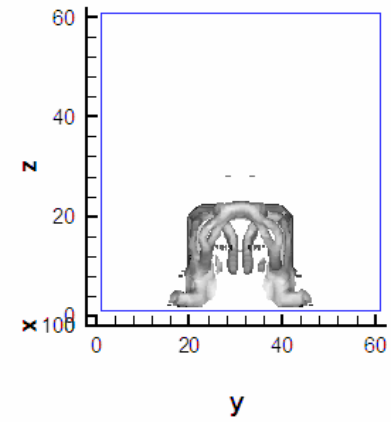

(d) 400 time steps

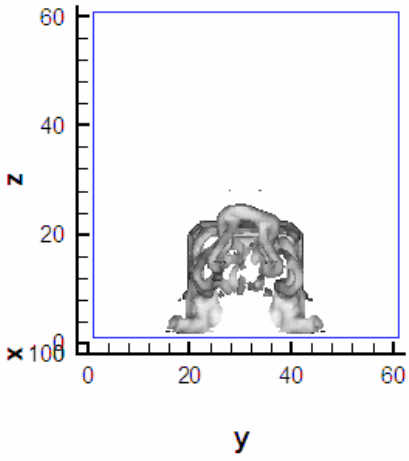

(e) 600 time steps

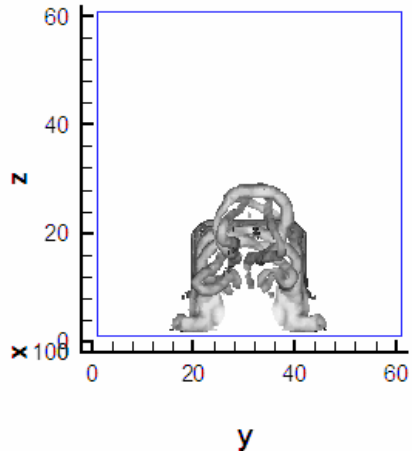

(f) 700 time steps

Fig. 4-37 Continued

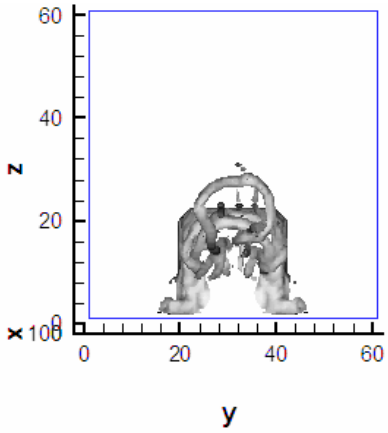

(g) 900 time steps

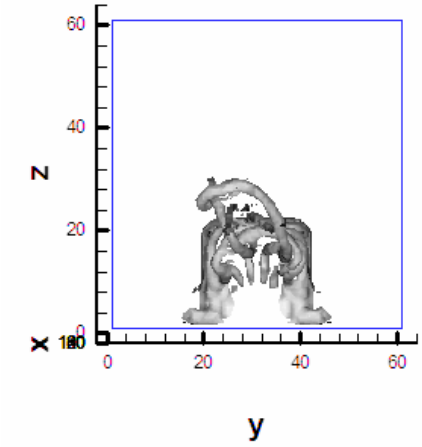

(h) 1200 time step

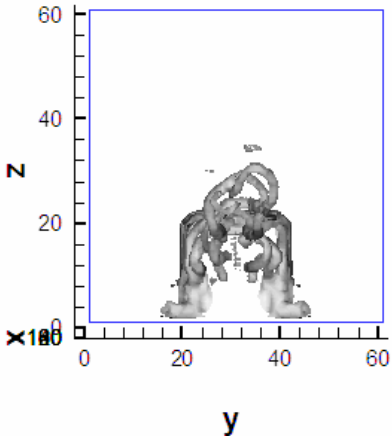

(i) 1600 time steps

Fig. 4-37 Continued

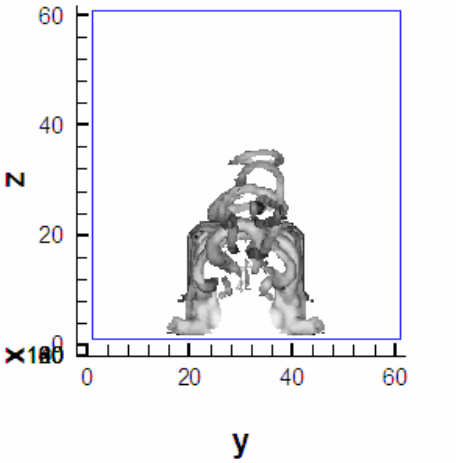

(j) 1800 time steps

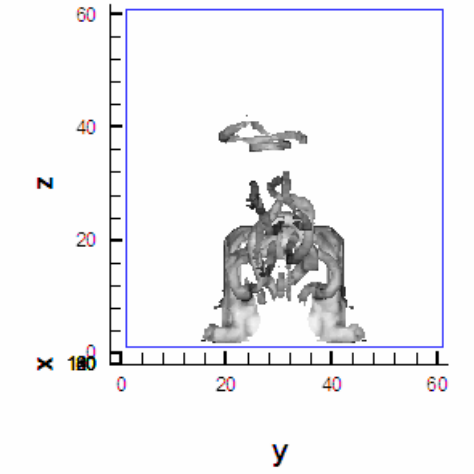

(k) 3000 time steps

Fig. 4-37 Continued

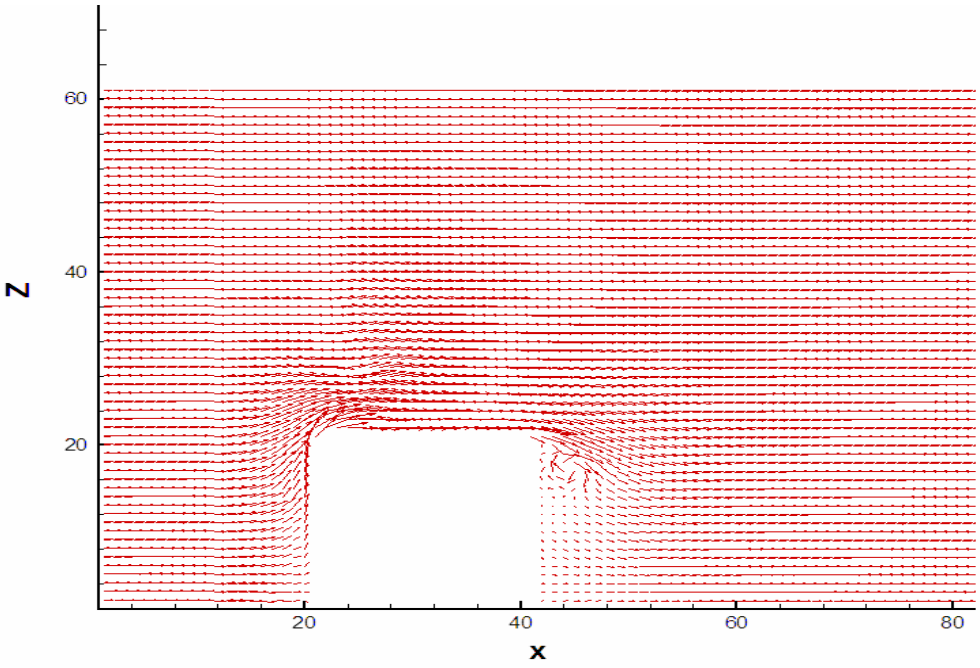

Fig 4-38 Velocity vector field for the symmetry plane after 50 time steps

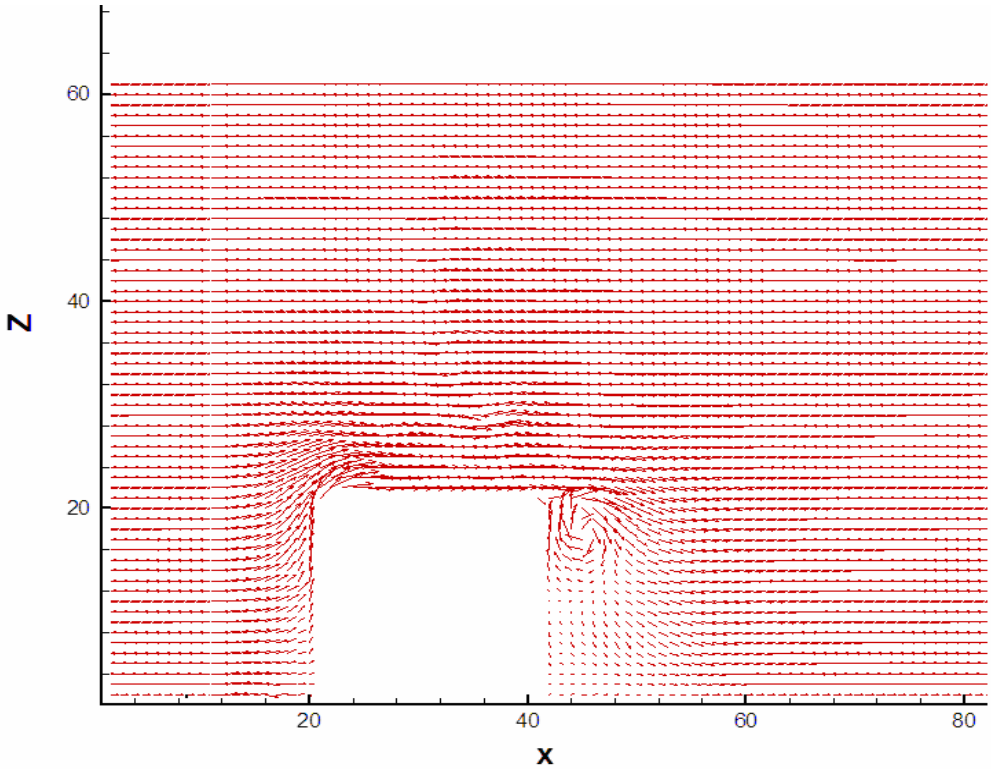

Fig 4-39 Velocity vector field for the symmetry plane, after 120 time steps

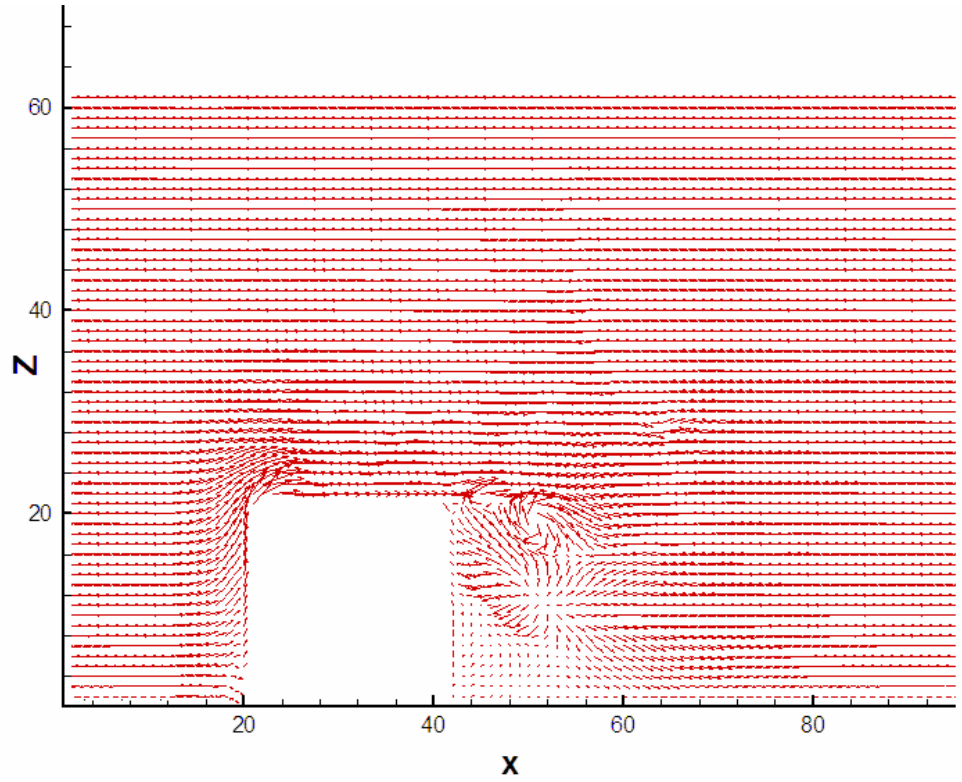

(a) Velocity vector field

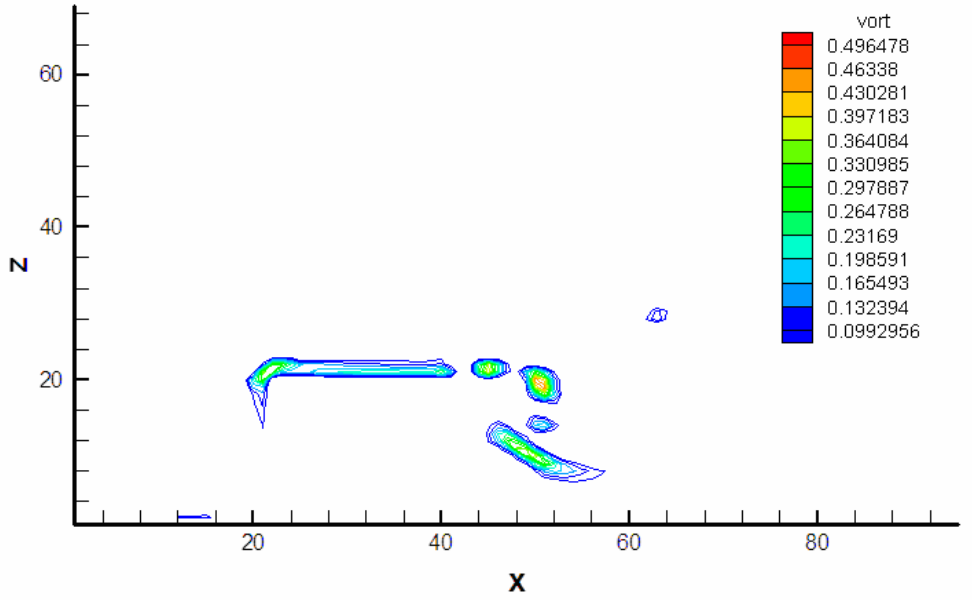

(b)Vorticity contours

Fig. 4-40 Velocity vector field and vorticity contours for the symmetry plane, 300 time steps

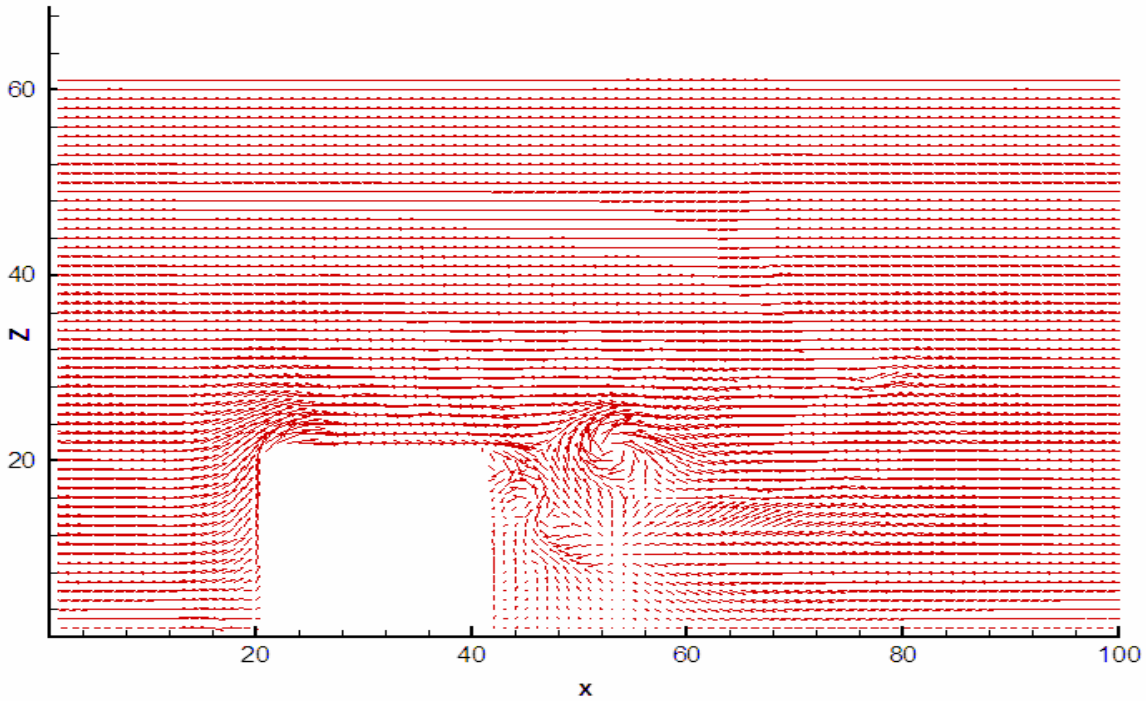

(a) Velocity vector field

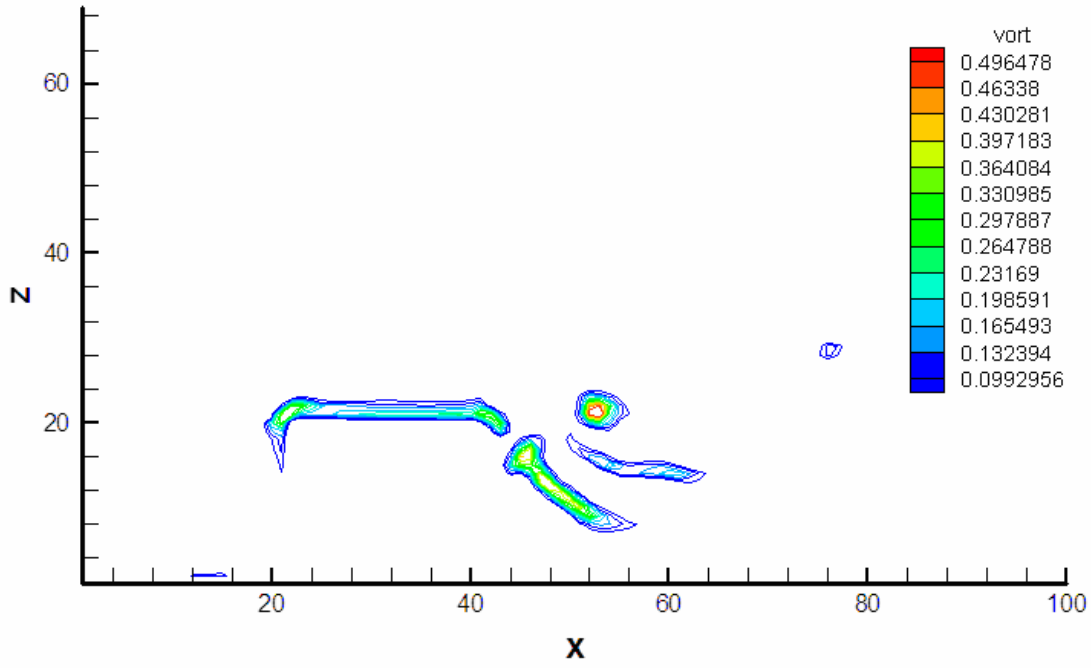

(b)Vorticity contours

Fig. 4-41 Velocity vector field and vorticity contours for the symmetry plane, 400 time steps

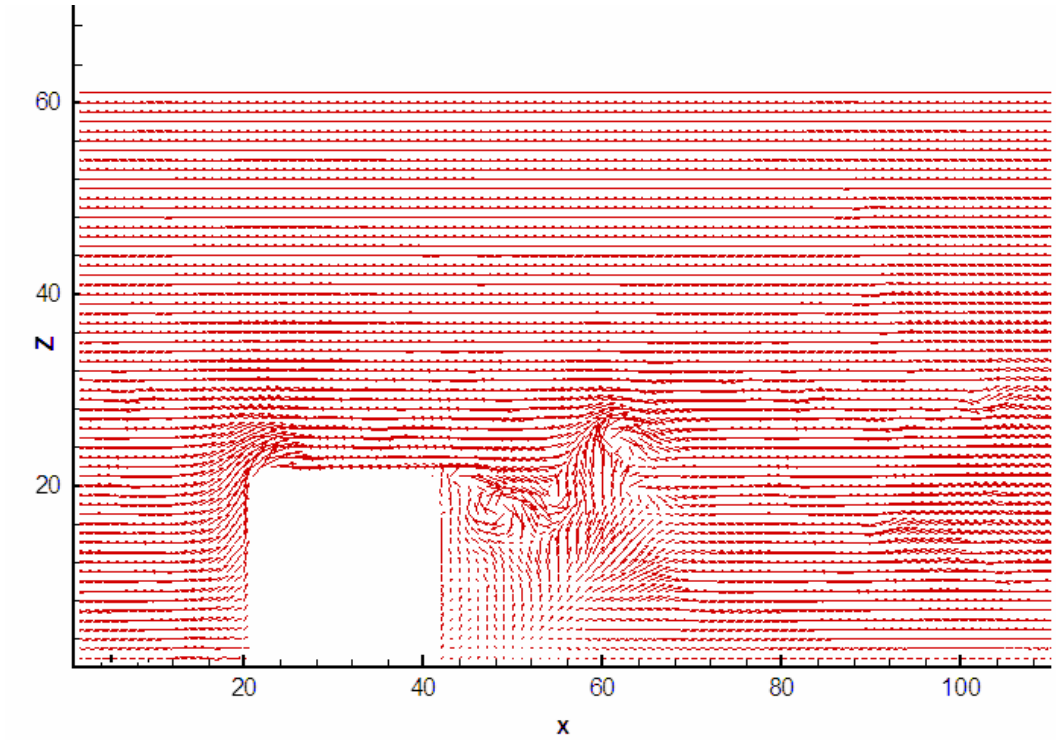

(a) Velocity vector field

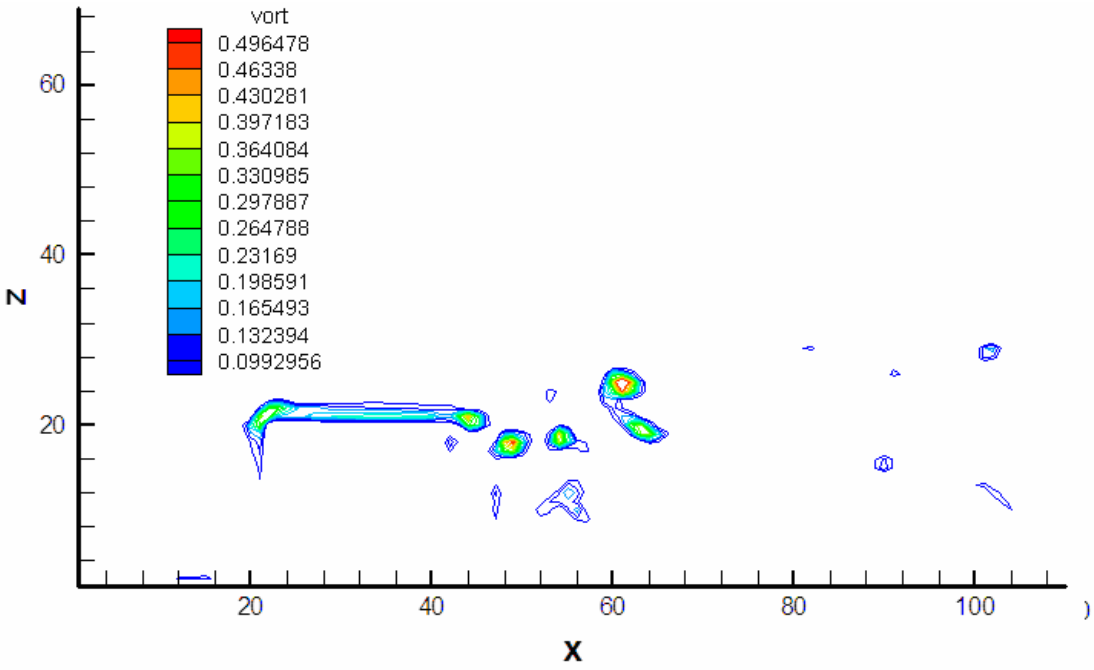

(b) Vorticity contours

Fig. 4-42 Velocity vector field and vorticity contours for the symmetry plane, 600 time steps

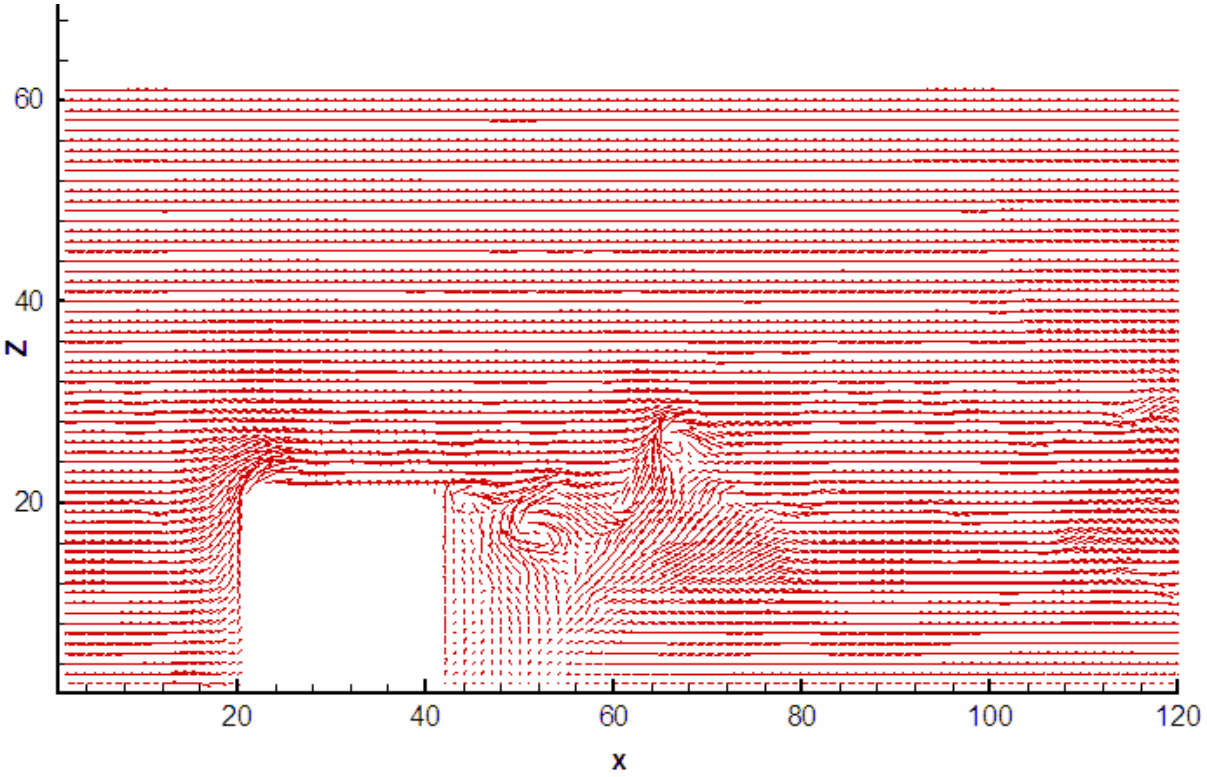

(a) Velocity vector field

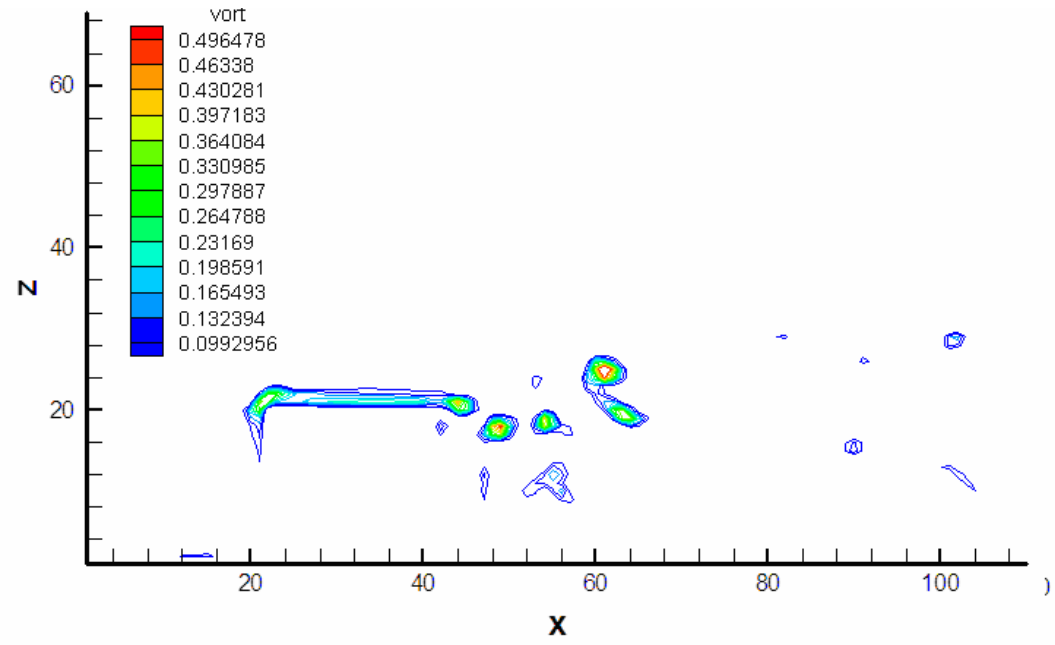

(b) Vorticity contours

Fig. 4-43 Velocity vector field and vorticity contours for the symmetry plane,700 time steps;

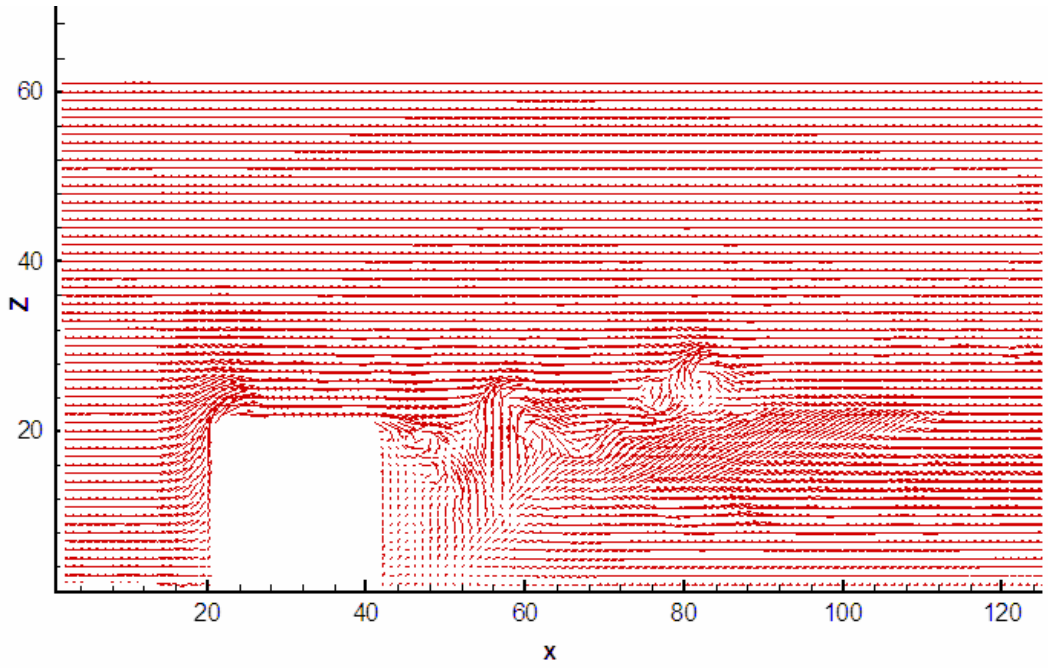

(a) Velocity vector field

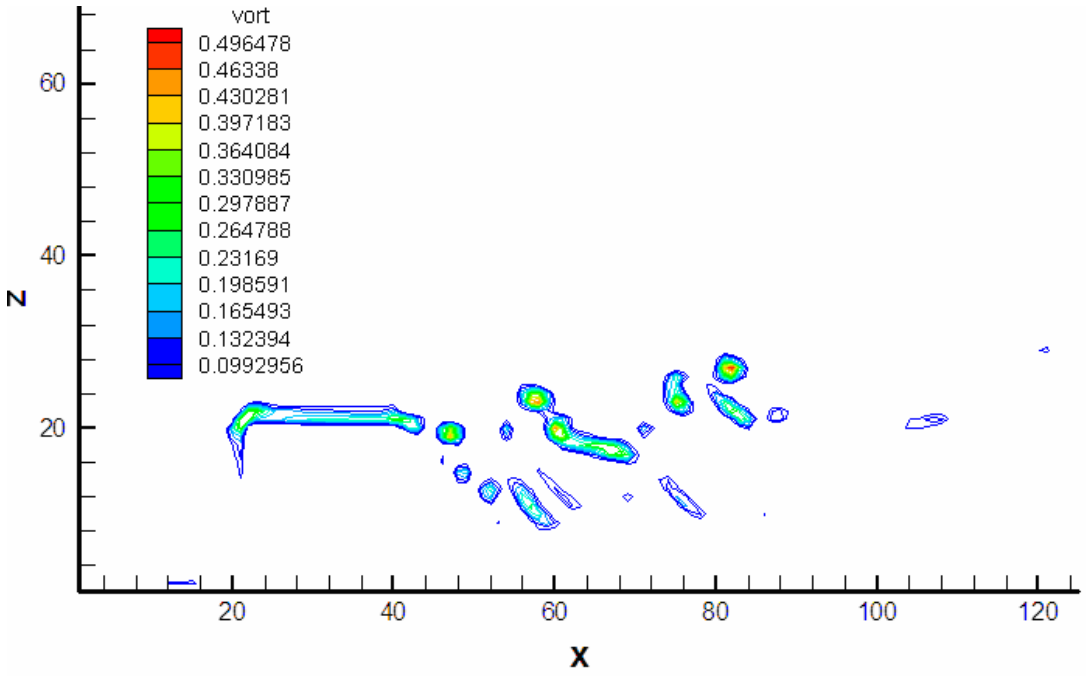

(b) Vorticity contours

Fig. 4-44 Velocity vector field and vorticity contours for the symmetry plane after 900 time steps

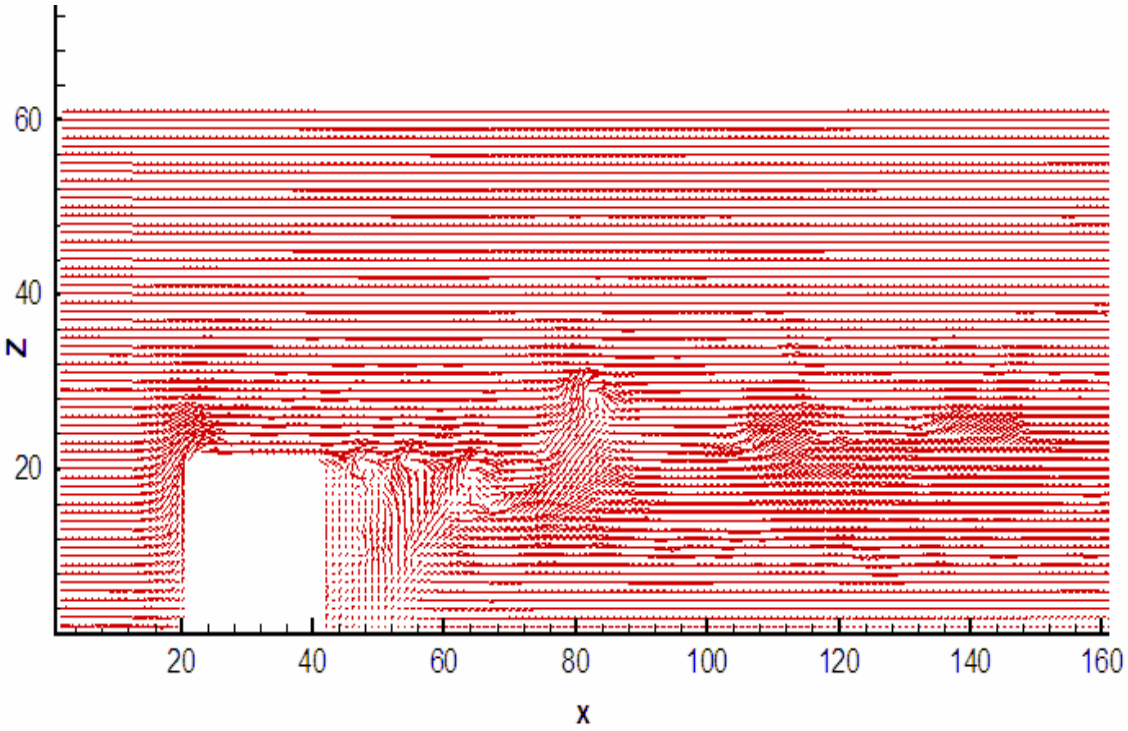

(a) Velocity vector field

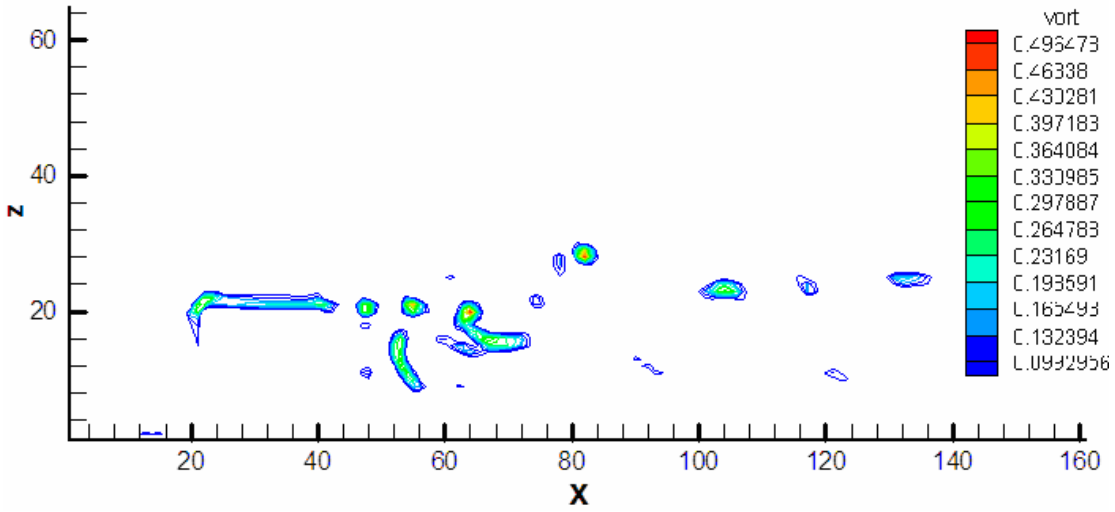

(b) Vorticity contours

Fig. 4-45 Velocity vector field and vorticity contours for the symmetry plane after 1200 time steps

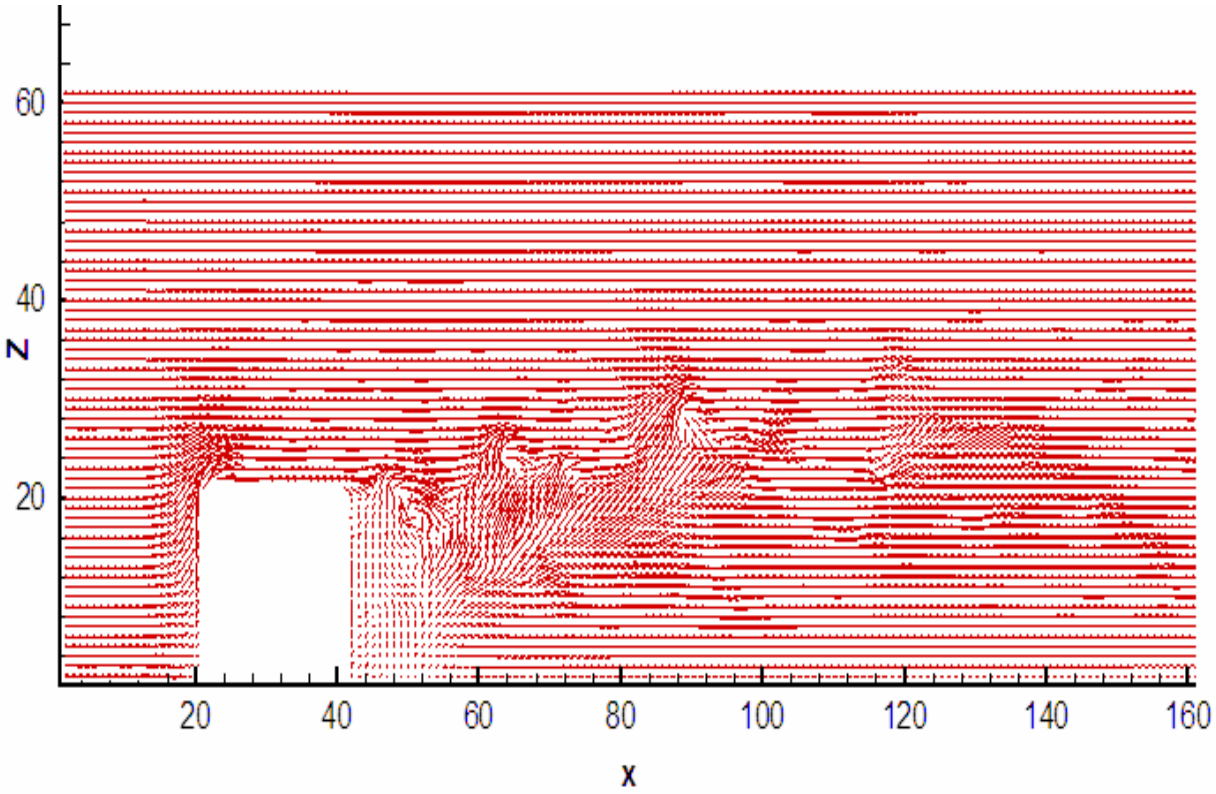

(a) Velocity vector field

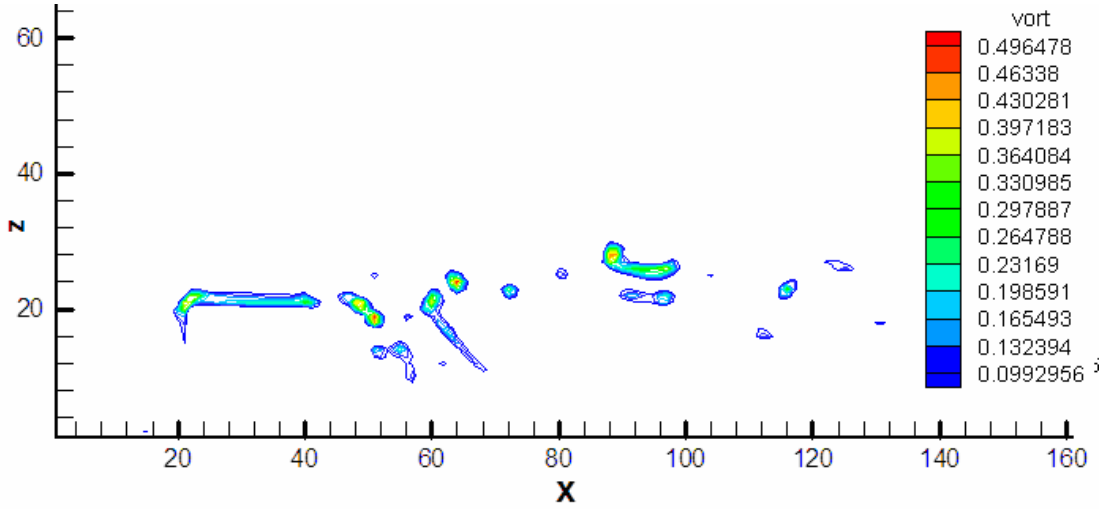

(b) Vorticity contours

Fig. 4-46 Velocity vector field and vorticity contours for the symmetry plane after 1600 time steps

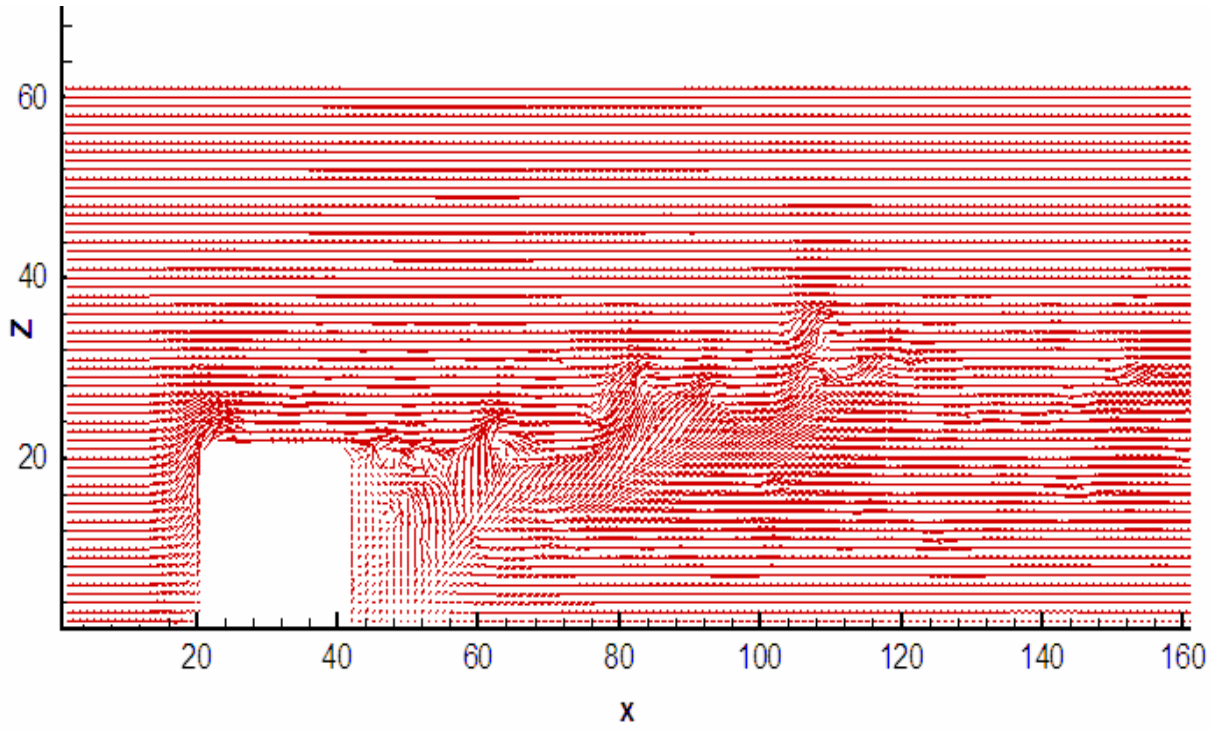

(a) Velocity vector field,

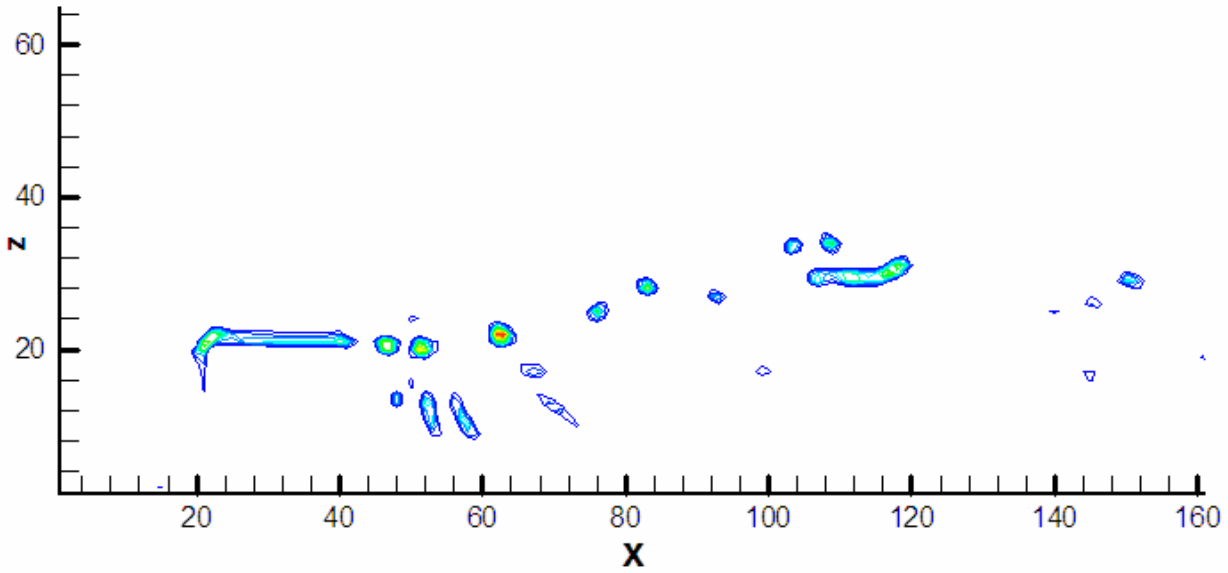

(b) Vorticity contours

Fig. 4-47 Velocity vector field and vorticity contours for the symmetry plane after 1800 time steps

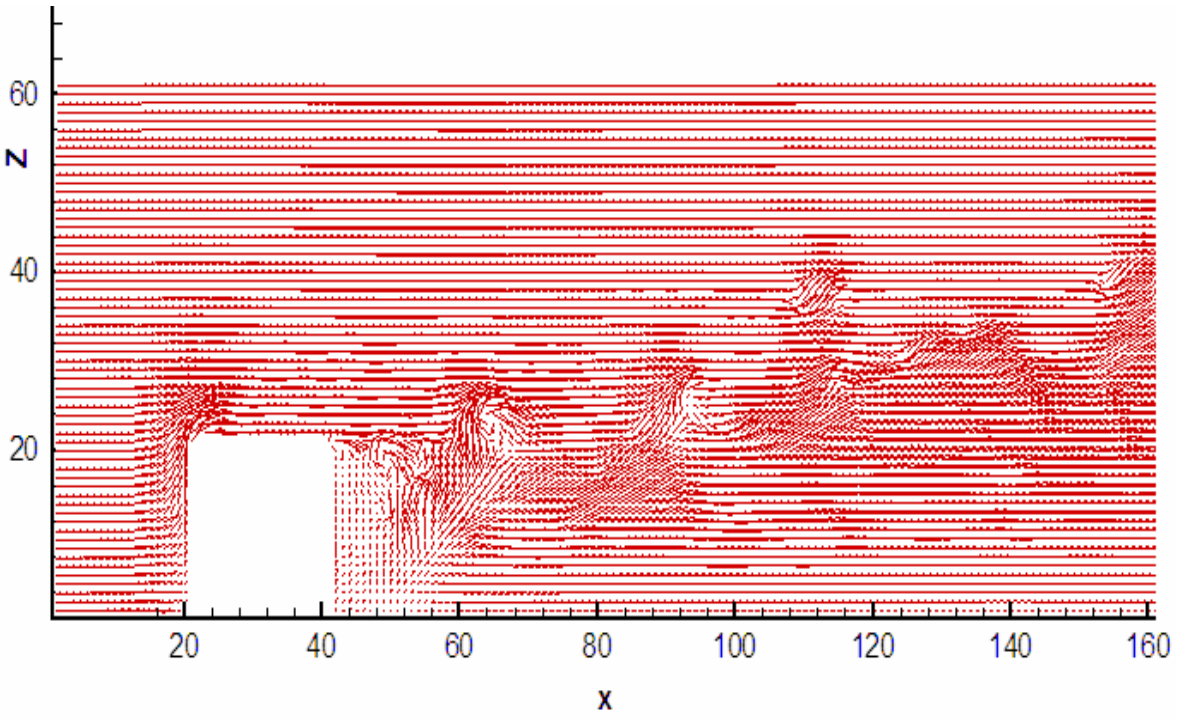

(a) Velocity vector field

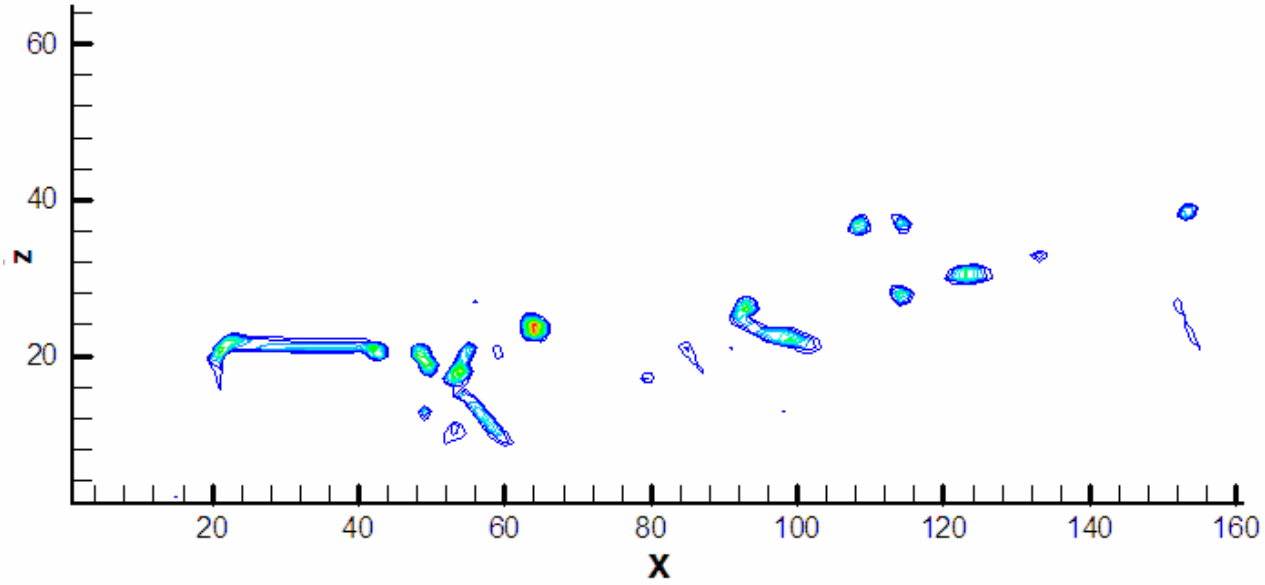

(b) Vorticity contours

Fig. 4-48 Velocity vector field and vorticity contours for the symmetry plane, 3000 time steps

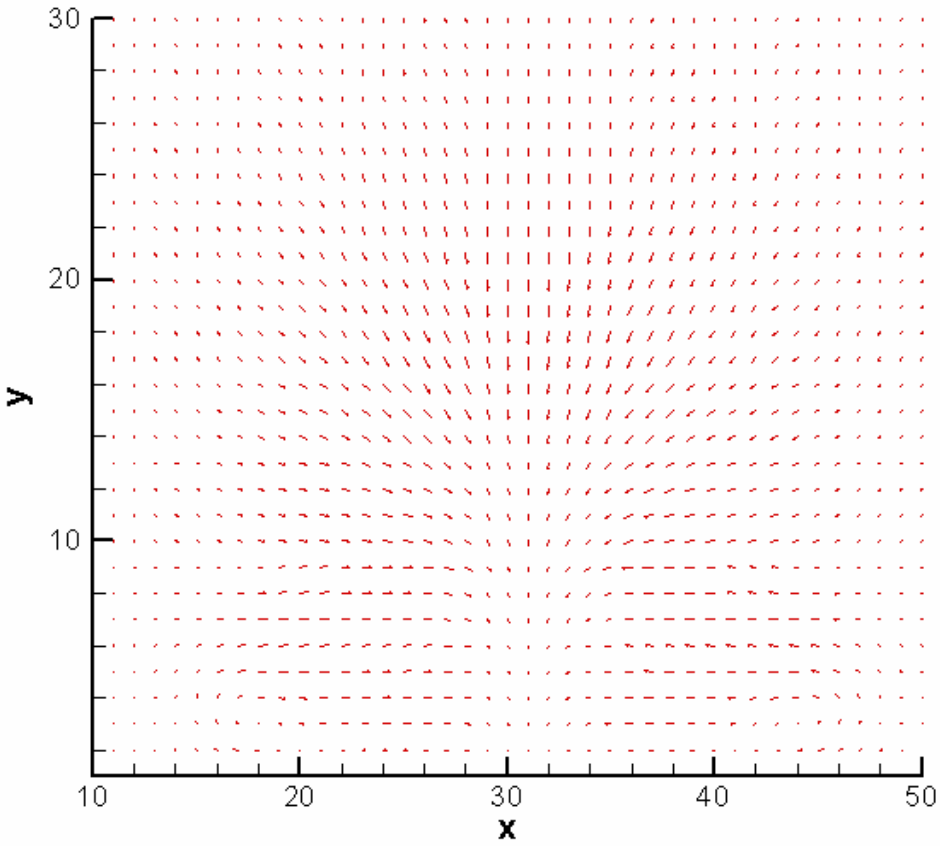

Fig. 4-49 Velocity vector field for the span-wise plane, x=50, after 50 time steps

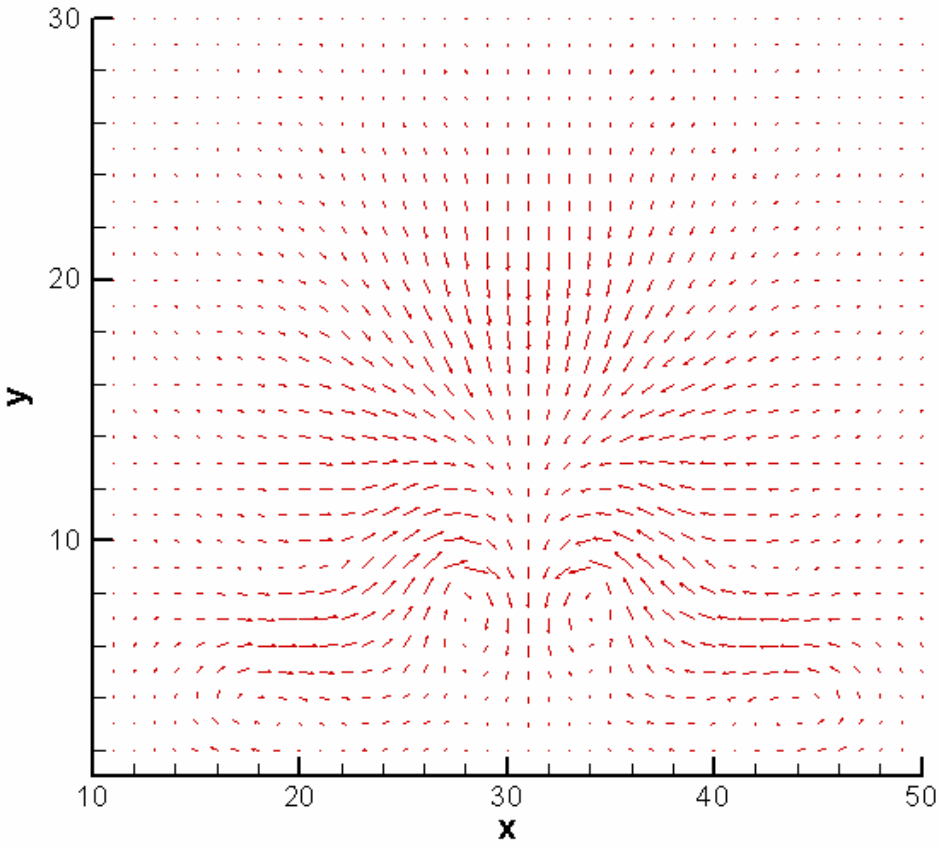

Fig. 4-50 Velocity vector field for the span-wise plane, x=50, after 120 time steps

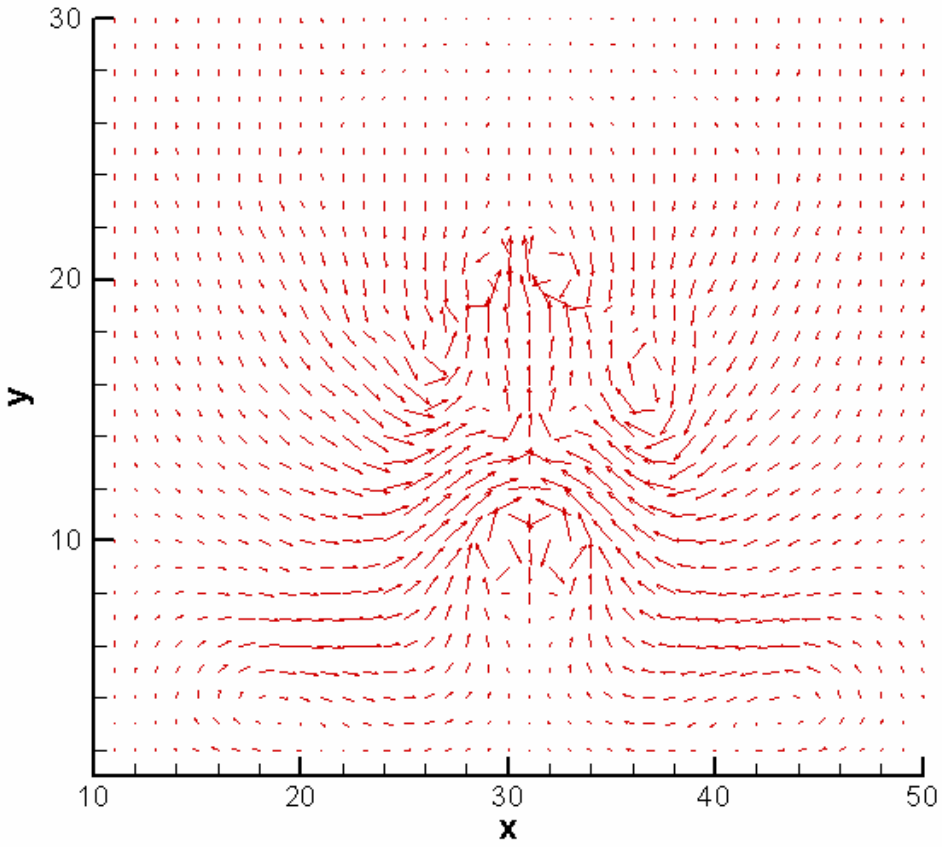

(a) Velocity vector field

Fig. 4-51 Velocity vector field and vorticity contours for the span-wise plane, x=50, after 300 time steps

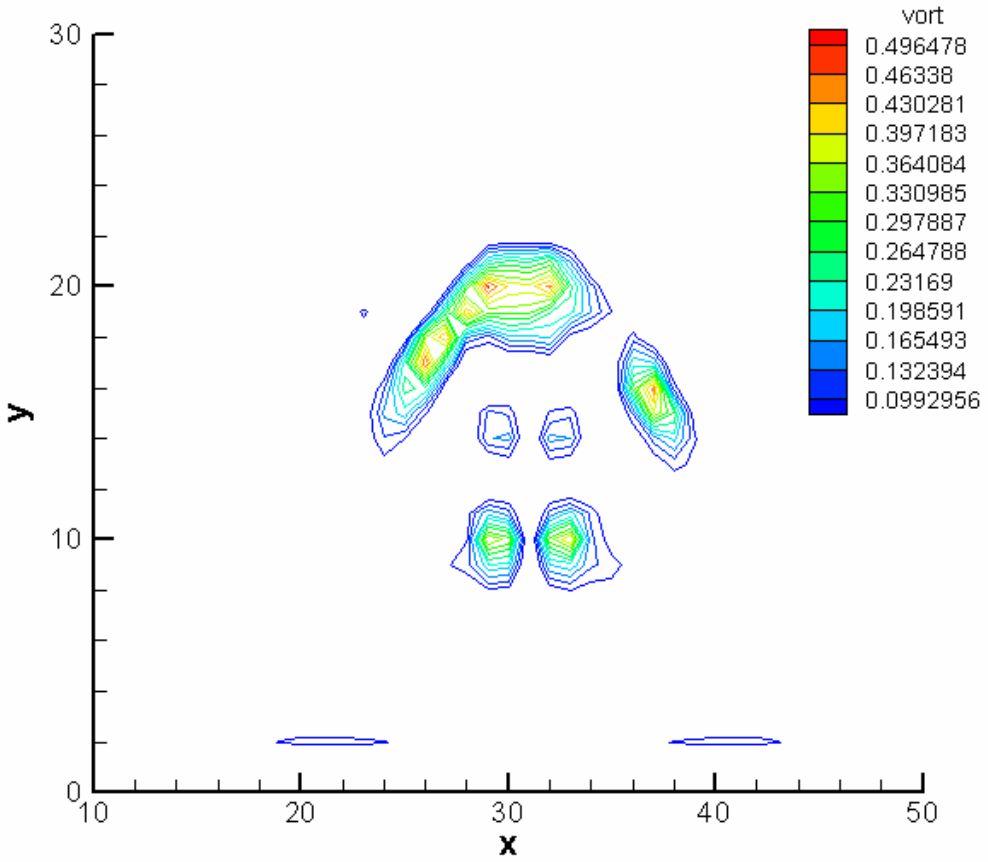

(b) Vorticity contours
Fig. 4-51 Continued

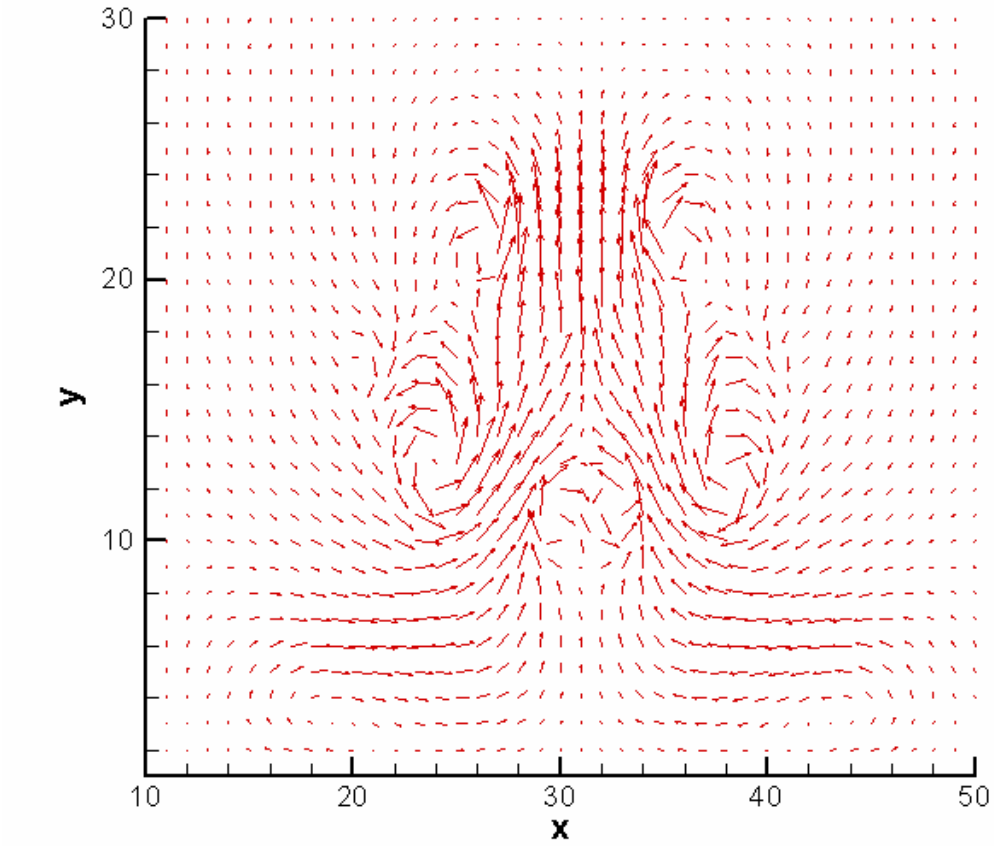

(a) Velocity vector field

Fig. 4-52 Velocity vector field and vorticity contours for the span-wise plane, x=50, after 400 time steps

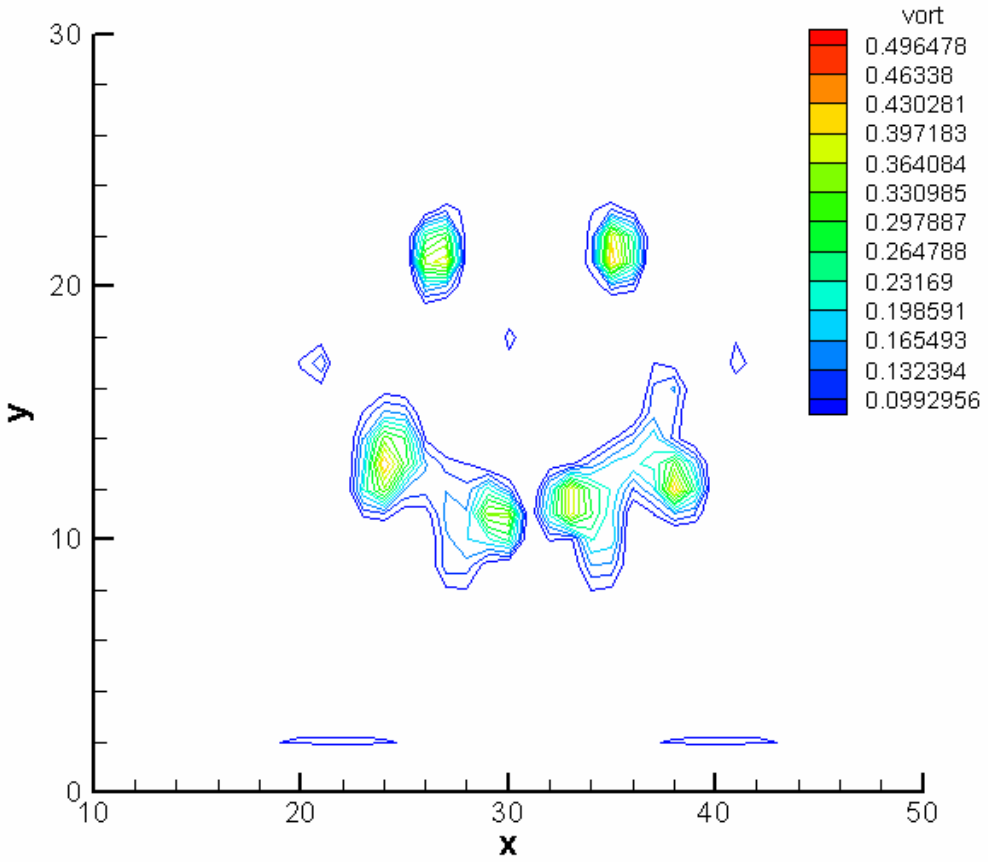

(b) Vorticity contours

Fig. 4-52 Continued

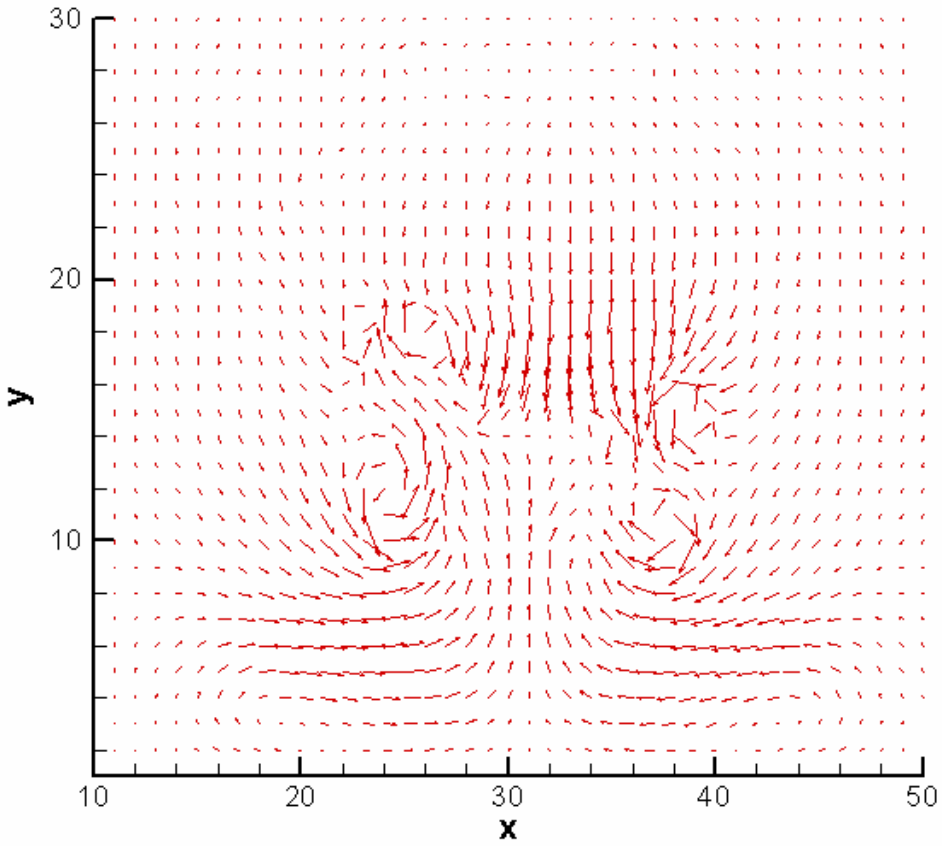

(a) Velocity vector field

Fig. 4-53 Velocity vector field and vorticity contours for the span-wise plane, x=50, after 600 time steps

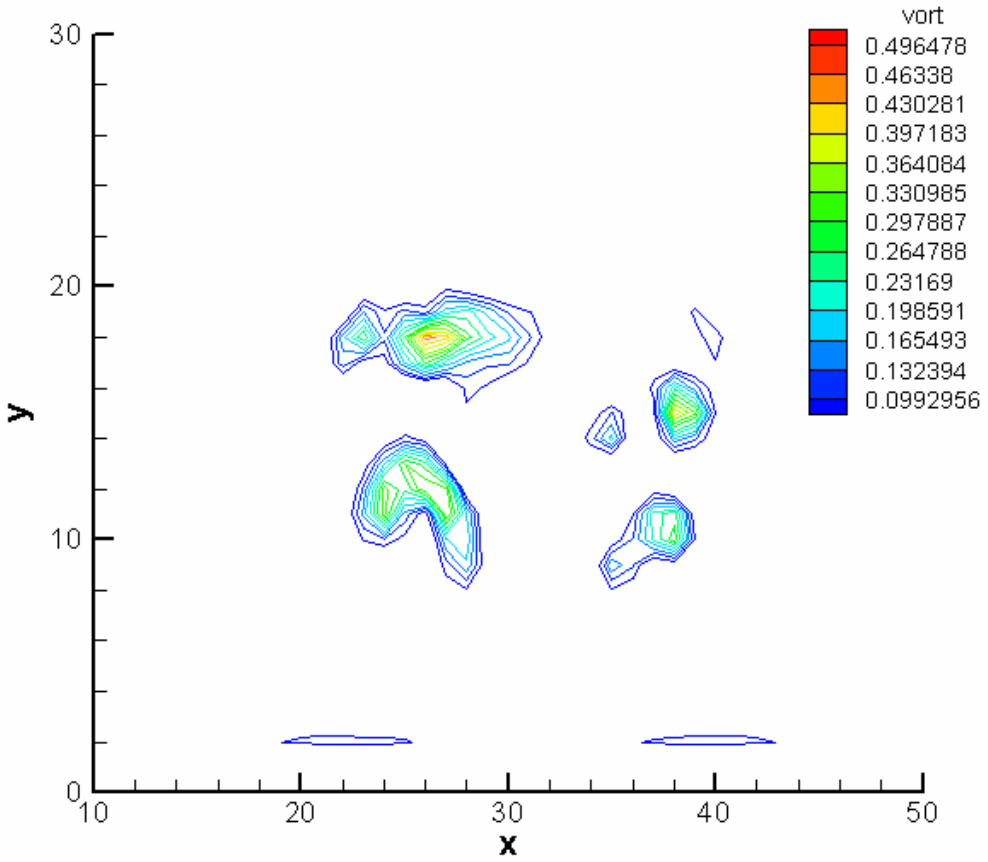

(b) Vorticity contours

Fig. 4-53 Continued

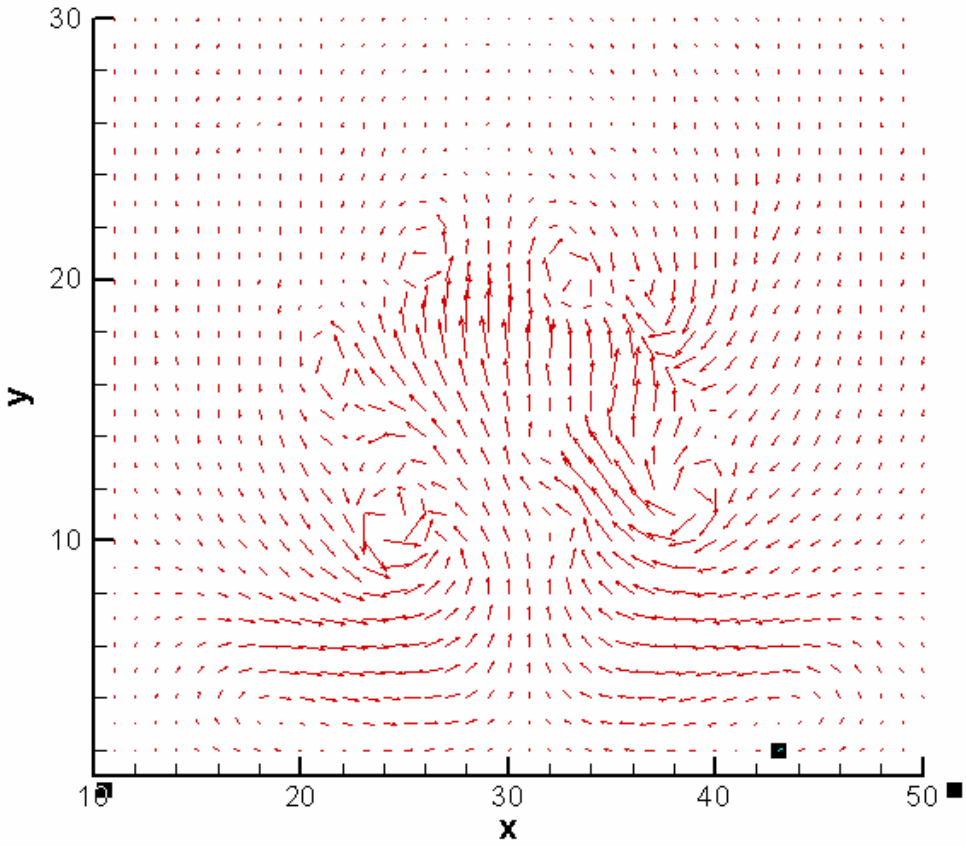

(a) Velocity vector field

Fig. 4-54 Velocity vector field and vorticity contours for the span-wise plane, x=50, after 700 time steps

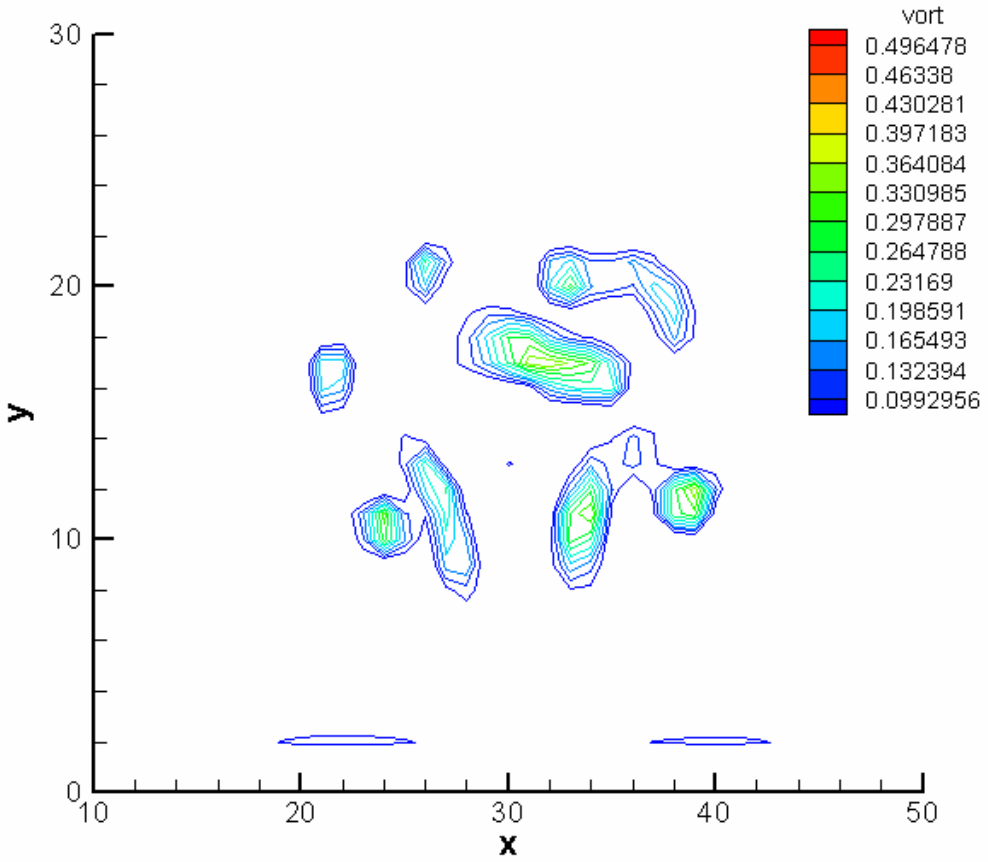

(b) Vorticity contours
Fig. 4-54 Continued

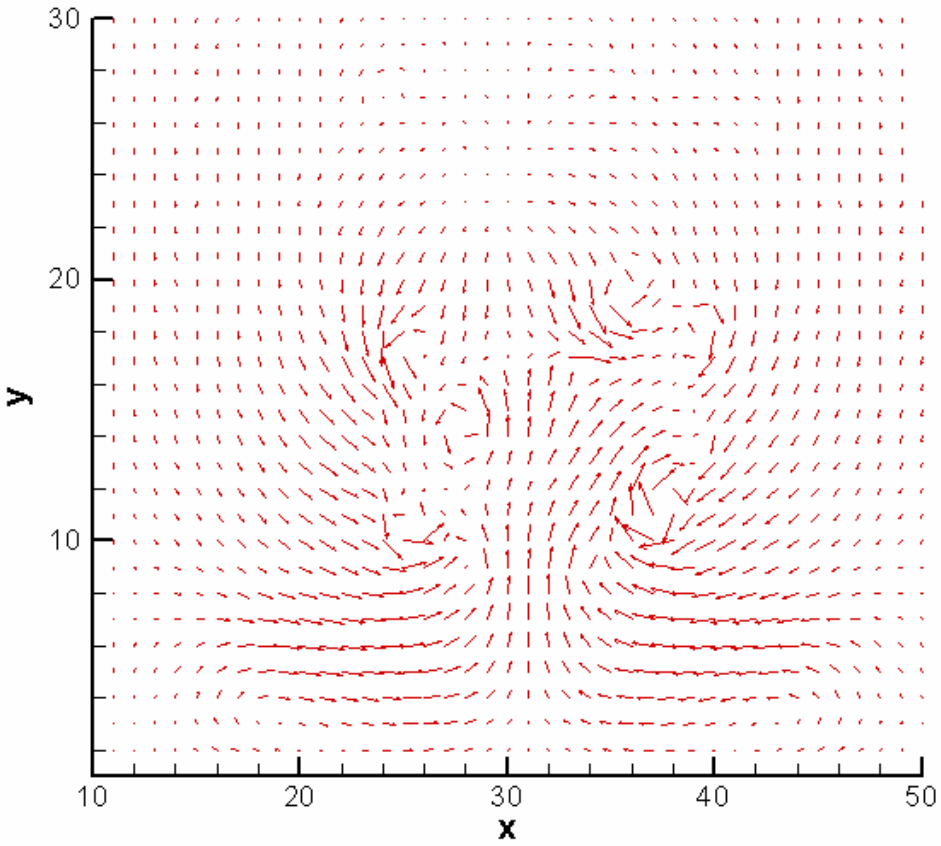

(a) Velocity vector field

Fig. 4-55 Velocity vector field and vorticity contours for the span-wise plane, x=50, after 900 time steps

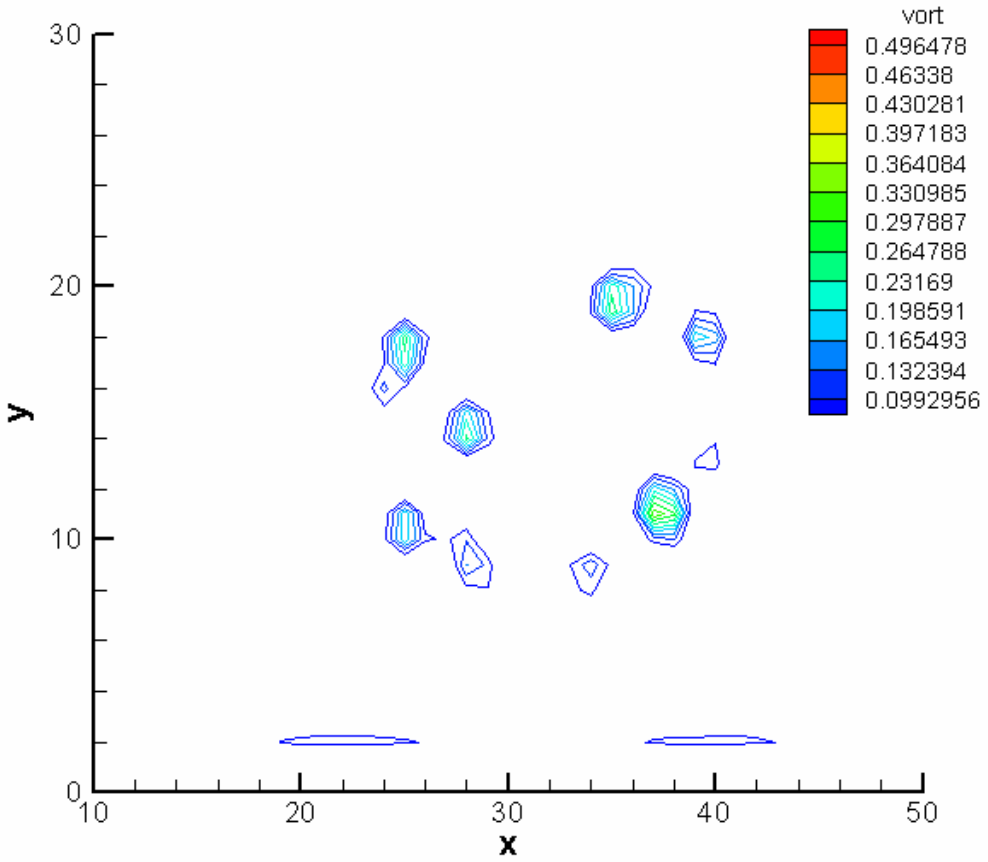

(b) Vorticity contours
Fig. 4-55 Continued

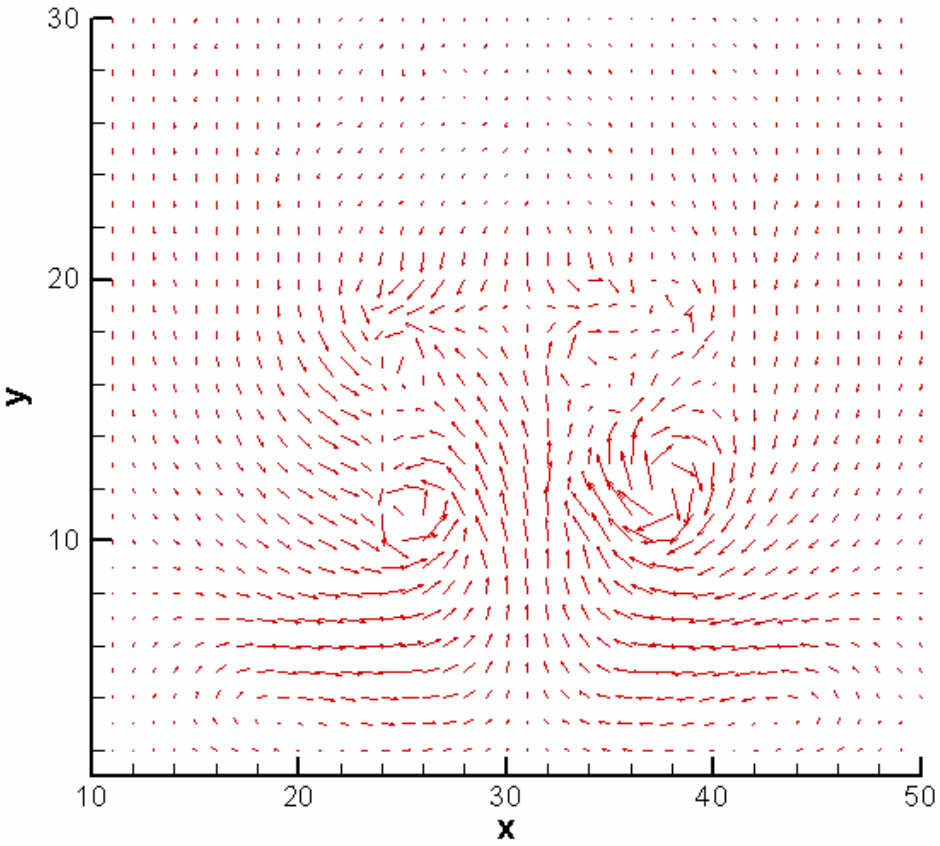

(a) Velocity vector field

Fig. 4-56 Velocity vector field and vorticity contours for the span-wise plane, x=50, after 1200 time steps

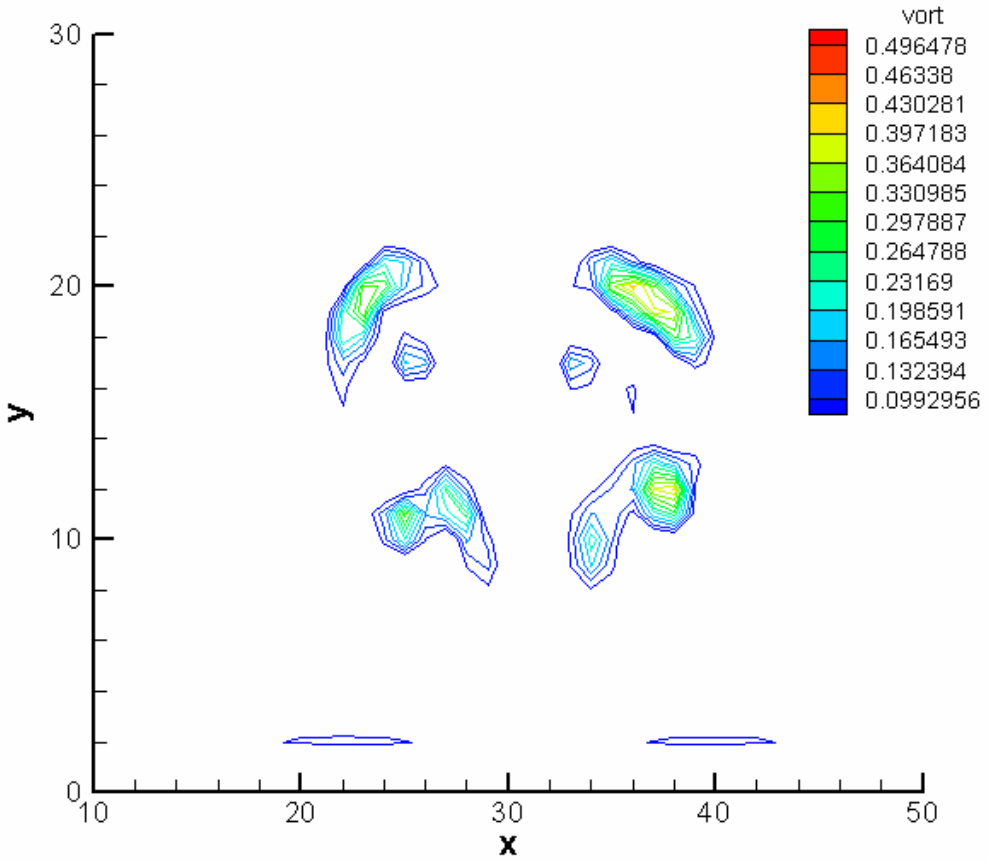

(b) Vorticity contours
Fig. 4-56 Continued

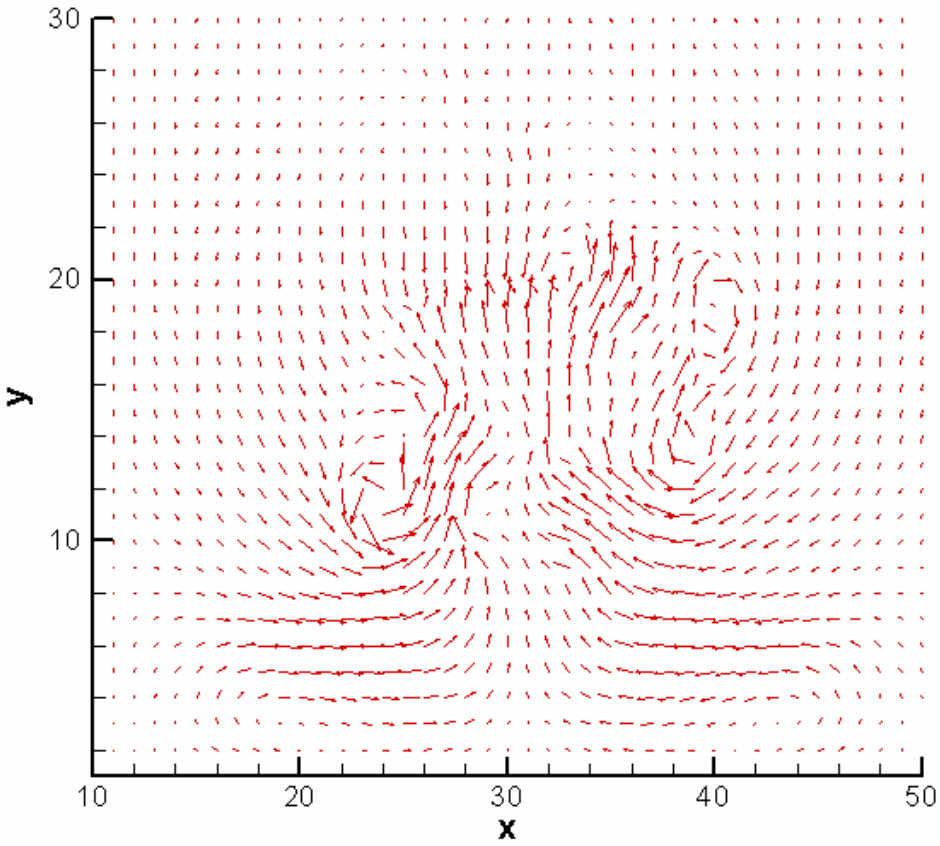

(a) Velocity vector field

Fig. 4-57 Velocity vector field and vorticity contours for the span-wise plane, x = 50, after 1600 time steps

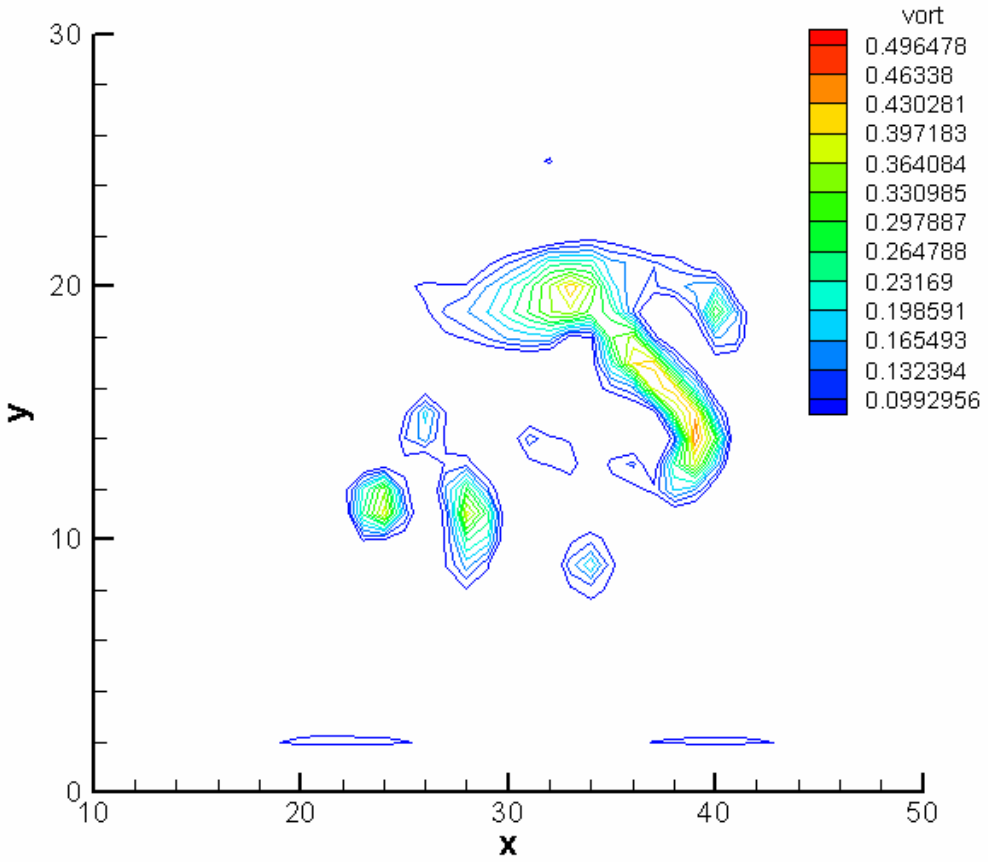

(b) Vorticity contour
Fig. 4-57 Continued

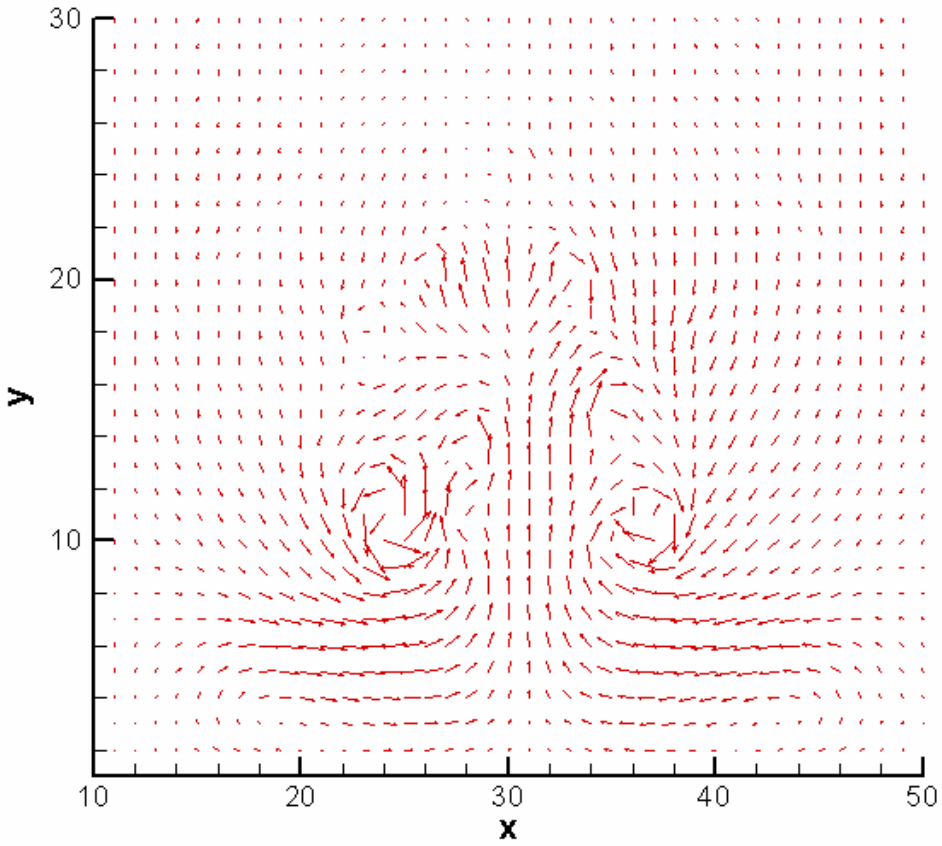

(a) Velocity vector field

Fig. 4-58 Velocity vector field and vorticity contours for the span-wise plane, x=50, after 1800 time steps

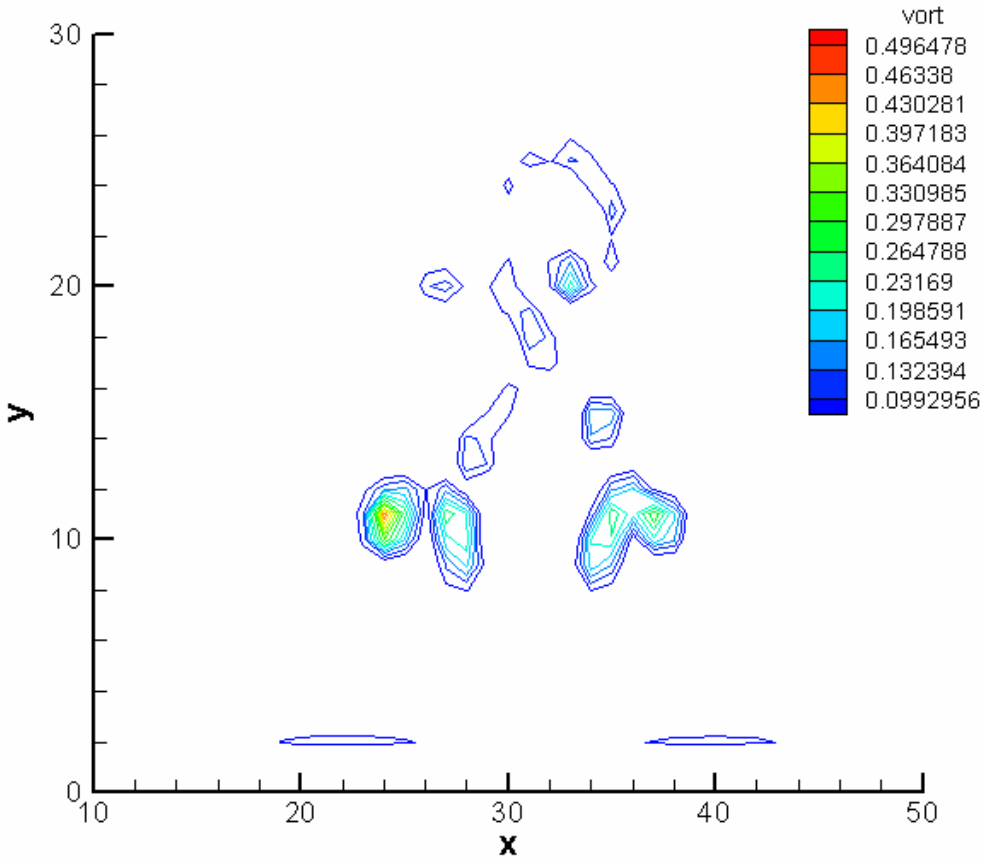

(b) Vorticity contours
Fig. 4-58 Continued

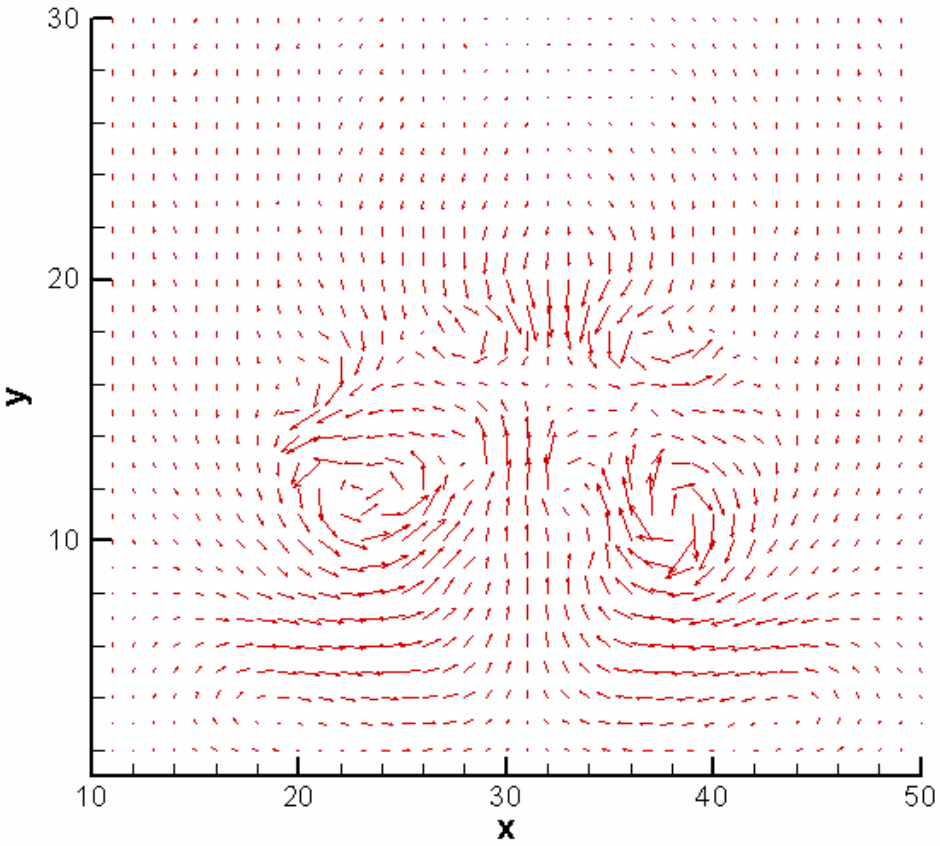

(a) Velocity vector field

Fig. 4-59 Velocity vector field and vorticity contours for the span-wise plane, x=50, after 3000 time steps

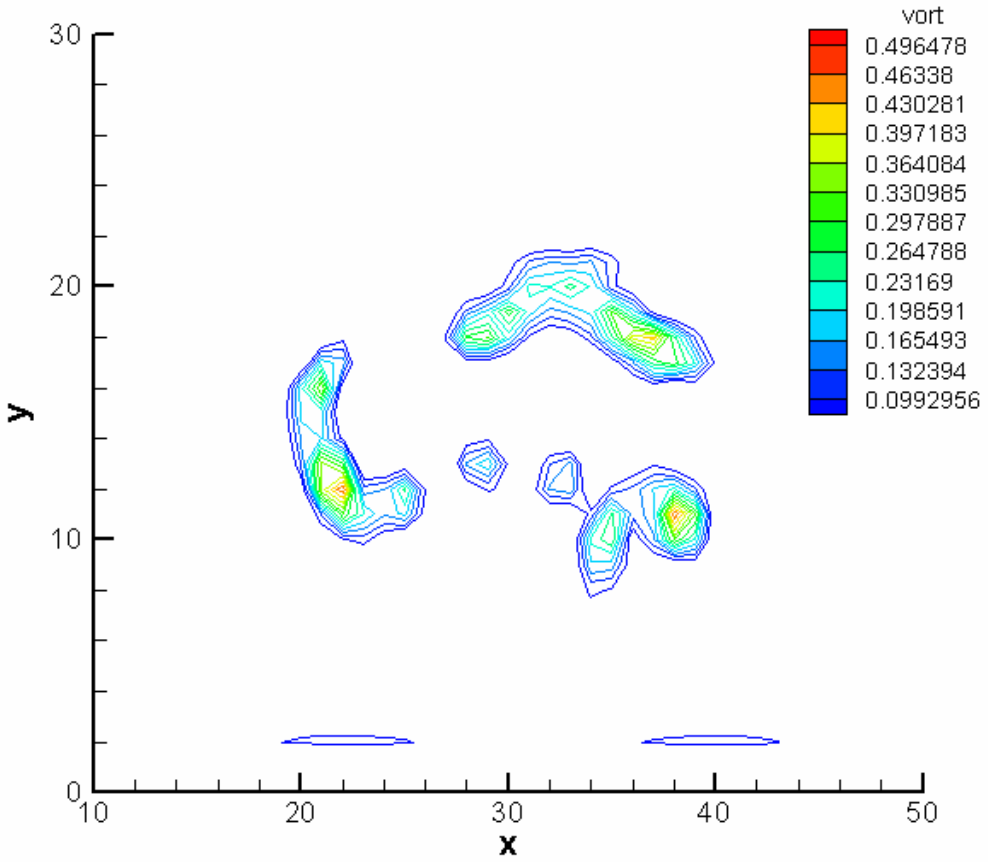

(b) Vorticity contours

Fig. 4-59 Continued

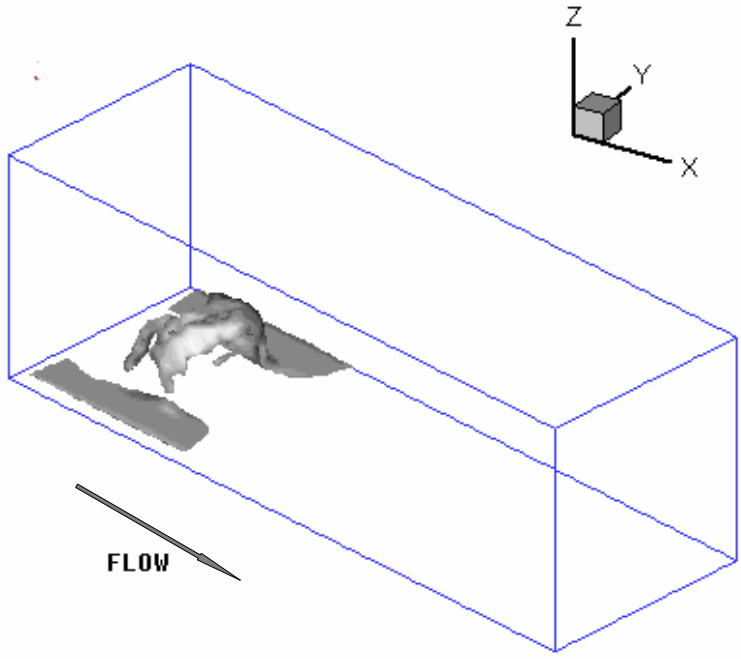

Fig. 4-60 Vorticity iso-surface, after 50 time steps, 6x6x6 cube

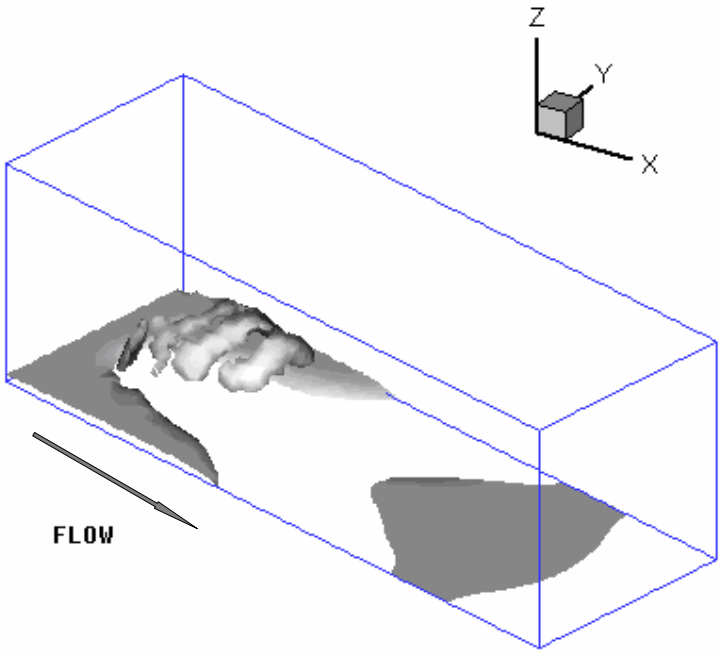

Fig. 4-61 Vorticity iso-surface, after 100 time steps, 6x6x6 cube

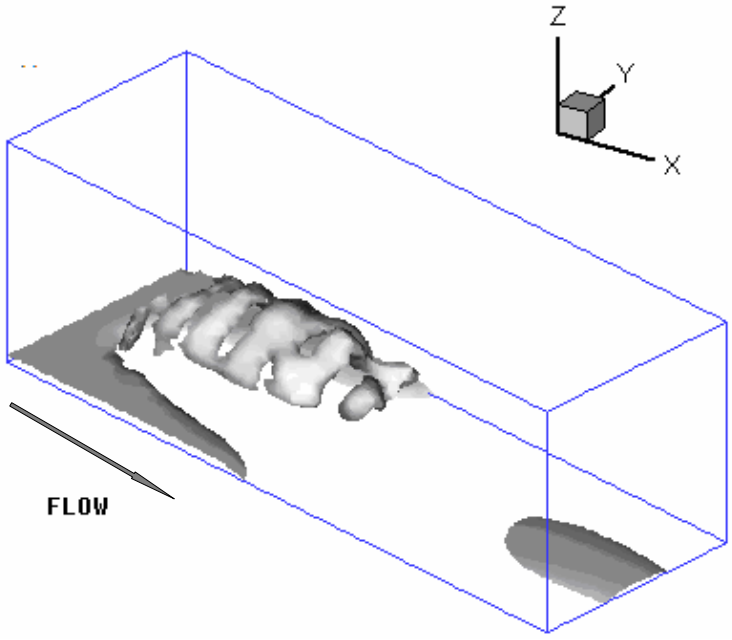

Fig. 4-62 Vorticity iso-surface, after 400 time step, 6x6x6 cube

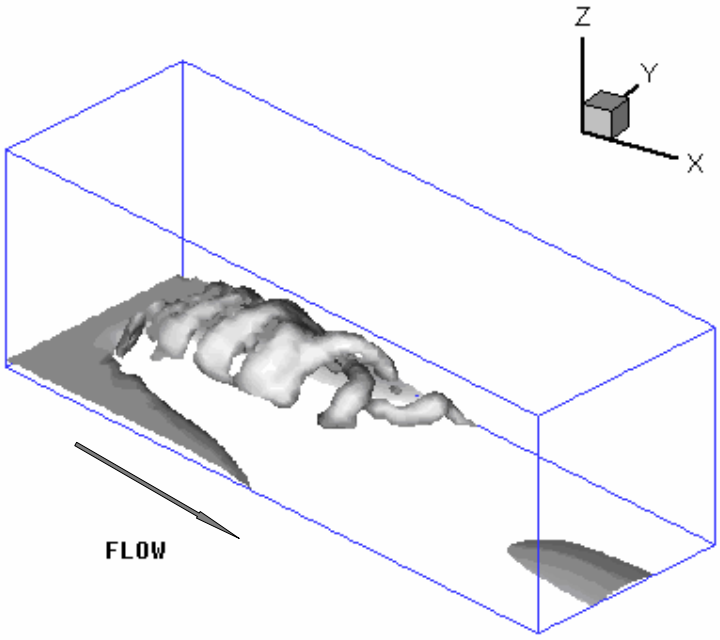

Fig. 4-63 Vorticity iso-surface, after 950 time step, 6x6x6 cube

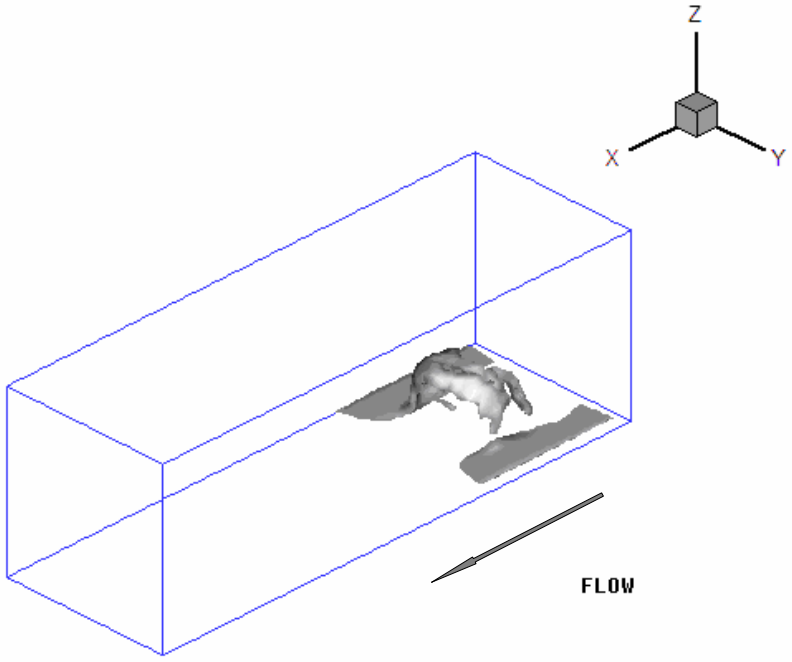

Fig. 4-64 Vorticity iso-surface from the different viewing angle, after 50 time steps

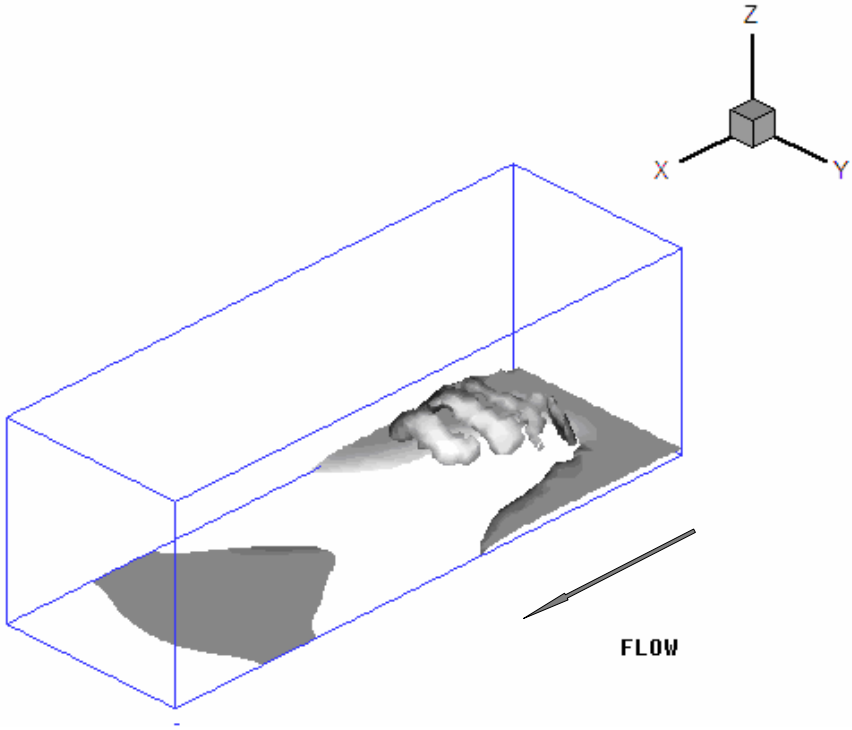

Fig. 4-65 Vorticity iso-surface from the different viewing angle, after100 time steps

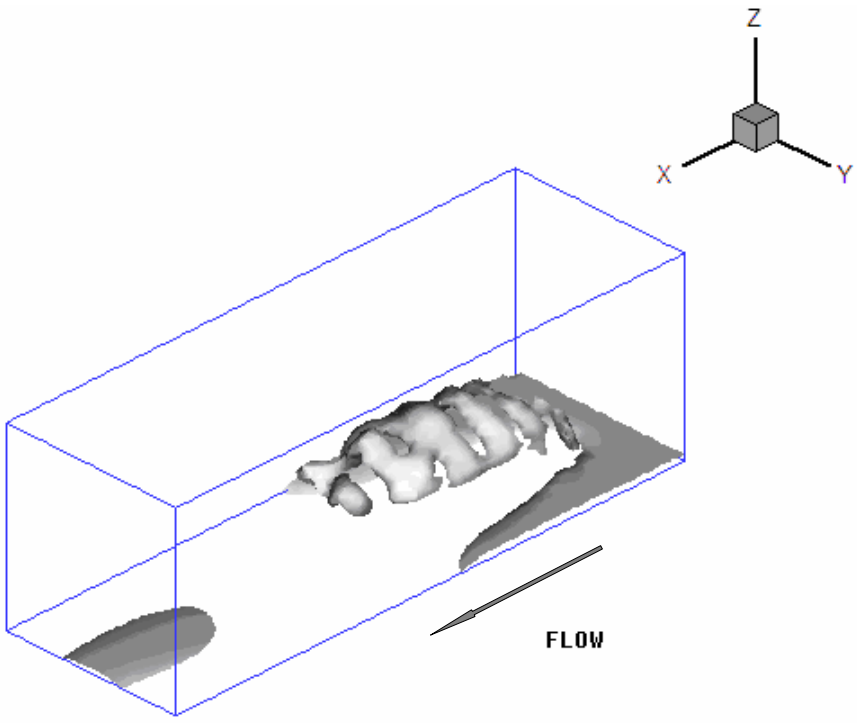

Fig. 4-66 Vorticity iso-surface from the different viewing angle, after 400 time steps

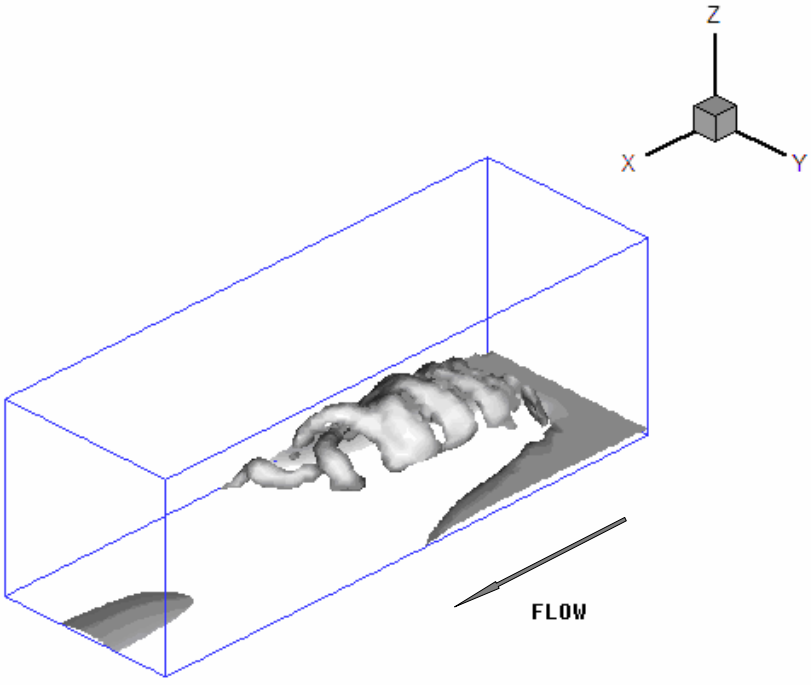

Fig. 4-67 Vorticity iso-surface from the different viewing angle, after 950 time steps

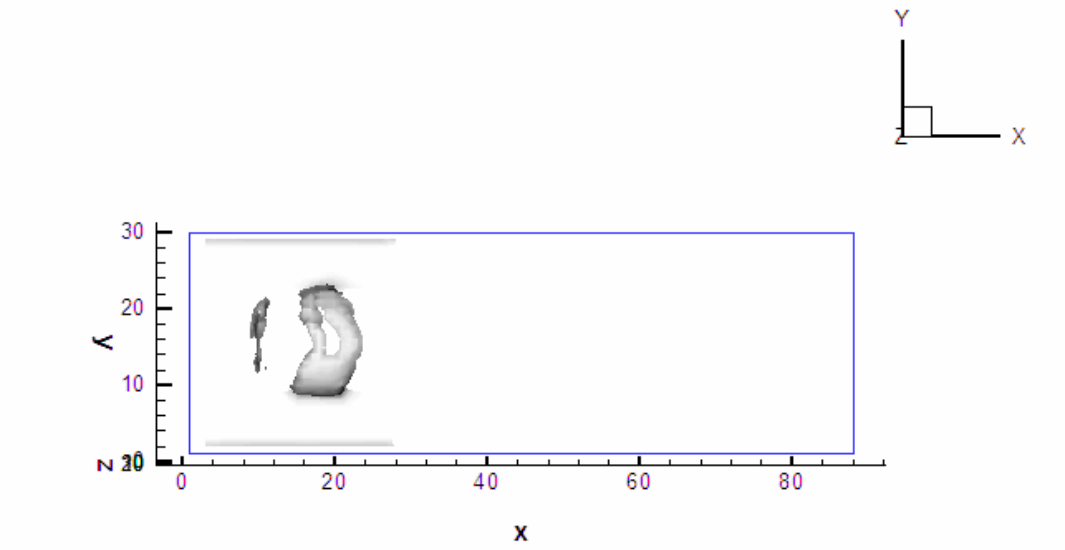

(a) 50 time steps

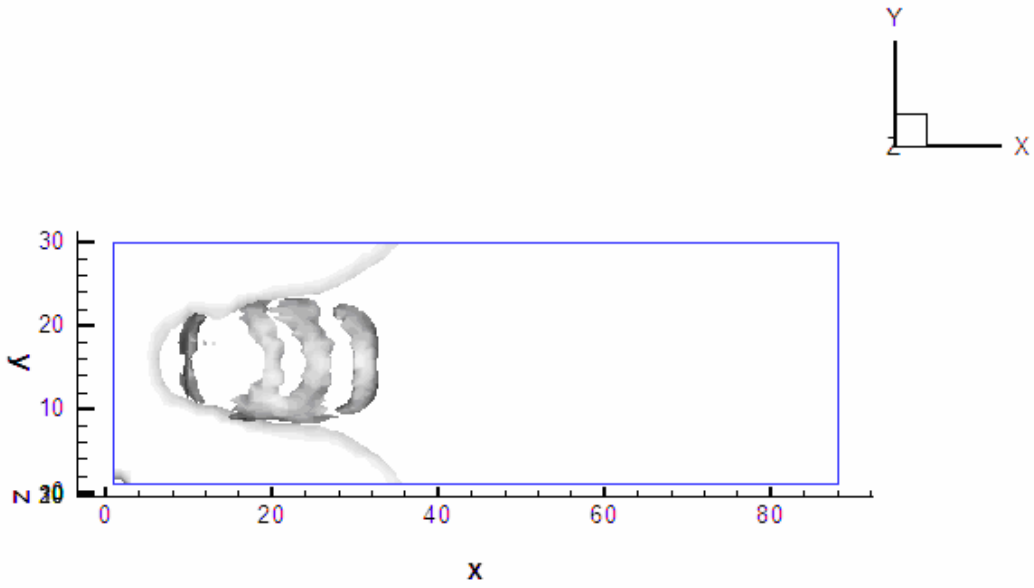

(b) 100 time steps

Fig. 4-68 Vorticity iso-surface, top views in a sequence of time steps

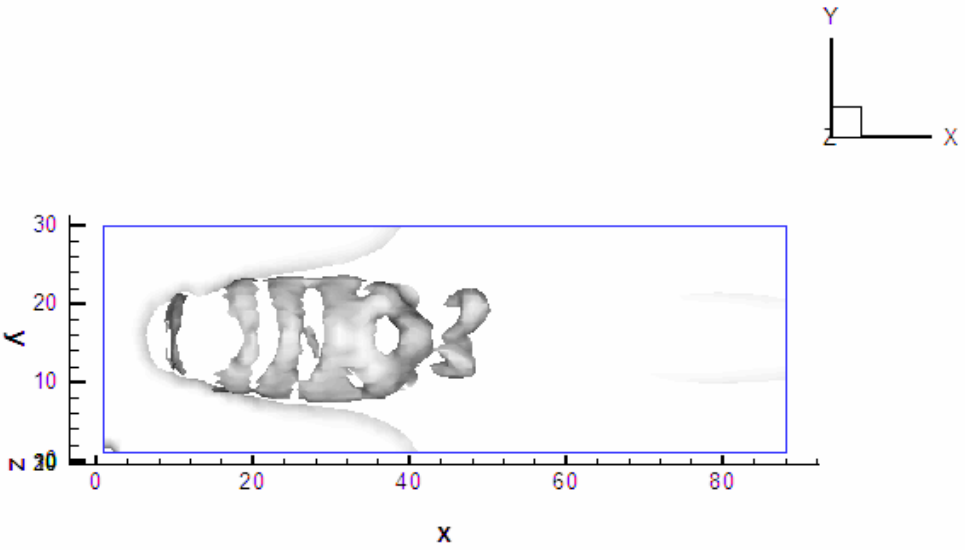

(c) 400 time steps

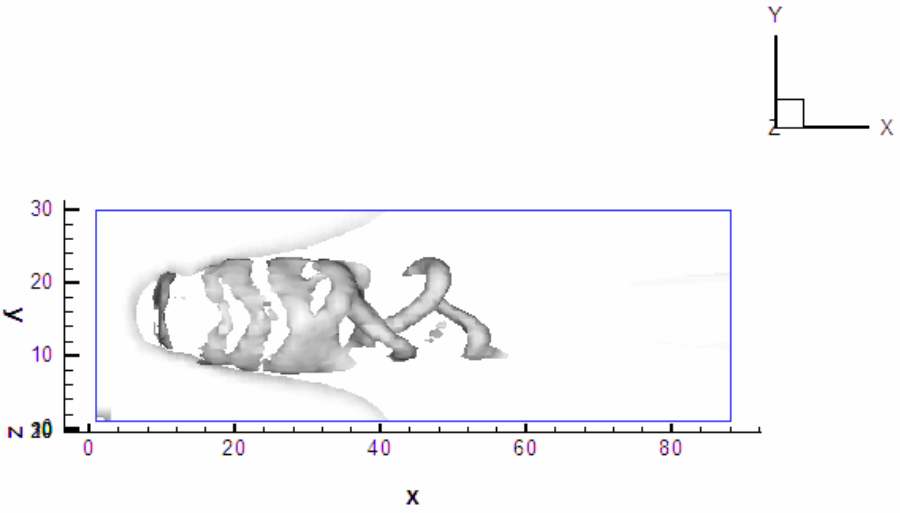

(d)950 time steps

Fig. 4-68 Continued

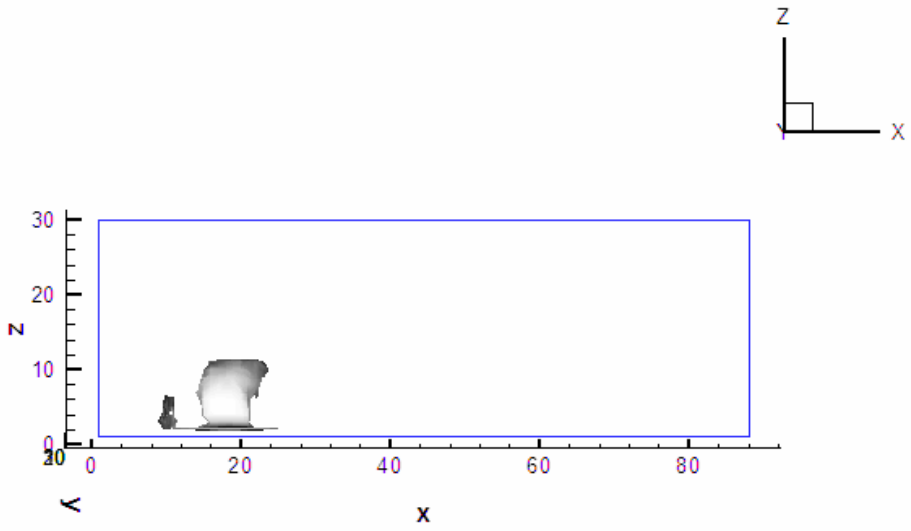

(a) 50 time steps

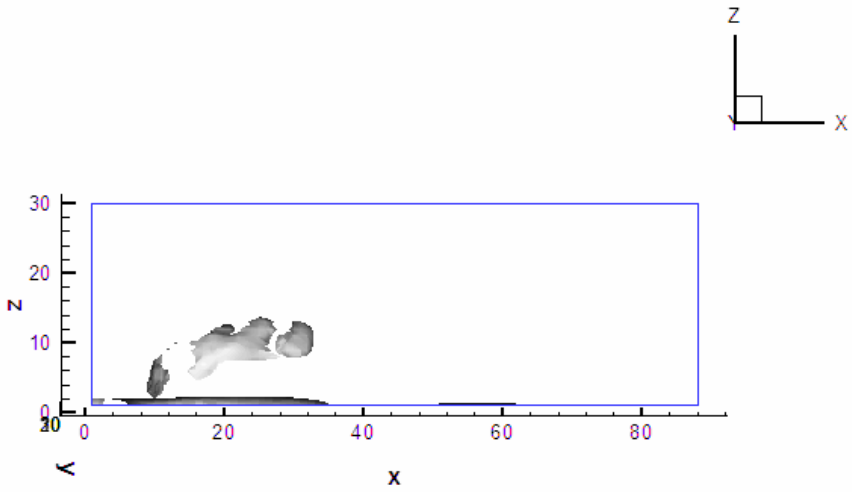

(b) 100 time steps

Fig. 4-69 Vorticity iso-surface, side- views in a sequence of time steps

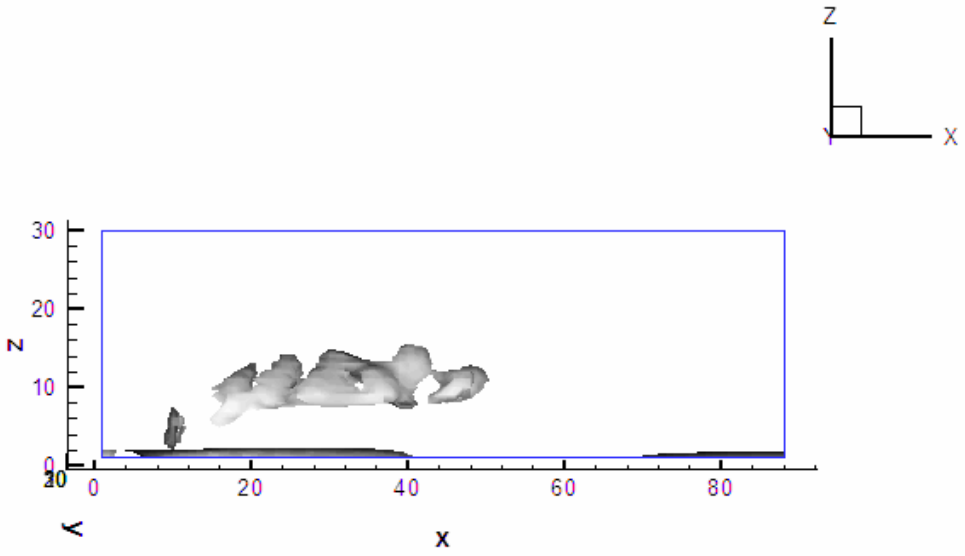

(c) 400 time steps

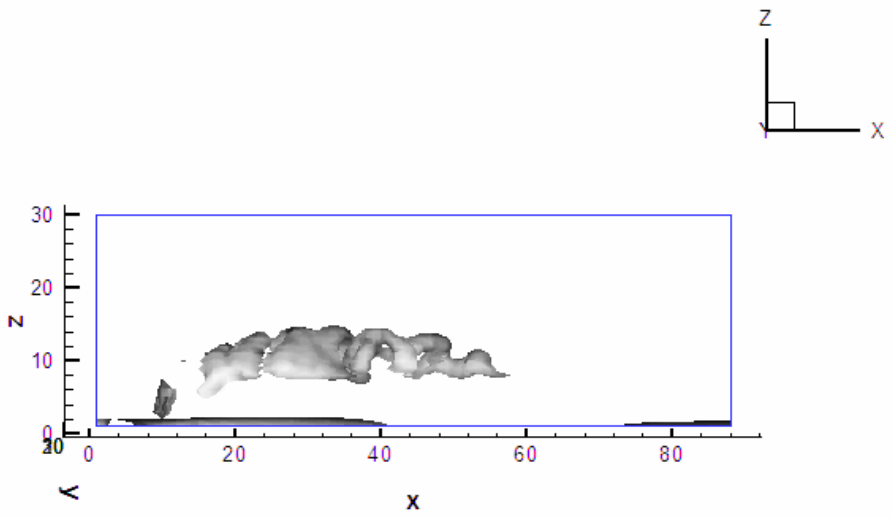

(d) 950 time steps

Fig. 4-69 Continued

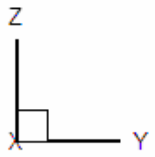

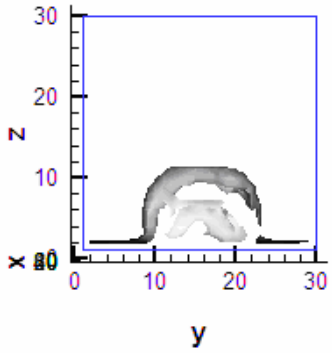

(a) 50 time step

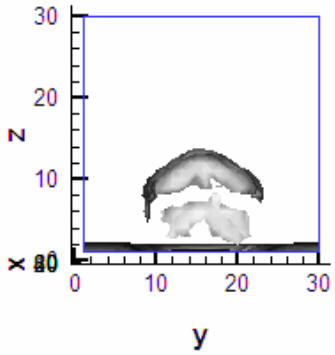

(b) 100 time steps

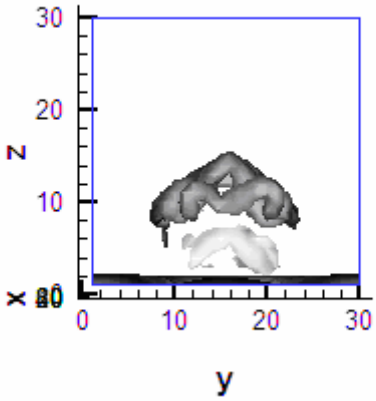

(c) 400 time steps

Fig. 4-70 Vorticity iso-surface, end-views in a sequence of time steps

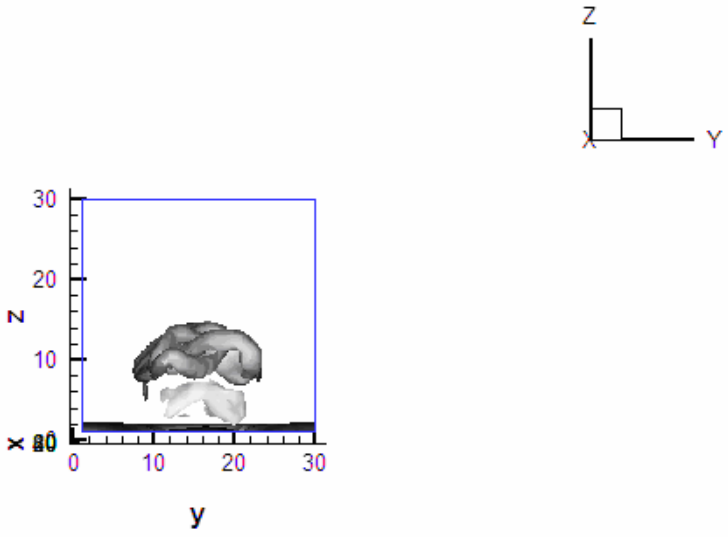

(d)950 time steps

Fig. 4-70 Continued

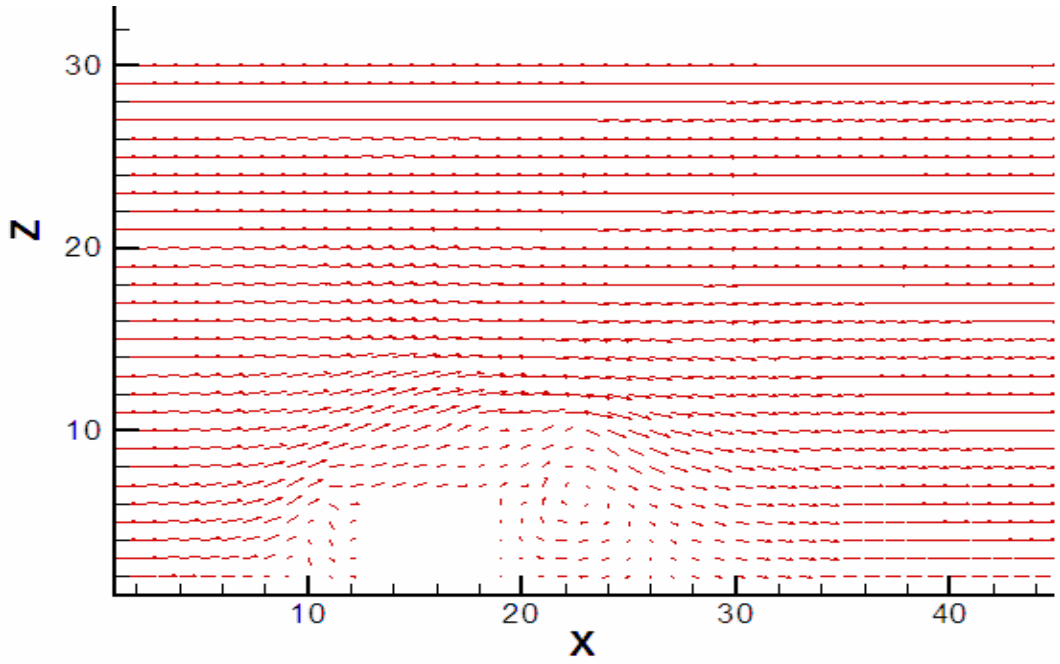

(a) Velocity vector field

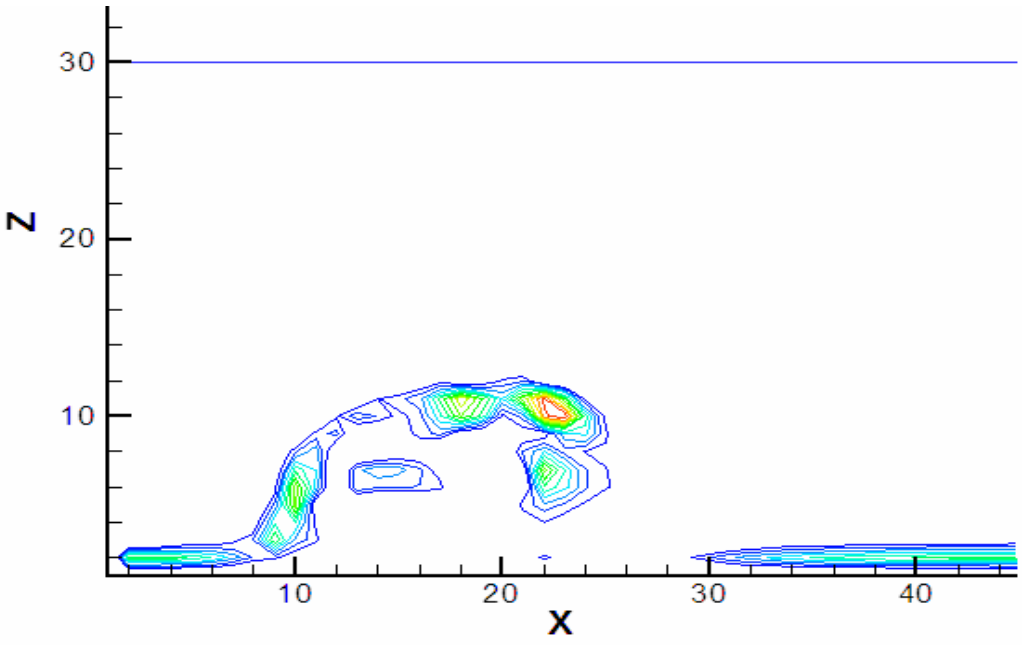

(b) Vorticity contours

Fig. 4-71 Velocity vector field and vorticity contours for the symmetry plane after 50 time steps

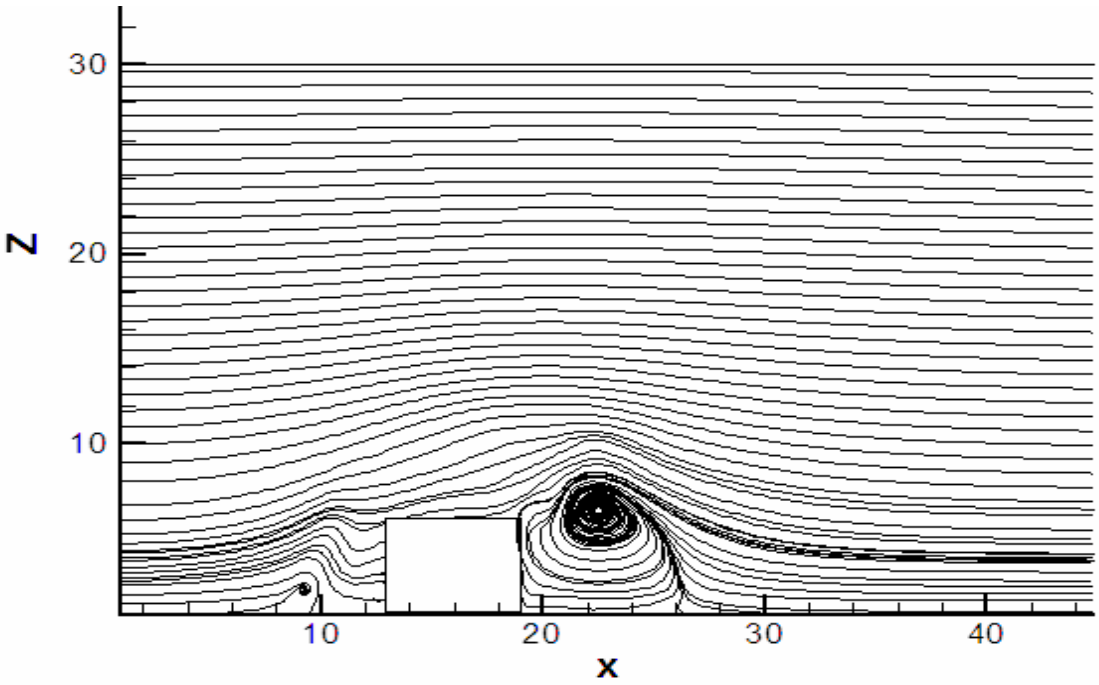

Fig. 4-72 Velocity streamlines for the symmetry plane after 50 time steps

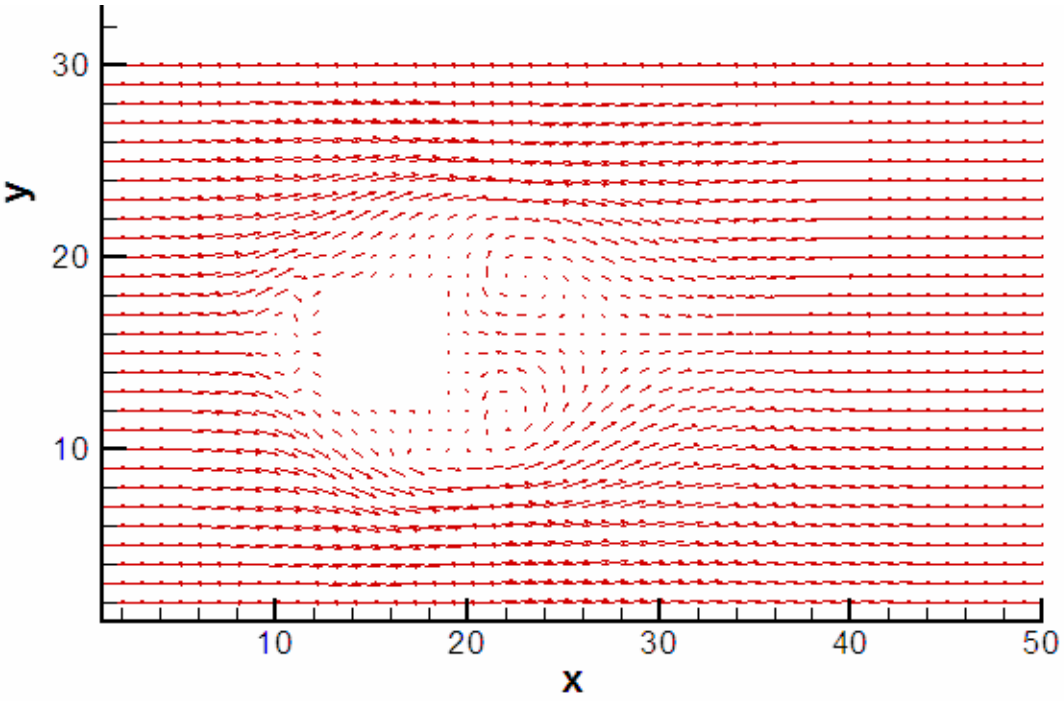

(a) Velocity vector field

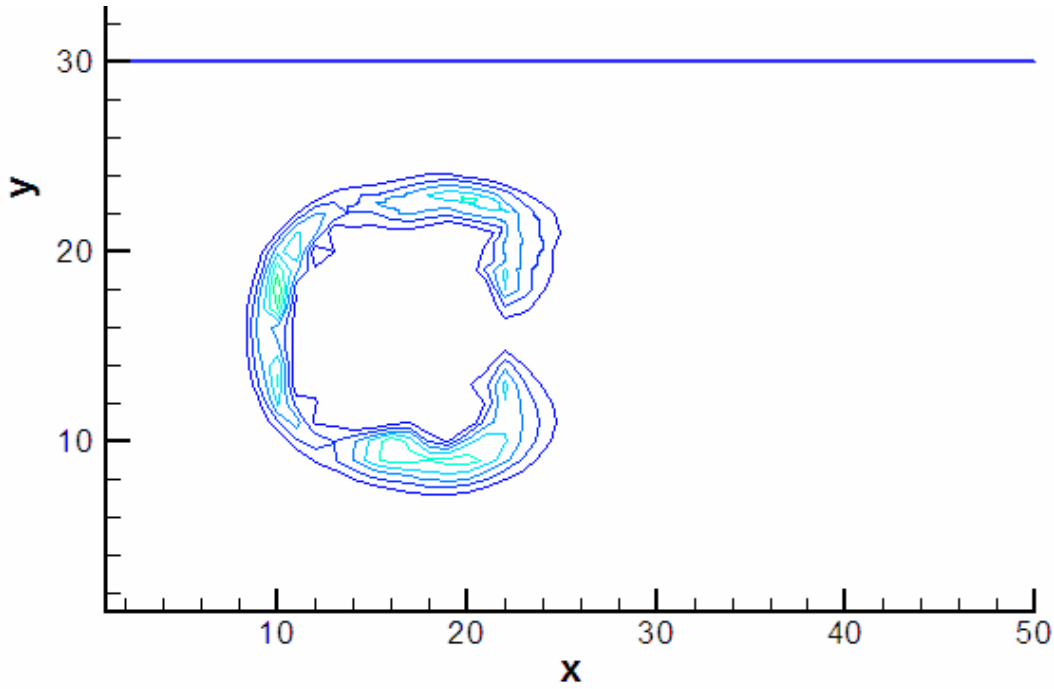

(b) Vorticity contours

Fig. 4-73 Velocity vector field and vorticity contours for the plane parallel to the surface, z=2, after 50 time steps;

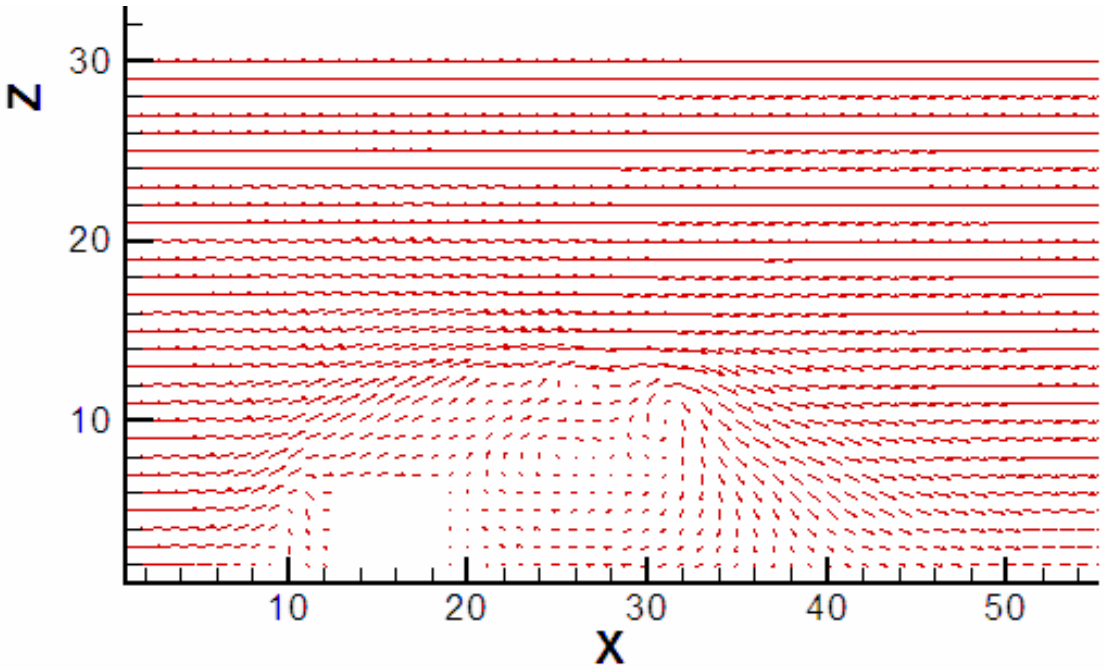

(a) Velocity vector field,

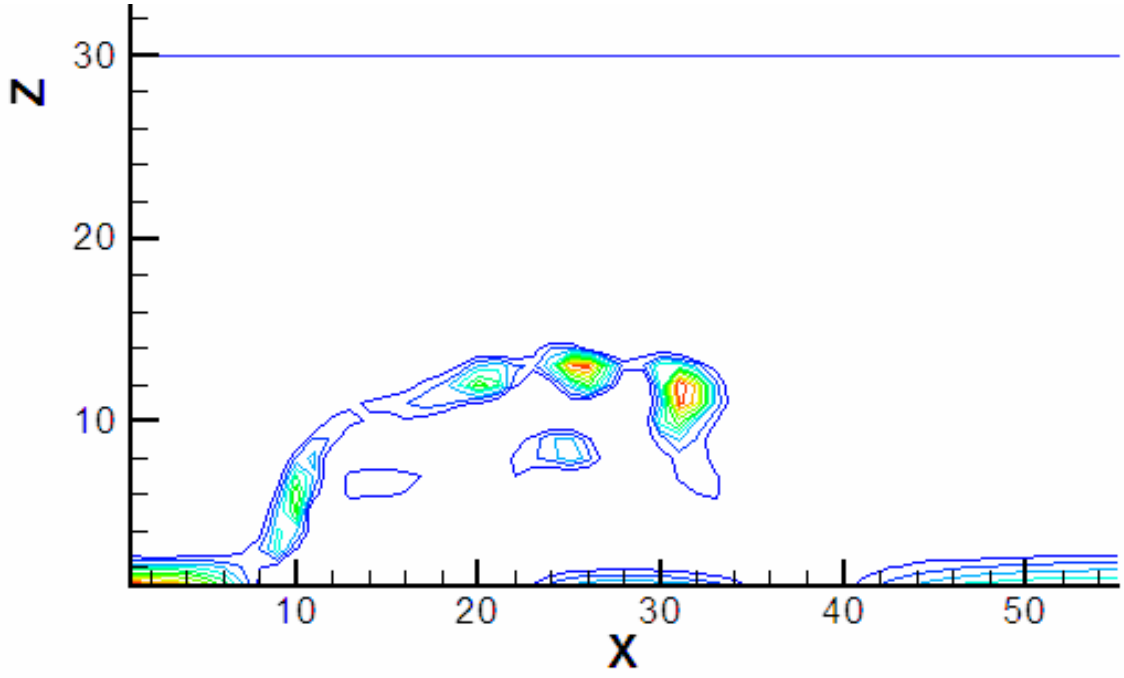

(b) Vorticity contours

Fig. 4-74 Velocity vector field and vorticity contours for the symmetry plane, 100 time steps;

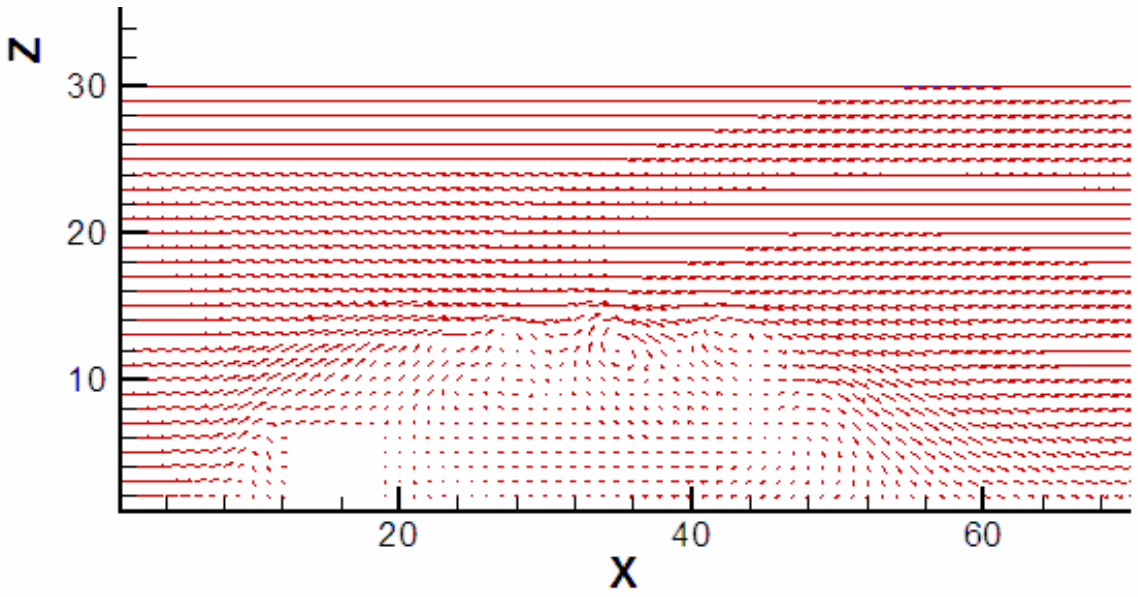

(a) Velocity vector field,

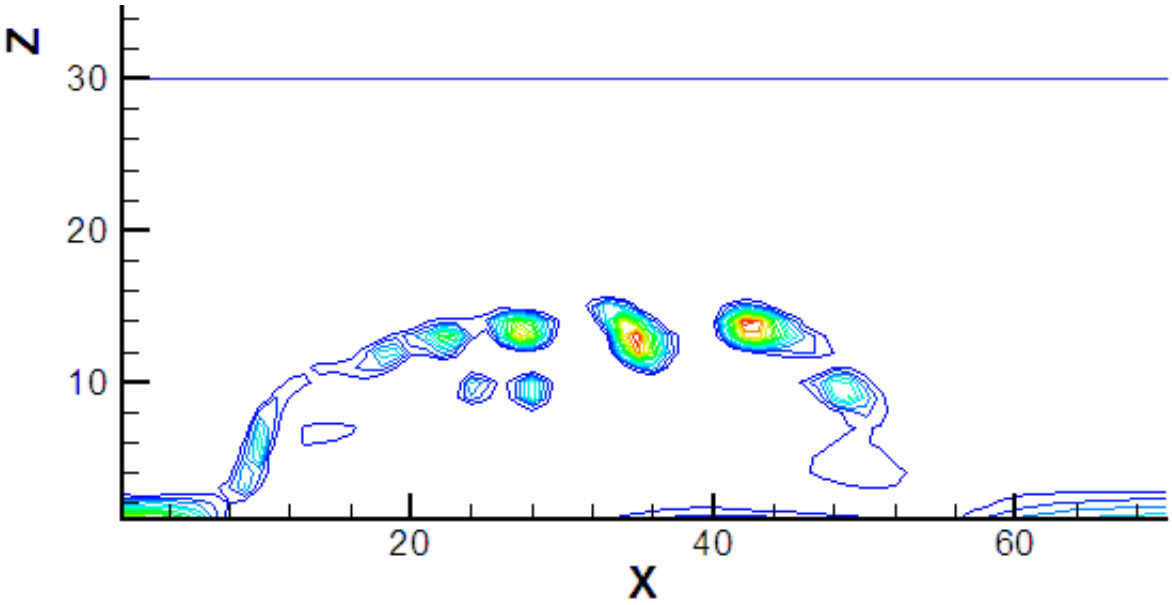

(b)Vorticity contours

Fig. 4-75 Velocity vector field and vorticity contours for the symmetry plane 400 time steps

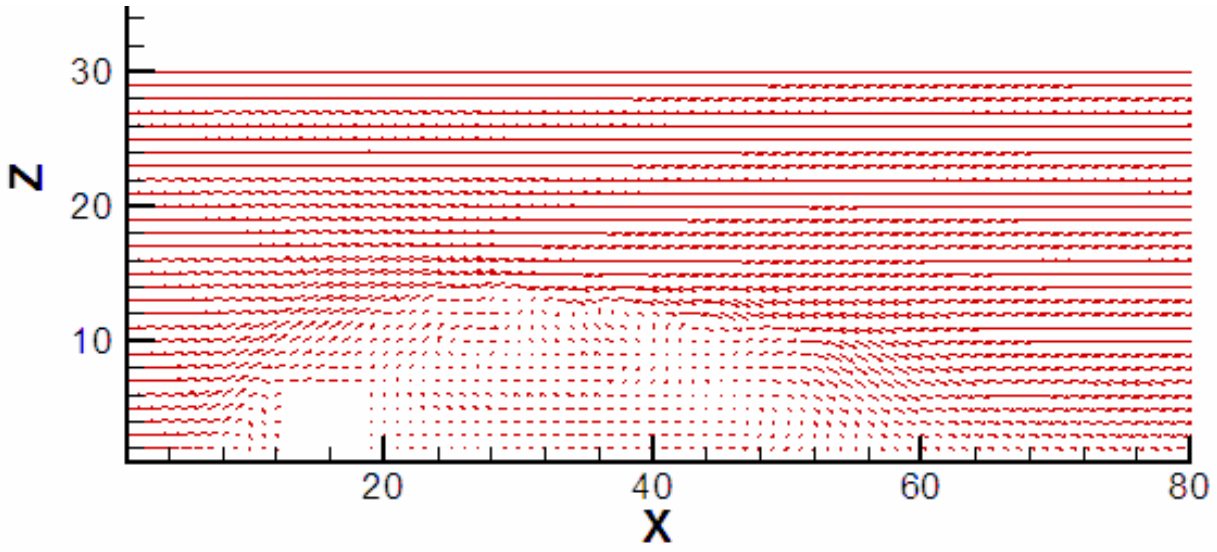

(a) Velocity vector field,

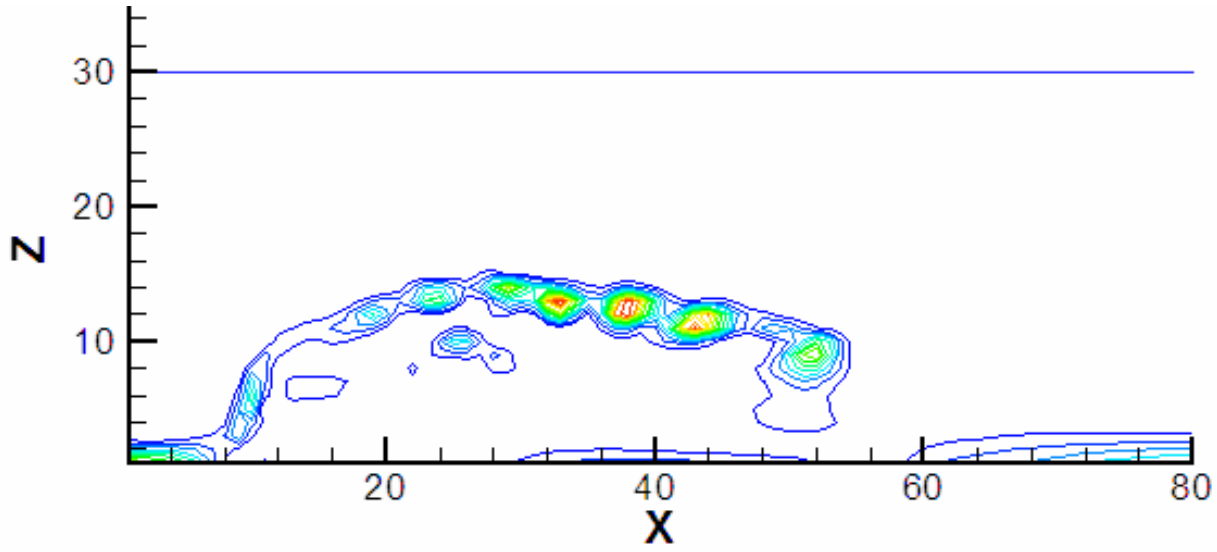

(c) Vorticity contours

Fig. 4-76 Velocity vector field and vorticity contours for the symmetry plane, 950 time steps;

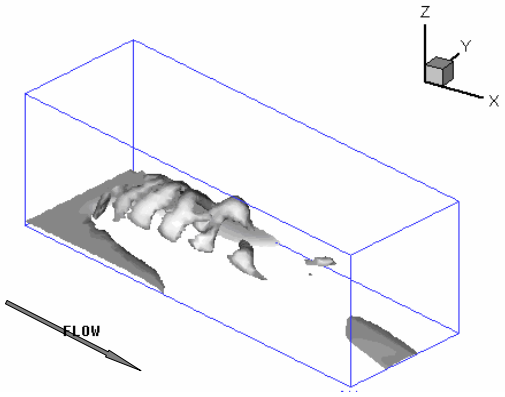

(a) 1200 time steps

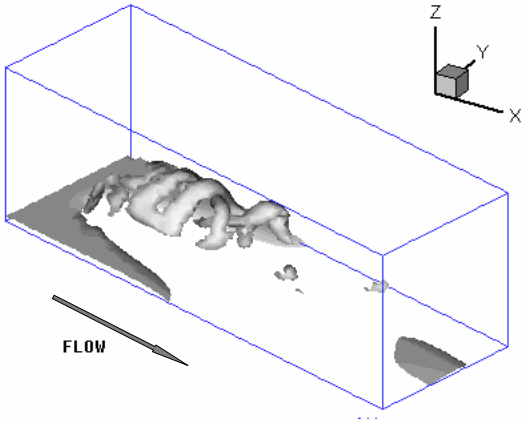

(b) 1220 time steps

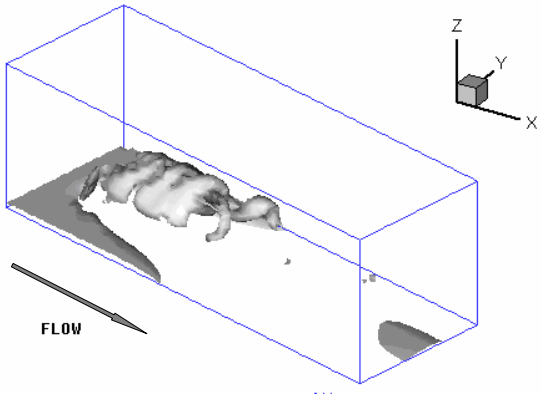

(c)1240 time steps

Fig. 4-77 Voticity iso-surface, the development of the hairpin vortex in a sequence of time steps

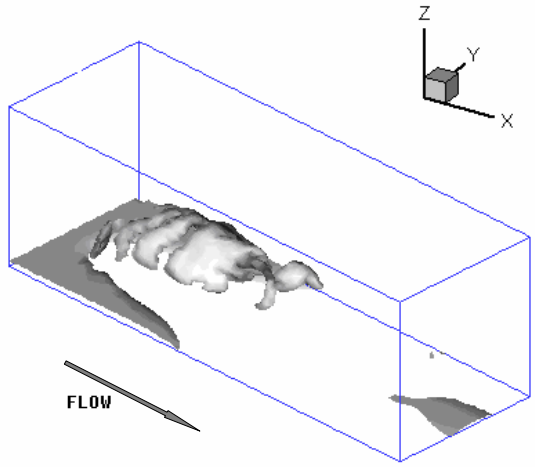

(d) 1260 time steps

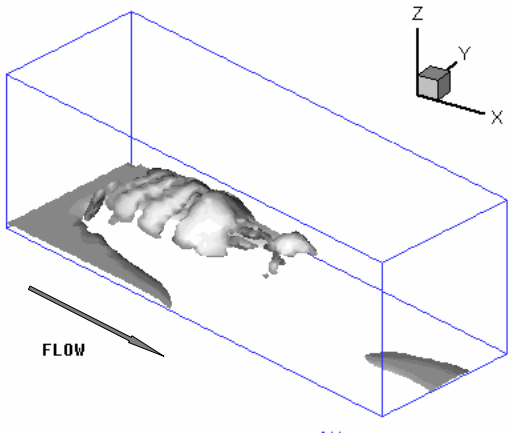

(e) 1280 time steps

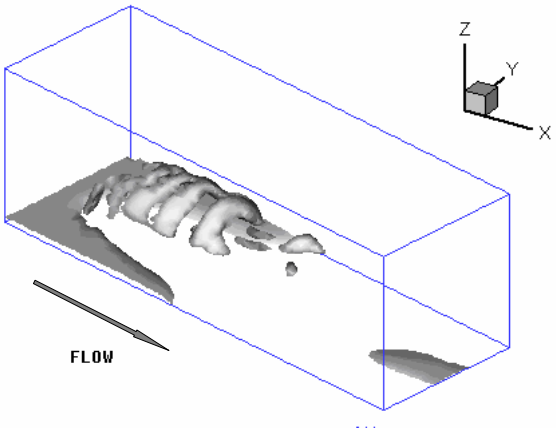

(f)1300 time steps

Fig. 4-77 Continued

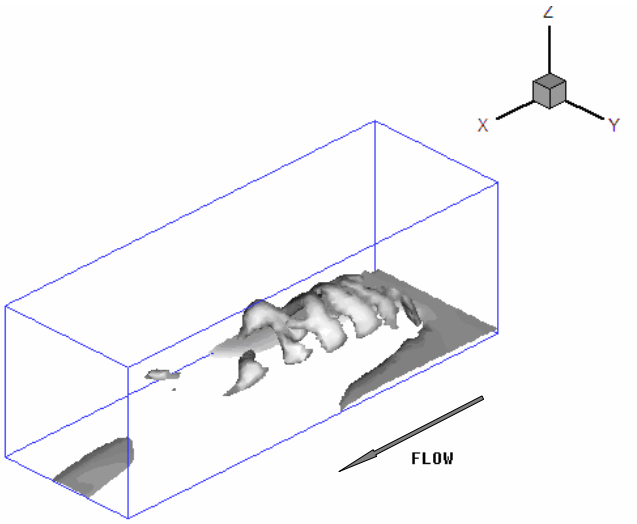

(a) 1200 time steps

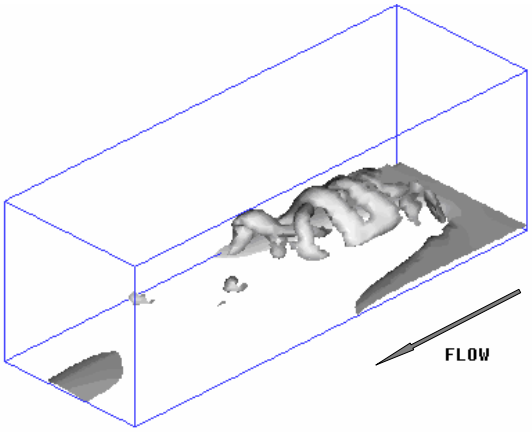

(b) 1220 time steps

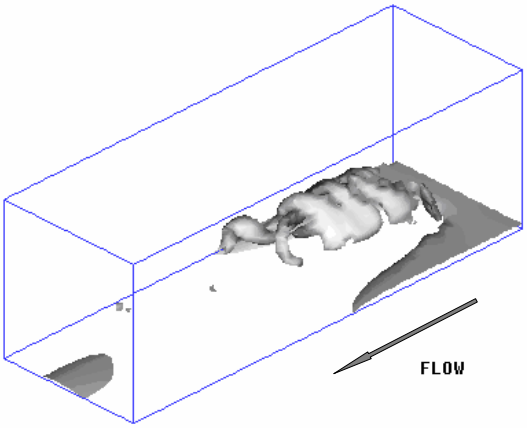

(c)1240 time steps

Fig. 4-78 Voticity iso-surface from the different viewing angle, the development of the hairpin vortex in a sequence of time steps

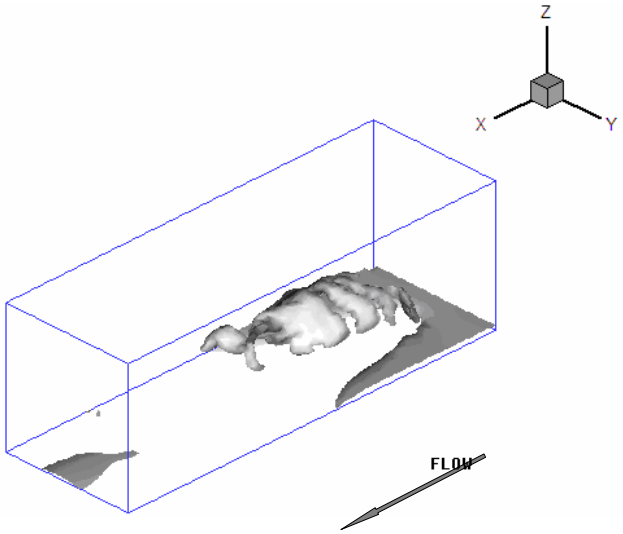

(d) 1260 time steps

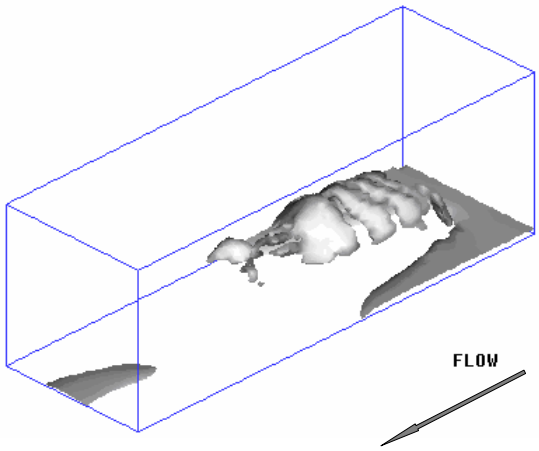

(e) 1280 time steps

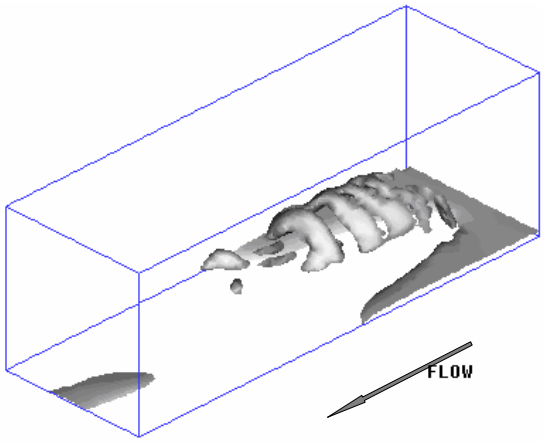

(f)1300 time steps

Fig. 4-78 Continued

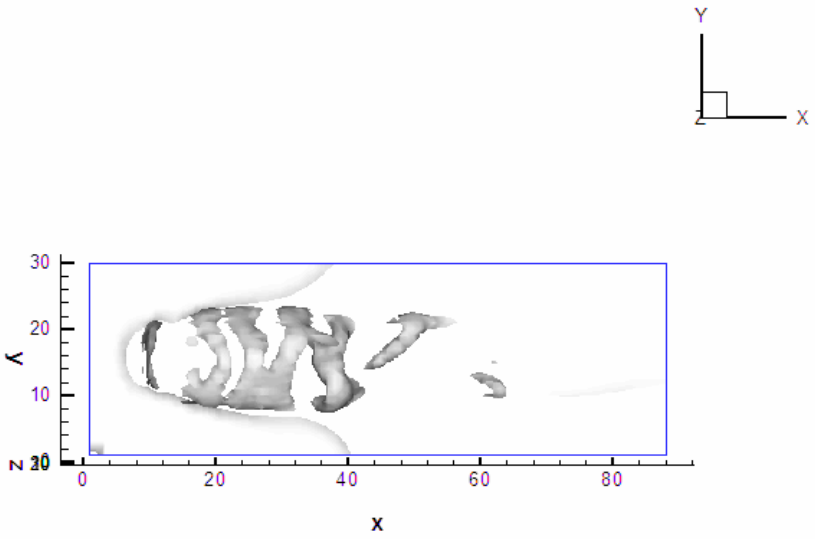

(a) 1200 time steps

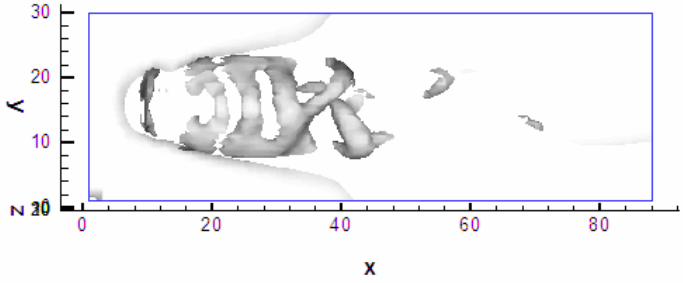

(b) 1220 time steps

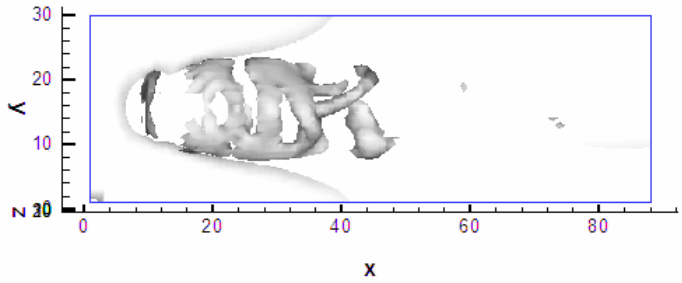

(c)1240 time steps

Fig. 4-79 Vorticity iso-surface, top views in a sequence of time steps

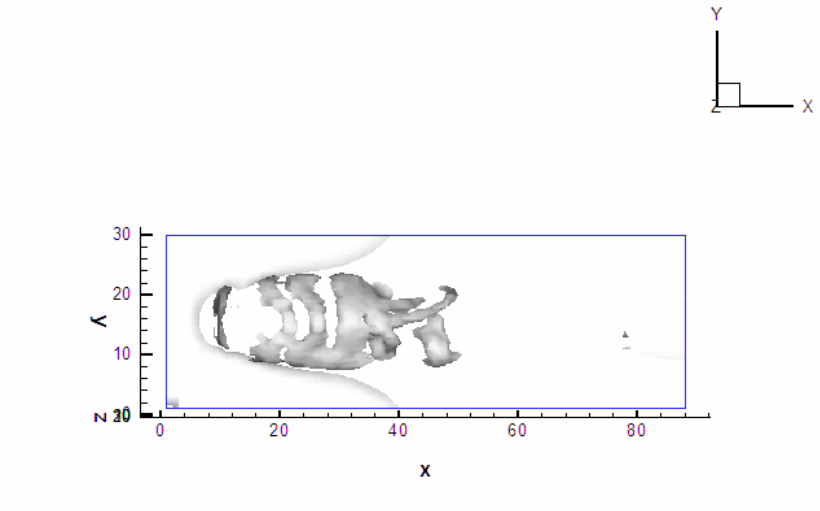

(d) 1260 time steps

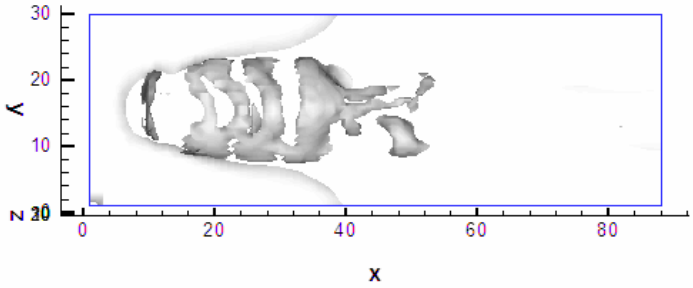

(e) 1280 time steps

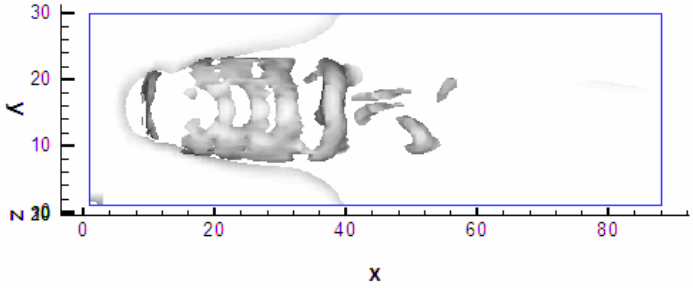

(f)1300 time steps

Fig. 4-79 Continued

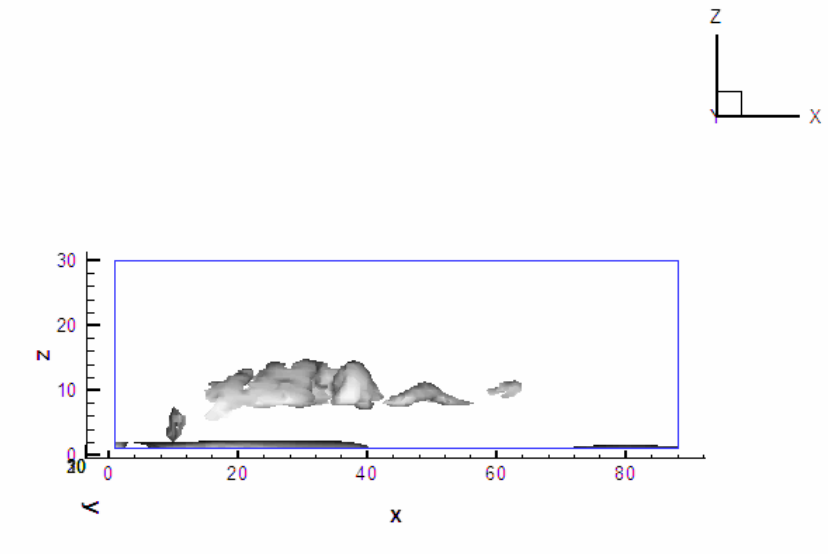

(a) 1200 time step

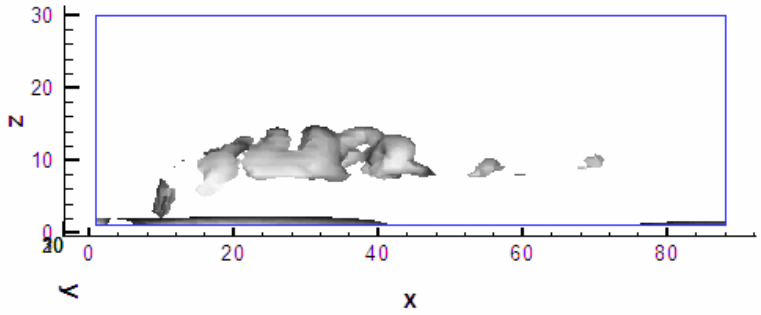

(b) 1220 time steps

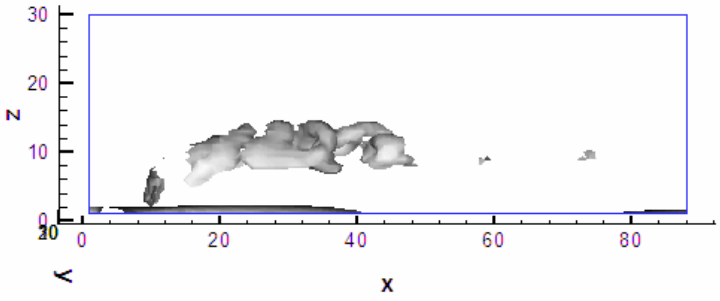

(c)1240 time steps

Fig. 4-80 Vorticity iso-surface, side views in a sequence of time steps

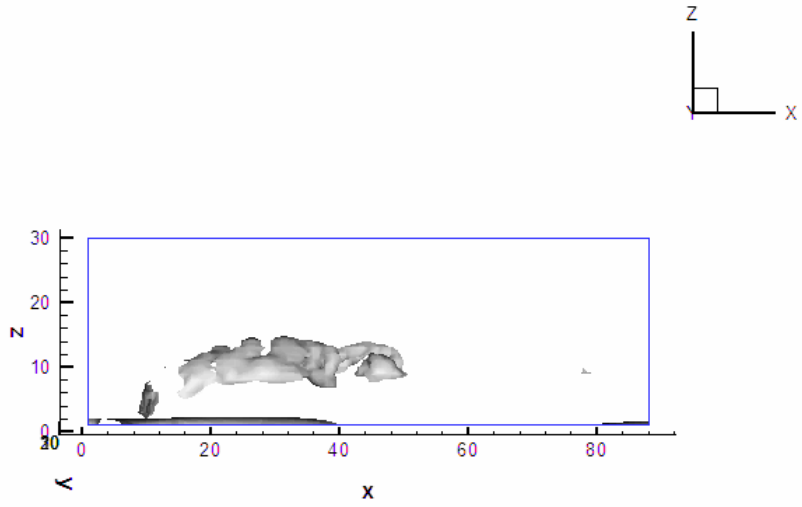

(d) 1260 time step

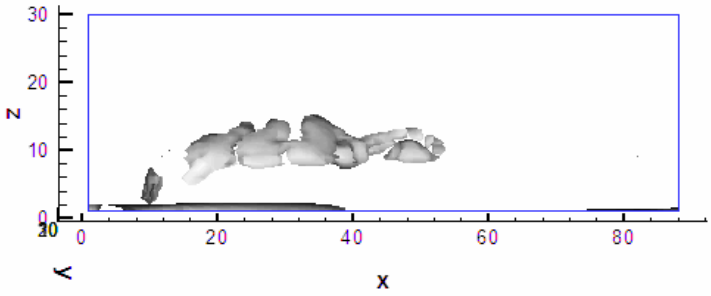

(e) 1280 time steps

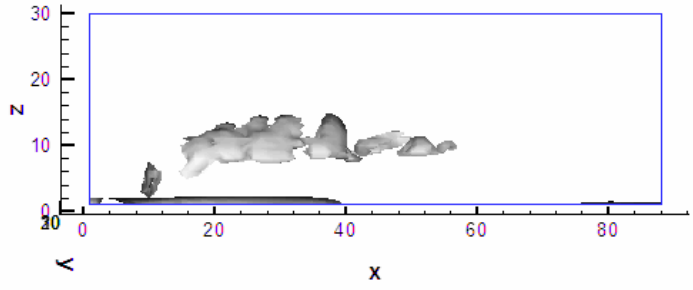

(f)1300 time steps

Fig. 4-80 Continued

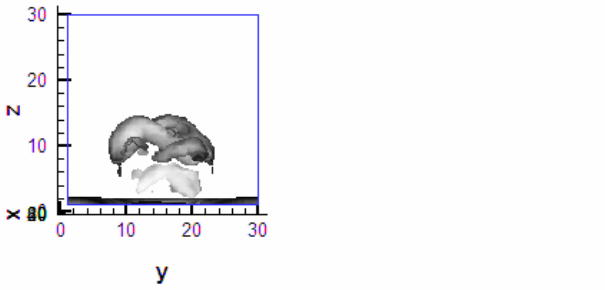

(a) 1200 time steps

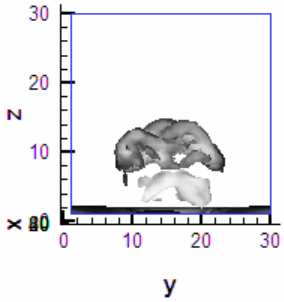

(b) 1220 time steps

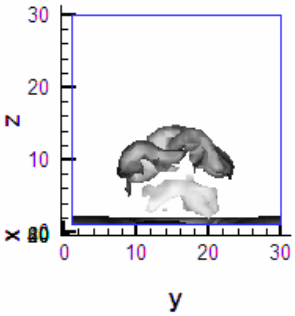

(c)1240 time steps

Fig. 4-81 Vorticity iso-surface, end views in a sequence of time steps

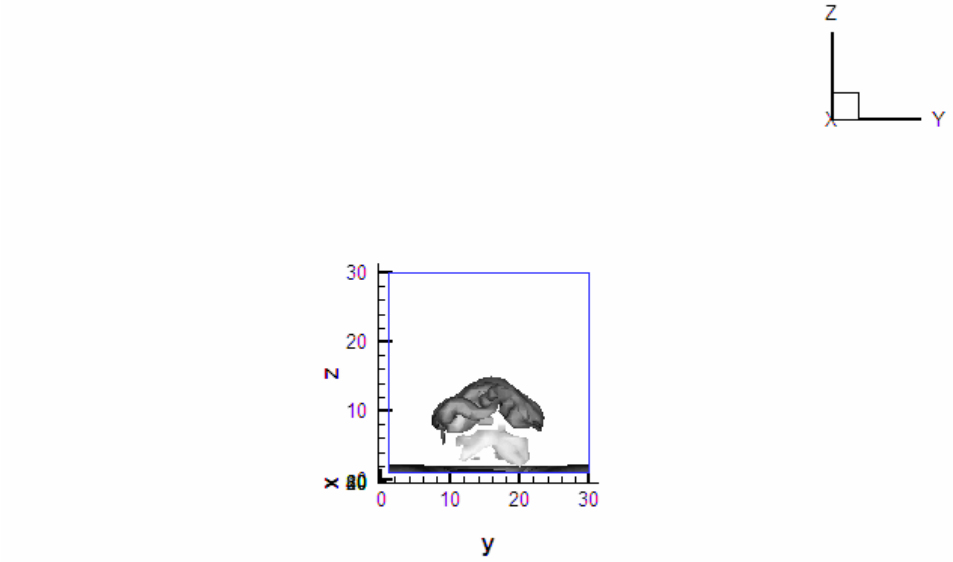

(d) 1260 time steps

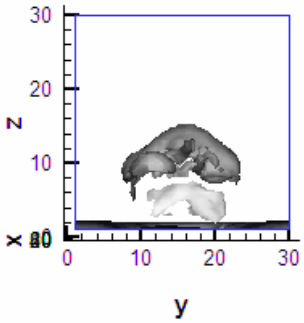

(e) 1280 time steps

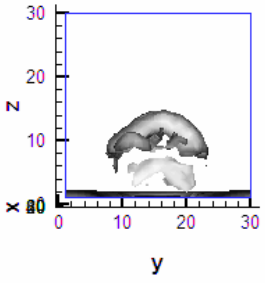

(f)1300 time steps

Fig. 4-81 Continued

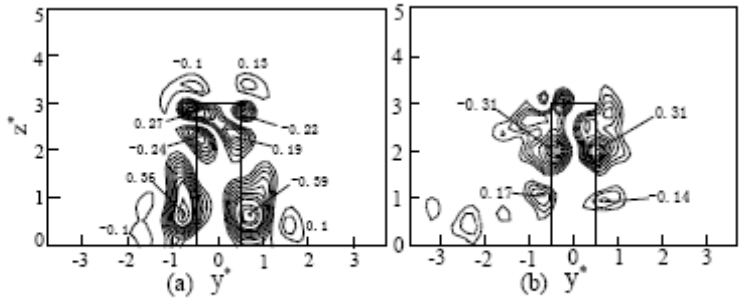

Fig.6 $\bar{\omega}_x^*$ - contours of H/d = 3. (a) x/d =1, (b) 3.

Fig. 4-82 Experimental result of the instantaneous contours of the x component of the vorticity vector

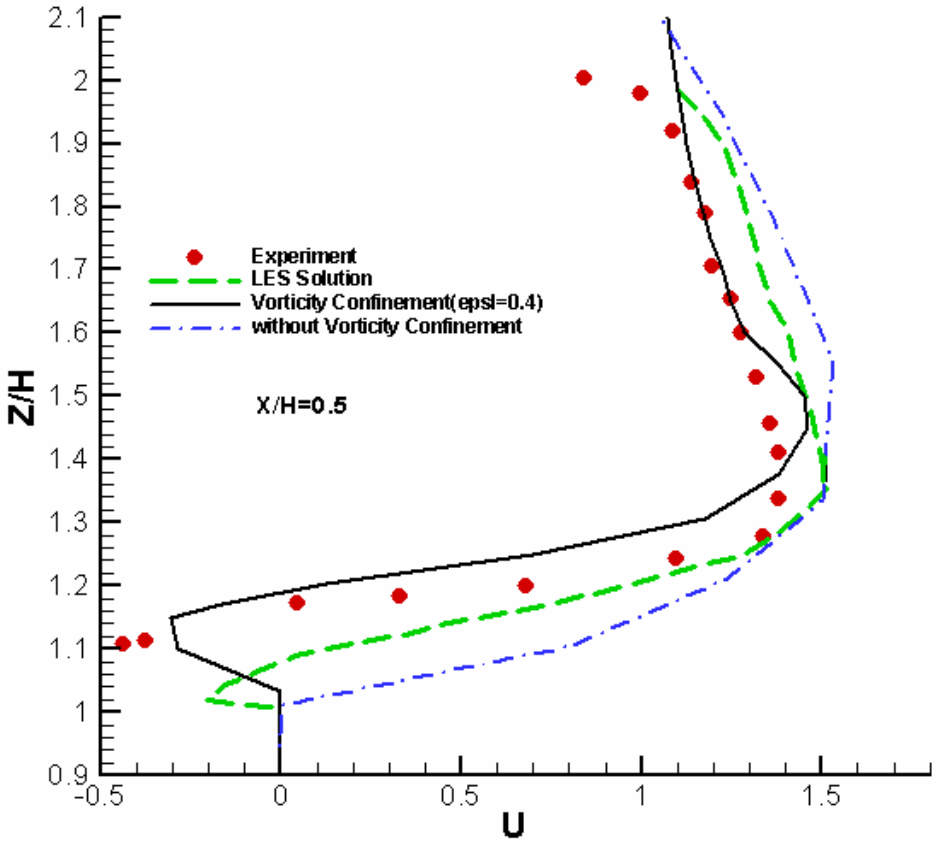

Fig. 4-83 Mean velocity component U at X/H=0.5 (20x20x20 cube)

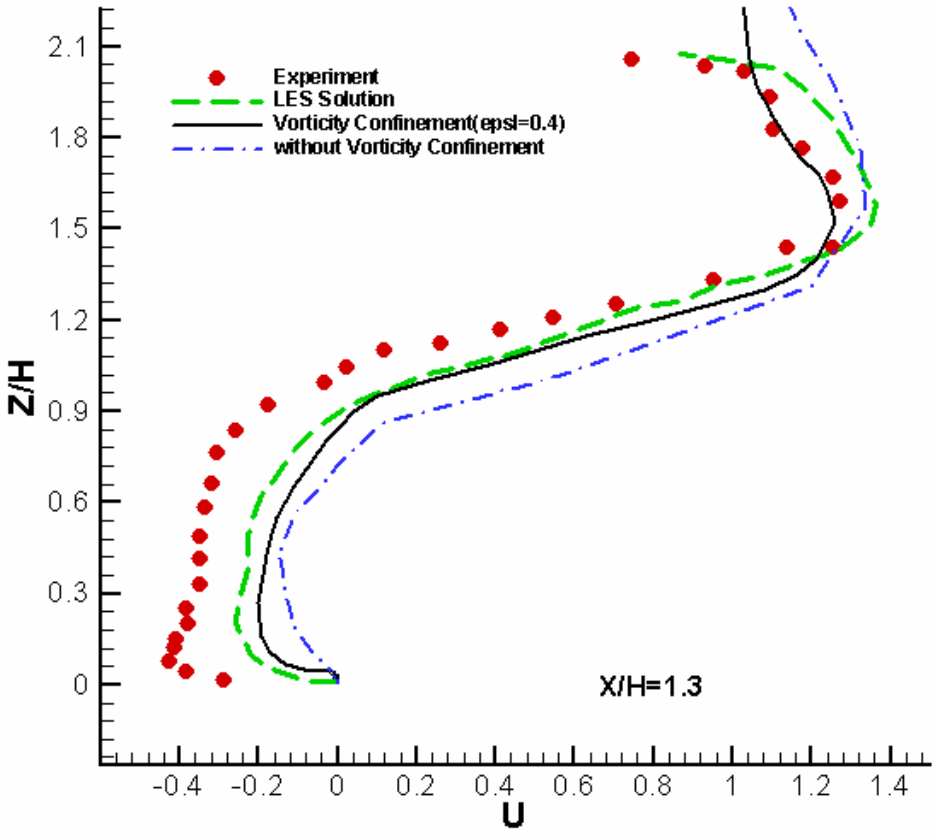

Fig. 4-84 Mean velocity component U at X/H=1.3 (20x20x20 cube)

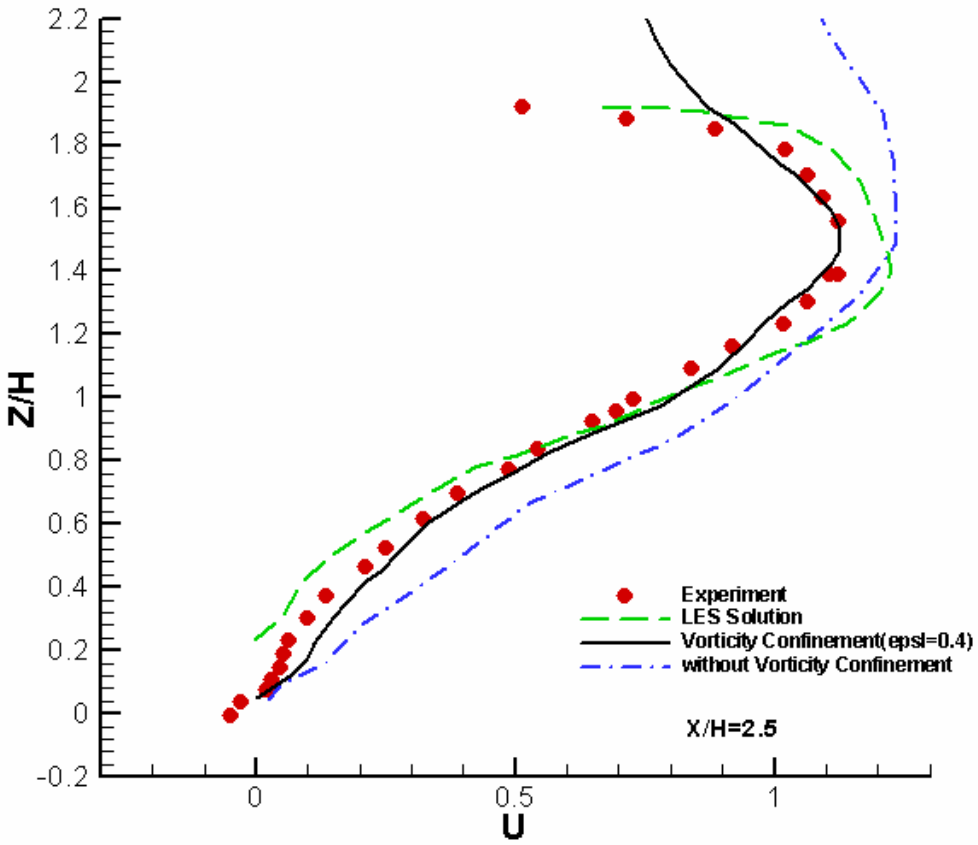

Fig. 4-85 Mean velocity component U at X/H=2.5 (20x20x20 cube)

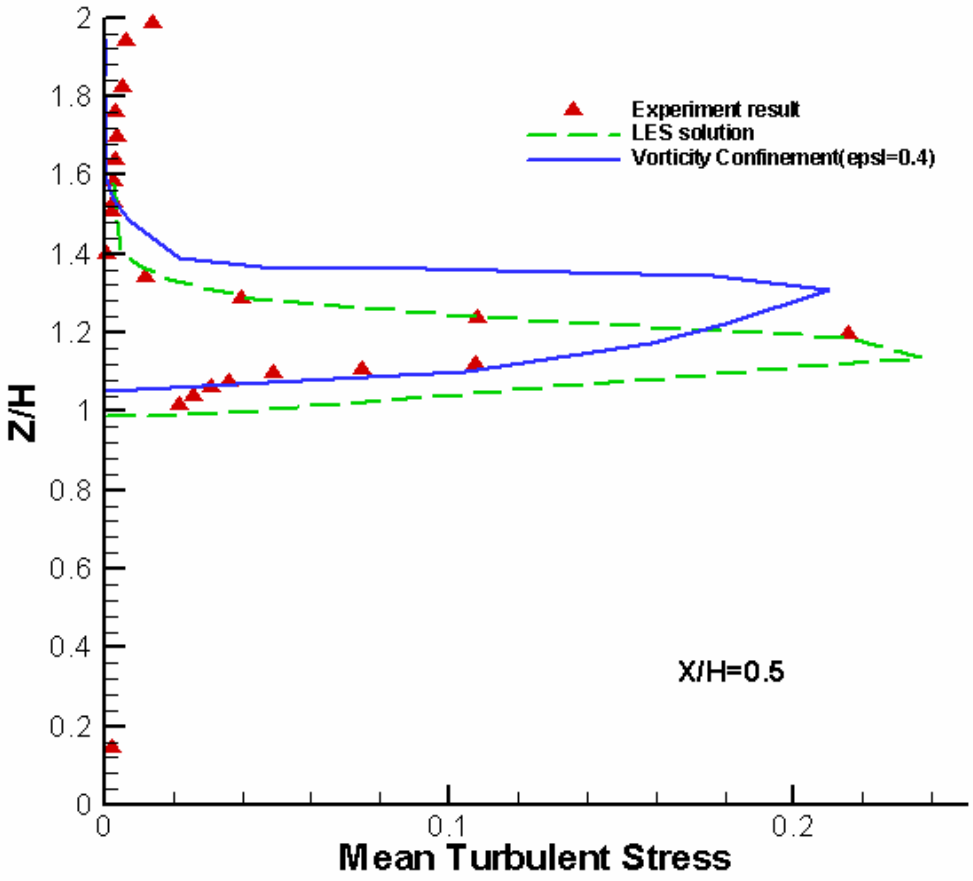

Fig. 4-86 Mean turbulent stress ($\overline{u'^2}$) at X/H=0.5 (20x20x20 cube)

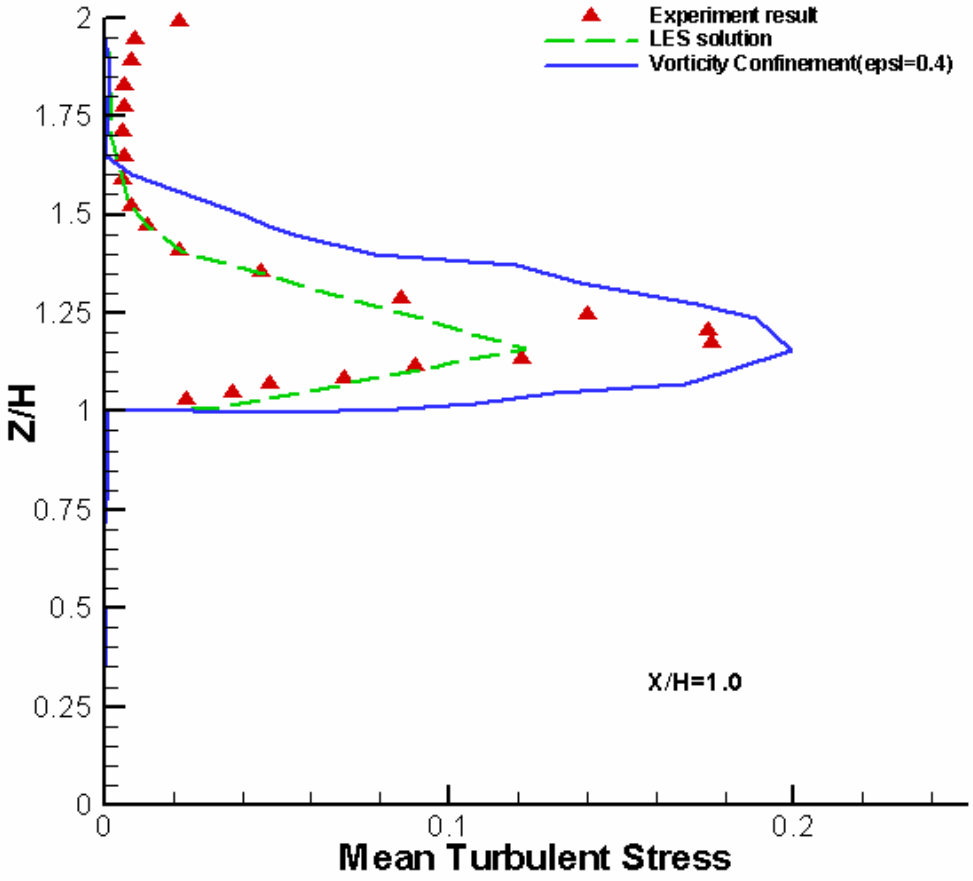

Fig. 4-87 Mean turbulent stress ($\overline{u'^2}$) at X/H=1.0 (20x20x20 cube)

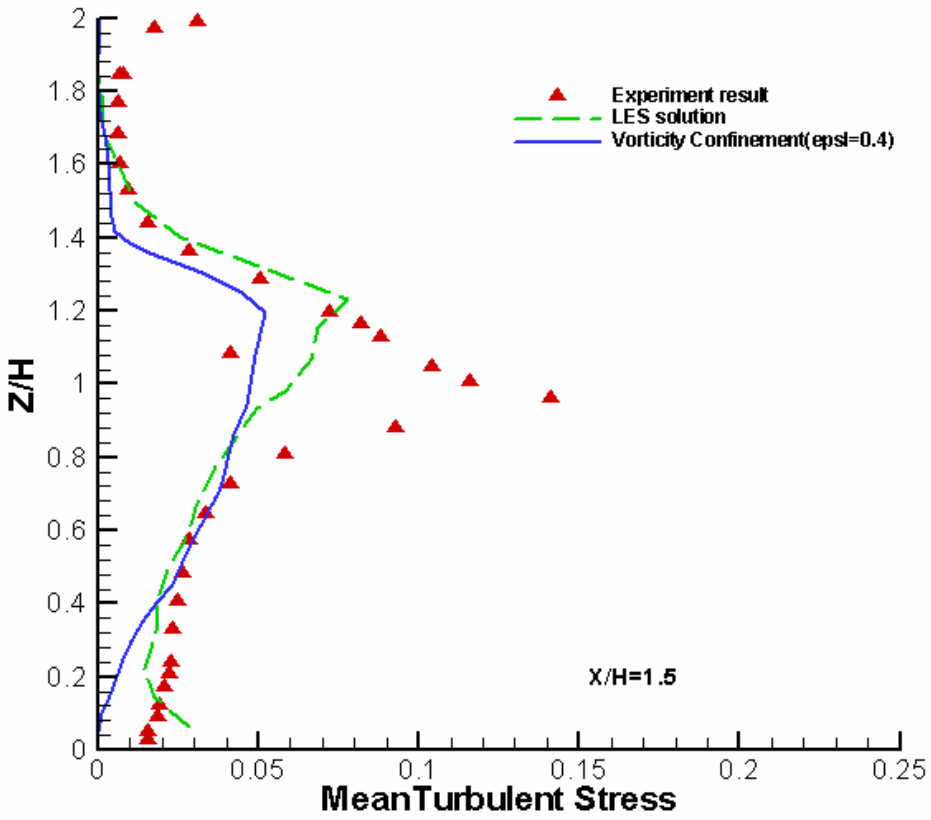

Fig. 4-88 Mean turbulent stress ($\overline{u'^2}$) at X/H=1.5 (20x20x20 cube)

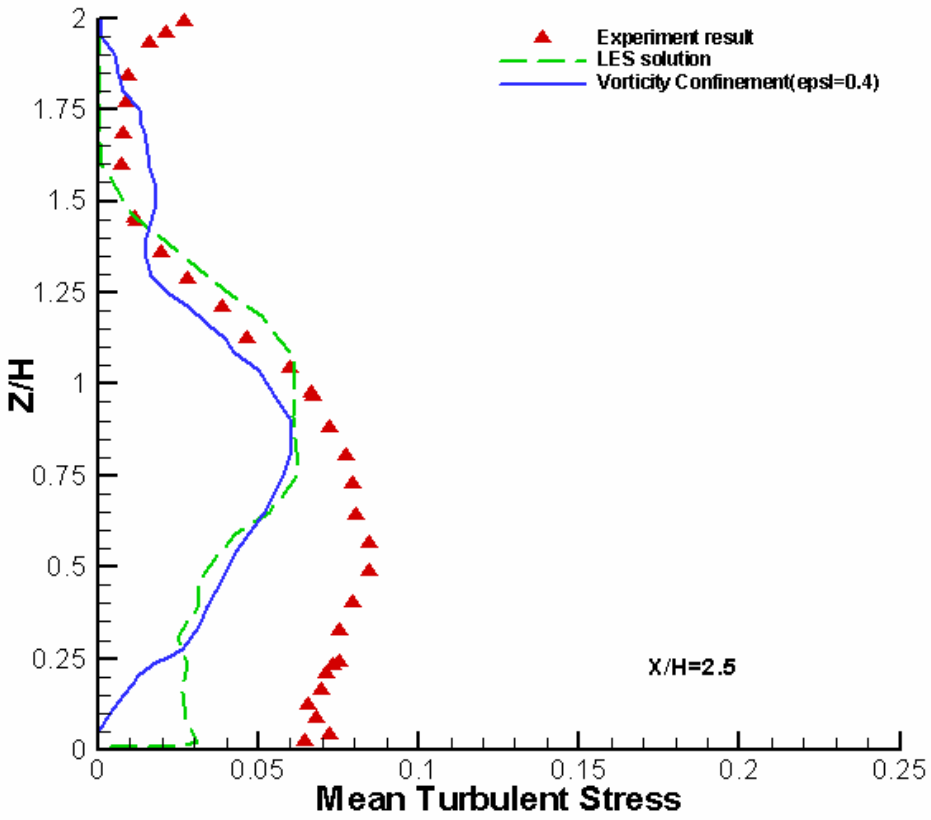

Fig. 4-89 Mean turbulent stress ($\overline{u'^2}$) at X/H=2.5 (20x20x20 cube)

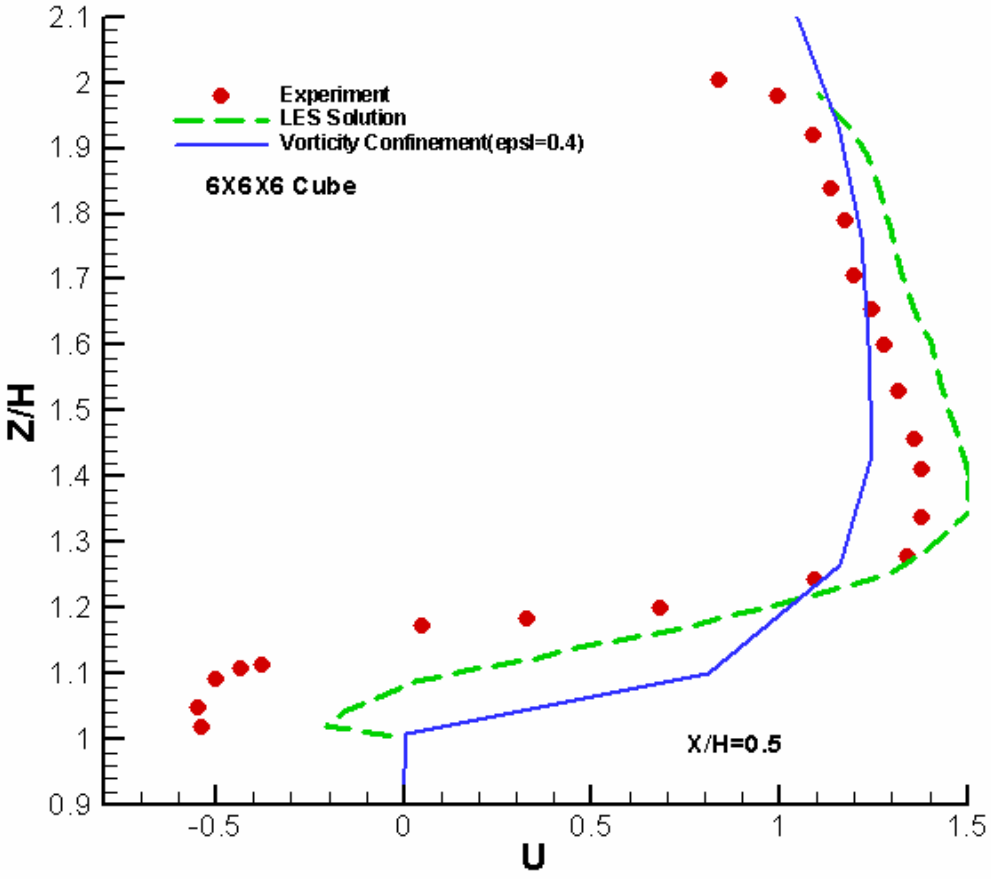

Fig. 4-90 Mean velocity component U at X/H=0.5 (6x6x6 cube)

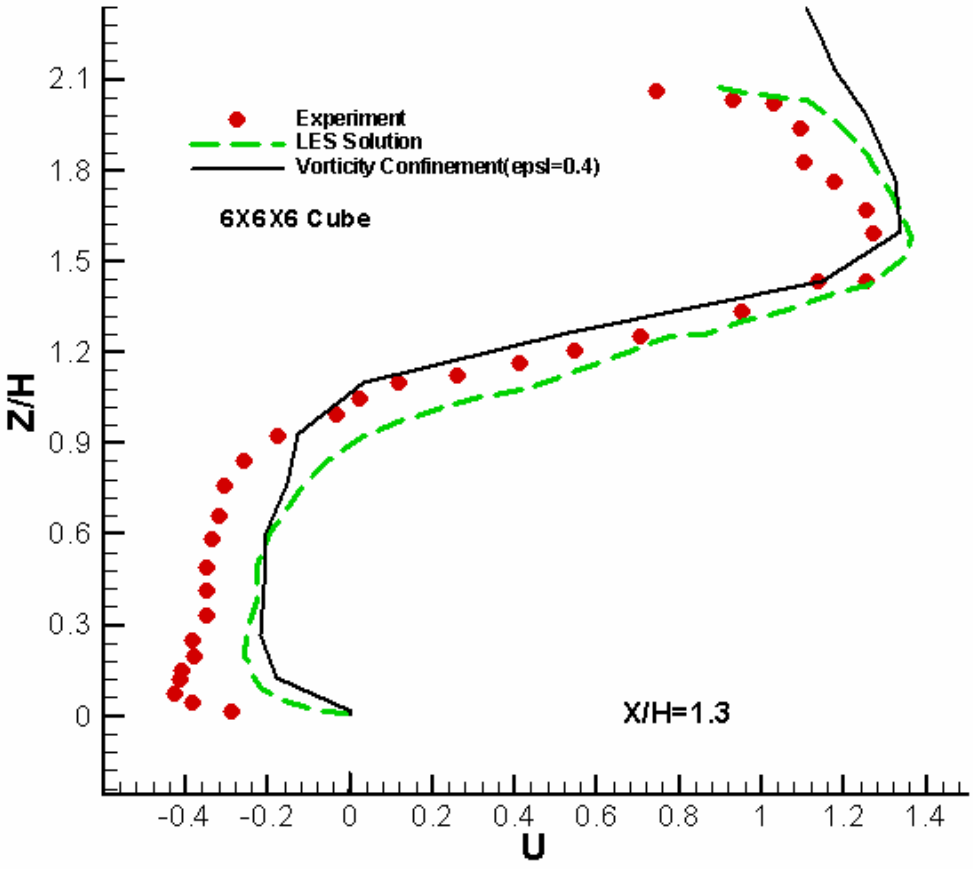

Fig. 4-91 Mean velocity component U at X/H=1.3 (6x6x6 cube)

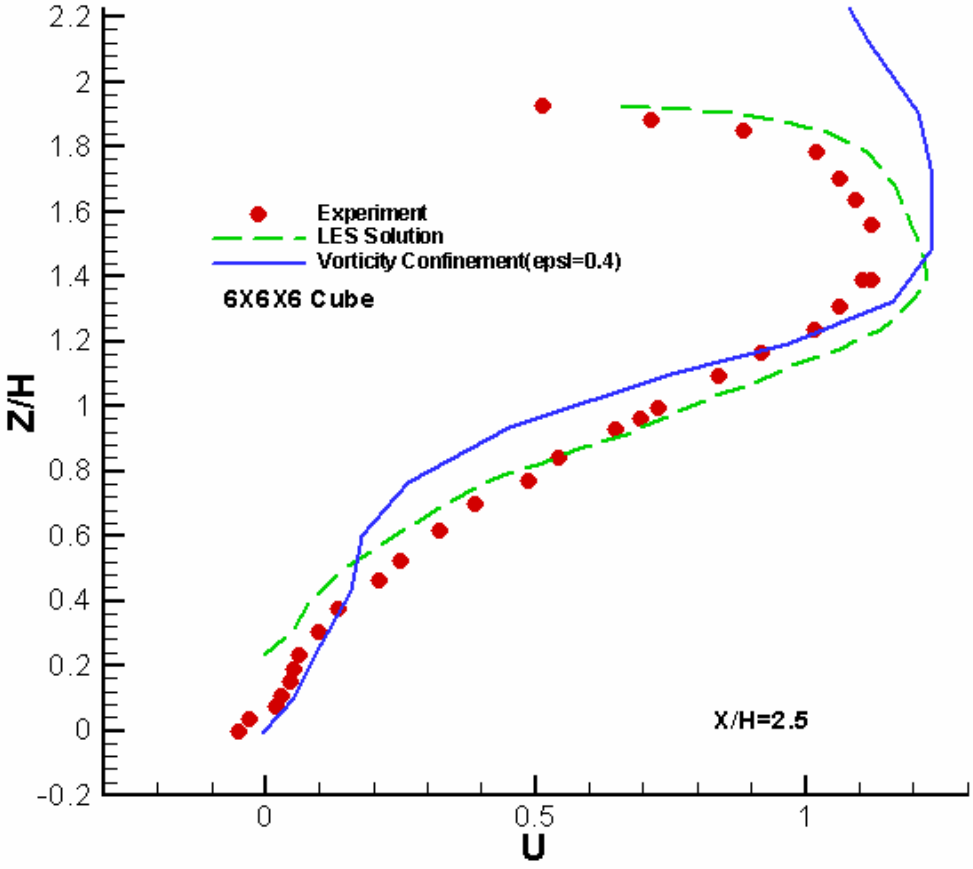

Fig. 4-92 Mean velocity component U at X/H=2.5 (6x6x6 cube)

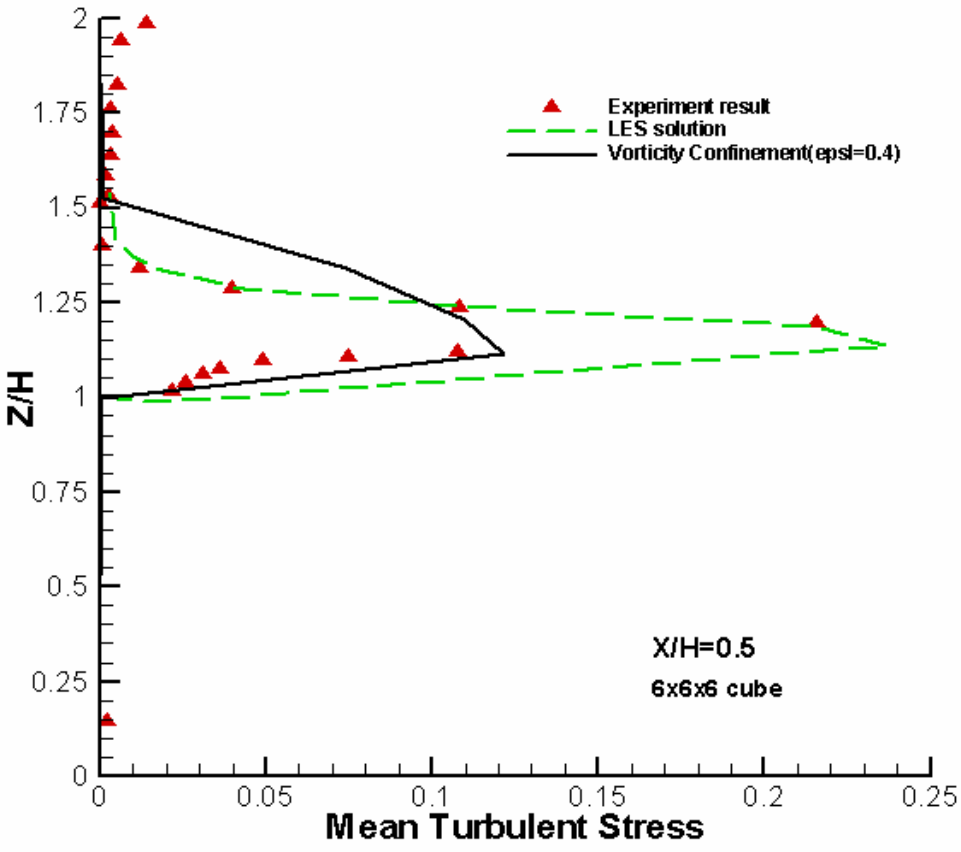

Fig. 4-93 Mean turbulent stress ($\overline{u'^2}$) at X/H=0.5 (6x6x6 cube)

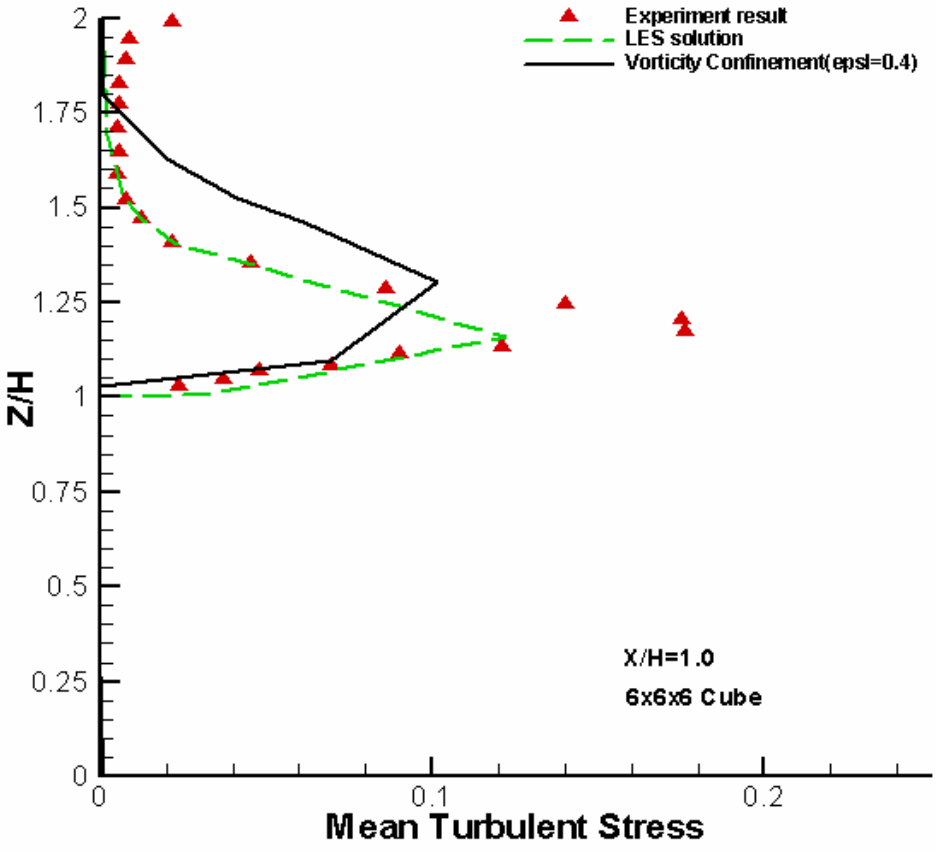

Fig. 4-94 Mean turbulent stress ($\overline{u'^2}$) at X/H=1.0 (6x6x6 cube)

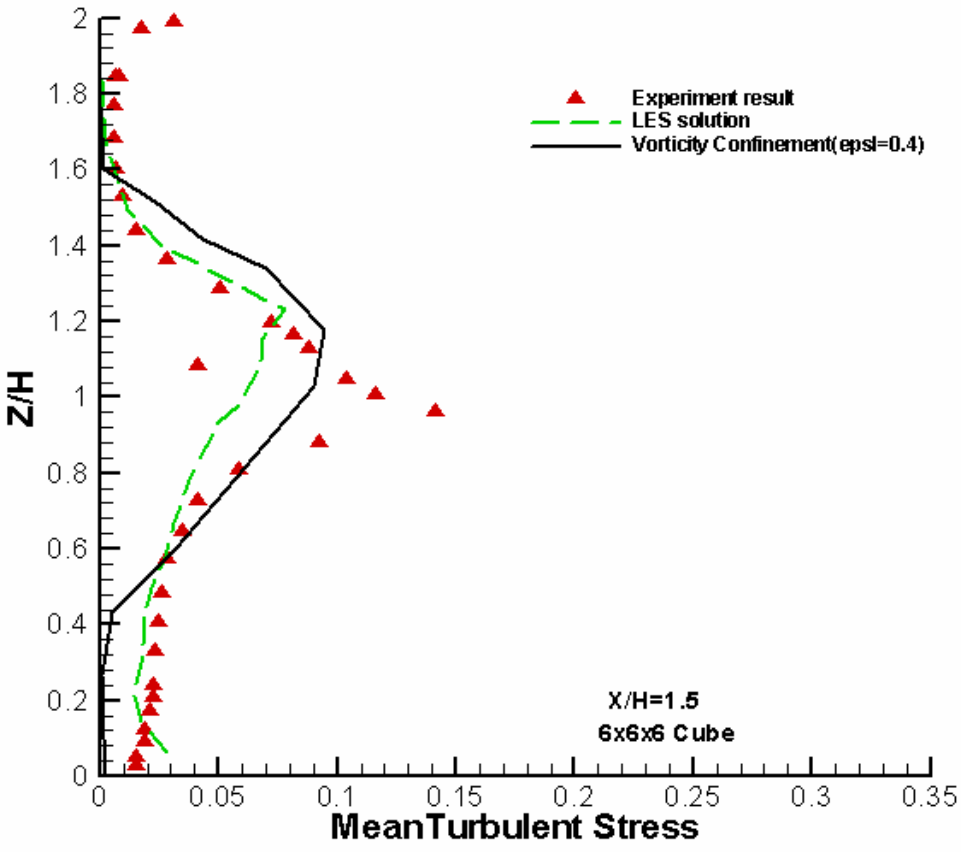

Fig. 4-95 Mean turbulent stress ($\overline{u'^2}$) at X/H=1.5 (6x6x6 cube)

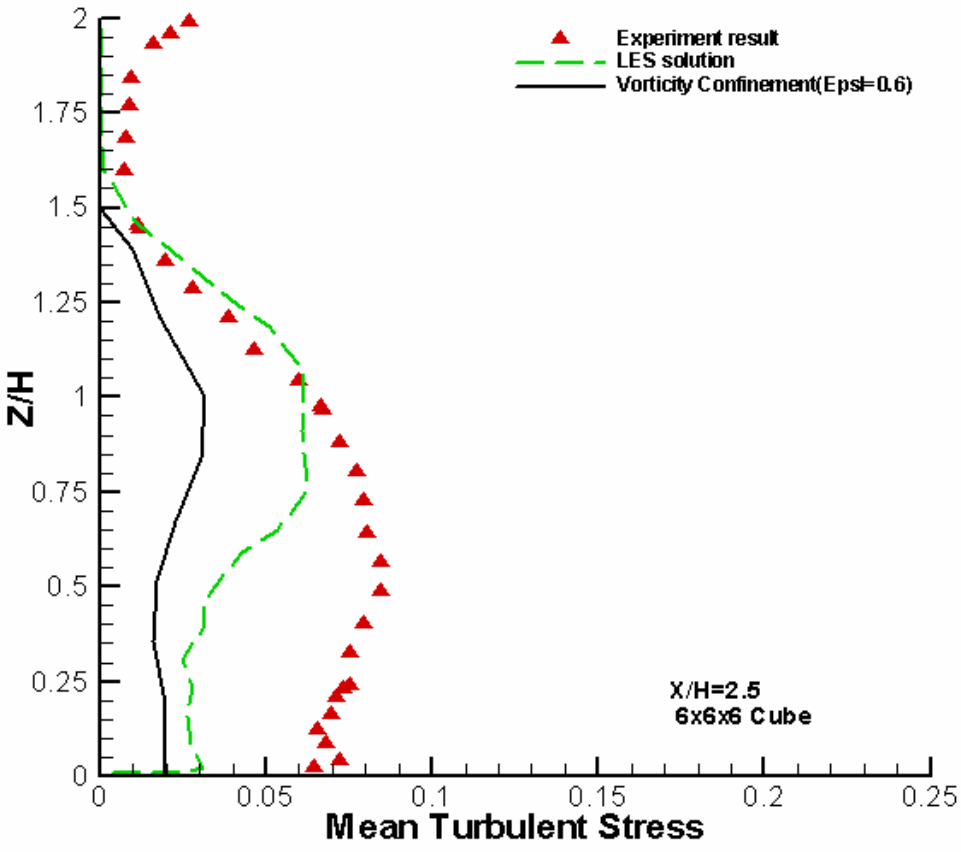

Fig. 4-96 Mean turbulent stress ($\overline{u'^2}$) at X/H=2.5 (6x6x6 cube)

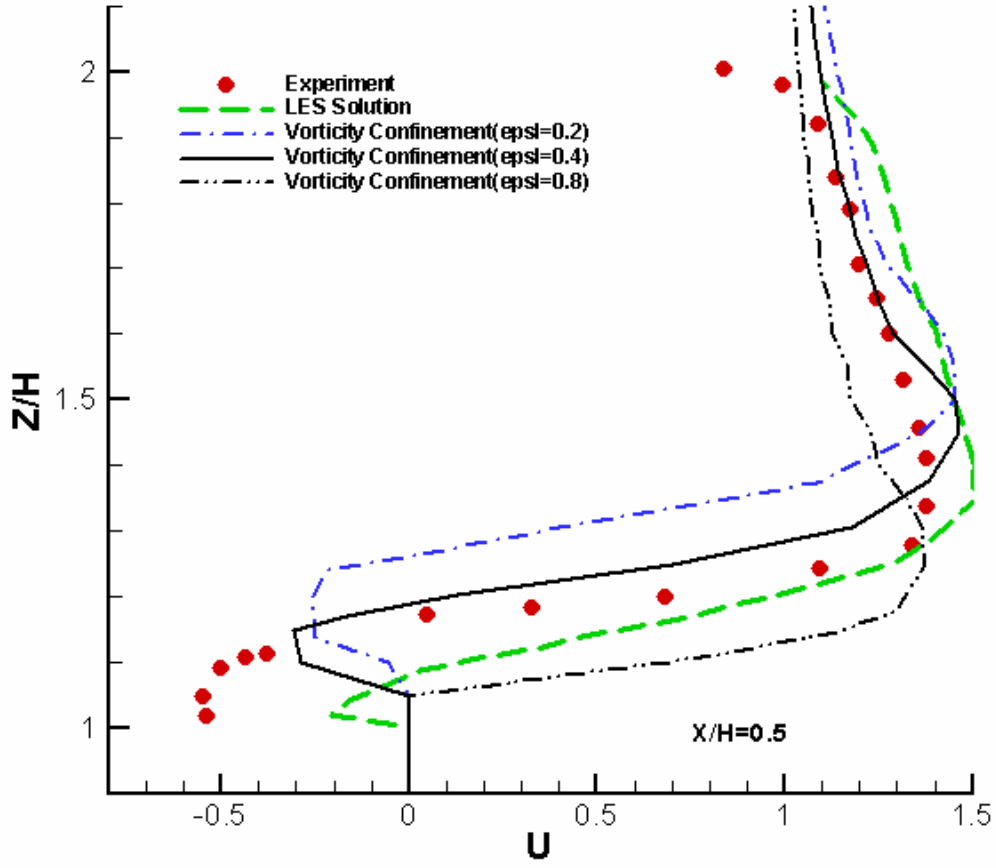

Fig. 4-97 the comparison of mean velocity component U for the different confinement coefficients at X/H=0.5 (20x20x20 cube)

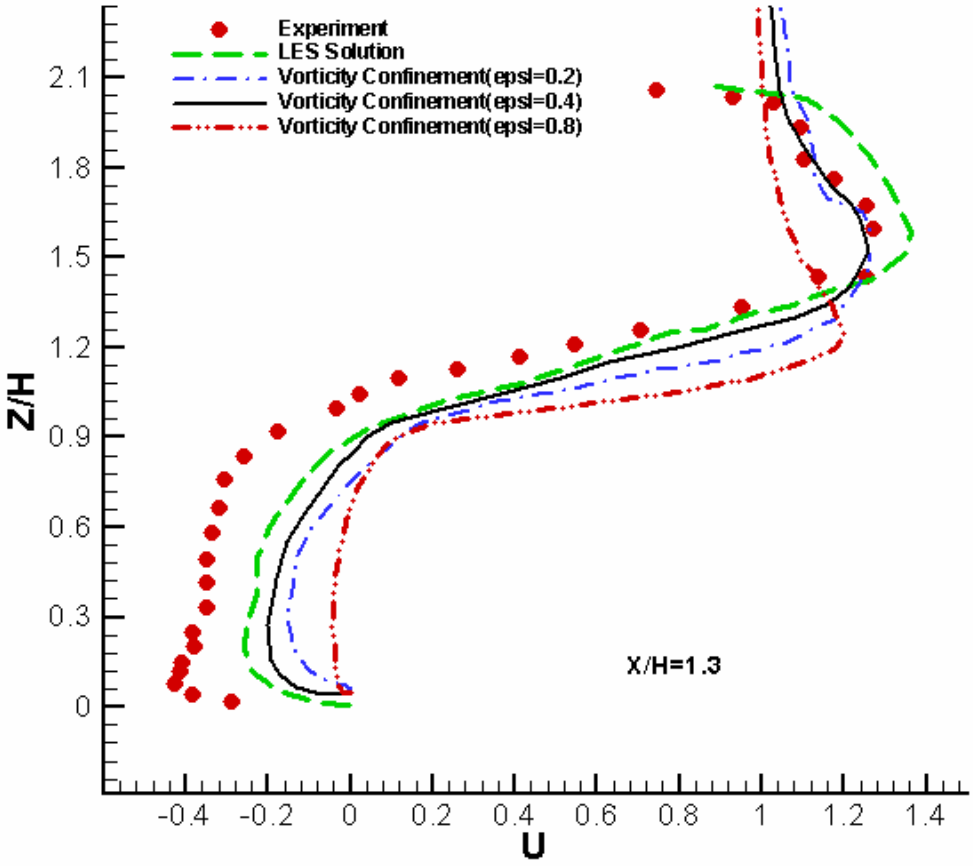

Fig. 4-98 the comparison of mean velocity component U for the different confinement coefficients at X/H=1.3 (20x20x20 cube)

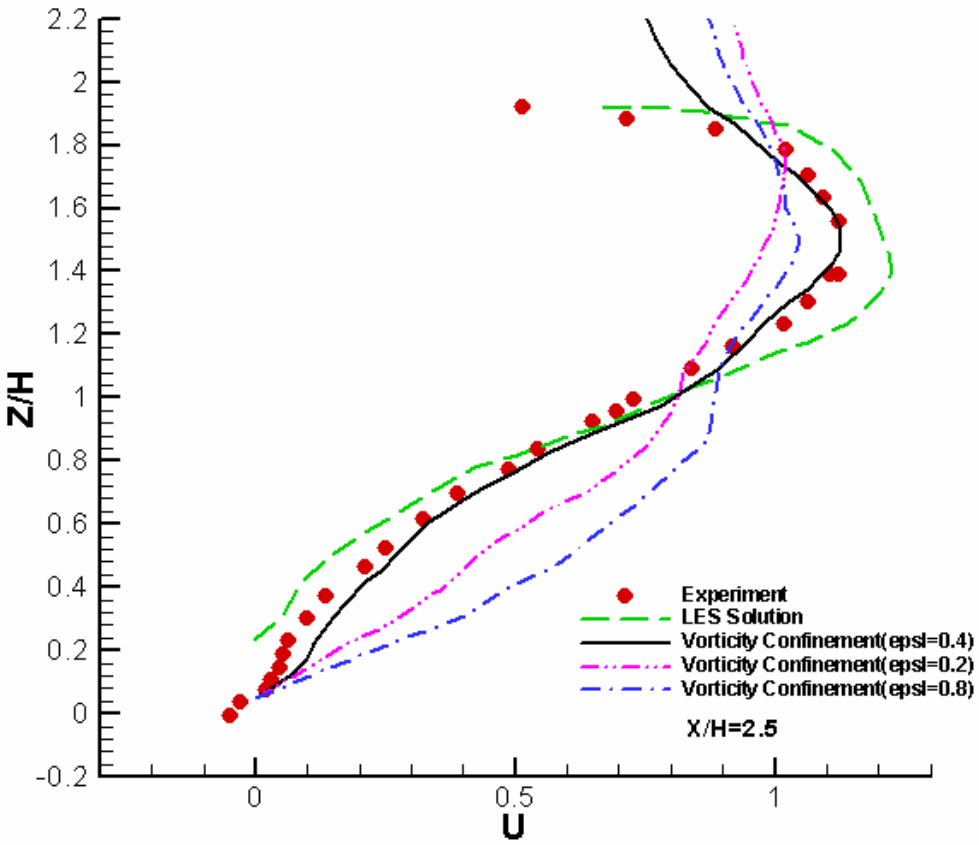

Fig. 4-99 the comparison of mean velocity component U for the different confinement coefficients at X/H=2.5 (20x20x20 cube)

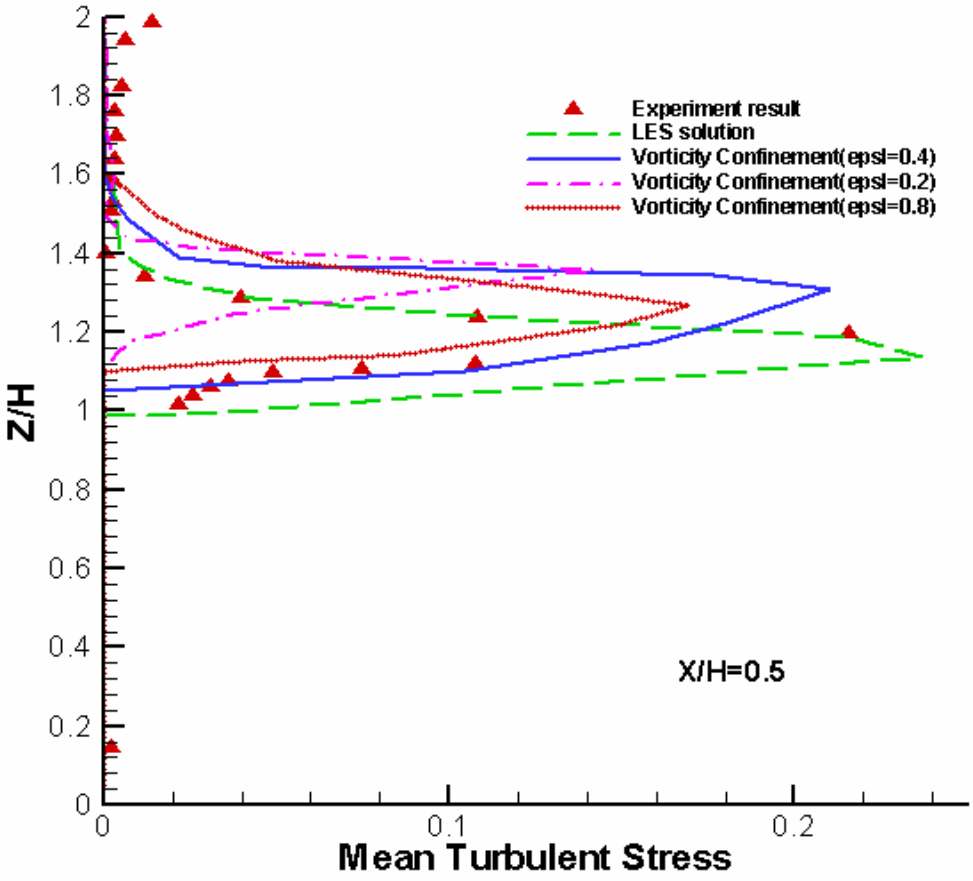

Fig. 4-100 Comparison of mean turbulent stress ($\overline{u'^2}$) for different confinement coefficients at X/H=0.5 (20x20x20 cube)

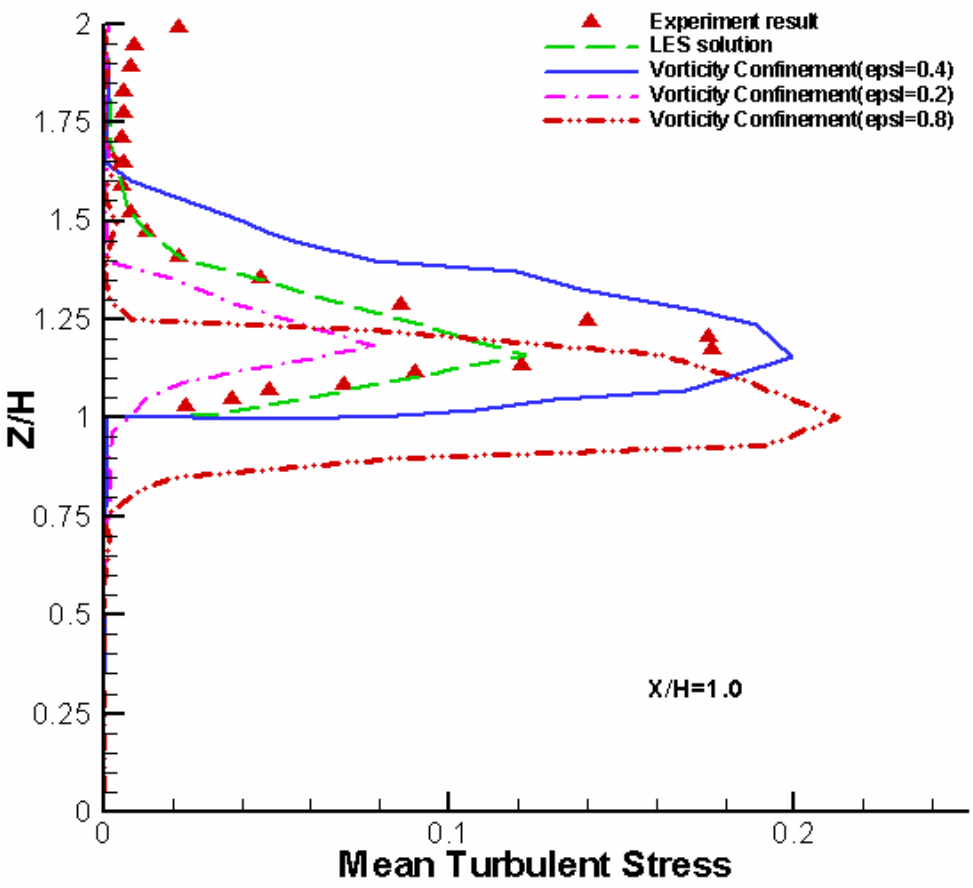

Fig. 4-101 Comparison of mean turbulent stress ($\overline{u'^2}$) for different confinement coefficients at X/H=1.0 (20x20x20 cube)

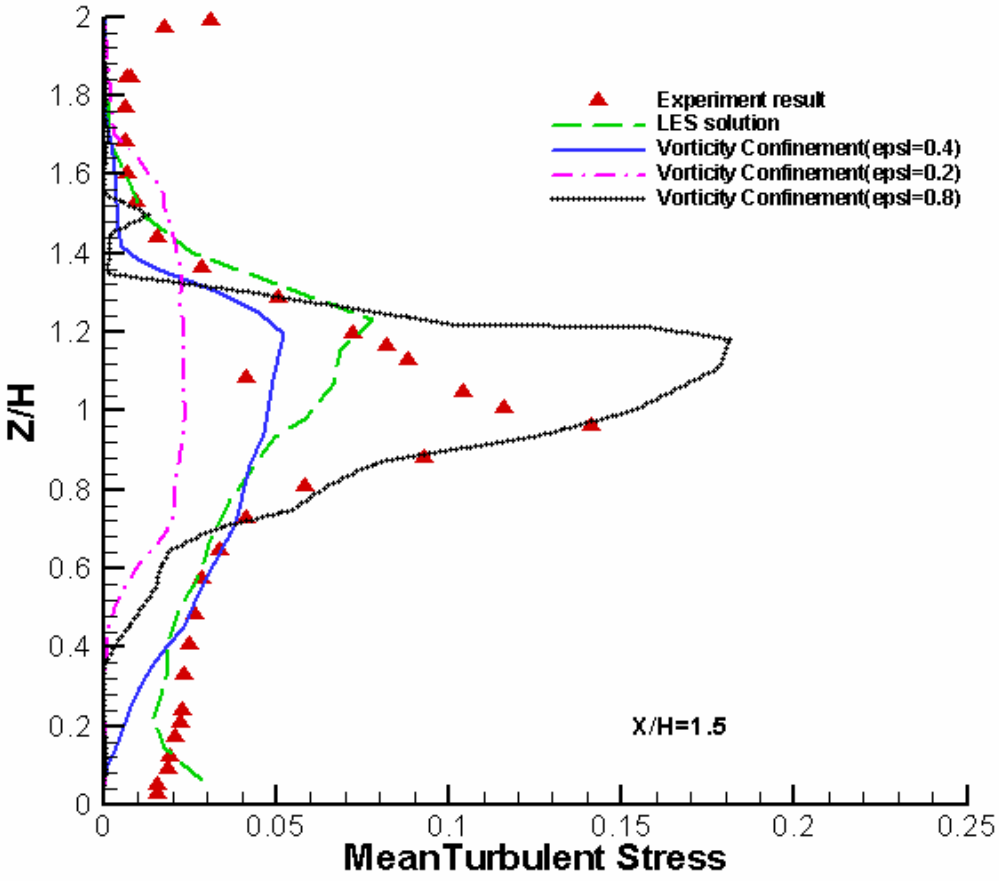

Fig. 4-102 Comparison of mean turbulent stress ($\overline{u'^2}$) for different confinement coefficients at X/H=1.5 (20x20x20 cube)

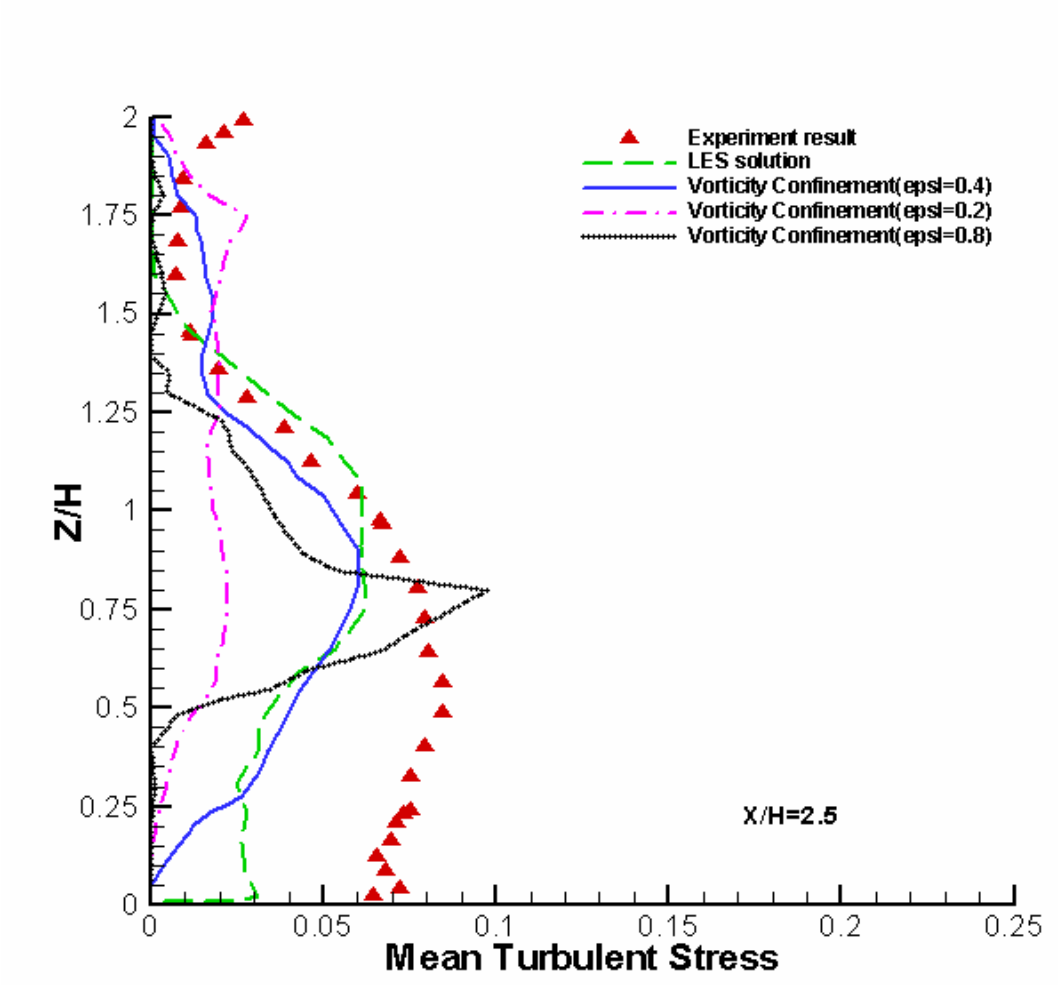

Fig. 4-103 Comparison of mean turbulent stress ($\overline{u'^2}$) for different confinement coefficients at X/H=2.5 (20x20x20 cube)

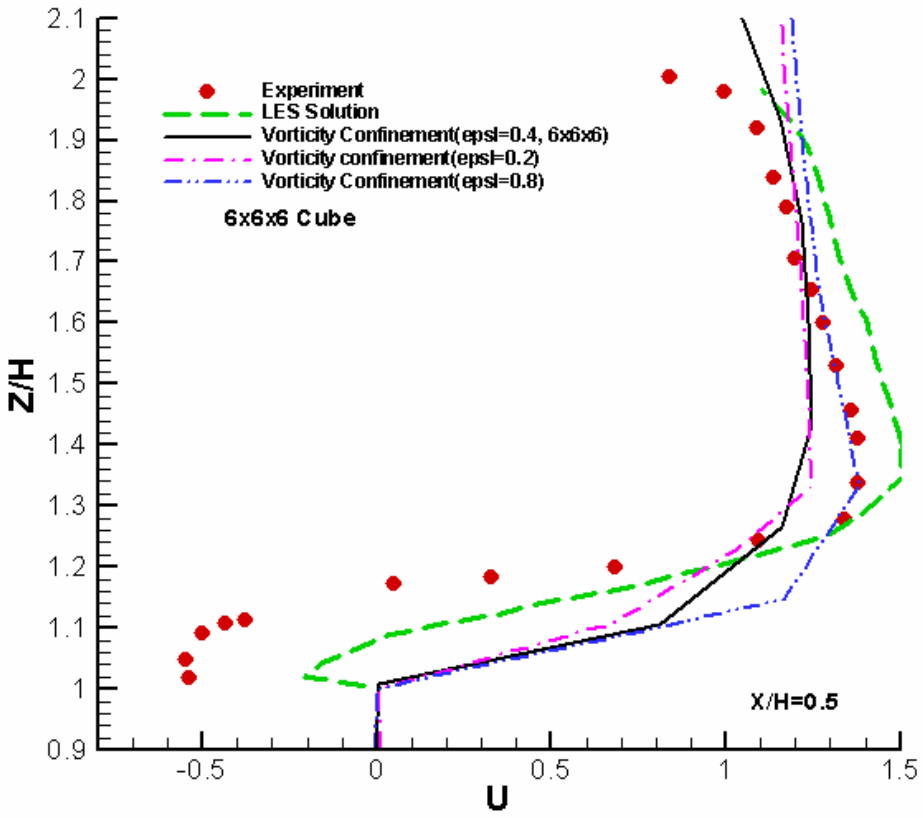

Fig. 4-104 Comparison of mean velocity component U for the different confinement coefficients at X/H=0.5(6x6x6 Cube)

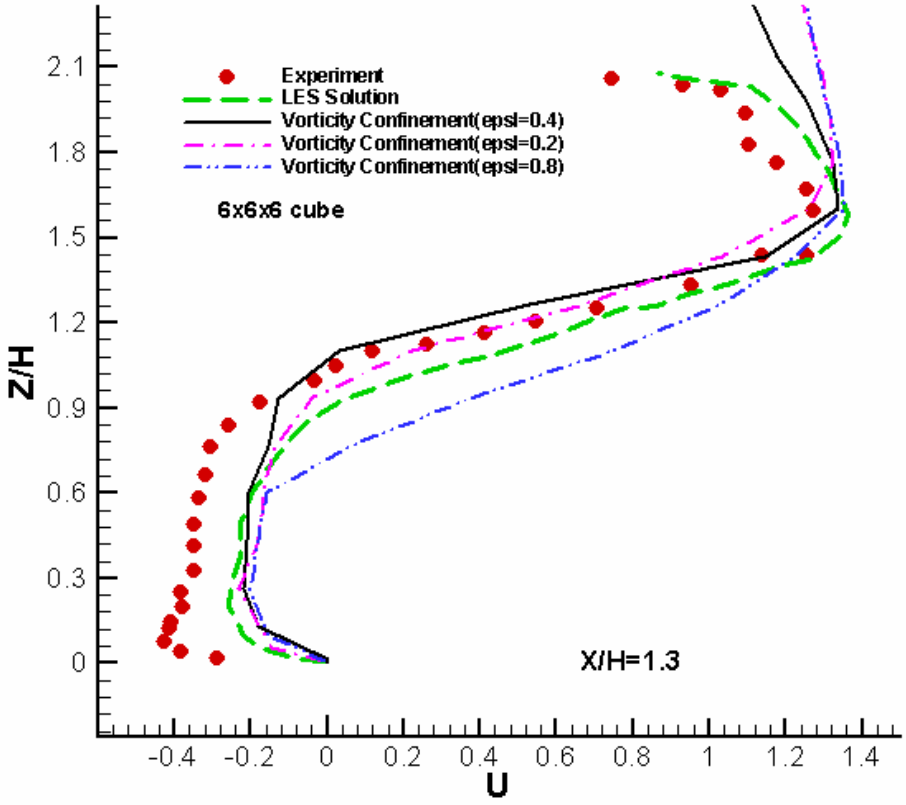

Fig. 4-105 Comparison of mean velocity component U for the different confinement coefficients at X/H=1.3 (6x6x6 Cube)

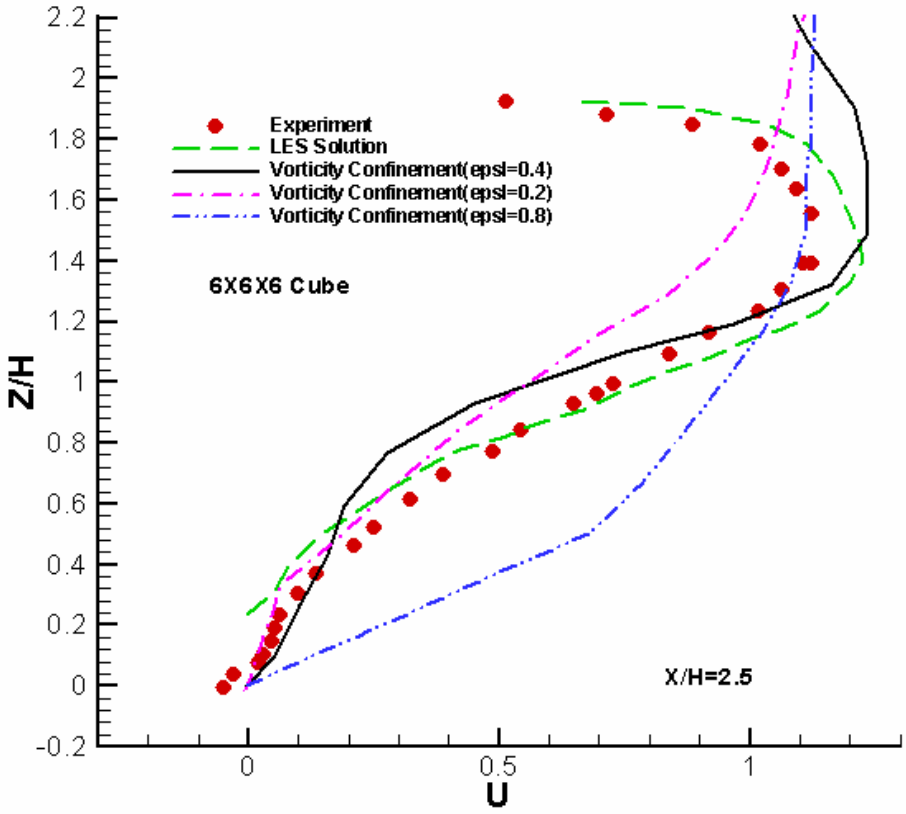

Fig. 4-106 Comparison of mean velocity component U for the different confinement coefficients at X/H=2.5 (6x6x6 Cube)

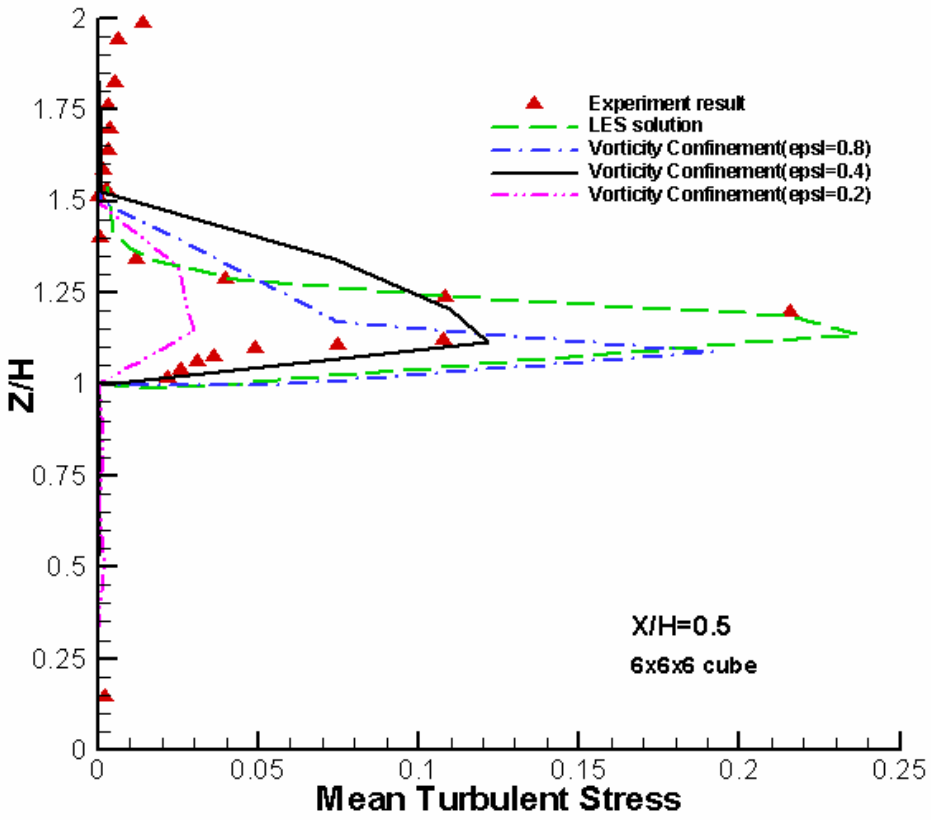

Fig. 4-107 Comparison of mean turbulent stress ($\overline{u'^2}$) for different confinement coefficients at X/H=0.5 (6x6x6 cube)

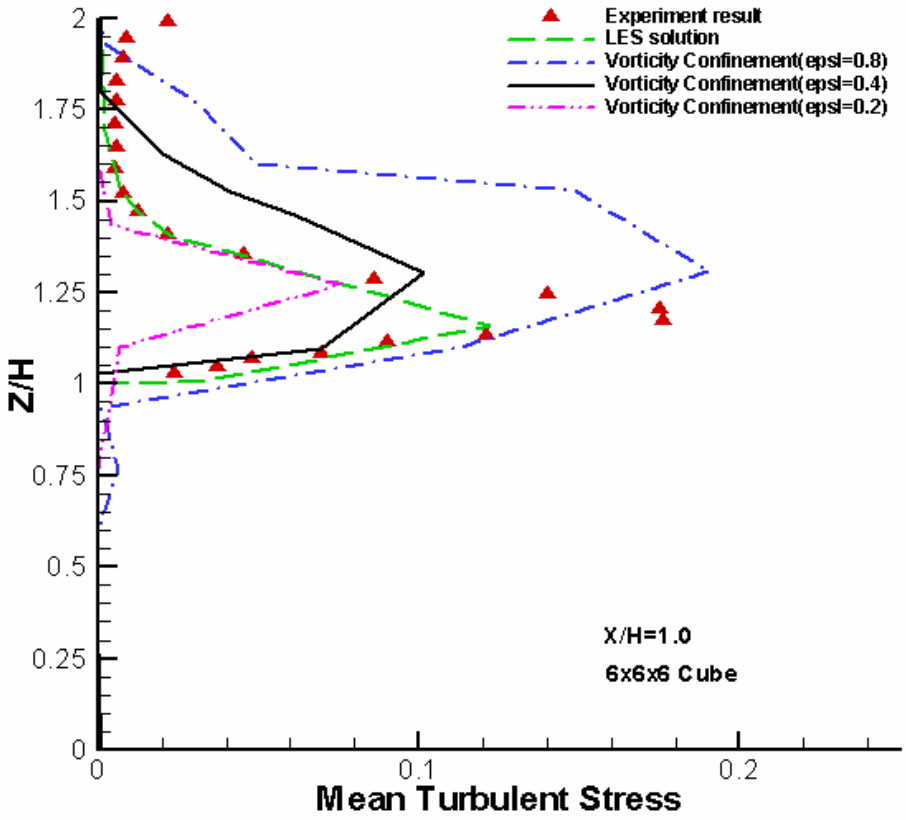

Fig. 4-108 Comparison of mean turbulent stress ($\overline{u'^2}$) for different confinement coefficients at X/H=1.0 (6x6x6 cube)

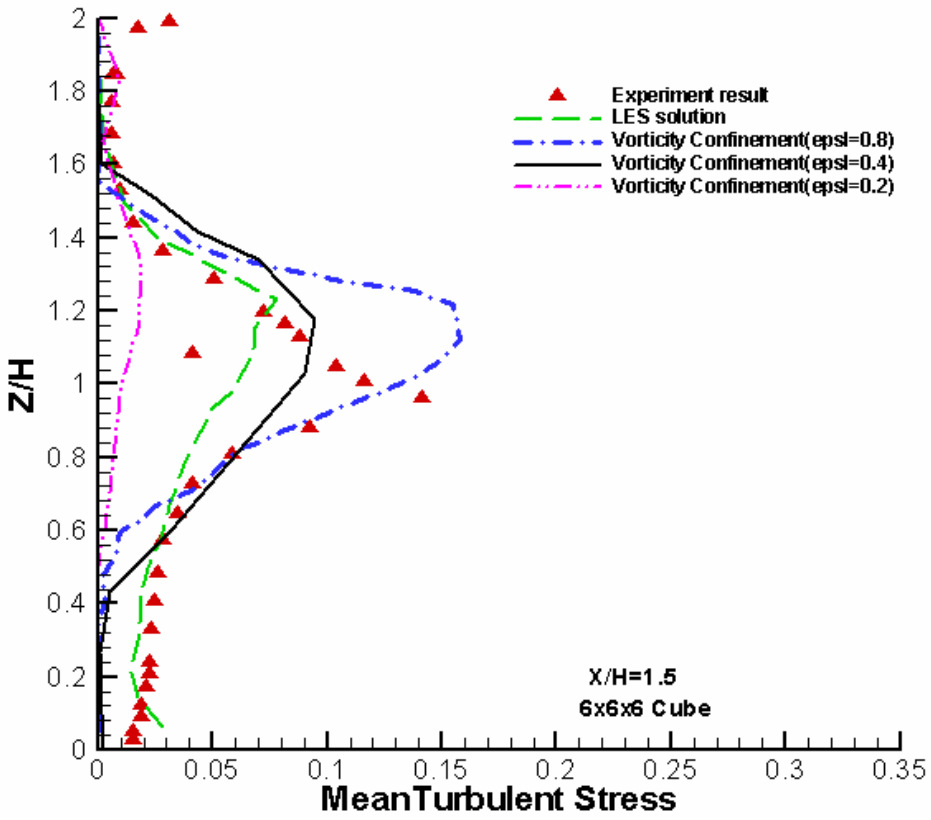

Fig. 4-109 Comparison of mean turbulent stress ($\overline{u'^2}$) for different confinement coefficients at X/H=1.5 (6x6x6 cube)

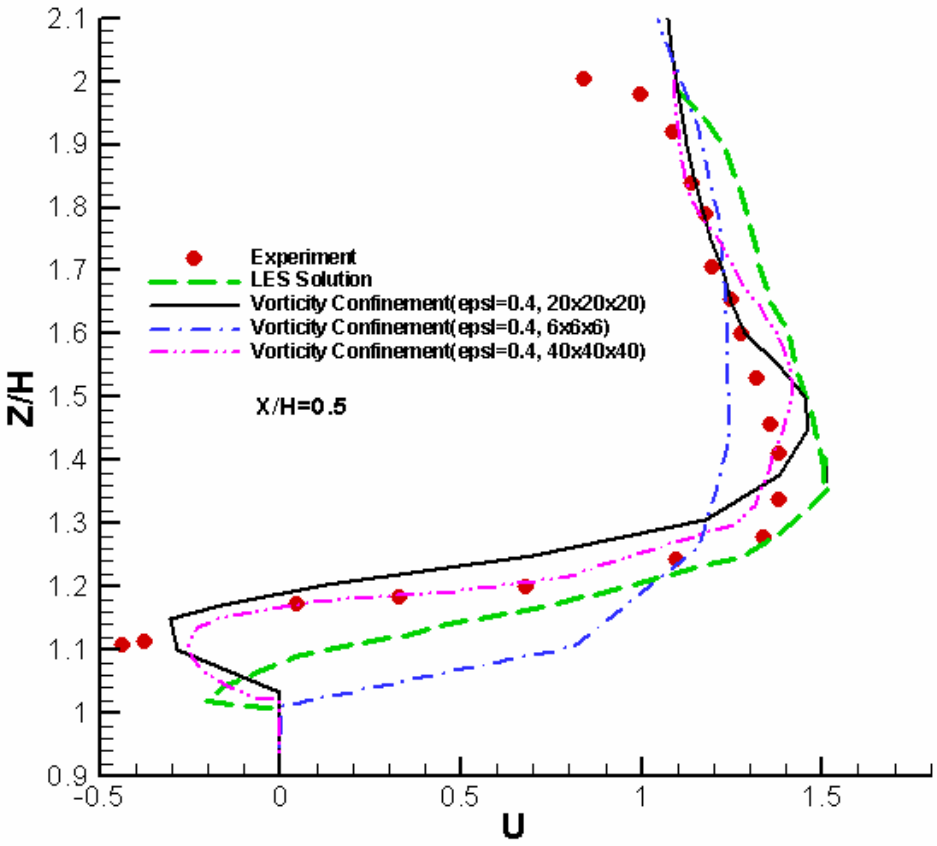

Fig. 4-110 comparison of mean velocity component U for different cube size at X/H=0.5

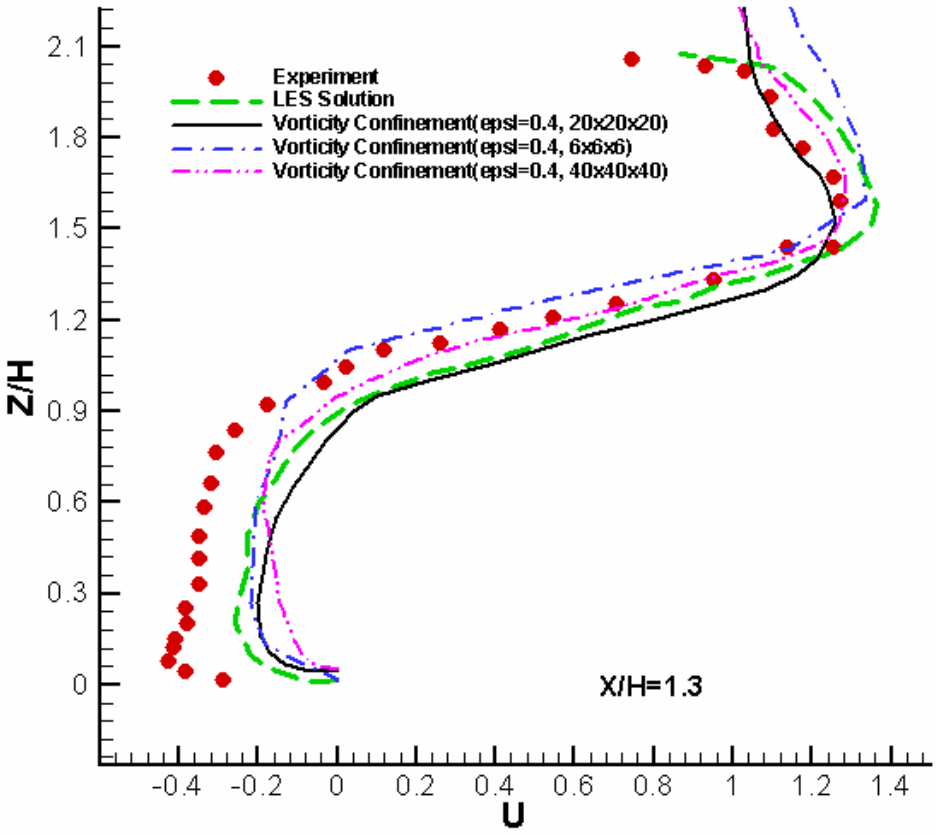

Fig. 4-111 comparison of mean velocity component U for different cube size at X/H=1.3

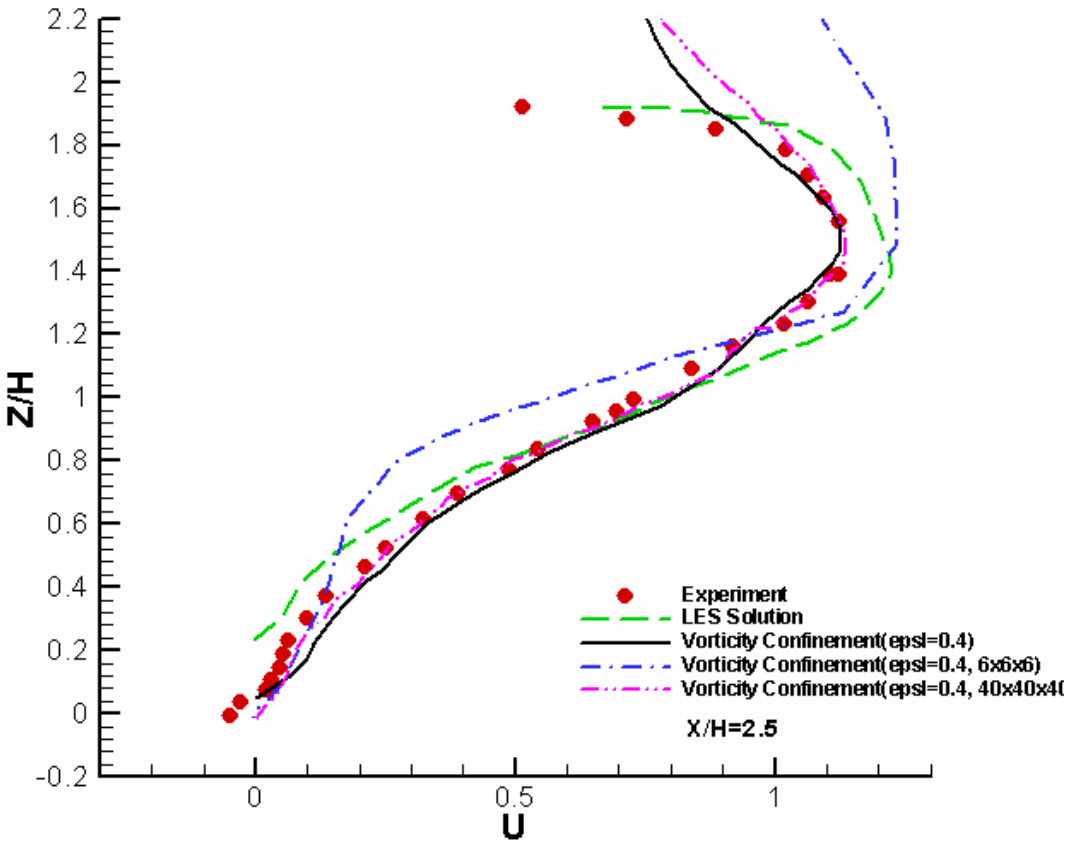

Fig. 4-112 comparison of mean velocity component U for different cube size at X/H=2.5

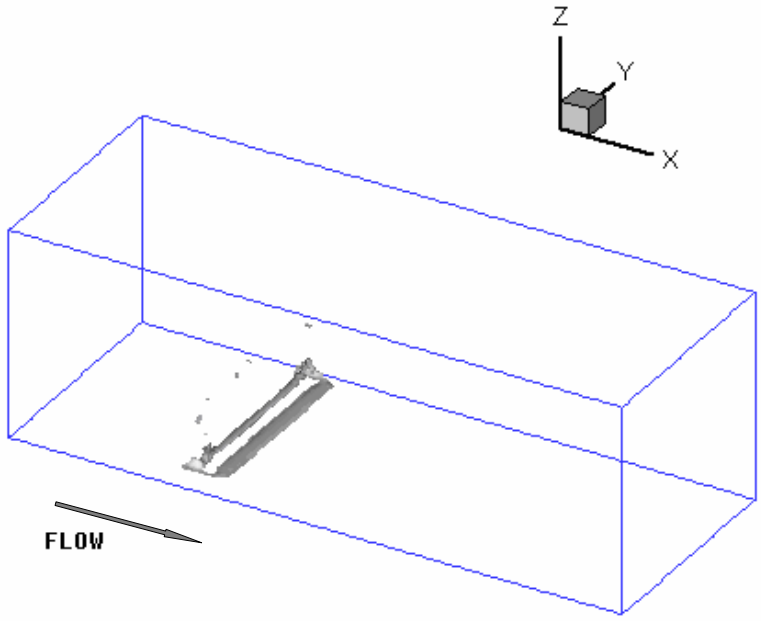

Fig. 4-113 Vorticity iso-surface, after 100 time steps

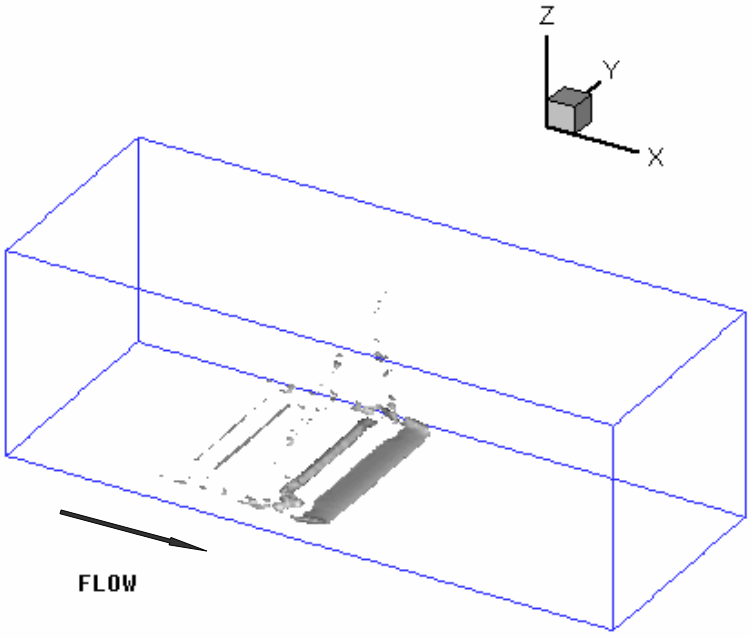

Fig. 4-114 Vorticity iso-surface, after 150 time steps

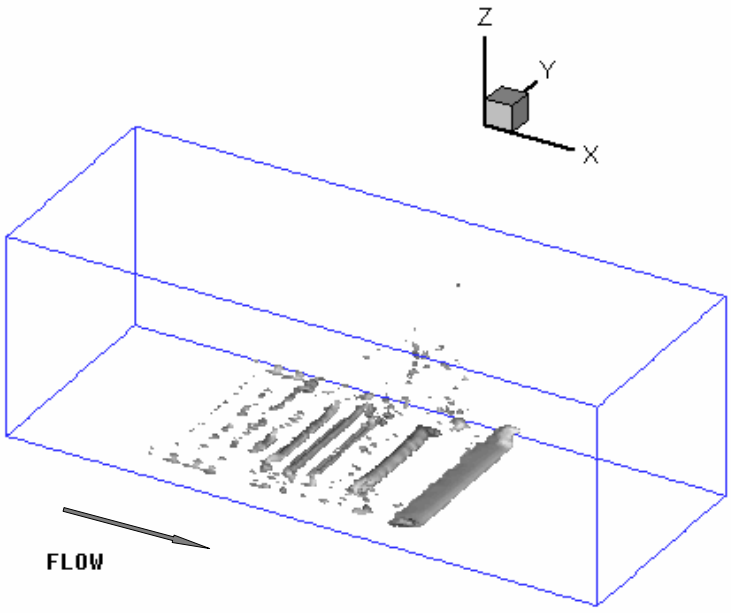

Fig. 4-115 Vorticity iso-surface, after 200 time steps

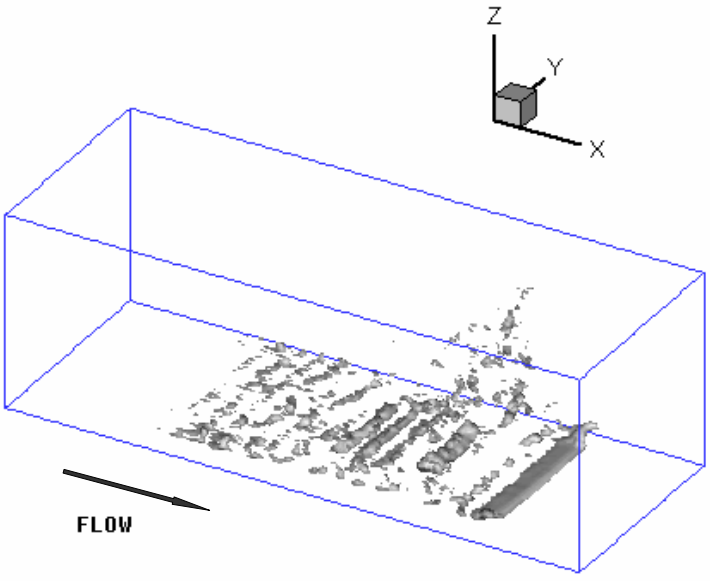

Fig. 4-116 Vorticity iso-surface, after 250 time steps

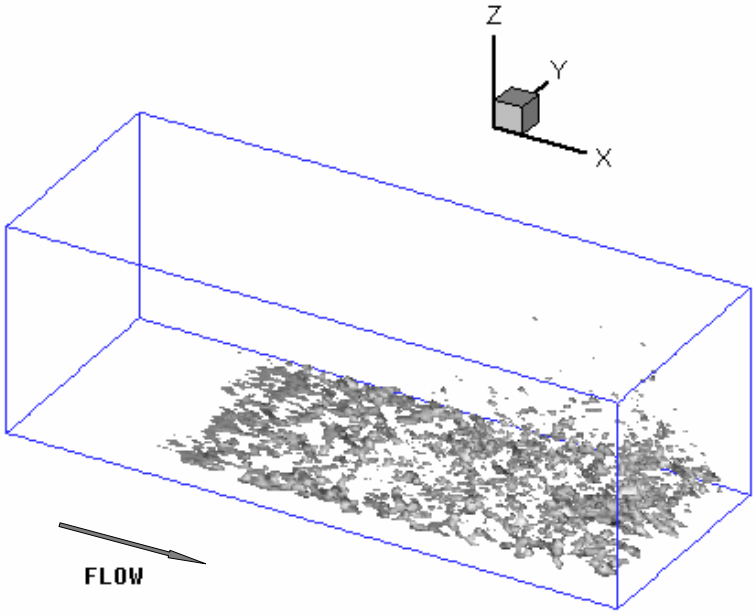

Fig. 4-117 Vorticity iso-surface, after 350 time steps

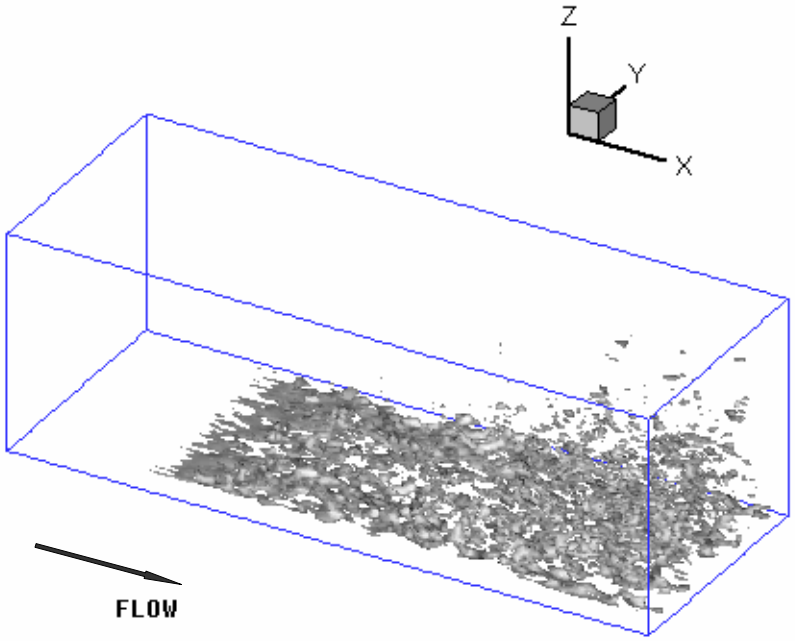

Fig. 4-118 Vorticity iso-surface, after 1000 time steps

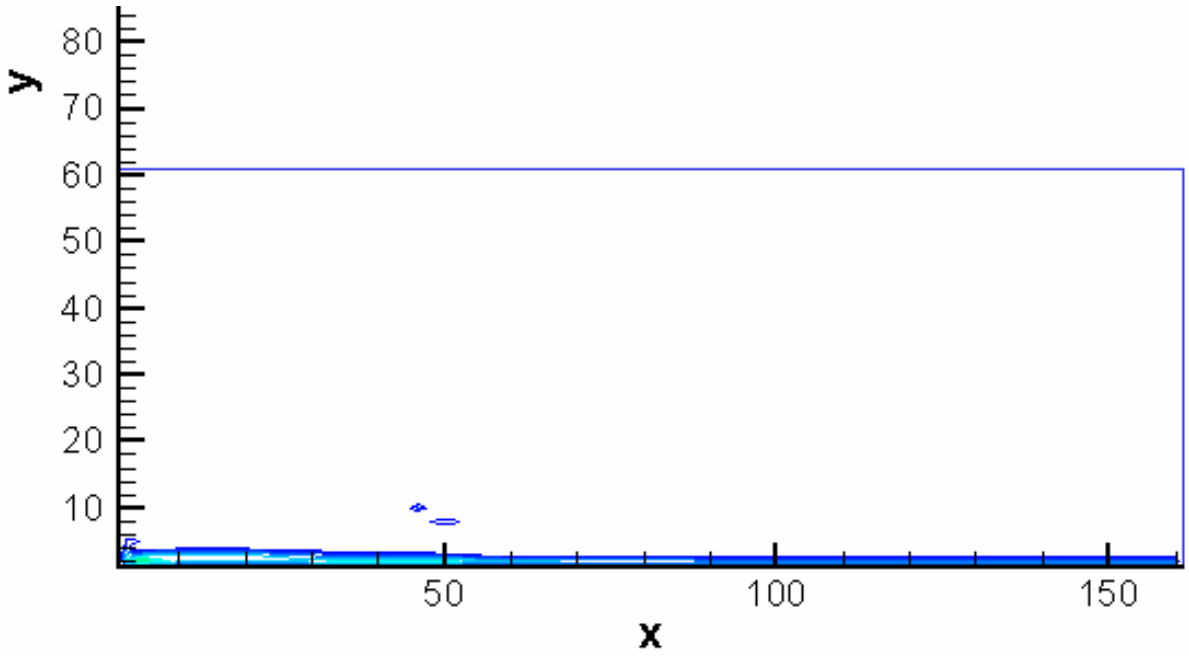

Fig. 4-119 Vorticity contours for the symmetry plane after 100 time steps

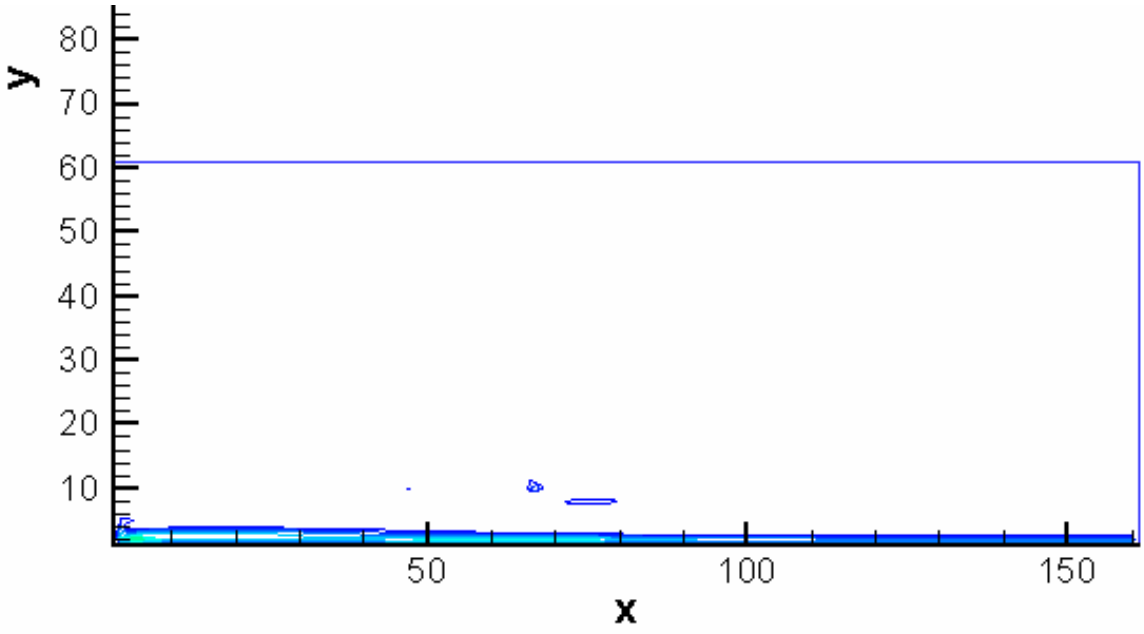

Fig. 4-120 Vorticity contours for the symmetry plane after 150 time steps

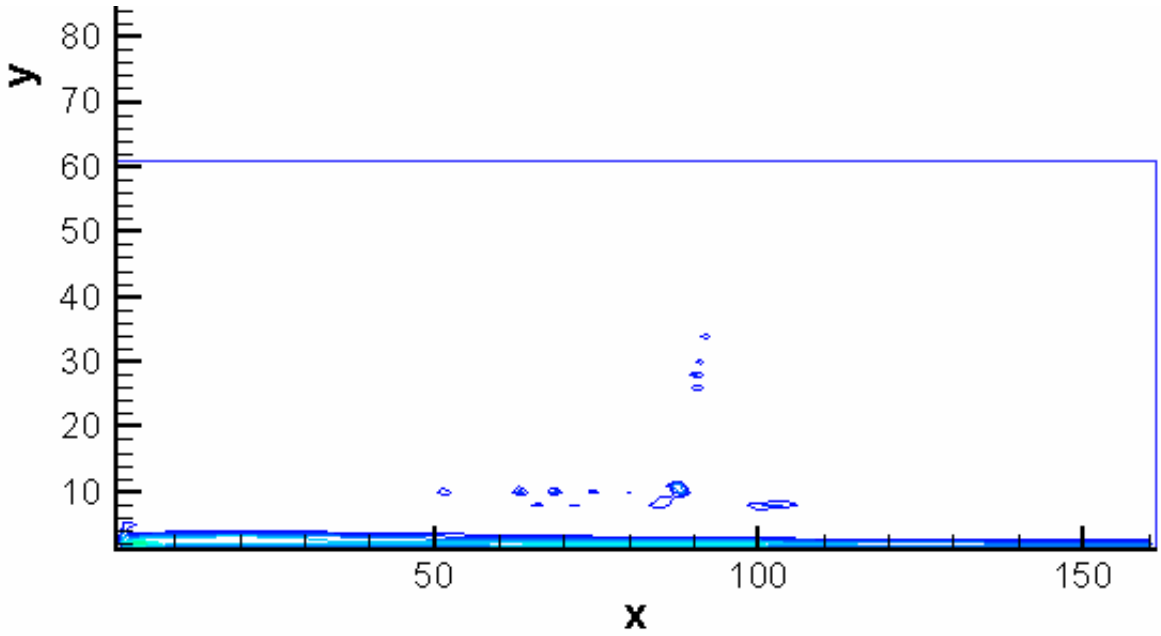

Fig. 4-121 Vorticity contours for the symmetry plane after 200 time steps

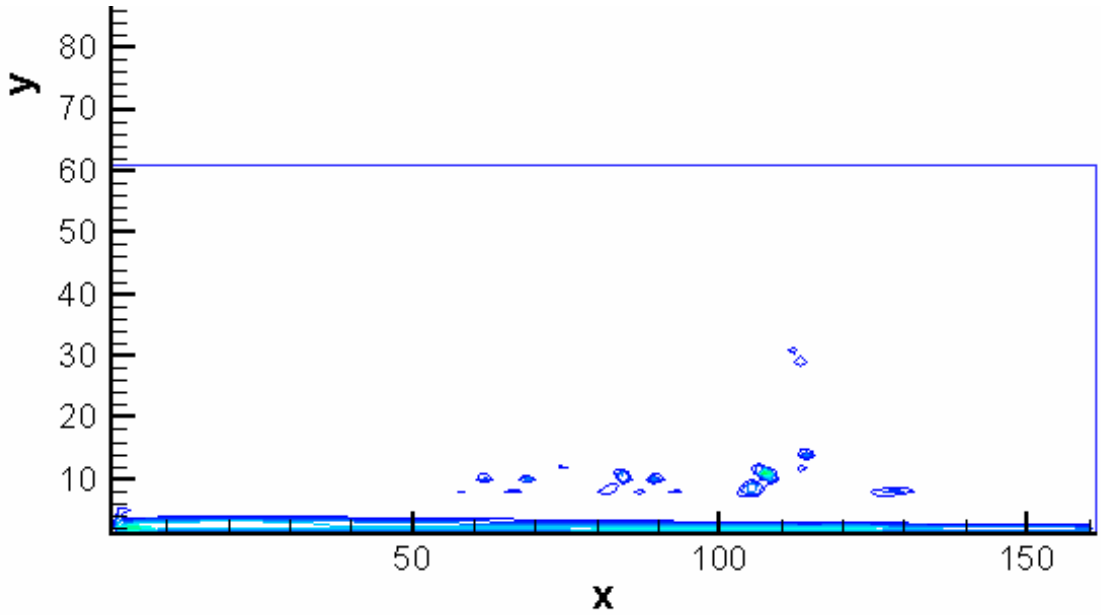

Fig. 4-122 Vorticity contours for the symmetry plane after 250 time steps

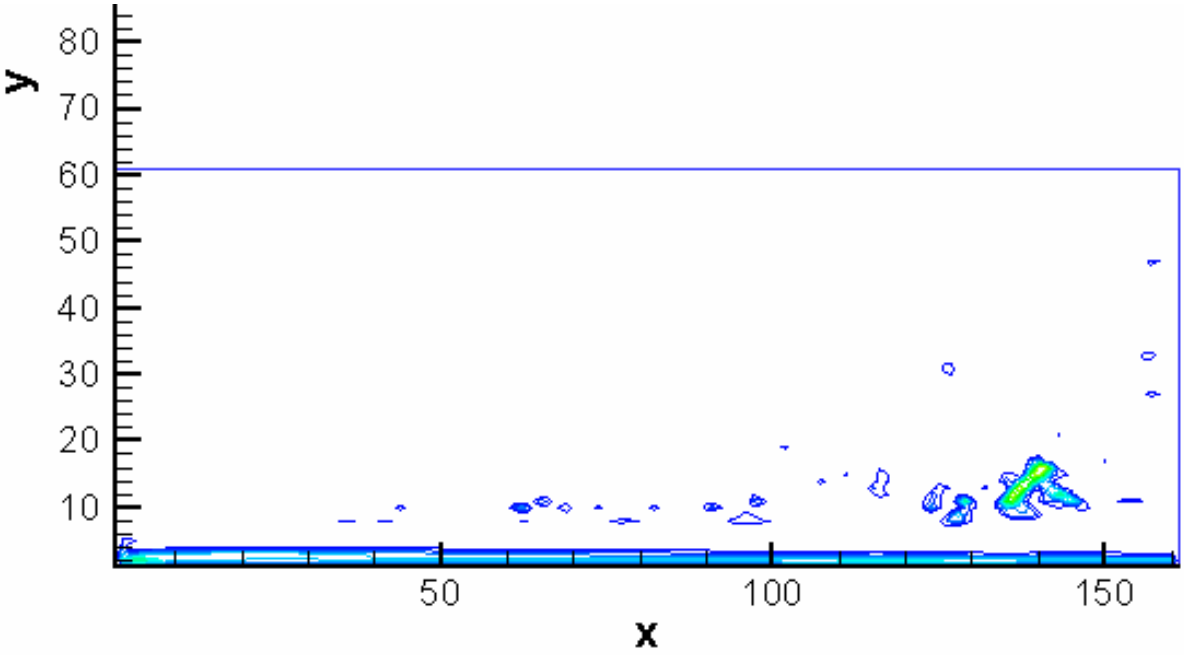

Fig. 4-123 Vorticity contours for the symmetry plane after 350 time steps

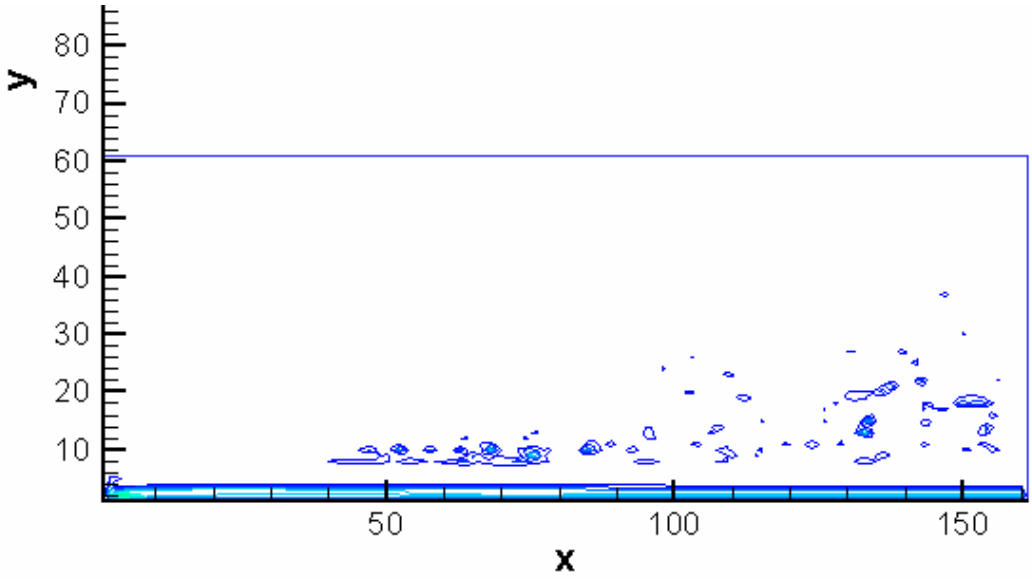

Fig. 4-124 Vorticity contours for the symmetry plane after 1000 time steps

Vita

The author, Min Xiao, was born on October 05, 1975 in Changsha, Hunan Province, P. R. China. She graduated with a Master's Degree in Fluid Mechanical Engineering from Xi'an Jiaotong University in 1999 in P. R. China. She began his Ph.D. study at Engineering Science Department of University of Tennessee Space Institute in the summer of 1999.